STUDY OF THE ELECTRON COMPONENT OF THE SOLAR WIND AND MAGNETOSPHERIC PLASMA

by

Edward Charles Sittler, Jr.
B.S., Hofstra University, 1972

SUBMITTED IN PARTIAL FULFILLMENT
OF THE REQUIREMENTS FOR
THE DEGREE OF

DOCTOR OF PHILOSOPHY

at the

MASSACHUSETTS INSTITUTE OF TECHNOLOGY
(February, 1978)

Signature of Author..Signature redacted.....
Department of Physics, February, 1978

Certified by..Signature redacted.....
Thesis Supervisor

Accepted by..Signature redacted.....
Chairman, Department Committee

STUDY OF THE ELECTRON COMPONENT OF THE SOLAR WIND AND MAGNETOSPHERIC PLASMA

by

Edward Charles Sittler, Jr.

Submitted to the Department of Physics
on February 3, 1978
in partial fulfillment of the requirements
for the Degree of Doctor of Philosophy

ABSTRACT

In this thesis a general method for analyzing electron data from the M.I.T. plasma detector on Imp 8 is formulated. This approach, which lays the groundwork for any future analysis of electron data, is also applicable for the analysis of subsonic proton data. The following topics are studied in detail.

The effects of a positively charged spacecraft upon the electron measurements is investigated. To bypass the theoretical difficulties in solving this problem, a Yukawa type screening potential with spherical symmetry is assumed. The screening distance (the Debye length) for the space charge is treated as a free parameter; varying this parameter allows us to determine the range of corrections expected for the electron distribution. Using Boltzmann equation,electron distribution function at the surface of the spacecraft is determined for a given form of this distribution far from the spacecraft. The corrections

are not found to be trivial and highly dependent upon the size of the screening distance relative to the spacecraft radius. For example, the corrections to the observed electron temperatures are on the order of 20%. There appear apparent electron drifts on the order of $\pm$50 km/sec for spacecraft potentials on the order of 5 volts. Similarly, an apparent heat flow on the order of $\pm 3 \times 10^{-3}$ ergs/cm^2/sec develops.

Semi-empirical radial profiles of the wind velocity, effective temperature, and effective heat flux vector are derived for the inner planet region of the solar system. The task is accomplished by using the basic conservation relations of mass, momentum, energy, and magnetic flux, along with empirically determined electron density distribution within the solar corona and interplanetary medium as well as an empirically determined magnetic field line topology. The calculations assume a steady state under MHD approximation.

Observations in the solar corona and solar wind are reviewed along with the present status of solar wind theory. A review of the transport theories for interplanetary electrons, more specifically the convection model by Feldman et al. (1975)[9] and the conduction model by Scudder and Olbert (1978)[14], is given.

Finally, a few samples of M.I.T. Imp 8 electron data are analyzed, showing the applicability of the analysis program developed. Core electrons are shown to be Maxwellian, moving at the same velocity as the proper frame of the plasma, and the electron temperature can be extracted from the data. The presence of pickup in the measured currents prevents us from seeing the

suprathermal electrons. Because of this, the heat flux cannot be determined.

Thesis Supervisor: Stanislaw Olbert, Professor of Physics

dedicated to my wife, Linda M. Sittler

ACKNOWLEDGEMENT

The author greatly appreciates the moral and financial support, the guidance and encouragement of Professor Herbert Bridge, Professor Stanislaw Olbert, and Doctor Alan Lazarus. Without their continued support, this research could not have been accomplished. A personal note of gratitude to Doctor Bridge for giving the author the opportunity to do research in the Department of Physics at M.I.T. The author is most greatly indebted to his thesis supervisor, Professor Stanislaw Olbert, who provided continuous support and guidance throughout the development of this thesis. Many of the ideas contained in this thesis are Professor Olbert's and the author is grateful for having had the opportunity to share them.

A special note of thanks to Doctor Michael Heinemann and Doctor Keith McGregor for their personal help and friendship while they were graduate students at M.I.T. The author is thankful for the assistance given by Doctor James Sullivan and Doctor John Belcher. Finally, he would like to thank Ralph McNutt for one of the figures contained in this thesis.

TABLE OF CONTENTS

ILLUSTRATIONS

Fig. 1 Observed electron distribution function (data points) derived from observations made by the LASL detector on board the Imp 8 spacecraft, from Feldman et al.[9] The angles indicated in parentheses give the ϕ ($\phi = \phi_C - \phi_B$) angle as defined in Figure 11, the detector is pointing relative to B. The curves are fits made by Feldman et al.[9] using a convected bi-Maxwellian for the core electrons and a truncated convected bi-Maxwellian for the halo electrons (see text).

Fig. 2 Top left figure is a schematic view of Imp 8 detector mounted perpendicular to spin axis of the spacecraft pointing in the $+Z_{SE}$ direction (X_{SE}, Y_{SE}, Z_{SE} corresond to the X, Y, Z axis of the solar ecliptic (SE) coordinate system); Y_{SE} axis points out of the paper; X_C, Y_C, Z_C are the X, Y, Z axis of the cup coordinate system; ϕ_C is the azimuthal angle of the detector normal relative to the X_{SE} axis; acceptance cone of detector is indicated (20^o in the Y_C direction, 120^o in the $X_C$direction). Top right figure displays the angular sectors, current measurements are made; 33 3/4^o and 28^o are the angular widths of

angular sectors 1 to 7 and 8, respectively. Measurements are not made in shaded region because of photo-effects. The lower figure is a cross-sectional view of the detector; the dashed lines indicate grid planes (grids 1, 3, 4, 5, and 6 are shielding grids); I_c is the collector current; ΔI is the ac component of I_c that is amplified and recorded as the measured current; the voltage Φ applied to the modulator and possible electron path are indicated.

Fig. 3a Cross-sectional View of Two Slats

Fig. 3b Cross-sectional View of Two Grid Wires

Fig. 4 Common Area of Collector Circle and Aperture Circle

Fig. 5 Normalized Response Function R versus Beta; Alpha equal to Zero

Fig. 6 Normalized Response Function R versus Alpha for various v_z in the range v_{z-} to v_{z+} (step size 2% of Δv_z used, see text); Beta equal to Zero.

Fig. 7 View of Electron Distribution Function f_e and Normalized Response Function R in v_y direction; $v_x = 0$; $v_z = 3100$ km/sec and 7000 km/sec

Fig. 8 View of Electron Distribution Function f_e and Normalized Response Function R in the v_x

direction; $v_y = 0$; v_z = 3100 km/sec, 4400 km/sec, and 6600 km/sec.

Fig. 9 Mean Response Function $\bar{R}$ versus $\varphi = v_x/v_z$ for Energy Channels 1, 2, and 4.

Fig.10 Mean Response Function $\bar{R}$ and the Double-Gaussian Fit to $\bar{R}$ versus Alpha for the Fourth Energy Channel (both were normalized to equal unity at Alpha = 0).

Fig.11 Top figure defines the electron velocity $\vec{w}$ in a coordinate system moving at the same velocity as the proper frame of the plasma. The z axis of the coordinate system is aligned along the magnetic field direction. Bottom figure shows the relationship between the cup coordinate system, the solar ecliptic coordinate system, and the magnetic field vector.

Fig.12 View of a charged perfectly conducting spherical spacecraft surrounded by a fully ionized plasma. The inner circle represents the s/c while the outer circle represents the Debye sphere. The dashed curve represents a possible electron trajectory, where r is the radial vector of the electron, $\vec{v}$ is the electron velocity, and $\vec{v}_o$ is the electron velocity at r_o.

Fig.13 Effective Potential V_{eff} versus $z = r/\lambda_D$ for fixed electron energy $\mathcal{V}$; impact parameters

b_D varied.

Fig.14 Effective Potential V_{eff} versus $z = r/\lambda_D$ for fixed impact parameter b_D; electron energy $\mathcal{V}$ varied.

Fig.15 Effective Potential V_{eff} versus z for Special Critical Trajectory; $\mathcal{V} = \mathcal{V}_S$ and fixed; impact parameter b_D varied.

Fig.16 Critical Impact Parameter Squared versus the Critical Point Distance z_c.

Fig.17 Critical Electron Energy $\mathcal{V}_c$ versus the Critical Point Distance z_c.

Fig.18 Parametrically Drawn Locus of Critical Points in $(\mathcal{V}_c, (b_D^2)_c)$ Space.

Fig.19 Graphic solution for the maximum critical energy $(U_c)_{max}$ for various spacecraft radii z_o, where the parametric solution given by Figure 18 is used.

Fig.20 $\sin^2\theta_c$ versus the Critical Point Distance z_c, where θ_c is the maximum angle θ for allowed directions.

Fig.21 Parametric Solutions of $\sin^2\theta_c$ versus the Critical Electron Energy $\mathcal{V}_c$ for various Spacecraft Radii z_o.

Fig.22 Electron Trajectories in Debye Screening Potential;Curve 1 corresponds to a critical

trajectory, where $U = (U_c)_{max}$, $b_D = (b_D)_c$, while Curves 2 and 3 are trajectories with smaller impact parameters.

(a) $z_o = 0.1$

(b) $z_o = 1.0$

(c) $z_o = 10.0$

Fig.23 Electron Trajectories in Debye Screening Potential; trajectories rotated so they strike the spacecraft at the same point "P". Angles next to solid curves indicate the asymptotic directions of the actual trajectories; angles in parentheses next to the dashed lines indicate the apparent asymptotic direction the electrons appear to be coming from. The electron energy U = 1.0 is the same for all trajectories.

(a) $z_o = 0.1$

(b) $z_o = 1.0$

(c) $z_o = 10.0$

Fig.24 View Showing Spacial Dependence of $f_e(\vec{r}_o, \vec{v}_o)$. Inner circle represents the spacecraft, which is rotating; spin axis perpendicular to ecliptic plane and pointing north; ϕ_c indicates angle of rotation; outer circle represents Debye sphere; direction of wind velocity indicated at bottom of figure.

Fig. 25 Iso-contours of the ln $f_e(\vec{r}_o, \vec{v}_o)$. Convected Maxwellian assumed at infinity; electron temperature $T_c = 1.2 \times 10^5$ °K; spacecraft potential $\Phi_o = 4.5$ volts for solid contours; dashed circles for $\Phi_o = 0$ volts; wind velocity is pointing in radial direction away from sun and has a magnitude equal to 400 km/sec (arrow in center of figure indicates wind velocity vector in spacecraft frame); Φ_c indicates angle at which ln f_e $(\vec{r}_o, \vec{v}_o)$ is observed at $r = r_o$; refer to Fig.24; shaded region indicates forbidden zone; w_n normal velocity of electron (-r direction) in thermal speeds, w_t transverse velocity relative to $\vec{r}$ of electron in thermal speeds. Contours numbered 1 to 7 correspond to electron velocities equal to 0.4, 0.6, 0.8, 1.0, 1.2, 1.4, 1.6.

(a) $\phi_c = 0^o$, $z_o = 0.1$

(b) $\phi_c = 45^o$, $z_o = 0.1$

(c) $\phi_c = 90^o$, $z_o = 0.1$

(d) $\phi_c = 135^o$ $z_o = 0.1$

(e) $\phi_c = 180^o$, $z_o = 0.1$

Fig. 26 Same as Fig. 25, except $z_o = 10.0$

(a) $\phi_c = 0^o$, $z_o = 10.0$

(b) $\phi_c = 45^o$, $z_o = 10.0$

(c) $\phi_c = 90^o$, $z_o = 10.0$

(d) $\phi_c = 135^o$, $z_o = 10.0$

(e) $\phi_c = 180^o$, $z_o = 10.0$

Fig. 27 Same as Fig. 25, except normalization correction factored out (see text)

(a) $\phi_c = 0^o$, $z_o = 0.1$

(b) $\phi_c = 45^o$, $z_o = 0.1$

(c) $\phi_c = 90^o$, $z_o = 0.1$

(d) $\phi_c = 135^o$, $z_o = 0.1$

(e) $\phi_c = 180^o$, $z_o = 0.1$

Fig. 28 Same as Fig. 26, except normalization correction factored out (see text)

(a) $\phi_c = 0^o$, $z_o = 10.0$

(b) $\phi_c = 45^o$, $z_o = 10.0$

(c) $\phi_c = 90^o$, $z_o = 10.0$

(d) $\phi_c = 135^o$, $z_o = 10.0$

(e) $\phi_c = 180^o$, $z_o = 10.0$

Fig. 29 Iso-contours of $\ln f_e (\vec{r}_o, \vec{v}_o)$ seen by detector with angular response perfectly differential in angle; w_x, w_y are the X, Y components of the electron velocity in solar ecliptic coordinate system; otherwise figure is the same as Fig. 25 (see text for details).

Fig. 30 Same as Fig. 29, except normalization correction has been factored out (see text)

Fig. 31 One-dimensional Analog of Spherical Model; plot of "spacecraft" potential 0 versus z; surface of spacecraft for this problem occurs at z = 0; outer surface of Debye sphere occurs at $|z| = \lambda_D$: wind velocity direction indicated; electric field E from potential indicated.

Fig. 32 Log-Log Plot of Electron Number Density versus the Radial Distance r from the Sun ($r_\odot$ = radius of sun); densities characteristic of equatorial regions of the sun, curves plotted are model fits to data (see text);"Spherical Model"

Fig. 33 Log-Log Plot of Wind Velocity versus r; "Spherical Model"

Fig. 34 Log-Log Plot of Effective Temperature versus r; "Spherical Model"

Fig. 35 Log-Log Plot of Effective Heat Flux Vector versus r; "Spherical Model"

Fig. 36 Magnetic Field Line Topology of Model Fit to Observed Hole Boundary of Polar Coronal Hole studied by Munroe and Jackson (1977); pluses are data points from Munroe and Jackson; angles next to field lines indicate co-latitude of field line at solar surface, $r = r_\odot$.

Fig. 37 Log-Log Plot of Electron Number Density for Polar Regions of the Sun versus r; Polar

Polar Coronal Hole Model; wind velocity 500 km/sec at 1 AU; curves number 1, 2, and 3 correspond to density profiles 1, 2, and 3 in Fig. 37.

Fig. 47 Same as Fig. 46, except that Effective Temperature is plotted.

Fig. 48 Same as Fig. 46, except that Effective Heat Flux Vector is plotted

Fig. 49 Plot of $\overline{f}^*$ versus Particle Velocity in Proper Frame of Plasma. Solid curve corresponds to model by Scudder and Olbert (1978)[14] where f_o^* is a kappa distribution function. Dashed curve corresponds to model by Feldman et al. (1975)[9] using typically observed parameters at 1 AU (see text).

Fig. 50 Plot of F versus $\overline{v}_z$ ("energy" spectrum) for spectrum # 1. Numerals on the graph symbolize the angular sector for that data point (see Fig. 2). Circled numbers along abscissa indicate energy channels 1 to 8 for the data points. Lines drawn through data points are not fits, are only drawn to aid the eye ($\theta_B = 70.5^o$, $\phi_B = 119^0$, n_p =42, V = 346 km/sec, flow coming slightly from the east at -6^o) (see text)

Fig. 51 Same as Fig. 50, except Plot of Data for Spectrum #2 ($\theta_B = 150^o$, $\phi_B = 115^o$, $n_p = 27$, $V = 338$ km/sec, flow coming from the east at $\pm 5^o$)

Fig. 52 Same as Fig. 50, except lines drawn are an actual fit to the data where a convected Maxwellian is assumed for f_e (Result of fit is $T_c = 1.1 \times 10^5$ ^oK, $\Phi_o = 0$ volts)

Fig. 53 Same as Fig. 51, except lines drawn are an actual fit to the data where a convected Maxwellian is assumed for f_e. (Result of fit is $T_c = 1.12 \times 10^5$ ^oK, $\Phi_o = 0$ volts)

Fig. 54 Angular Plot of Observed F versus ϕ_c for Spectrum # 1. Numerals used for data points indicate the energy channel number for that data point (see Chapter I). Circled numbers along abscissa indicate the number of the angular sector for the data points (see Fig. 2) Solid curves are a fit to the data using a convected Maxwellian for f_e. Vertical dashed lines indicate directions along $\vec{B}$. Horizontal dashed line indicates 5 picoamp level.

Fig. 55 Same as Fig. 54, except for Spectrum #2

Fig. 56 Same as Fig. 54, except data plotted corresponds to spectra more typical of the solar wind

(n_p = 7 cm^{-3}, v = 547 km/sec) (Result of fit is T_c = 1.3 x 10^5 ^oK, Φ_o = 0 volts

Fig. 57 Plot of F versus $\bar{v}_z$ derived from Preliminary Electron Measurements on Voyager 2; pluses are data points; solid curve is a model fit to the data using two non-convected Maxwellians for f_e (n_p = 4.1 cm^{-3}, V = 410 km/sec), total electron temperature T = 1.06 x 10^5 ^{o} K), see text for details.

INTRODUCTION AND SUMMARY

The primary objective of this thesis is to understand the physics of interplanetary electrons. One of the means of accomplishing this goal is the analysis of electron measurements made by the M.I.T. detector on Imp 8. Because of unexpected difficulties in the detector, not all ofthe original goals could be achieved. More specifically, the heat flux due to electrons cannot be acquired from the data. However, we are able to show that estimates of the electron temperature can be extracted from the measured currents quite well.

Our effort to carry out the electron analysis is the first real attempt within the M.I.T. Space Plasma Group in this direction. Heretofore, the major emphasis at M.I.T. had been confined to studying the positive ion component. Since I was the first one to attempt the analysis of electron measurements by M.I.T. detectors, a new analysis program had to be developed. Methods of analysis had been developed for proton measurements; since, in contrast to protons, electrons are highly subsonic, these methods specifically designed for proton measurements did not apply. In Chapter I after giving a brief description of the detector, the general expression relating the measured currents and the electron distribution function is given. From this expression,it is apparent that an accurate knowledge of the transmission (response) function of the detector is required if any quantitative information about the electron distribution function is to be acquired from the measured currents. This

expression is shown to be reducible to a simpler form, taking advantage of the subsonic character of the electrons. Fitting the response function by a sum of two Gaussians we are able to express the measured currents in such a form that analytical expressions for the current can be derived. These expressions are a function of both model dependent distribution function parameters and detector parameters; they can be fitted to the currents giving us estimates of various model dependent physical parameters such as the electron temperature.

In Chapter II the effects of spacecraft charging upon electron measurements is investigated. This detailed study was initiated by the controversial paper by Feldman et al. (1975)[9]. In this paper, which contains the results of electron measurements made on Imps 6, 7, and 8, the authors corrected the data improperly for the effects of spacecraft charging. Thus, there was a need to re-analyze the problem. Since the actual solution of the spacecraft charging problem is virtually impossible to obtain, we make the ad hoc but qualitatively reasonable assumption that the potential is described by a Yukawa type screening potential (spherical symmetry), where the screening distance (Debye length) is an adjustable parameter. Since we do not know the screening distance, we can only estimate the range of corrections which occur. A form for the electron distribution function far from the spacecraft is then assumed and, using Boltzmann's equation, the electron distribution function at the spacecraft surface is determined.

As expected, spacecraft charging effects are not trivial for electron energies on the order of the electron thermal speed (13 eV). It was discovered that depending upon the detector design (integral, differential in angle), one will observe different corrections to the data (electrons seemingly drifting away from the sun, toward the sun). The corrections are found to be very sensitive to the size of the screening distance relative to the spacecraft radius (spherical geometry, plane-parallel geometry). This study shows that corrections on the order of 20% to the observed electron temperature must be expected. A shift in energy experienced by electrons and applicable for electron energies sufficiently above the spacecraft potential (electron energies $\gtrsim$ 10 eV for spacecraft potential $\lesssim$ 2 eV) was derived. Finally, because most of the heat is carried by the suprathermal electrons, it was concluded that the heat flux measurements are not affected by spacecraft charge provided the spacecraft potential is not too large ($\lesssim$ 5 eV).

One needs for a proper analysis of the electron data some theoretical understanding of the physics of interplanetary electrons. For this reason, in the first half of Chapter III, a brief review of coronal and solar wind observations is given along with a review of the present status of solar wind theory. In Chapter IV, a review of electron observations is given along with a review of the two present contending models for the energy transport (convection, conduction) by interplanetary electrons. First, the model proposed by Feldman et al. (1975)[9] is discussed. This model, where the authors suggest two separate electron

populations (core, halo) described by bi-Maxwellian distributions drifting relative to each other in the proper frame, is difficult to justify from general physical arguments. According to this model, the thermal energy is transported in the proper frame (heat flux vector) purely by convection. We felt that the more conservative point of view, where the heat flux vector results from a skewness in the electron distribution function (conduction) must first be considered. In the process of developing a thoery of energy transport by conduction in the interplanetary medium, it became apparent that the macroscopic parameters (wind velocity, density, temperature, heat flow vector) of the interplanetary medium as a whole was needed. By using the basic conservation relation for mass, momentum, energy, and magnetic flux, along with empirically determined electron density distributions in the corona and interplanetary medium, and empirical coronal magnetic field line topologies, we were able to determine these macroscopic parameters forthe interplanetary medium as a whole. In the second half of Chapter III, the results of these calculations are given.

Finally, in Chapter V a few samples of electron data from the M.I.T. detector on Imp 8 are given and analyzed, showing the applicability of the method developed in Chapter I, and that measurementsofthe electron temperature can be derived from the data. We show the core electrons to be Maxwellian and moving at about the same velocity as the protons. The presence of pickup prevents us from seeing the suprathermal electrons so that we cannot determine by how much the higher energy electrons deviate

from isotropy; therefore, we cannot acquire estimates of the heat flow vector from the data. Before concluding, a preliminary sample of Voyager 2 data is displayed, showing the significantly improved dynamical range of M.I.T. type detector over that on Imp 8. Voyager measurements demonstrate the presence of the suprathermal electrons.

CHAPTER I

PROPERTIES AND ANALYSIS OF M.I.T. PLASMA DETECTORS

(1.) Introductory Remarks

In this chapter, we discuss the development of an analysis program for electron measurements made by the M.I.T. Imp 8 detector in the solar wind. In order to understand better the approximations made and the motivations behind the approach used in developing this analysis program, some of the observational properties of solar wind electrons are reviewed.

Electron observations in the solar wind have been made by a number of different spacecrafts: Pioneer, Explorer, Vela, Ogo 5, Imp 6, 7, and 8, Mariner 10, Helios A and B. Results of these observations have been given by Wolfe and McKibben (1968),[1] Wolfe et al. (1967),[2] Montgomery et al. (1968, 1970),[3,4] Ogilvie et al. (1971),[5] Montgomery (1972),[6] Serbu (1972),[7] Feldman et al. (1973, 1975),[8,9] Scudder et al. (1973),[10] and Rosenbauer et al. (1976).[11] Most of these observations have been made near the vicinity of the earth, and thus confined to the ecliptic plane and one astronomical unit (AU) from the sun. Exceptions to this are Mariner 10 and the Helios A and B spacecrafts, which, respectively, came as close as 0.46 AU and 0.3 AU to the sun, though still confined to the ecliptic plane.

Solar wind electrons with energies less than 60 ev, commonly called "core" electrons, are observed to be approximately isotropic and Maxwellian. In contrast, the distribution of electrons with energies greater than 60 ev deviates from that Maxwellian, exhibiting a high-energy tail in excess of a Maxwellian profile.[3] This component is commonly referred to as "suprathermal" or "halo" electrons. As an example, refer to Figure 1, which is a plot of the electron distribution function determined from electron measurements made by the Los Alamos Scientific Laboratory (LASL) plasma detector on Imp 8 and published by Feldman et al.[9]

The bulk velocity of the electrons is found to be about the same as the bulk velocity of the positive ions (wind velocity). Bulk speeds for electrons and ions during quiet times vary over the range from 300 km/sec to 500 km/sec with an average of 425 km/sec or equivalently energies of 930 ev for protons and 0.5 ev for electrons. The average electron density, n_e, is about 10 electrons - cm^{-3}, and within experimental error, is found to be equal to the positive ion density.[9] A typical electron temperature T_e is 1.5×10^5 $^oK \approx$ 13 ev.[6,9,10] For that temperature, the rms electron thermal speed $\bar{w}_e$ is about 2600 km/sec, and since wind speeds V are about 400 km/sec, the electrons are "subsonic." In most instances, the electrons are found to be two to three times hotter than protons $T_p \sim 6 \times 10^4$ ^oK [Feldman et al. (1976)[12]]. Exceptions to this rule are found in high speed streams,

$V > 650$ km/sec, where proton temperatures have been observed to be two to three times greater than electron temperatures.[12] The distribution function for electrons, though nearly isotropic for low energies, is skewed at higher energies along the magnetic field direction such that a non-zero third moment in the proper plasma frame, i.e., heat flow vector $\vec{q}_e$ results. The $\vec{q}_e$ varies in the range 10^{-3} to 10^{-2} ergs $-cm^{-2}$ - sec^{-1} and generally has been observed to point in a direction away from the sun along the magnetic field.[3,5,6,8,9] The q_e is observed to be about 40 to 100 times greater than that for protons, as expected on theoretical grounds.[3,8,9] Since the electrons dominate the transport of thermal energy in the solar wind, detailed study of the third moment of the electron distribution function f_e deserves special attention. To obtain a reliable estimate of $\vec{q}_e$ one needs to know the shape of f_e in quite some detail. The empirical knowledge of f_e depends strongly on the quantitative understanding of the response of the detector and the method of data analysis. Therefore, we begin our discussion with the description of the M.I.T. electron detector.

(2.) A Description of the M.I.T. Detector on Imp 8

As shown in Figure 2, the detector is cylindrical in shape with an aperture at one end and a collector plate at the other. It contains numerous plane grids.[13] Any charged particles striking the collector plate will contribute to the current I_c shown leaving the collector plate. Since the collector plate is ac coupled to the amplifier network, only the alternating component of I_c will contribute to the current ΔI shown entering the amplifier network. A modulated voltage is applied to grid 2; it is composed of a dc potential Φ_o with a superposed 1 khz square wave of amplitude $\Delta\Phi = \Phi_+ - \Phi_-$ as shown. The sign of the dc potential relative to ground imposed on grid 2 ("ground" stands for the surface of the spacecraft), is the same as that of the charged particle being detected (positive for protons, negative for electrons), the peak-to-peak value of the square wave defines the energy "window," and the average value or dc component defines the energy "level." Grids 1, 3, 4, 5, and 6 and the walls of the cup are at ground potential. Grid 1 allows for a well-defined potential barrier between grids 1 and 2, while grids 3, 4, 5, and 6 are shielding grids preventing the ac voltage on the modulator grid from inducing currents on the collector by direct capacitive coupling. Grid 7, the suppressor grid, is biased to a negative potential in order to prevent the escape of the photoelectrons and secondary electrons from the

collector plate. The suppressor voltage is -200 volts for proton measurements and -20 volts for electron measurements.

The operation of the instrument can be described in the following way: Let Φ_+ and Φ_- represent, respectively, the upper and lower levels of the square wave potential applied to the modulator grid. Due to geometry, only the normal component of the electron velocity v_z will be affected by the potential barrier between grids 1 and 2. The corresponding upper and lower v_z limits are given by

$$\frac{1}{2} m_e v_{z\pm}^2 = e \Phi_\pm \tag{1.1}$$

When the modulator is at potential Φ_+ only electrons with $v_z > v_{z+}$ will penetrate the potential barrier, while particles of opposite charge are virtually unaffected by the potential barrier and thus contribute only a dc current to the collector. Furthermore, there is a contribution to this dc current for electrons with $v_z > v_{z+}$, for the modulator potential $\Phi_m = \Phi_+$. Since more electrons pass through this potential barrier for $v_z > v_{z-}$ than for $v_z > v_{z+}$, the collector receives an ac current from electrons 180^o out of phase with the modulator potential for electrons satisfying the condition

$$v_{z-} < v_z < v_{z+} \tag{1.2}$$

If the collector is ac coupled to the amplifier network of the instrument, then only those electrons within the range indicated by expression (1.2) are measured.

Briefly, the electronics is, in part, composed of a high

gain preamplifier ac coupled to the collector whose output is connected to a series of intermediate amplifiers. The instrument is designed to measure currents over a four decade range with a minimum sensitivity approximately equal to two picoamps. The size of the input signal determines at what point along the amplifier string the output signal is sampled (intermediate amplifiers are connected in series such that the total gain $G_T + N_S G$, where N_S is the number of amplifiers the signal passes through, and G is the gain of each amplifier). The output of these amplifiers then passes through a synchroneous detector which only selects signals of the proper phase (180^o out of phase with modulator potential). Those signals are rectified and provide a current which charges an integrating capacitor. The total charge accumulated (voltage) is proportional to the initial signal strength, total amplifier gain, and integration time. Then a logarithmic analog-to-digital (A/D) converter converts this output voltage to an 8-bit word, which is temporarily stored in a memory until asked for by the spacecraft and sent back to Earth in the spacecraft telemetry stream. Due to the logarithmic conversion, a constant quantization error relative to the current I on the order of 1.6% results.

(3.) Operational Modes of the Detector on Imp 8

The M.I.T. detector is mounted perpendicular to the spin axis of the Imp 8 spacecraft (s/c) as shown in Figure 2, such that the detector normal sweeps through a 360^{o} circle in the ecliptic plane.

The angular response of the detector is directionally differential in the ecliptic plane along the azimuthal direction of rotation (y-axis of cup) and integral perpendicular to the ecliptic plane along the spin axis (x-axis of cup). The corresponding acceptance angles are, respectively, $\pm 10^{o}$ and $\pm 60^{o}$ wide with respect to the cup normal.

The energy range is from 50 ev to 7 kev for ions, and for electrons the energy range can either be 22 ev to 140 ev or 22 ev to 2 kev depending upon the instrument mode. In all, there are 26 energy levels or channels which are displayed in Table 1 along with the corresponding velocity range for protons and electrons. The energy levels are contiguous and logarithmically spaced and except for the first few energy levels, which are used only for electrons, the ratio of the width of the energy channel to the mean channel energy is constant and on the order of 21%. Note, that when we use the word "energy" in this context (energy level, energy channel), we more precisely mean the energy of an electron with velocity normal to the modulator grid plane. The corresponding resolution for the normal velocity, v_z, into the sensor $\Delta v_z / \bar{v}_z$ is 10.5%

where

$$\overline{V_z} = (V_{z+} + V_{z-})/2 \tag{1.3}$$

and

$$\Delta V_z = V_{z+} - V_{z-} \tag{1.4}$$

Each s/c rotation is subdivided into a number of angular sectors. The size of each angular sector and their number are determined by the instrument mode. In the case of electron measurements, the angular sector size and sequence as shown in Figure 2 are the same for all modes, i.e., tracking mode (TMS), non-tracking mode (NTMS), and acquisition mode (AMS). Referring to Figure 2, one can see that no measurements are made in the forward 90° sector centered on the sunward direction because of a photoelectric effect. The remainder of the angular sweep is subdivided into seven 33.75°, and one 25.31^{0} angular sector. The 25.31° angular sector is always the last one measured in an angular sweep where the remaining 8.44° is used to perform various logic operations by the instrument, such as stepping the modulator voltage to the next energy level.

The energy coverage for electrons in NTMS and AMS are identical and ranges between 22 ev and 2 kev, using 21 energy levels in all. As for TMS, the energy range occurs between 22 ev and 140 ev, using only 8 energy levels. In this mode, for every proton spectrum, two electron energy levels are sampled, so that 4 proton spectra are taken for each 8-level

electron spectrum (25 seconds and 2 minutes, respectively, for each proton and electron spectrum). In doing this, a 25 second gap exists between each subsequent pair of energy levels so that time fluctuations on the order of this interval will tend to make one unable to distinguish time and energy variations between data point pairs. Therefore, one must compare subsequent spectra to be sure time variations are not affecting the measurements. Note, even though the time to take an NTMS or AMS spectrum is about 2 minutes, the energy sweep for electrons is carried out continuously with no time gaps, such that only about 20 seconds is required to cover the first 8 energy channels. (In most cases the electron current is at the noise level beyond the eighth energy channel.)

A complete angular-energy scan of a spectrum is performed by integrating the sensor signal while the instrument sweeps through a selected angular sector and then sampling the integrated current at the end of the angular sector sweep. This is done for all angular sectors of an angular sweep at a fixed energy level. The instrument then steps to the next higher energy level before another angular sweep is done, etc., until the desired energy range is covered.

The characteristic feature of TMS is to track the proton peak, using only 8 energy channels centered around the proton peak determined in the previous spectrum. This is done in order to reduce the time interval between spectra to 25 seconds and to allow one to see structure on a shorter time scale.

For example, the thickness of a shock is about equal to one proton gyroradius $R_p \sim 80$km and since the spacecraft velocity is $\sim$ 2 km/sec, the time for the spacecraft to pass through the bow shock is on the order of 40 seconds or two TMS spectra.

The instrument operates in TMS when high flux conditions prevail (integrated flux in any angular sector greater than some threshhold T_1 will keep the instrument locked in TMS), while in low flux conditions the instrument is in NTMS. Because of this, the instrument operates in TMS for typical solar wind and magnetosheath conditions, and in NTMS when the spacecraft is in the outer magnetosphere and magnetotail. The main function of the AMS mode is to perform a general survey of the plasma conditions to avoid the instrument being locked in the wrong mode.

Since the angular distribution is narrow for ions in the solar wind, the 90^o sector centered around the sunward direction is subdivided into eight 11.25^o sectors, while the remaining sectors are 45^o wide. In NTMS these eight 11.25^o sectors are replaced by two coarser 45^o sectors because of the lower particle fluxes. The AMS mode has the same angular sweep as TMS, while having the same energy sweep as NTMS. For this instrument the cup has a split collector allowing for determination of the north/south angle of the wind velocity. However, for NTMS and electron measurements, only the full collector (signals from both halves) is used because of low current conditions.

(4.) Transmission Function of the Detector

(a.) Relation between the collector current and the electron distribution function

The mathematical relation between the measured current and the electron distribution function f_e must be known if one is to extract detailed quantitative information on f_e. This relation is analyzed in terms of the so-called "transmission function" defined as the fraction of a monoenergetic, broad, parallel uniform electron beam incident at a given direction upon the entrance aperture and detected by the collector. Thus the current produced by a beam of electrons is equal to the product of the flux density of the electron beam, area of the entrance aperture A, electric charge e, and the transmission function $T(\vec{v}; v_{z\pm})$, where $v_{z\pm}$ is displayed because T is a function of the modulator grid potential (energy dependent response).

In reality, we do not deal with a monoenergetic beam of electrons, but rather with an unknown distribution of electrons in velocity space. One can imagine an infinite number of such monoenergetic beams, which are composed of an infinitesimal number of electrons, coming from all directions and with different energies. The expression

$$f_e(\vec{v})\, v_z\, d^3v$$

represents the incident flux density of electrons upon the

cup aperture from one of these infinitesimal beams, where

$$f_e(\vec{v})\,d^3v$$

represents the number density of particles with velocity $\vec{v}$ in the range from $\vec{v}$ to $\vec{v} + d\vec{v}$, and v_z is the normal component of the velocity into the cup.

The ac component of the current received by the collector will then be given by the following integral expression:

$$\Delta I = eA\left\{\int_{v_{z-}}^{\infty} f_e(\vec{v})\,T(\vec{v};v_{z-})\,v_z\,d^3v - \int_{v_{z+}}^{\infty} f_e(\vec{v})\,T(\vec{v};v_{z+})\,v_z\,d^3v\right\} \quad (1.5)$$

where each integral represents the integrated flux received by the collector when the potential on the modulator grid is equal to $\mathbb{V}_{\mp}$. Note that the arguments for $T(\vec{v};\ v_{z_{\mp}})$ in the two integrals are different, indicating the energy dependence of the transmission function. Therefore we are unable to combine the two integral expressions. Also note that the positive values for the electric charge e and the potential $\mathbb{V}_{+}$ will be assumed throughout this chapter. One can see from (1.5) that a prerequisite for the determination of f_e is knowledge of the transmission function for the detector. The actual details for the inversion of this equation in solving for f_e shall be reserved for the next section.

(b.) The structure of the transmission function

The transmission function of the M.I.T. Imp 8 Faraday

cup is determined by (1) the "effective transparency" of the slats T_S, (2) the grid transparency T_G, and (3) the "geometrical intercept area coefficient," T_O. The coefficient T_O represents that fraction of the electron beam cross-section, parallel to the aperture plane, that is intercepted by the collector. The energy dependence is implied by $v_{z\pm}$ in the arguments for T_G, T_S, and T_O. We thus have

$$T(\vec{v}; v_{z\pm}) = T_G(\vec{v}; v_{z\pm})\, T_S(\vec{v}; v_{z\pm})\, T_O(\vec{v}; v_{z\pm}) \qquad (1.6)$$

Brief discussion concerning T_G, T_S, and T_O will now be given along with pertinent derivations.

(1) "Effective transparency" of slats

In Figure 3a we have a drawing of two slats. The purpose of the slats is to produce an angular response which is differential in the y-direction but broad in the x-direction, giving the detector a capability of determining f_e as a function of angle as the spacecraft rotates. It follows from the definition for $T(\vec{v}; v_{z\pm})$ that one needs only to consider monoenergetic broad parallel uniform beams coming from an arbitrary direction in deriving T_S, T_G, or T_O. The principle behind the slats is identical to that of blinders letting only the light at normal incidence upon the slats get through (shadow effect). Thus, by referring to Fig. 3a we have

$$T_S \equiv a/b$$

where a represents the fraction of the beam getting through

the slats, and b represents the total beam incident upon the slats. Then from Figure 3a it is easy to see that

$$D = a + H \tan\beta$$

and $b = D + W$, where D is the distance between slats, H and W are, respectively, the height and the width of the slats, and

$$\beta = \tan^{-1} \left| \frac{v_y}{v_z} \right|$$

is the incident angle of the beam upon the slats. Thus, using the above relations we have

$$T_s(\vec{v}) = \begin{cases} T_{SN}\left(1 - \frac{H}{D}\left|\frac{v_y}{v_z}\right|\right) & \text{for } \beta < \beta_{max} \\ 0 & \text{for } \beta \geq \beta_{max} \end{cases} \qquad (1.7)$$

where

$$T_{SN} = D/(D + W)$$

is the normal transparency of the slats and β_{max} is the maximum acceptance angle. From Table 2, which gives all pertinent physical parameters of the Imp 8 detector, $D/H = 0.1735$ gives us $\beta_{max} \approx \pm 10^{\circ}$, and $T_{SN} = 0.8675$. Note, the energy dependence in the argument for T_s has been dropped since the slats are at ground potential.

(2) Grid transparency

The grids are a mesh of finely woven tungsten wire which can be approximated by two sets of parallel wires aligned perpendicular to each other in the x,y plane of the cup. Thus, the transparency for one grid plane is

$$T_{G_i} \equiv (T_{G_x} T_{G_y})_i \tag{1.8}$$

where the index i specifies the grid plane, and $T_{G_{x_i}}$, $T_{G_{y_i}}$ are, respectively, the transparency of the i^{th} grid plane in the x and y directions. Then if one assumes no correlations of wires in one grid plane with those in another grid plane (very good approximation when one rotates the grid wires in different grid planes at different angles relative to one another) one gets

$$T_G \equiv \prod_{i=1}^{n} T_{G_i} \tag{1.9}$$

where n specifies the total number of grid planes. Figure 3b is a cross-sectional view of two grid wires representing a single layer of parallel wires of a grid plane. The quantities b and a have the same meaning as those for the slats; thus the grid transparency along the x-axis, for example, is

$$T_{G_x} \equiv a/b$$

It is easy to see from Fig. 3b that

$$b = a + d \sec \theta_G$$

where d is the diameter of the grid wires and $\sec \theta_G = \sqrt{1 + v_x^2/v_z^2}$. Using the definition of T_{G_x} along with the expression for $\sec_{G}$ one gets the following

$$T_{G_{x_i}} = 1 - \left(\frac{d}{b}\right)_i \sqrt{1 + v_x^2/v_z^2} \tag{1.10}$$

and for the transverse velocity $v_t = 0$, the normal transparency is

$$T_{GN_i} = (1 - (\frac{d}{b})_i)^2.$$

To get the total transparency of the grids $T_G(\vec{v}, v_{z\pm})$, one needs to substitute expressions of the type (1.10) for T_{Gx_i}, T_{Gy}, into (1.8) for each grid plane, and then substitute these expressions into (1.9). Table 2 shows d/b equal to 0.07 for the modulator grid and 0.02647 for the remaining grids. Using the above expressions for T_{GN_i} and equation (1.9), one obtains for the normal transparency of the grids $T_{GN} = 0.627$. Thus, the total normal transparency

$$T_N = T_{SN}T_{GN} = 0.544$$

The angular width of the grid transparency T_G is much broader than T_S. For example, the maximum angle of acceptance for the modulator grid, which has a larger d/b ratio compared to the other grid planes and thus the narrower angular width, is about 84^o, which is much larger than the angular width for the slats $\beta_{max} \approx \pm 10^o$.

(3) Geometrical intercept area coefficient, T_o

The transmission coefficient T_o is equal to the fraction of a broad parallel beam passing through the aperture at a particular angle θ_o that is intercepted by the collector plate. In other words, refer to Figure 4, the common area of the collector circle and the aperture circle, which is projected down upon the collector at the angle θ_o. Then this common area divided by the area of the aperture circle is

equal to T_o. The distance Δx shown in Figure 4 is the total transverse displacement of an electron between the aperture and collector. The common area of the two circles A_{com} is equal to twice the sum of A_1, the area of the triangle LMN, and the areas A_2, A_3 of the arc segments 2, 3 defined, respectively, by the area between chords $\overline{MN}$, $\overline{ML}$ and their corresponding arc segments. Thus

$$T_o = A_{com} / \pi r_A^2 \qquad (1.11)$$

where $A_{com} = 2(A_1 + A_2 + A_3)$, and r_A is the radius of the aperture circle ($r_A < r_C$). Now $A_1 = 2\ (\overline{OM})\ (\overline{LN})$, and A_2, A_3 are equal, respectively, to the difference between the areas of the arcs KMN, QML and the triangles KMN, QML. In order to determine the areas of these triangles, one must know the height $\overline{OM}$ and thus x. The distance x is given by the simultaneous solution of the equations $r_c^2 = x^2 + y^2$, and $r_A^2 = (x-\Delta x^2) + y^2$, where r_c is the radius of the collector Solving for x and substituting into (1.11), one gets the following expression for T_o:

$$T_o = \begin{cases} 1 & \text{for } \Delta x \le r_c - r_A \text{ or } \theta_o = 8.2^\circ \\ \frac{1}{\pi}\left[\cos^{-1}\left(\frac{\Delta x - x}{r_A}\right) + \left(\frac{r_c}{r_A}\right)^2 \cos^{-1}\frac{x}{r_c} - \frac{\Delta x}{r_A^2}\sqrt{r_c^2 - x^2}\right] & \text{for} \\ \qquad r_c - r_A < \Delta x < r_c + r_A \text{ or } 8.2^\circ < \theta_o < 64^\circ & \\ 0 & \text{for } \Delta x \ge r_c + r_A \text{ or } \theta_o \ge 64^\circ \end{cases} \qquad (1.12)$$

One can see from looking at (1.12) that the angular response for T_o is much wider than that for T_s.

(c.) Plots of the transmission function

Now we are ready to discuss the behavior of the total $T(v; v_{z\pm})$ as a function of the electron velocity. It is apparent that we may look upon T as a function of the following variables, the two angles

$$\beta = \tan^{-1} v_y/v_z \tag{1.13}$$

$$\alpha = \tan^{-1} v_x/v_z \tag{1.14}$$

and the normal velocity v_z and $v_{z\pm}$.

Figure 5 is a plot of the normalized response $R \equiv T/T_N$ versus β, for $\alpha = 0^o$ and for fixed normal velocity v_z set equal to $\bar{v}_z$. One sees that the β dependence of T is mainly determined by the transparency of the slats, which accounts for the cut off shown at $\beta \approx \pm 10^o$. Though not previously mentioned, there is an intermediate ring between the aperture and collector having a diameter slightly less than the aperture. The shadow effect due to this intermediate ring accounts for the narrower shape in T near $\beta = 0^o$, instead of the that implied by (1.7).

Figure 6 is a plot of R versus α for $\beta = 0^o$, and for various values of the normal velocity v_z ranging from v_{z-} to v_{z+} with a step size equal to 2% of the velocity window width. As one can see, a family of curves results, explicitly showing the dependence of T upon the normal velocity v_z (energy dependence in T) for fixed α and β. This energy dependence stems from the refraction of the electron

trajectories as they pass through regions of non-zero electric field. One can see from Fig. 2 that an electron experiences a repulsive force as it enters the potential barrier between grids 1 and 2 (trajectory is concave upward), and an acceleration between grids 2 and 3 (trajectory concave down). The same will hold for the suppressor grid.

To show further how this comes about, consider the transmission coefficient T_o. It is apparent from looking at Figure 2 that the electrons experience a transverse displacement relative to the point they would normally strike the collector plane if their trajectories were rectilinear. This is equivalent to an increase in Δx, the distance between, respectively, the projected aperture circle and the collector circle. For example, the relative displacement ΔL due to refraction can be shown to be[13]

$$\Delta L = L \tan\alpha \left[\frac{1-(1-\mu)^{1/2}}{1+(1-\mu)^{1/2}} \right] \qquad (1.15)$$

where $\mu \equiv 2e\phi_m/m_e v_z^2$, L is the distance between grids 1 and 3, and α is the angle of incidence at grid 1. For $v_z \gg v_{z-}$, $\mu \approx 0$, there is no deflection ($\Delta L \approx 0$), while in the other extreme $v_z = v_{z-}$, $\mu = 1$, the deflection is twice that for rectilinear motion ($\Delta L = L \tan\alpha$). For instance, one can show from using Eq. (1.15) that for $\alpha = 45^o$ there will be an effective increase in α due to refraction, from 45^o to 47.5^o and 51^o for v_z equal to, respectively, v_{z+} and v_{z-}. This gives rise to a small decrease in T_o from 0.47 to

0.42 for $v_z = v_{z+}$ but a significant reduction from 0.47 to 0.27 for $v_z = v_{z-}$.

The refraction of electrons between the grid planes partially accounts for the reduction in T shown in Figure 6. The remaining energy dependence in T resides in T_G. The effect is predominant at the modulator grid where electrons in passing through the potential barrier between grids 1 and 2 experience a decrease in v_z, while the transverse velocity is unaffected. This results in an increase in the angle of incidence at the modulator plane Θ_G with respect to that at grid 1, Θ_o, and thus a reduction in T_G. This deflection becomes greater as v_z (note: by v_z we mean the value of v_z at the entrance aperture) approaches v_{z-} from above. Correspondingly, the transparency T_G decreases such that it vanishes for v_z sufficiently close to v_{z-}. For example, T_G will decrease by 10% as v_z varies from $v_{z+} + v_{z-} + \Delta v/10$, where α is fixed and set equal to 30^o. It is important to note that this dependence of the angular response upon v_z only becomes important for electrons with

$$v_z < v_{z-} + 10\%(\Delta v_z)$$

This means that R is only weakly dependent upon v_z inside an energy window, and allows us to replace this R by a mean normalized response $\bar{R} \approx R(\alpha, \beta ; \bar{v}_z)$.

It is worth mentioning that the bell shapelike behavior of T for α's less than $|\pm 10^o|$ is due to the presence of the intermediate ring. If the ring were absent, the response T

with respect to α would be flat for $\alpha \leq |\pm 10^{o}|$.

One should also note that the angular response in the x-direction, (predominantly determined by T_o) is much broader than that in the y-direction, where T has the following limits in α and β:

$$T = 0 \text{ for } \alpha \geq |\pm 62^{o}| \text{ and all } \beta\text{'s.}$$

$$T = 0 \text{ for } \beta \geq |\pm 10^{o}| \text{ and all } \alpha\text{'s.}$$

(d.) Secondary and extraneous effects on transmission function

Most of the effects introduced in this section could go under the heading of pickup, which one normally tries to reduce as much as possible in the detector design. This section is mentioned for the sake of completeness and follows the general outline given in the paper by V. M. Vasyliunas.[13] First, electrons with $v_z > v_{z+}$ may have trajectories where they do reach the collector for $\Phi_m = \Phi_-$, but for $\Phi_m = \Phi_+$ miss the collector because of an increase in the refraction of their trajectories. The same sort of argument will hold concerning the transparency of the modulator grid. These effects produce a current 180^{o} out of phase with the modulator (increase current) which is on the order of a few percent for f_e decreasing with energy.

Another problem is the extraneous modulated current produced by photoelectrons from the modulator. The photoelectrons strike the suppressor grid at different energies

as Φ_m varies between Φ_+. Since the yield of secondaries from the suppressor is a function of primary energy E_p, and if the yield is greater for larger E_p (true for $E_p <$ 1 kev), then an ac current in phase with the modulator is produced. Due to the high flux of photons from the sun, photo currents $\sim 10^{-11}$ amp result. Thus, electron measurements cannot be made toward the sun. The presence of slats insures that one should have no problem for

$$45^o \leq \phi_{s/c} \leq 315^o$$

where $\phi_{s/c}$ is the scan angle of the spacecraft shown in Figure 2. Still another problem is the secondary electrons produced by protons hitting the modulator at different energies as Φ_m varies between Φ_+. Since the yield is proportional to the primary energy ($E_p <$ 10 kev), this current is in phase with the modulator. But for regions the Imp 8 spacecraft passes through, this effect should be small.[13] Then there is the secondary emission of electrons at the modulator and suppressor from electrons striking them, and since the yield is proportional to the primary flux F_p, where F_p is greater for $\Phi_m = \Phi_-$, a current 180° out of phase from the modulator results. This effect may be sufficiently large to require corrections.[13]

Among the remaining effects, the following one should be mentioned: For the modulator grid wires, the equipotential assumption at the grid plane is somewhat violated. For example, the potential may drop as much as 9% of the modulator

potential halfway between adjacent grid wires. Since the window size is only 21%, the idea of a uniform potential barrier is not rigorously valid. One tries to reduce such effects by reducing the wire spacing of the modulator grid without reducing the sensitivity of the detector or normal transparency of grids too much. Corrections introduced by such effects can only be determined experimentally. Experiments seem to show such corrections to be small for reasonable wire spacings and distances between grid planes.

(5.) Analytical Evaluation of Equation (1.5)

(a.) Simplification of the expressions for ΔI

The main objective of this section is the explicit evaluation of Equation (1.5). This equation as written is not in a form amenable for numerical computations. In reviewing the observational characteristics of solar wind electrons and the properties of the detector response (see Figures 7 and 8), one may conclude that f_e is broad compared to the detector's response in the y-direction, while comparable in width with respect to T in the x-direction. Using this information, one can simplify Eq. (1.5) considerably without need for explicit knowledge of f_e, except that it be broad in a certain sense to be explained later. If the distribution function f_e is sufficiently steep (Maxwellian, for instance), the corrections to ΔI by setting $T(\vec{v}; v_{z+}) = T(\vec{v}; v_{z-})$ may be ignored. Complete numerical integrations of Eq. (1.5) were performed without any approximations concerning the transmission function T. Using a Maxwellian distribution for f_e, we found that the error in combining the two integrals in Eq. (1.5) is less than 1%. We thus are justified to use instead of (1.5)

$$\Delta I = e A T_N \int_{V_{z-}}^{V_{z+}} \int_{V_y=-\infty}^{\infty} \int_{V_x=-\infty}^{\infty} f_e(\vec{v})\, R(\vec{v}; v_{z-})\, v_z\, d^3v \qquad (1.16)$$

Further simplifications result if f_e is broad compared to the angular response. In such situations one may resort to the mean value theorem. One has:

$$\Delta I = e A T_N \int_{v_x=-\infty}^{\infty} dv_x f_e(v_x, \eta, \zeta) \left\{ \int_{v_{z-}}^{v_{z+}} \int_{-\frac{D}{H}v_z}^{\frac{D}{H}v_z} R(\vec{v}; v_{z-}) v_z \, dv_y \, dv_z \right\} \quad (1.17)$$

where the limits of integration in v_y are explicitly shown, and the parameters η, ζ lie, respectively, somewhere within the ranges $v_{z-} < \zeta < v_{z+}$, $-\frac{D}{H} v_z < \eta < +\frac{D}{H} v_z$. If the detector response in β and v_z is differential with respect to f_e, one can make the approximation that $\eta \approx 0$ and $\zeta \approx \bar{v}_z$. In order to estimate the error in making this approximation, let us write the Taylor series expansion of f_e around $v_y = 0$, $\bar{v}_z$ and substitute it into (1.16). We thus have:

$$\Delta I = e A T_N \int_{v_x=-\infty}^{\infty} dv_x f_e(v_x, 0, \bar{v}_z) \left\{ \int_{v_{z-}}^{v_{z+}} \int_{-\frac{D}{H}v_z}^{\frac{D}{H}v_z} R(\vec{v}; v_{z-}) v_z \, dv_y \, dv_z \right. \quad (1.18)$$

$$\left. \left[1 + \left[\frac{1}{f_e} \frac{\partial f_e}{\partial v_y} \right]_{v_x, 0, \bar{v}_z} \left(\frac{I_1}{I_0} \right) + \left[\frac{1}{f_e} \frac{\partial f_e}{\partial v_z} \right]_{v_x, 0, \bar{v}_z} \left(\frac{I_2}{I_0} \right) + \frac{1}{2} \left[\frac{1}{f_e} \frac{\partial^2 f_e}{\partial v_y^2} \right]_{v_x, 0, \bar{v}_z} \left(\frac{I_3}{I_0} \right) + \cdots \right] \right\}$$

where

$$I_0 \equiv \int_{v_{z-}}^{v_{z+}} \int_{-\frac{D}{H}v_z}^{+\frac{D}{H}v_z} R(\vec{v}; v_{z-}) v_z \, dv_z \, dv_y$$

I_1, I_2, and I_3 are similar in form to the above expression for I_0. They may be obtained by replacing v_z in the integrand

for I_o by $v_z\, v_y$, $v_z\,(v_z - \bar{v}_z)$ and $v_z\, v_y^2$. The second and fourth terms on the r.h.s. of (1.18) are correction terms to the integral for ΔI, resulting from the detector not being perfectly differential in v_y, while the third term is a correction due to finiteness of the width of a given energy window. The response is even in v_y, thus the integral I_1 vanishes by inspection. In order to get an estimate of the size of the I_3 term relative to unity, we may take into account the fact that $R(\vec{v};\, v_{z-})$ is not a strong function of v_z in the range from v_{z-} to v_{z+}. Using Eq. (1.7) for R and a Maxwellian for f_e one gets:

$$\frac{1}{2}\left[\frac{1}{f_e}\frac{\partial^2 f_e}{\partial v_y^2}\right]_{v_x,0,\bar{v}_z}\left(\frac{I_3}{I_o}\right) = \frac{1}{6}\left(\frac{D}{H}\right)^2\left(\frac{\bar{v}_z}{w_e}\right)^2\left(1 - \frac{2\bar{v}_y^2}{w_e^2}\right) \qquad (1.19)$$

Since electrons are subsonic, the correction term $2V_y^2/w_e^2$ is small compared to unity for typical values of v_y and w_e, and thus can be dropped. In order to obtain an estimate of (1.19), it is convenient to proceed graphically. For this purpose, refer to Figure 7, which shows a typical f_e in the solar wind. Superimposed upon f_e is the normalized response of the slats R, where the lower refers to v_z = 3100 km/sec and the upper to v_z = 7000 km/sec. Recalling that $v_y = \frac{D}{H}v_z$, we see that $v_{y\ max}$ = 540 km/sec for the lowest energy channel and $v_{y\ max}$ = 1200 km/sec for the eighth energy channel. Since w_e is typically 2000 km/sec, Eq. (1.19) varies in the range between 1.2% and 6%. Thus, we see that we are justified

in dropping the I_3 term in Eq. (1.18).

Using the same approach for the third term in (1.18), one gets:

$$\left[\frac{1}{f_e}\frac{\partial f_e}{\partial v_z}\right]_{v_x,0,\bar{v}_z}\left(\frac{I_2}{I_0}\right) = -\frac{5}{24}\left(\frac{\Delta v_z}{w_e}\right)^2 \qquad (1.20)$$

For all energy channels used, Δv_z is always less than 700 km/sec. Thus, even for w_e as small as 1500 km/sec (i.e., $T = 7.4 \times 10^4\ ^oK$), Eq. (1.20) is less than 4.5%. In order to show that the detector is differential for all v_z and to obtain more typical estimates of (1.20), it is convenient to separate the electrons into two separate energy regimes. Electrons with energies less than 60 ev ("core" electrons) have thermal speeds $w_e \sim 1900$ km/sec, while electrons with energies greater than 60 ev (suprathermal electrons) have thermal speeds $w_e \sim 4700$ km/sec. Thus, for energies less than 60 ev (first six energy channels), (1.20) is only 1.3%; while for energies greater than 60 ev, (1.20) is negligable until one approaches the highest energy channels ~ 2 kev, where $\Delta v_z \sim 2800$ km/sec gives a value for (1.20) $\sim 8\%$. One might then expect $w_e >> 4700$ km/sec at these energies. Thus, the approximation that the detector is differential in v_z is very good. Neglecting the correction terms, which are no larger than 6%, (1.18) reduces to the following:

$$\Delta I = eAT_N \int_{v_x=-\infty}^{\infty} dv_x \, f_e(v_x, 0, \bar{v}_z) \left\{ \int_{v_{z-}}^{v_{z+}} \int_{-\frac{D}{h}v_z}^{+\frac{D}{h}v_z} R(\vec{v}; v_{z-}) \, v_z \, dv_y \, dv_z \right\} \qquad (1.21)$$

(b.) Evaluation of the integral involving $R(\vec{v}; v_{z-})$

Shown in Figure 8 is a drawing identical to that in Figure 7 except that the normalized angular response R is plotted as a function of v_x for various values of v_z in the range 3100 km/sec $\leq v_z \leq$ 7000 km/sec and $v_y = 0$. One can see that f_e and R have the same width, while at higher energies R extends out to many thermal speeds and becomes very broad compared to f_e. For example, $v_{x\,max} = v_z \tan \alpha_{max}$, where $\alpha_{max} \approx 62^o$, and for v_z in the range noted to above, $v_{x\,max}$ varies in the range 5830 km/sec $\leq v_{x\,max} \leq$ 13,165 km/sec, or in thermal speeds $3w_e \leq v_{x\,max} \leq 6.6\, w_e$. This means that one cannot use the mean value theorem for the variable v_x. Because the v_z dependence of R (see Figure 6) is very complicated, the evaluation of the integral involving R in an analytical form appears hopeless. However, one notices that the term in braces in (1.21) does not depend on v_z. One can define the mean response function $\bar{R}$ as follows:

$$\bar{R} \equiv \frac{\int_{v_{z-}}^{v_{z+}} \int_{-\frac{D}{H}v_z}^{+\frac{D}{H}v_z} R(\vec{v}; v_{z-})\, v_z\, dv_y\, dv_z}{\int_{v_{z-}}^{v_{z+}} \int_{-\frac{D}{H}v_z}^{\frac{D}{H}v_z} v_z\, dv_y\, dv_z} \tag{1.22}$$

In Figure 9 is a plot of $\bar{R}$ (ξ, v_{z-}) as a function of

$$\xi = v_x/\bar{v}_z$$

for various values of v_{z-} (energy channels). Note that $\bar{R}$ (ξ; v_{z-}) is essentially independent of the energy channel and one is justified in omitting the dependence in v_{z-} from the argument for $\bar{R}$. Thus, one gets the following expression for Equation (1.21):

$$\Delta I = \frac{2}{3} e A T_N \frac{D}{H} (v_{z+}^3 - v_{z-}^3)\, \bar{v}_z \int_{-\infty}^{\infty} f_e(\xi, 0, \bar{v}_z)\, \bar{R}(\xi)\, d\xi \tag{1.23}$$

Figure 9 shows that $\bar{R}$ (ξ) is even in ξ, as one might expect. It turns out that $\bar{R}$ may be fitted well by a sum of two Gaussians,

$$\bar{R} = \sum_{\ell=1}^{2} a_\ell\, e^{-\alpha_\ell^2 \xi^2} \tag{1.24}$$

where a_ℓ, α_ℓ^2 are adjustable parameters. We have determined α_ℓ and a_ℓ using the first eight energy channels; the results are shown in Figure 10. Note an excellent fit, except for the slight deviation beyond $\pm 60^\circ$, where $\bar{R} \approx 0$, when one

chooses $a_1 = 6.69 \times 10^{-2}$, $\alpha_1^2 = 1.116$, $a_2 = 9.1 \times 10^{-3}$, $\alpha_2^2 = 21.472$. Substituting (1.24) into Equation (1.23), one obtains

$$\Delta I = 2eAT_N \frac{D}{H} \Delta V_z \bar{V}_z^3 \sum_{\ell=1}^{2} a_\ell \int_{-\infty}^{\infty} f_e(v_x, o, \bar{v}_z) e^{-\alpha_\ell^2 \xi^2} d\xi \qquad (1.25)$$

where we made use of the (excellent) approximation

$$V_{z_+}^3 - V_{z_-}^3 \approx 3 \Delta V_z \bar{V}_z^2$$

Equation (1.25) represents the basic equation for our analysis of electron data. Note that the limits of integration $v_x = \pm\infty$ may be retained because the Gaussian fit to $\bar{R}$ deviates only by a few percent from zero for angles larger than 60^o. (For the lowest energy channel $v_x = \pm 5400$ km/sec at $\pm 60^o$ and thus about three times larger than the thermal speed. Hence, the contributions to the integral for $v_x >$ 5400 km/sec are negligable.)

(c.) Explicit formulas for ΔI for various models of f_e

We have reduced the problem in the previous section to a one-dimensional integral expression for f_e (v_x, o, $\bar{v}_z$). The most useful approach found thus far is to assume a model form for f_e containing a sufficient number of "free" parameters to be determined by best fit procedures. (For example, nonlinear least-square-fit routines can be employed to

determine the model parameters from the set of currents for each spectrum.)

For the purpose of demonstration, we quote here two different models for f_e. They are as follows: (1) bi-Maxwellian distribution function $f_{BM}(\vec{v})$, and (2) the transport model distribution recently proposed by Scudder and Olbert (1977).[14] (The details of the latter example are discussed in Chapter 4.)

(1) Bi-Maxwellian distribution function

For this model, f_e is given by

$$f_e = \frac{n_e \beta_\perp \sqrt{\beta_\parallel}}{\pi^{3/2}} e^{-(\beta_\perp w^2 + \Delta\beta w_\parallel^2)} \tag{1.26}$$

where $\vec{w} = \vec{v} - \vec{V}$

$\vec{v}$ is the electron velocity, $\vec{V}$ is the bulk velocity of the solar wind, n_e is the electron density, $w_\parallel = \vec{w} \cdot \hat{b}$, $\hat{b} = \vec{B}/B$. ($\vec{B}$ is the magnetic field vector),

$$\beta_\perp \equiv \frac{m_e}{2kT_\perp}$$

$$\beta_\parallel \equiv \frac{m_e}{2kT_\parallel}$$

where $T_\parallel$ and $T_\perp$ are, respectively, the temperatures parallel and perpendicular to the magnetic field, and

Using (1.26), one gets the following expression for the current ΔI (see Appendix A):

$$\Delta I = I_o \sqrt{\frac{\beta_{11}}{\beta_\perp}}\, U_o^3\, e^{-[U^2 + \epsilon U_{11}^2/(1+\epsilon\cos^2\theta_B)]} \sum_{\ell=1}^{2} \frac{a_\ell}{\sqrt{\alpha_\ell^2 + U_o^2(1+\epsilon\cos^2\theta_B)}} \qquad (1.27)$$

where $$I_o \equiv \frac{2}{\pi} e A T_N \frac{D}{H} n_e \Delta V_z$$

$$U_o^2 \equiv \beta_\perp \bar{V}_z^2$$

$$U_{11} \equiv \sqrt{\beta_\perp}\left[V_y \sin(\phi_B - \phi_c) - (\bar{V}_z - V_z)\cos(\phi_B - \phi_c)\right]\sin\theta_B$$

$$U^2 \equiv \beta_\perp\left[(\bar{V}_z - V_z)^2 + V_y^2\right]$$

and $$\epsilon \equiv \Delta\beta/\beta_\perp$$

The angles θ_B and ϕ_B are, respectively, the polar and azimuthal angles of the $\vec{B}$ vector in the solar ecliptic coordinate system (see Figure 11). If we set $\epsilon = 0$, Eq. (1.27) reduces to the special case where f_e is a Maxwellian, i.e.,

$$\Delta I = I_o U_o^3 e^{-U^2} \sum_{\ell=1}^{2} \frac{a_\ell}{\sqrt{\alpha_\ell^2 + U_o^2}} \qquad (1.28)$$

In Eqs. (1.27) and (1.28) the expression preceding the summation sign is the familiar expression for the current ΔI. The summed expression is a new term that displays the

convolution (mixing) of the detector response and the distribution function f_e. To further show this we will make some simplifying approximation of Eq. (1.28). From looking at the coefficients a_ℓ and α_ℓ^2, i.e., $a_2/a_1 \sim .1$ and $\alpha_1^2/\alpha_2^2 << 1$, one finds the second term of Eq. (1.28) to be only a 5% correction. Also, the term V_y^2/w_c^2 introduces a 5% correction in the normalization. Dropping these terms one gets for ΔI for directions at 90° to the wind velocity, to a good approximation:

$$\Delta I = \frac{a_1 I_o U_o^3 e^{-U_o^2}}{\sqrt{1+U_o^2}} \tag{1.29}$$

where $\alpha_1^2 \approx 1$ was set equal to one. Thus for $U_o \sim 1$, there is a definite mixing of the response function and f_e parameters. For the limit $U_o \rightarrow 0$, the response function becomes narrow compared to f_e and one gets the expression normally expected for a differential detector

$$\Delta I = a_1 I_o U_o^3 e^{-U_o^2} \tag{1.30}$$

while for $U_o \rightarrow \infty$, the response function becomes broad compared to f_e, see Figure 8, and one gets the correspondingly familiar case

$$\Delta I = a_1 I_o U_o^2 e^{-U_o^2} \tag{1.31}$$

which is an approximation often used for protons. Note: in

all of the above the term V_x/w_c was dropped because the bulk velocity vector is confined to the ecliptic plane such that $(V_x/w_c) << 1$ and results in an error $< 1\%$.

(2) Conduction model[14]

In this model

$$f_e = f_\kappa + f_1$$

where $$f_1 << f_\kappa$$

and (see Appendix A):

$$f_e(\vec{v}) = f_\kappa(1 + \tau(P_e + P_o)) \tag{1.32}$$

$$f_\kappa = C_\kappa \frac{n_e}{\pi^{3/2} w_c^3} \frac{1}{(1 + u^2/\kappa)^{\kappa+1}} \tag{1.33}$$

where f_κ is the kappa distribution function first proposed by S. Olbert,[15] κ is an adjustable parameter, $\vec{u} = (\vec{v}-\vec{V})/w_c$, w_c is the most probable thermal speed for electrons,

$$C_\kappa = \frac{\Gamma(\kappa+1)}{\Gamma(\kappa-1/2)\kappa^{3/2}}$$

τ is the effective collision time, and P_e, P_o are, respectively, even and odd polynomials in the velocity $\vec{u}$. Expressions for τ, P_e, and P_o are given in Chapter 4 and Appendix A. The distribution function f_κ has the property that for $v \leq \sqrt{\kappa} w_c$ it is almost identical to a Maxwellian, and for $v^2 >> \kappa w_c^2$ it goes over to a power law in v or in energy. Note that f_κ is isotropic in the frame of reference, moving with velocity $\vec{V}$. For small κ the high energy tail is emphasized,

while for large κ it approaches a Maxwellian. One can easily check that

$$\lim_{\kappa \to \infty} C_\kappa = 1$$

$$\lim_{\kappa \to \infty} (1 + u^2/\kappa)^{-(\kappa+1)} = e^{-u^2}$$

Substituting the above expression for f_e, Eq. (1.32) in Eq. (1.25) and integrating (see Appendix A for details), one gets the following:

$$\Delta I = I_o \sum_{l=1}^{2} a_l F_{\kappa l} M_{\kappa l} \tag{1.34}$$

where

$$F_{\kappa l} = \frac{C_\kappa U_o^3}{(1+U^2/\kappa)^{\kappa+1} \sqrt{\alpha_l^2 + \eta_o U_o^2}} \tag{1.35}$$

and

$$M_{\kappa l} = 1 + \left(\frac{\lambda\omega}{r}\right)\left(\frac{V_r}{\omega_c}\right)\left\{\left(-\tfrac{3}{2}\alpha_B + \alpha_n + \zeta(\kappa)\alpha_\kappa \frac{h_{1l}}{h_{ol}} + \alpha_\kappa \frac{h_{4l}}{h_{ol}} + \frac{\kappa+1}{\kappa}\left[(2\alpha_n + \alpha_B)(U_\parallel^2 - U^2\cos^2\theta_B)\frac{h_{2l}}{h_{ol}}\right.\right.\right.$$

$$\left.\left.\left. + (\alpha_\beta - \alpha_\kappa + 2\alpha_n \cos^2\theta_B + \alpha_B \sin^2\theta_B)\frac{h_{3l}}{h_{ol}}\right]\right\}$$

$$+ \left(\frac{\lambda\omega}{r}\right) U_\parallel \cos\chi \left\{-\left(\tfrac{3}{2}\alpha_\beta + \alpha_n + \zeta(\kappa)\alpha_\kappa \frac{h_{1l}}{h_{ol}} + \alpha_\kappa \frac{h_{4l}}{h_{ol}}\right.\right.$$

$$\left.\left. + \frac{\kappa+1}{\kappa}\left[(\alpha_\beta - \alpha_\kappa)\frac{h_{3l}}{h_{ol}} - \alpha_r \frac{h_{2l}}{h_{ol}}\right]\right\} \tag{1.36}$$

where $\frac{h_{1\ell}}{h_{o\ell}} = \frac{U^3}{U^4+\delta}\frac{\gamma_{o\ell}}{\gamma_{1\ell}}$, $\frac{h_{2\ell}}{h_{o\ell}} = \frac{U^3}{(U^4+\delta)(1+U^2/\kappa)}\frac{\gamma_{o\ell}}{\gamma_{2\ell}}$,

$\frac{h_{3\ell}}{h_{o\ell}} = \frac{U^5}{(U^4+\delta)(1+U^2/\kappa)}\frac{\gamma_{o\ell}}{\gamma_{3\ell}}$, $\frac{h_{4\ell}}{h_{o\ell}} = \frac{U^3 \ln(1+U^2/\kappa)}{U^4+\delta}\frac{\gamma_{o\ell}}{\gamma_{4\ell}}$,

$\gamma_{o\ell}^2 = \alpha_\ell^2 + \eta_o U_o^2$, $\gamma_{1\ell}^2 = \gamma_{o\ell}^2 + \frac{U_o^2}{2U^2}\left[\frac{U^4-3\delta}{U^4+\delta}\right]$,

$\gamma_{2\ell}^2 = \gamma_{1\ell}^2 + \frac{\eta_o}{\kappa+1}U_o^2$, $\gamma_{3\ell}^2 = \gamma_{2\ell}^2 - U_o^2/U^2$,

$\gamma_{4\ell}^2 = \gamma_{1\ell}^2 - \frac{\eta_o U_o^2}{(\kappa+1)\ln(1+U^2/\kappa)}$, $\eta_o = \frac{\kappa+1}{\kappa}\frac{1}{1+U^2/\kappa}$,

$\delta \equiv \lambda_w / \bar{\lambda}_{coul}$,

and for higher energy channels $U_o >> 1$, $\frac{h_{1\ell}}{h_{o\ell}} \approx \frac{1}{U}$,

$\frac{h_{2\ell}}{h_{o\ell}} \approx \frac{1}{U^3}$, $\frac{h_{3\ell}}{h_{o\ell}} \approx \frac{1}{U}$

and $\frac{h_{4\ell}}{h_{o\ell}} \approx \frac{1}{U}$

Also, $U_o^2 \equiv \bar{V}_z^2/w_c^2$, $U^2 \equiv [(\bar{V}_z - V_z)^2 + V_y^2]/w_c^2$,

$U_{11} \equiv [V_y \sin(\phi_B - \phi_c) - (\bar{V}_z - V_z)\cos(\phi_B - \phi_c)]\sin\theta_B / w_c$,

$B(z) = \frac{1}{2}\left[\psi\left(\frac{z+1}{2}\right) - \psi\left(\frac{z}{2}\right)\right]$ is the beta function,

$\psi(z) = \frac{d}{dz}\ln\Gamma(z)$ is the Psi-function, and

$S(\kappa) = 2B(2\kappa-1) - \frac{1}{2} \geq 0$ for all κ and approaches zero as κ approaches infinity. In evaluating these integrals, we have used the saddle point method (see Appendix). The accuracy of the integration was checked by comparing the integrations in (1.34) with numerical integrations of the same expressions

for regions of parameter space of interest. The error was found to be less than 5 percent in general. Errors $\sim 10\%$ for special combination of parameters do occur for integrals $h_{3\ell}$ and $h_{4\ell}$ at the lowest energy channel when $T_c \geq 2.5 \times 10^5$ ^oK (i.e., angular width of f_e becomes comparable to the angular width in R).

One may also want the expression ΔI for $\varkappa \to \infty$, which holds when the electrons are collision dominated and described by a Maxwellian. For $\varkappa \to \infty$, the saddle point method yields:

$$\Delta I = I_o \sum_{\ell=1}^{2} a_\ell F_{\infty\ell} M_{\infty\ell} \tag{1.37}$$

where

$$F_{\infty\ell} = \frac{U_o^3 e^{-U^2}}{\sqrt{\alpha_\ell^2 + U_o^2}} \tag{1.38}$$

and

$$M_{\infty\ell} = 1 + \left(\frac{\lambda_w}{r}\right)\left(\frac{V_r}{w_c}\right)\left[-\left(\frac{3}{2}\alpha_\beta + \alpha_n\right)\frac{h_{1\ell}}{h_{o\ell}} + \alpha_\varkappa \frac{h_{1\ell}}{h_{o\ell}}\right.$$
$$+ (2\alpha_n - \alpha_B)(U_{||}^2 - U^2\cos^2\theta_B)\frac{h_{1\ell}}{h_{o\ell}} + (\alpha_\beta - \alpha_\varkappa$$
$$\left. + 2\alpha_n\cos^2\theta_B + \alpha_B \sin^2\theta_B)\frac{h_{3\ell}}{h_{o\ell}}\right] + \left(\frac{\lambda_w}{r}\right) U_{||}\cos\chi$$
$$\left[-\left(\frac{3}{2}\alpha_\beta + \alpha_n - \alpha_r\right)\frac{h_{1\ell}}{h_{o\ell}} + \alpha_\varkappa \frac{h_{2\ell}}{h_{o\ell}} + (\alpha_\beta - \alpha_\varkappa)\frac{h_{3\ell}}{h_{o\ell}}\right] \tag{1.39}$$

where

$$\frac{h_{1\ell}}{h_{o\ell}} = \frac{h_{2\ell}}{h_{o\ell}}, \quad \frac{h_{2\ell}}{h_{o\ell}} = \frac{U^3}{U^4+\delta}\frac{\gamma_{o\ell}}{\gamma_{1\ell}}, \quad \frac{h_{3\ell}}{h_{o\ell}} = \frac{U^5}{U^4+\delta}\frac{\gamma_{o\ell}}{\gamma_{3\ell}},$$

$$\frac{h_{4\ell}}{h_{o\ell}} = \frac{U^5}{U^4+\delta}\frac{\gamma_{o\ell}}{\gamma_{4\ell}}, \quad \gamma_{o\ell}^2 = \alpha_\ell^2 + U_o^2, \quad \gamma_{1\ell}^2 = \gamma_{o\ell}^2 + \frac{U_o^2}{2U^2}\left(\frac{U^4-3\delta}{U^4+\delta}\right),$$

$$\gamma_{2\ell}^2 = \gamma_{1\ell}^2 \,, \quad \gamma_{3\ell}^2 = \gamma_{1\ell}^2 - U_o^2/U^2 \,, \text{ and } \gamma_{4\ell}^2 = \gamma_{1\ell}^2 - U_o^2/U^2$$

For large energies $U_o >> 1$, the following holds

$$\frac{h_{1\ell}}{h_{o\ell}} = \frac{1}{U} \,, \quad \frac{h_{2\ell}}{h_{o\ell}} = \frac{h_{3\ell}}{h_{o\ell}} \,, \quad \frac{h_{3\ell}}{h_{o\ell}} = U \,, \text{ and } \frac{h_{4\ell}}{h_{o\ell}} = U$$

For large κ this model breaks down at large energies, since terms like $\frac{h_{3\ell}}{h_{o\ell}}$ and $\frac{h_{4\ell}}{h_{o\ell}}$ become unbounded for $U_o >> 1$.

One should note that in the case of finite κ, the term proportional to $(\frac{\lambda_w}{r})$ $(\frac{V_r}{r})$ in Eq. (1.36) for $M_{\kappa\ell}$, goes to zero like 1/U for large U. Thus, at high energies this term, which describes the pressure anisotropy of the electron gas, drops out. The second term, which is proportional to $(\frac{\lambda_w}{r})$, contributes to the third moment or heat flow vector of electrons in the proper frame of reference, does not go to zero as $U \to \infty$, but approaches some non-zero constant. This term is less than one if $(\frac{\lambda_w}{r})$ is less than some critical $(\frac{\lambda_w}{r})_{\text{critical}}$.

In the event that there is no transport (all thermodynamic gradients are zero), then $M_{\kappa\ell} = 1$ and Eqs. (1.34), (1.36) reduce to the special case where f_e is described by the isotropic kappa distribution, i.e.,

$$\Delta I = I_o \sum_{\ell=1}^{2} a_\ell F_{\kappa\ell} \tag{1.40}$$

where $F_{\kappa\ell}$ is given by Eq. (1.35).

In the limit as κ approaches infinity, Eq. (1.40) further

reduces to the special case of a Maxwellian for f_e. Under these conditions, $\kappa \to \infty$, $M_{\kappa\ell} = 1$, the saddle point method yields rigorously:

$$\Delta I = I_o \sum_{\ell=1}^{2} a_\ell F_{\infty\ell} \tag{1.41}$$

where $F_{\infty\ell}$ is given by Eq. (1.38). Eq. (1.41) is identical to Eq. (1.28), which was derived using a bi-Maxwellian for f_e and setting $\epsilon = 0$.

Finally, in order to check the accuracy of Equation (1.25), numerical integrations for ΔI (ΔI_{NUM}) were computed for a Maxwellian using the most general Equation (1.5). A similar set of currents for ΔI were computed using Eq. (1.28). By referring to Table 3, which gives a comparison between currents computed numerically and those computed using Eq. (1.28), one can see that for $w_c > 2000$ km/sec the error is $\lesssim 3\%$. Thus, it seems that Eq. (1.25) represents the currents ΔI quite well.

(6.) Closing Remarks

In this chapter we have shown that the very complicated three-dimensional integral relation for ΔI given by Eq. (1.5) may be reduced to the relatively simple and easy to handle one-dimensional integral relation given by Eq. (1.25). This was possible because of the differential property of the detector response relative to f_e and the fact that the angular

response for R may be expressed by a mean response $\bar{R}$ [see Eq. (1.22)]. As was shown, the essential features of the response may be characterized by the angular variables α and β. The explicit dependence of R upon v_z within the velocity window of the detector, which is due to refraction, was shown to be relatively weak. Because of this, we were able to replace R by $\bar{R}$ as noted to above. Furthermore, it was possible to replace $\bar{R}$ by a sum of two Gaussians which when fitted to $\bar{R}$ gave an almost perfect reproduction of it. It was then shown that Eq. (1.25), within a few percent, gave an accurate description of the currents when compared with laborious numerical integrations using Eq. (1.5).

We would like to stress that once we have an expression like Eq. (1.25) for ΔI, a tremendous simplification in the analysis is obtained. For instance, since the precise form for f_e is not a priori known, Eq. (1.25) for ΔI allows us simply to substitute any model for f_e in this equation (i.e., bi-Maxwellian, kappa, kappa plus transport, which can be evaluated for most cases of interest etc.), by using the saddle point method, thus giving us analytical expressions for ΔI in terms of detector and model dependent parameters. (Note that the integrations can be evaluated rigorously for Maxwellian and bi-Maxwellian distributions.) By having such expressions one may easily develop fitting procedures for the purposes of doing data analysis along with the ability for relatively easy comparison with the data. For instance,

at right angles to $\vec{B}$, the transport terms are small, allowing for tremendous simplification in ΔI [for example, see Eq. (1.40)]; and thus one can obtain a quick estimate of κ and w_c if we are using a kappa distribution for f_o.

Finally, it should be pointed out that the current recorded by the detector is an average current over an angular sector, i.e.,

$$\langle f_e(\vec{v},t)\rangle = \frac{1}{\Delta t}\int_{t_o}^{t} f_e(\vec{v},t')\,dt' \qquad (1.42)$$

where $\Delta t \equiv t - t_o$ is the integration time. In our analysis, we have not done a proper average of the currents over angle. We have simply set ϕ_c for each angular sector equal to the following:

$$\cos\phi_c = \frac{1}{\Delta\phi_c}\int_{\phi_{c_1}}^{\phi_{c_2}} \cos\phi\,d\phi \qquad (1.43)$$

where

$$\Delta\phi_c = \phi_{c_2} - \phi_{c_1}$$

Errors introduced by using this averaging procedure in general will be small, because electrons are very subsonic and nearly isotropic in the proper frame (current does not change appreciably with angle), thus allowing us to avoid further complications in our analysis program. If need be, once a final form for f_e has been decided upon, and if the accuracy of the data justifies a more precise analysis, then a more

appropriate averaging procedure may be built into the analysis routine.

CHAPTER II

SPACECRAFT CHARGING

(1.) Qualitative Statement of the Problem

The problem of spacecraft charging is an old one and has been of considerable interest for many years. It is a problem that is very difficult to treat quantitatively (as will become clearer later on in the discussion); one is forced to make drastic approximations and assumptions in order to get a rough feeling for what is happening. The actual charging up of the spacecraft is the result of a complicated interplay between two competing processes. The first of these processes results from electrons in the plasma surrounding the spacecraft having thermal speeds many times greater than protons, so that the average electron flux striking the spacecraft is about 40 times greater than the average proton flux striking it ($T_e \approx T_p$), thus causing the spacecraft to charge up to a negative potential relative to the surrounding plasma. (Note: the potential of the surrounding plasma shall be arbitrarily set equal to zero.) Since this negative "plasma" current incident upon the spacecraft is proportional to the electron density and thermal speed, one might expect the spacecraft to acquire a more negative charge in regions of higher density and temperature than that in cooler and more rarified regions of space. Other complicating factors are the scattering of electrons

and the secondary emission of electrons from the surface of the spacecraft, which tend to reduce the negative charge accumulated by the spacecraft. The other process is due to the photo emission of electrons on the sunward side of the spacecraft, causing it to charge up to a positive potential. Some factors important in determining the effectiveness of this process are: (1) the intensity of the sunlight incident upon the spacecraft, (2) reflection and absorption properties of the surface material, (3) work function of the surface material, and (4) energy spectrum of the sunlight incident upon the spacecraft (e.g., increasing the ultraviolet spectrum produces a greater photo current, since only photons with energies greater than the work function of the surface material can contribute to the emission of photoelectrons). Then, depending on which process dominates, the spacecraft will either charge up to a positive or a negative potential. The total current incident upon the spacecraft ("plasma" current plus photocurrent) initially raises the potential of the spacecraft. This potential in turn tends to reduce this current so that under steady state conditions the current is zero (zero current condition). As the spacecraft charges, a non-zero space charge density forms around the spacecraft. This space charge density tends to shield the surrounding plasma from the charged spacecraft. (The effectiveness of this shielding (screening) is qualitatively measured by the Debye length (λ_D) of the surrounding plasma near the surface

of the spacecraft, thus giving rise to a screened potential around the spacecraft.)

The purpose of this chapter is to investigate in a crude but quantitative manner the effects of spacecraft charging on electron measurements. Since the experimentally estimated s/c potentials compare in magnitude to the kinetic energy of the bulk of the electrons, there is need for detailed study of this problem. In the case of positive ions, this problem does not arise because ions have much larger masses. For example, the Imp 8 spacecraft appears to have a potential of about +2 volts[9] (photoeffect is dominant); electrons have convective energies of only 0.5 ev (400 km/sec) and thermal energy of about 10 ev (10^5 ^oK). Thus, a bulk of the electrons have energies comparable to the spacecraft potential, causing their trajectories to be appreciably perturbed, resulting in significant changes in their distribution in velocity space. Thus, it is necessary to determine the relation between the desired "unperturbed" f_e and the "perturbed" $\tilde{f}_e$ measured at the spacecraft. In contrast, protons have convective energies of 800 ev and thermal energies of about 10 ev (10^5 ^oK). This means that the spacecraft potential is only a small fraction of a proton's energy, causing only a negligable perturbation of their trajectories.

The perturbations experienced by f_e are expected to contain three separate effects: (1) an energy shift equal to the potential energy at the spacecraft surface experienced

by the electrons as they are accelerated in the Debye sphere surrounding the positively charged spacecraft, (2) a concentration of their trajectories (focusing) as they approach the spacecraft, and (3) a rarefraction of the electrons as they are accelerated in the Debye sphere. The actual form for f_e is, in practice, impossible to determine. For example, if one were to try to solve this problem in a self-consistent way, even for the simplifying assumption of spherical symmetry [Ira B. Bernstein and Irving N. Rabinowitz, (1959)[16]], one would find himself faced with trying to solve a very complicated non-linear integro-differential equation. In actuality, such a simple configuration does not exist for any given spacecraft. For example, for Imp 8, some of these complications are: (1) Imp 8 spacecraft is a cylinder with a radius of about 1 meter and a height comparable to its diameter (spherical symmetry does not hold); (2) a number of antennas are protruding from it; (3) the Debye lengths for the spacecraft potential may have an angular dependence relative to the sun--s/c line [More specifically, λ_D should be a few centimeters on the sunward side (photoelectrons contribute to the formation of a relatively dense cloud of plasma compared to that in the ambient solar wind, over the illuminated surface of the spacecraft), and λ_D about 10 meters on the backward side (average λ_D for ambient solar wind is about 10 meters)]; (4) surface of spacecraft is a poor conductor such that it may become differentially charged,

thus giving rise to a dipole term to the potential. [On the sunward side the surface will acquire a positive potential (photo effect), while on the backward or dark side of the spacecraft it will acquire a negative potential (negative "plasma" current). Then, since the surface is a poor conductor, currents in the surface will not flow at a sufficient rate so as to equalize the potential difference in the surface material.] Furthermore, aging suffered by the spacecraft surface material through interactions with the surrounding plasma and radiation will bring about unknown changes in the surface properties of this material and make any calculations questionable no matter how sophisticated they may be.

All of these complications clearly imply that any self-consistent quantitative solution for this problem is just about impossible. With these facts in mind, one must resort to some rough estimate of the size of the effect. The approach we chose was to assume that a plausible spacecraft potential is known; this allows us to use the collisionless Boltzmann equation, and thus to solve for $\tilde{f}_e$ in terms of an assumed f_e at infinity. If the potential qualitatively meets the expected characteristics (proper magnitude, screened profile, etc.), one expects that the estimates as to the magnitude of the distortions in $\tilde{f}_e$ will not be too far off. We present the details of our approach in the following sections.

(2.) General Quantitative Considerations for a Spherical Model

Boltzman equation is

$$\frac{d}{dt} f_e(\vec{r}, \vec{v}, t) = \left(\frac{\delta f_e}{\delta t}\right)_{coll} \tag{2.1}$$

where

$$\frac{d}{dt} \equiv \frac{\partial}{\partial t} + \vec{v} \cdot \nabla + \frac{\vec{F}}{m_e} \cdot \nabla_v$$

is the total phase space time derivative, and

$$\left(\frac{\delta f_e}{\delta t}\right)_{coll} \tag{2.2}$$

represents changes in f_e due to collisions (i.e., close encounters with other particles, strong resonant interactions with waves, etc.), $\vec{v}$ is the electron velocity, and

$$\vec{F} = -e\left(\vec{E} + \vec{v} \times \vec{B}\right) + m_e \vec{g} \tag{2.3}$$

is the force on the electron due to the macroscopic electric, magnetic, and gravitational fields of the medium; $\vec{B}$ is the magnetic field of the surrounding plasma, $\vec{g}$ is the gravitational acceleration vector, and

$$\vec{E} = -\nabla \Phi - \vec{V} \times \vec{B} \tag{2.4}$$

is the electric field, Φ is the spacecraft potential, and $\vec{V}$ is the wind velocity of the plasma. Referring to Figure 12, which gives a pictorial description of the problem, one sees that the electrons mainly experience the effects of the potential inside the Debye sphere. This means that the electric field due to the spacecraft potential ($E \sim \Phi_o / \lambda_D$) is about equal to 0.2 volts/meter for Φ_o = 2 volts and λ_D = 10

meters. The gravitational term in Eq. (2.3) is negligable compared to the electric fields around the spacecraft, while the induction term $-\vec{V} \times \vec{B} \approx 0.2 \times 10^{-2}$ volts/meter for V = 400 km/sec and B = 5 gammas is only a 1% correction and may also be dropped. Therefore, we may put to a good approximation:

$$\vec{E} \cong -\nabla \Phi \tag{2.5}$$

The collision term in Eq. (2.1) may also be dropped, since the m.f.p. for collisions involving electrons is on the order of an AU, so the electrons while traversing the Debye sphere ($\lambda_D \sim 10$ meters) will experience no collisions. Furthermore, since R_e, the electron gyro-radius, is on the order of kilometers ($\lambda_D/R_e \ll 1$), the electrons will not experience any significant deflections from the magnetic field while traversing the Debye sphere. Thus, we may also neglect the effects of the magnetic field in Eq. (2.3). Finally, we drop the $\frac{\partial}{\partial t}$ term by assuming steady state.

We shall now impose the ad hoc assumption of spherical symmetry, $\Phi(\vec{r}) = \Phi(r)$ (central force problem) which brings about considerable simplification to the problem. (As we shall see later, it reduced the problem to quadratures.) The form of the potential to be used in describing Φ shall be the spherically symmetric screened potential (monopole term), which may be written the following ways:

$$\Phi(r) = \frac{\Phi_0}{x} e^{-z_0(x-1)} \tag{2.6}$$

$$\Phi(r) = \frac{\Phi_o Z_o}{Z} e^{-(z-z_o)} \tag{2.7}$$

where r is the radial distance from the center of the spacecraft, r_o is the radius of the spacecraft, $x = r/r_o$, $z = r/\lambda_D$, $z_o = r_o/\lambda_D$, and $\Phi_o = \Phi(r_o)$. Once the form of the potential $\Phi(r)$ is specified, one can proceed to study the form of $\tilde{f}_e$ at the spacecraft's surface (entrance aperture of the detector). To do this we specify the form of the initial distribution f_e at "infinity" (far from the spacecraft), and then require that $\tilde{f}_e$ satisfy the Boltzmann equation, Eq. (2.1), at r_o.

It is possible to express the distribution function f_e in the following way:

$$f_e(\vec{r},\vec{v}) = \Psi(H) \tag{2.8}$$

where Ψ is some arbitrary function of the scalar quantity $H(\vec{r},\vec{v})$. Note that all the velocity and coordinate dependences in f_e are contained in H. The reason for doing this is that the same function H can be used for various functional forms of Ψ. Thus, the actual solution for H must be its solution at infinity plus some correction term. Substituting Eq. (2.8) into Eq. (2.1), we get:

$$\Psi'(H)\frac{dH}{dt} = 0$$

which reduces to:

$$\frac{dH(\vec{r},\vec{v})}{dt} = 0 \tag{2.9}$$

One can split the function $H(\vec{r},\vec{v})$ into two functions, i.e.,

$$H(\vec{r},\vec{v}) = h(\vec{r},\vec{v}) + G(\vec{r},\vec{v}) \tag{2.10}$$

where h is the expression for H when $\Phi = 0$, while G is the correction term when $\Phi \neq 0$. For example, the Maxwellian

$$f_e = \text{const.}\, e^{-h}$$

has

$$h = \frac{\frac{1}{2} m_e (\vec{v} - \vec{V})^2}{kT} \tag{2.11}$$

while the bi-Maxwellian has

$$h(\vec{r},\vec{v}) = \beta_{ik} w_i w_k \tag{2.12}$$

where

$$\beta_{ik} = \beta_\perp \delta_{ik} + \Delta\beta\, b_i b_k$$

and

$$\vec{w} = \vec{v} - \vec{V} \quad , \quad \hat{b} = \vec{B}/B$$

In order to obtain solutions of Eq. (2.9), we make use of the fact that the electron energy and angular momentum are conserved, i.e.,

$$U = \frac{1}{2} m_e v^2 - e\Phi(r) = \text{const.} \tag{2.13}$$

$$\vec{\ell} = \vec{r} \times \vec{v} = \text{const.} \tag{2.14}$$

For a central force, the electric field simplifies to the following:

$$\vec{E} = -\frac{d}{dr}\Phi(r)\,\hat{r} \tag{2.15}$$

where $\hat{r} = \vec{r}/r$. It will be convenient to introduce the quantity

$$\xi \equiv (\hat{b} \times \vec{\ell}) \cdot \vec{r} \tag{2.16}$$

which can be rewritten as:

$$\xi \equiv v_{to} r_o \cos \chi \tag{2.17}$$

where χ is the angle between the $\vec{B}$ vector and $\vec{v}_{ot}$, and $\vec{v}_{ot}$ is the transverse velocity of the electron at $r = r_o$. Thus, according to Eqs. (2.9), (2.10), and (2.12), the correction term G obeys the equation:

$$\frac{dG}{dt} = \frac{2e}{m_e} \left[\beta_\perp \vec{E} \cdot \vec{w} + \Delta\beta \, E_\parallel w_\parallel \right] \tag{2.18}$$

where

$$E_\parallel \equiv \vec{E} \cdot \hat{b}$$

Due to the fact that $\vec{\ell}$ and U are conserved, one can express the radial velocity of the electron as a function of r alone:

$$v_r = -\sqrt{\frac{2(U + e\Phi)}{m_e} - \frac{\ell^2}{r^2}} \tag{2.19}$$

Note that since we are considering trajectories coming from infinity, we have chosen the negative sign for v_r. We thus have for the differential time interval dt:

$$dt = \frac{-dr}{\sqrt{\frac{2(U + e\Phi)}{m_e} - \frac{\ell^2}{r^2}}} \tag{2.20}$$

Substituting Eq. (2.20) into Eq. (2.18) and integrating from infinity to r_o, we get

$$G(\vec{r}_o, \vec{v}_o) = e \int_\infty^{r_o} \frac{dr}{v_r} \left[2E_r (v_r - \bar{v}_r) \beta_\perp + 2\Delta\beta \, E_r b_r w_\parallel \right] \tag{2.21}$$

where $E_r = \vec{E} \cdot \hat{r}$, $b_r = \hat{b} \cdot \hat{r}$ and $V_r = \vec{V} \cdot \hat{r}$. From expressions (2.14), (2.16), (2.17), and the definition for $\vec{w}$, we have

$$W_{\parallel} = V_r b_r + \frac{\varphi}{r} - V_{\parallel} \tag{2.22}$$

Substituting this expression into Eq. (2.21) and rearranging terms, we get

$$G(\vec{r}_o, \vec{v}_o) = -u_o^2 \beta_\perp \left[1 + \epsilon_B b_r^2 + \frac{(V_r + \epsilon b_r V_{\parallel})}{u_o} K_1 - \frac{\epsilon_B b_r V_{to}}{u_o} \cos \chi \, K_2 \right] \tag{2.23}$$

where

$$K_1 = -\sqrt{\frac{e\Phi_o}{u}} \int_{r_o}^{\infty} \frac{\frac{1}{\Phi_o} \frac{d\Phi}{dr} dr}{\sqrt{1 + \frac{e\Phi}{u} - \frac{b^2}{r^2}}} \tag{2.24}$$

$$K_2 = -\sqrt{\frac{e\Phi_o}{u}} \int_{r_o}^{\infty} \frac{r_o}{r} \frac{\frac{1}{\Phi_o} \frac{d\Phi}{dr} dr}{\sqrt{1 + \frac{e\Phi}{u} - \frac{b^2}{r^2}}} \tag{2.25}$$

are positive definite integral expressions to be evaluated once the potential $\Phi(r)$ is specified. The other symbols above have the following meaning:

$$\frac{1}{2} m_e u_o^2 \equiv e\Phi_o \tag{2.26}$$

defines the velocity u_o for an electron at the spacecraft r_o, which has zero energy at infinity [U = 0, see Eq. (2.13)];

$$\epsilon_B \equiv \frac{\Delta\beta}{\beta_\perp} \tag{2.27}$$

and we have introduced the impact parameter b

$$\ell \equiv \sqrt{\frac{2U}{m_e}}\, b \tag{2.28}$$

We have thus reduced the problem to quadratures, the integral expressions K_1 and K_2. The substitution of Eq. (2.23) into Eq. (2.10) gives us via Eqs. (2.12) and (2.8) the desired expression for $\tilde{f}_e$,

$$\tilde{f}_e(\vec{r}_o, \vec{v}_o) = \frac{n_e \beta_\perp \sqrt{\beta_\parallel}}{\pi^{3/2}}\, e^{-[\beta_\perp(\vec{v}_o - \vec{V})^2 + \Delta\beta(v_{\parallel o} - V_\parallel)^2 + G(\vec{r}_o, \vec{v}_o)]} \tag{2.29}$$

It should be emphasized that now $\tilde{f}_e$ is not only a function of the electron velocity, but also a function of position; (the distribution function $\tilde{f}_e$ is different for different points on the sphere of radius r_o). For instance, by referring to Eq. (2.23) one can see that there are terms proportional to the components of the bulk velocity $\vec{V}$ along the radial direction and parallel to the magnetic field vector $\vec{B}$, along with terms proportional to the cosine of the angle between $\vec{B}$ and $\vec{r}$. Therefore, as one moves along the surface of the spacecraft r_o at different angles relative to the directions defined by $\vec{V}$ and $\vec{B}$, the distribution function $\tilde{f}_e$ will have a different velocity dependence. In essence, the anisotropies introduced by the bulk velocity and magnetic field removed the spherical symmetry characteristic of the potential.

The first term in Eq. (2.23) is the familiar solution one gets for a dilute gas in the presence of a spherically symmetric potential. This term, which is present even when there are no bulk motions and anisotropies in the electrons, introduces a normalization correction which is more important at lower electron temperatures (i.e., thermal energy approaches potential energy of spacecraft $\mathfrak{T}_0$). The second term which arises from the temperature anisotropy modifies the corrections of the first term so that the corrections in $\tilde{f}_e$ are largest along directions where the electrons are colder (i.e., at right angles to $\vec{B}$ when $T_{\parallel} > T_{\perp}$). The third and fourth terms result merely from the fact that the electron gas as a whole is moving in the spacecraft frame. By referring to Figure 24, one can see that the third term in Eq. (2.23) will cause a reduction in $\tilde{f}_e$ for an observer at $\phi_c = 0^o$, and an increase in $\tilde{f}_e$ for an observer at $\phi_c = 180^o$. Therefore, this term appears to have the tendency for making the electrons have an apparent drift back toward the sun. To see this better, consider the expression for the differential work done by the potential upon the electrons in the spacecraft frame along the differential direction $d\vec{r}$

$$dW_{s/c} = \vec{F} \cdot d\vec{r} \tag{2.30}$$

which for $\phi_c = 0^o$ is

$$dW_{s/c} = F_r (w_r + V)\, dt \tag{2.31}$$

while for $\phi_c = 180^o$ is

$$dW_{s/c} = F_r (w_r - V) dt \qquad (2.32)$$

where w_r is the electron velocity in the proper frame, while the work $dW_{s/c}$ is the same in both cases. Thus, when the electron gas is, respectively, approaching, receding from the spacecraft along the radial direction, the time interval dt over which the electrons experience this force is, respectively, smaller, larger than that for V = 0. Therefore, the work upon the electrons in the electron frame of reference

$$dW_e = F_r w_r dt \qquad (2.33)$$

is, respectively, lesser, greater than that for V = 0. Thus, the electron flux for $\phi_c = 0^o$ is less than that for $\phi_c = 180^o$. Furthermore, since $V_r = 0$ for $\phi_c = 90^o$, the work performed is the same in both frames of reference, i.e., there is no effect due to the motion of the plasma in this direction. The fourth term, as in the case of the second term, modifies the corrections resulting from the motion of the plasma so that the corrections are larger along directions where the electrons are colder (i.e., for $T_{\parallel} > T_{\perp}$ electrons will acquire an apparent drift across the field). The last term arises purely from the initial anisotropy in f_e and is present even for the case of no convection ($\vec{V} = 0$). This term introduces no corrections along directions parallel or perpendicular to $\vec{B}$ where the distribution function f_e is symmetric relative to the radial direction. At all other

directions this symmetry of f_e relative to $\vec{r}$ no longer holds, and corrections from this term will result. For these situations more electrons along $\vec{B}$ relative to $\vec{r}$ are available for convergence toward the spacecraft than there are perpendicular to $\vec{B}$ relative to $\vec{r}$. Therefore, this term will have a tendency to remove the initial anisotropy of the electrons. The leading term in Eq. (2.23) shows that corrections to $\tilde{f}_e$ will be important when the spacecraft potential becomes comparable to the thermal energies of the electrons. The correction terms in Eq. (2.23) proportional to K_1 and K_2 are important for electron energies $\sim \Phi_o$ ($U \to 0$), while unimportant at higher energies $U \gg \Phi_o$. To see this better, consider the special limiting case of plane parallel geometry, where $\lambda_D \to 0$. For this limit, one merely has to replace the normal component of the electron velocity v_n ($-v_r$ direction) by (see Appendix B for proof)

$$v_n \to \sqrt{v_n^2 - u_o^2} \tag{2.34}$$

in the expression for H when G = 0. This is simply a statement of conservation of energy; the electrons experience an energy shift equal to $e\Phi_o$. Therefore, for electron energies large compared to $e\Phi_o$, $v_n \gg u_o$, we have to a very good approximation

$$v_n \to v_n \left[1 - \frac{1}{2} \left(\frac{u_o}{v_n} \right)^2 \right] \tag{2.35}$$

As can be seen, the correction term drops linearly with energy and will introduce corrections no larger than 5% for electron energies an order of magnitude greater than the spacecraft potential Φ_o (e.g., for Φ_o = 2 volts, $K_{Eo} > 20$ ev where $K_{Eo} = \frac{1}{2}m_e v_o^2$). Thus, if the suprathermal electrons, $K_{Eo} > 60$ ev, contribute to most of the heat flux q_e [say, $q_e \sim 10^{-2}$ ergs/cm^2/sec (see section 2.4)], and if spacecraft potentials are no larger than 5 ev, one should be able to measure the heat flow vector to a reasonable degree of accuracy considering present experimental uncertainties $\sim \pm 2 \times 10^{-3}$ ergs/cm^2/sec.

We would now like to consider the relative order of the corrections in Eq. (2.23) for electron energies on the order of the electron thermal speed, $kT \approx 10$ ev, and typical spacecraft potentials $\Phi_o \approx 2$ ev. Furthermore, these energies correspond to the lower energy channels of the M.I.T. Imp 8 detector and the more recent Voyager detector, whose measurements are confined, respectively, to energies greater than 20 ev and 10 ev. Using the ordering scheme where corrections due to convection and anisotropy are first order small, i.e., convection

$$\frac{V}{w_c} \sim 0.2 \tag{2.36}$$

and anisotropy

$$\epsilon_B \sim 0.1 \tag{2.37}$$

we would like to compare the corrections introduced by spacecraft charging, given by Eq. (2.23). For the energies referred to above, the integrals K_1, K_2 are no larger than 0.3 (first order small). The leading term $u_o^2\beta$ is $\sim 1/5$ or first order small, while the corresponding second term due to anistropy is second order small. The third term, which introduces corrections due to convection is second order small (first order small relative to convection) [see Eq. (2.36)], while the corresponding fourth term from anisotropy is third order small. The last term, when we consider only those electrons striking the spacecraft at angles no larger than 45^o from the radial direction (approximate angular width of M.I.T. detectors), will be third order small. We may thus conclude that the corrections due to anisotropy are no larger than third order small (second order small relative to the anisotropies of convective and temperature anisotropy), except for the second term which is second order small, and may be dropped. Therefore, keeping terms second order small or larger we get for G

$$G(\vec{r}_o, \vec{v}_o) = -u_o^2 \beta_\perp \left[1 + \epsilon_B b_r^2 + \frac{v_r}{u_o} K_1\right] \qquad (2.38)$$

We will now drop the second order correction due to anisotropy, which only effects the normalization. Then by considering either the limit where $\lambda_D \to 0$ or the fact that for these energies >10 ev and typical detector angular widths $\sim 45^o$, the corrections to the integral K_1 due to the transverse

velocity of the electrons are small. The appropriate correction to the data reduces to that given by Eq. (2.34), where one only needs to account properly for the energy shift experienced by the electrons.

Finally, if one wishes to measure drift velocities of the "core" electrons, which as quoted by Feldman et al.[9] are $\sim$ 50-100 km/sec and thus second order small, one must consider the fact that the corrections introduced by spacecraft charging are of the same order [see Eq. (2.38)]. Thus, any attempt to measure such small effects must be considered questionable, even if the corrections given by Eq. (2.34) or the more rigorous expression (2.23) for G are used, since spherical symmetry is probably violated (e.g., λ_D is a function of angle).

(3.) Analytical Studies of the Formal Solutions--Particle Trajectories in Debye Potentials

In order to obtain numerical estimates of the effects due to spacecraft charging, one must evaluate the integral expressions K_1, K_2. To do this, the spherically symmetric screened potential given by Eqs. (2.6) and (2.7) is substituted into Eqs. (2.24) and (2.25). The integral expressions for K_1, K_2 then become:

$$K_n = \sqrt{\frac{e\Phi_0}{u}}\, e^{z_0} \int_1^\infty \frac{(1+z_0 x)}{x^n} \frac{e^{-z_0 x}\, dx}{\sqrt{x^2 + \frac{e\Phi_0}{u} x\, e^{z_0(1-x)} - b_0^2}} \tag{2.39}$$

or

$$K_n = \sqrt{\frac{1}{\nu}}\, z_0^{n-\frac{1}{2}} e^{\frac{1}{2}z_0} \int_{z_0}^\infty \frac{(1+z)}{z^n} \frac{e^{-z}\, dz}{\sqrt{z^2 + \frac{z e^{-z}}{\nu} - b_D^2}} \tag{2.40}$$

where we have introduced the dimensionless energy

$$\nu \equiv \left(\frac{u}{e\Phi_0}\right) \frac{e^{-z_0}}{z_0} \tag{2.41}$$

into Eq. (2.40),

$$b_0 \equiv b/r_0 \tag{2.42}$$

$$b_D \equiv b/\lambda_D \tag{2.43}$$

are the impact parameter in units of, respectively, the spacecraft radius r_0, and the Debye length λ_D, and the index

$n = 1,2$. The integrals K_n given by Eqs. (2.39) and (2.40) must be integrated numerically except for the limiting case of the Coulomb potential ($z_o = 0$, $\lambda_D \to \infty$, see Appendix B).

In section 2.4 we evaluate various velocity moments of $\tilde{f}_e$ in order to acquire numerical estimates of the apparent density, drift velocity, temperature, and heat flow vector that a detector would observe on a spinning spacecraft which is positively charged. One cannot carry out these calculations until one determines the regions in velocity space where the K_n's become imaginary, giving rise to "forbidden" zones in velocity space. These forbidden zones or more appropriately forbidden zone boundaries determine the limits of integration in velocity space. In order to take into account properly the effects of these forbidden zone boundaries, one must understand the properties of the electron trajectories within the potential given by Eqs. (2.6) and (2.7).

In studying the electron trajectories in a spherically symmetric potential it is useful to consider the radial motion in a fictitious or effective potential which is comprised of the potential Φ itself, and the potential due to the "centrifugal force." Thus, we introduce the dimensionless effective potential

$$V_{eff} = \frac{b_D^2}{z^2} - \frac{e^{-z}}{\sqrt{z}} \tag{2.44}$$

and rewrite the radial velocity v_r the following way:

$$v_r = -v_\infty \sqrt{1 - V_{eff}} \qquad (2.45)$$

where $\frac{1}{2}m_e v_\infty^2 = U$, and the screened potential given by Eq. (2.7) has been substituted for Φ. The potential V_{eff} vanishes at infinity and is normalized in such a way that $V_{eff} = 1$ at the point $v_r = 0$ (i.e., the turning point for an electron coming from infinity).

In Fig. 13 we have a plot of V_{eff} versus z for the fixed parameter ν and for various values of the parameter b_D. An interesting feature of these curves is the presence of a trapping region allowing only bound trajectories. Such trapping regions do not occur in the case of the Coulomb potential. In our case the shielded potential Φ goes to zero more rapidly than the "centrifugal potential" as r approaches infinity (Φ decreases exponentially and the centrifugal potential goes to zero as $1/r^2$). In Fig. 14 we have an identical set of curves as those in Fig. 13, except that now the parameter b_D is held fixed and the parameter ν is varied. As may be seen, the curves display the usual dependence expected from varying the electron's energy. Figure 15 is identical to Figure 13, except that these curves correspond to a special limiting case to be discussed later on.

Among the curves in Figures 13, 14, and 15 are special ones labeled with the number "1". For these curves the effective potential is equal to one, and its first derivative with respect to z is equal to zero at a point which we call

the "critical" point z_c, i.e.,

(1) $$V_{eff} = 1 \tag{2.46a}$$

and

(2) $$\frac{d}{dz} V_{eff} = 0 \tag{2.46b}$$

at $z = z_c$. Equation (2.46) is equivalent to the statement that the radial velocity of an electron and its acceleration in the radial direction $\dot{v}_r$ are both equal to zero at $z = z_c$ (i.e., $v_r = 0$, $\dot{v}_r = 0$ at $z = z_c$, unstable circular orbit). These special curves correspond to certain trajectories which define the forbidden zone boundaries. These trajectories will be referred to as "critical" trajectories, which define the boundary separating the allowed and forbidden directions of an electron at fixed energy U for an observer at $r = r_o$ (more precise definition of allowed and forbidden directions given later on in text).

Substituting Eq. (2.44) into Eq. (2.46a) and replacing z by z_c we get

$$1 + \frac{e^{-z_c}}{v_c z_c} - \frac{(b_D^2)_c}{z_c^2} = 0 \tag{2.47}$$

Similarly Eqs. (2.46b) and (2.44) yield

$$v_c e^{z_c} = \frac{z_c (z_c + 1)}{2 (b_D^2)_c} \tag{2.48}$$

Combining Eqs. (2.47) and (2.48) we get the following relation for the critical impact parameter $(b_D)_c$ in terms of z_c:

$$(b_D^2)_c = \frac{z_c^2(z_c+1)}{z_c-1} \tag{2.49}$$

The quantity $(b_D^2)_c$ is plotted versus z_c in Fig. 16. Moreover, substituting Eq. (2.49) into Eq. (2.48) we get the following expression for the dimensionless critical energy ν_c in terms of z_c:

$$\nu_c = \frac{z_c-1}{2z_c} e^{-z_c} \tag{2.50}$$

which we have plotted versus z_c in Fig. 17. Eqs. (2.49) and (2.50) are a set of parametric equations relating the critical parameters $(b_D)_c$ and ν_c in terms of the parameter z_c. From these equations one can parametrically draw the locus of critical points in $(\nu_c, (b_D^2)_c)$ space which is shown in Fig. 18. Referring back to Fig. 15, where we have the special critical trajectory (curve 1), one can see that not only are Eqs. (2.46a) and (2.46b) satisfied by this trajectory but also

$$\frac{d^2V_{eff}}{dz^2} = 0 \quad \text{at} \quad z = z_s \tag{2.51}$$

where z_s is referred to as the "special critical" point. Because Eq. (2.51) gives us an added constraint, z_s is a

uniquely defined point in space. By doing the above differentiation and substituting Eqs. (2.49) and (2.50) in the resulting expression, we get a quadratic equation for z_s. Taking the positive root we get:

$$z_s = \frac{1+\sqrt{5}}{2} = 1.618 \tag{2.52}$$

The distance z_s may also be evaluated by taking the derivatives of Eq. (2.49) or Eq. (2.50) with respect to z_c and setting them equal to zero. Therefore z_s corresponds to the minima and maxima of $(b_D^2)_c$ and ν_c shown in Figures 16 and 17. Substituting Eq. (2.52) into Eqs. (2.49) and (2.50) we get corresponding special parameters for b_D and ν.

$$(b_D)_s = 3.33 \tag{2.53a}$$

$$\nu_s = 0.0379 \tag{2.53b}$$

It also follows from Figs. 13-15 that since the

$$\frac{d^2 V_{eff}}{dz^2} > 0$$

at the minima of V_{eff} at $z < z_s$, and

$$\frac{d^2 V_{eff}}{dz^2} < 0$$

at the maxima of V_{eff} at $z = z_c$, the point z_s must correspond to the trajectory, where the minimum and maximum in V_{eff} occur at the same point. Thus, all minima in V_{eff} must reside inside z_s, while all maxima in V_{eff} must reside outside z_s. Thus, trapping regions may only occur outside the

spacecraft for

$$z_o < z_s \tag{2.54}$$

This also says that the following condition must hold for all critical points:

$$z_c \geq z_s \tag{2.55}$$

i.e., all critical points not equal to z_s must reside outside z_s. Furthermore, it should be pointed out that these critical points z_c are present for all spacecraft radii z_o. It also follows from the preceding discussion that the upper branch in Fig. 18 corresponds to "z_c" z_s, where V_{eff} is a minimum and equal to one (i.e., V_{eff} 1 except at "z_c", where $V_{eff} = 1$). Thus, the upper branch in Fig. 18 does not impose any restrictions upon the trajectories. Therefore, curve one in Fig. 15, which corresponds to the special critical trajectory, divides the (U,ℓ) space into two regions: for large U and ℓ the centrifugal term completely dominates the 1/r attraction term of the potential at small r, and for smaller U, ℓ the opposite is true.

Referring back to Eq. (2.41) for the original definition of ν, we can solve for the critical energy U_c from ν_c, i.e.,

$$U_c = e\,\Phi_o \frac{(z_c-1)}{2}\left(\frac{z_o}{z_c}\right) e^{z_o - z_c} \tag{2.56}$$

It is apparent from Fig. 17 that for $z_c \geq z_s$, ν_c is a decreasing function of z_c. The same is true for U_c [see Eq. (2.56)]. Thus, if we consider spacecraft radii $z_o \geq z_s$,

the maximum energy at which critical trajectories can occur is determined by setting $z_c = z_o$, i.e.,

$$(U_c)_{max} = e\Phi_o \frac{(z_o - 1)}{2} \qquad \text{for } z_o \geq z_s \qquad (2.57)$$

Thus, for example, if Φ_o = 2 volts, and $\lambda_D = r_o/10$, then $(U_c)_{max}$ = 9 volts.

We would now like to define more precisely what we mean by "allowed" and "forbidden" directions referred to previously. To do this, let us consider an observer at a particular point on the spacecraft surface $r = r_o$. Allowed directions will then be considered to be those directions from which the observer detects an electron which has come from infinity and has not passed through the spacecraft. The contrary is true for the "forbidden" directions. In the case where the potential Φ is equal to zero, all allowed directions will be those directions coming from the upper hemisphere directly above the observer. Far from the spacecraft the electron trajectory becomes a straight line. We shall call the direction of this line the "asymptotic" direction of the trajectory. Because of the symmetry of the problem, allowed directions are degenerate in the sense that they represent "acceptance" cones whose axis of symmetry is the line along the zenith direction of the observer. Therefore, because of this symmetry, only those directions confined to an arbitrary plane need be specified. A particular

direction is thus given by one angle θ, which is the vertex angle of the acceptance cones. Therefore, for $\Phi_o = 0$, all allowed directions will correspond to those θ in the angular interval $0^o \leq \theta \leq 90^o$. When the potential $\Phi \neq 0$, critical trajectories will occur which will give rise to forbidden directions other than those below the horizon.

It will now be necessary for us to derive an expression relating the parameter b_D and the angle θ. To do this, one has only to take the square of Eq. (2.14) relating V_{t_o} and ℓ, substitute in place of $v_{t_o}^2$, $v_o^2 \sin^2\theta$, along with Eqs. (2.28) and (2.43), which together relate ℓ and b_D. Doing this, we get

$$b_D^2 = Z_o^2 \left(1 + \frac{e\Phi_o}{U}\right) \sin^2\theta \qquad (2.58)$$

As can be seen, large impact parameters for fixed U correspond to large angles of incidence θ, such that for b_D large enough, $\sin^2 \theta = 1$ (i.e., $\theta = 90^o$). Therefore, the "maximum" allowable b_D for fixed U is

$$(b_D^2)_{max} = Z_o^2 \left(1 + \frac{e\Phi_o}{U}\right) \qquad (2.59)$$

For situations when there are critical trajectories, the maximum allowable $b_D = (b_D)_c$ will be less than $(b_D)_{max}$, or equivalently $\theta_c < 90^o$, where θ_c is given by the relation:

$$(b_D^2)_c = Z_o^2 \left(1 + \frac{e\Phi_o}{U_c}\right) \sin^2\theta_c \qquad (2.60)$$

The case where $\theta_c = 90^o$ corresponds to $(U_c)_{max}$, the maximum energy at which critical trajectories will occur, or put in another way, the minimum energy at which critical trajectories will not occur. This is evident from Eq. (2.60) relating $(b_D)_c$, U_c, and θ_c and Eqs. (2.49) and (2.56) which show that $(b_D^2)_c$ increases quadratically while U_c decreases exponentially with increasing z_c for $z_c \geq z_s$. One way to solve for $(U_c)_{max}$ for arbitrary z_o is to combine Eq. (2.59) relating $(b_D^2)_{max}$ and U, and Eq. (2.41) relating ν and U, which gives us an expression for ν in terms of $(b_D^2)_{max}$ and z_o, i.e.,

$$\nu_{max} = \frac{z_o e^{-z_o}}{(b_D^2)_{max} - z_o^2} \tag{2.61}$$

One can then superimpose curves of ν versus $(b_D^2)_{max}$ from Eq. (2.61) for various z_o upon the parametric solution given in Fig. 18 relating ν_c and $(b_D^2)_c$ in (ν, b_D^2) phase space (lower curve). From the intersections between these two curves, which give us a ν_c that can be substituted into Eq. (2.41) for $(U_c)_{max}$, one can solve for $(U_c)_{max}$. Figure 19 gives an example where this method was used.

By substituting Eqs. (2.49) and (2.56), respectively, for $(b_D^2)_c$ and U_c into Eq. (2.60), we get the following expression for $\sin^2 \theta_c$ in terms of z_c and z_o:

$$\sin^2 \theta_c = \frac{z_c^2 (z_c + 1)}{z_o \left[(z_c - 1) z_o + 2 z_c e^{z_c - z_o} \right]} \tag{2.62}$$

which has been plotted in Fig. 20 as a function of z_c for various z_o. As already pointed out, all critical points z_c (i.e., $\sin^2 \theta_c \leq 1$) occur outside z_s for all z_o (specific examples given are $z_o = 0.1$, 1.0, z_s, and 10.0). Since $\sin^2 \theta_c$ is only a function of z_c and z_o, one can determine $\sin^2 \theta_c$ in terms of $\mathcal{V}_c$ for various z_o by solving the corresponding parametric equations given by Eq. (2.62) and Eq. (2.50) in terms of the parameter z_c. Fig. 21 displays the parametric solutions for $z_o = 0.1$, 1.0, z_s, and 10.0. As may be seen, the critical energy U_c increases with increasing z_o. For example, for $z_o = 0.1$, $(U_c)_{max}$ is only 0.50 mv, while for $z_o = 10$, $(U_c)_{max} = 9.0$ volts, where $\mathcal{I}_o = 2$ volts for both cases. Thus, it appears that in the case of small λ_D relative to r_o, the effects of the forbidden zone boundaries become important at energies on the order of the thermal energies of electrons.

We would now like to show a few trajectories of electrons in our screened potential. For this purpose one only needs the appropriate equation relating the azimuthal angle ϕ with the radial direction r. From the equation relating ϕ with ℓ, i.e.,

$$\ell = r^2 \frac{d\phi}{dt} \tag{2.63}$$

one can readily derive the following equation for ϕ in terms of z by substituting Eq. (2.20) for dt into Eq. (2.63) and then integrating. The result is

$$\phi = \pi - b_D \int_z^\infty \frac{dz}{z\sqrt{z^2 + \frac{z}{v} e^{-z} - b_D^2}} \qquad (2.64)$$

where Eq. (2.7) was used for Φ. The angle for ϕ at infinity ϕ_∞ was set equal to π.

In Figures 22a to 22c, we have three sets of trajectories, where for each set z_o is equal to, respectively, 0.1, 1.0, and 10.0. For each set there are three trajectories corresponding to three different values of the parameter b_D or angle of incidence θ at fixed energy U. The energy U was chosen to be approximately equal to the energy $(U_c)_{max}$ for that particular z_o. The outer trajectories correspond to $b_D \approx (b_D)_c$ (i.e., $\theta \simeq \pi/2$, since $U = (U_c)_{max}$), while the other two are for smaller values of the parameter b_D. The angle $\phi = \pi$ corresponds to electrons coming from the upper righthand quadrant of the figures.

As expected, far from the spacecraft the trajectories are rectilinear. (Note the change of scale as the Debye length λ_D is varied for fixed r_o). Then as the electrons approach the spacecraft at distances $z \sim z_c$ (even though z_c may be much greater than one), they begin to experience considerable deflections. For the special case where $b_D \approx (b_D)_c$, $z_o = 0.1$, the electrons go into an almost circular orbit at z_c for a number of revolutions before falling into the spacecraft. For $z_o = 10$, $b_D \approx (b_D)_c$, and $U = (U_c)_{max}$,

the critical point z_c as previously pointed out will occur at the spacecraft's surface z_o. This accounts of the electron skirting the outer edge of the spacecraft before striking it. These trajectories visibly suggest the possibility for electrons of sufficiently low energy to be orbiting around the spacecraft irregardless of whether the trapping regions occur inside or outside the spacecraft.

In Figs. 23a to 23c we have another set of electron trajectories for various z_o, where the electron energy U = 1.0 (3 ev electrons at z_o for Φ_o = 2 volts) is fixed and the same for all trajectories. We have arranged the trajectories so that they strike the spacecraft at the same point "P" where an observer could be assumed to reside. The solid curves in Figs. 23a to 23c (z_o = 0.1, 1.0, and 10.0) correspond to the actual electron trajectories, while the dashed lines represent the directions an observer at the point "P" would think the electrons were coming from. To each curve we assign an asymptotic direction (dashed line) and angle indicated in parentheses. Figure 23a (z_o = 0.1), which is representative of the limit $\lambda_D \gg r_o$, shows that the electrons experience significant deflections only for distances on the order of the spacecraft radius r_o from the spacecraft; i.e., the electric field decreases like $1/r^2$ so that the spacecraft radius r_o is the appropriate distance scale. While for the opposite limit $\lambda_D \ll r_o$, in Fig. 23c (z_o = 10.0), most of the deflections occur for distances on the order of the Debye

length λ_D from the spacecraft. Here we are approaching the plane parallel geometry, where the screening distance over which the electric fields are non-zero is the appropriate distance scale. Another important feature of these trajectories is that electrons which are approaching the detector from larger angles of incidence experience greater deflections. Therefore, the effects of trajectory convergence may be more important for detectors which are integral in angle, while less important for those differential in angle. In fact, for a perfectly differential detector, one may expect "focusing" effects (convergence of trajectories) to disappear completely, so that the only remaining effect to be corrected for is the energy shift experienced by the electrons. It is also apparent from comparing Figures 23a to 23c that as the screening distance λ_D is reduced (larger z_o), the deflections experienced by the electrons increase. In fact, referring to Figure 23c ($z_o = 10$), electrons coming from behind the spacecraft ($\theta = 167^o$) enter the detector at $\theta = 62^o$. This suggests that detectors which integrate over large angles of incidence may experience significant corrections at low electron energies for cases where $\lambda_D << r_o$.

It is interesting to note that for the short Debye length limit, the geometry for electrons coming in at large angles (electrons grazing the outer edge of the Debye sphere) is characteristic of that for curved-plate electrostatic analyzers where the inner plate is the surface of the spacecraft

and the outer one is the Debye sphere.

We are now ready to discuss the velocity moments of $\tilde{f}_e$. In carrying out the integrations it is convenient to use the (u_n, u_t) velocity space where

$$u^2 = u_n^2 + u_t^2 = v_o^2 / u_o^2 = 1 + \frac{U}{e\Phi_o} \tag{2.65}$$

u_n is the electron velocity pointing in the $-\vec{r}$ direction, while u_t is the transverse velocity relative to $\vec{r}$. Using Eq. (2.62) for $\sin^2\theta_c$ in terms of z_c, z_o, and Eq. (2.65), we get the following parametric equations relating $(u_n)_c$, $(u_t)_c$ in terms of the parameter z_c for fixed z_o:

$$(u_n^2)_c = 1 - \left(\frac{z_c^2(z_c+1) - z_o^2(z_c-1)}{2 z_o z_c} \right) e^{z_o - z_c} \tag{2.66a}$$

and

$$(u_t^2)_c = \frac{z_c(z_c+1)}{2 z_o} e^{z_o - z_c} \tag{2.66b}$$

which define the forbidden zone boundary in (u_n, u_t) velocity space, the principle objective of this section.

(4.) Contours of the Perturbed Electron Distribution Function $\tilde{f}_e$ and its "Moments" for a Positively Charged Spacecraft

(a.) Iso-contours of the ln $\tilde{f}_e$ $(\vec{r}, \vec{v})$

We would now like to display some iso-contours of the logarithm of the electron distribution function ln $\tilde{f}_e$ $(\vec{r}, \vec{v})$ at various points along the spacecraft surface, $r = r_o$. These contours will allow us to visualize the deformations of the electron distribution function by the spacecraft potential. In order to see the effects of the bulk velocity on $\tilde{f}_e$ more clearly, we have set the anisotropy parameter $\epsilon_B = 0$. Therefore, our contours will correspond to the special case where we have an isotropic convected Maxwellian at infinity. The form for $\tilde{f}_e$ in this case is the following [see Eqs. (2.29), (2.23)]:

$$\tilde{f}_e(\vec{r}_o, \vec{v}_o) = \frac{n_e}{\pi^{3/2} w_c^3} e^{-\frac{1}{w_c^2}\left[(\vec{v}_o - \vec{V}) - u_o^2\left(1 + \frac{V_r}{u_o} K_1\right)\right]} \tag{2.67}$$

where K_1 is given by Eq. (2.40). In this problem only the normal velocity v_{n_o} (-r direction) and the transverse velocity v_{t_o} have to be considered. Therefore, the contours of ln $\tilde{f}_e$ had only to be confined to a plane in velocity space, which for our purposes can be imagined to be coplanar with the ecliptic plane. In order to see better over what energy regimes spacecraft charging effects are important, we normalized the velocity components v_{n_o}, v_{t_o} in units of the most probable

thermal speed for a core electron (i.e., $T_c = 1.2 \times 10^5$ °K, $w_{no} = v_{no}/w_c, w_{to} = v_{to}/w_c$). Furthermore, since we plot contours of $\ln \tilde{f}_e$ for all directions in the velocity plane, we have in essence replaced the spacecraft by a point charge at the origin. Therefore, we are looking at $\tilde{f}_e$ at the radial distance r_o from the point charge at the origin at various angles ϕ_c relative to the earth-sun line ($\phi_c = 0^o$) (see Fig. 24 for a pictorial description of the problem). These contours were constructed so as to simulate the conditions seen by a detector on a spinning spacecraft where the spin axis is assumed to be normal to the ecliptic plane pointing north. The bulk speed was set equal to 400 km/sec and is aligned along the earth-sun line. In Figures 25 and 26 we have plotted these iso-contours for the two limiting cases $z_o = 0.1$ ($\lambda_D >> r_o$) and $z_o = 10.0$ ($\lambda_D << r_o$). For each case we have plotted five views of $\tilde{f}_e$, where $\phi_c = 0^o$, 45^o, 90^o, 135^o, and 180^o. The abscissa is the normal component of the velocity while the ordinate is the transverse component of the velocity. The velocity range in both directions is plus or minus two thermal speeds. Furthermore, the potential at the spacecraft surface $\underline{\Phi}_o$ was set equal to 4.5 volts, the dashed circles correspond to the case where the spacecraft potential is absent $\underline{\Phi}_o = 0$, while the solid curves are the iso-contours of $\ln f_e$ when the spacecraft potential is present $\underline{\Phi}_o \neq 0$. The iso-contours of $\ln \tilde{f}_e$, numbered one to seven, correspond to the levels that a Maxwellian distribution function would

have at electron velocities equal to 0.4, 0.6, 0.8, 1.0, 1.2, 1.4, and 1.6 thermal speeds. Therefore, curve number four is the one thermal speed contour. The darkened circles at the center of the figures for $z_o = 0.1$ correspond to the resulting forbidden zone due to the energy shift experienced by the electrons (radius equal to u_o/w_c). The football shaped darkened regions for $z_o = 10$ result from extensions of the forbidden zone boundaries due to critical trajectories out to higher energies as λ_D decreases relative to fixed r_o. [As a reminder to the reader, these boundaries were derived from Eq. (2.66) given in the preceding section.]

One of the most apparent features of these contours is that they have spread to larger radii when the potential is turned on, thus giving the electrons the appearance of being hotter. This effect is mainly due to the correction term referred to in section 2.2, which changes the normalization [see Eq. (2.67)]. Another important feature is that the deformations are largest near the forbidden zone boundaries or, equivalently, at lower electron energies. Furthermore, these distortions are important even out to two thermal speeds. In the case where $\phi_c = 90^o$, the iso-contours of $\ln \tilde{f}_e$ become circles with larger radii than the dashed circles. This results from the fact that $V_r = 0$ in this direction, as pointed out in section 2.2 (i.e., work done upon the electrons by the potential is the same in both electron and spacecraft frames).

To see better the effects of convection, we have plotted identical contours to those in Figs. 25 and 26, except that now we have factored out the correction term effecting the normalization in Eq. (2.67) for $\tilde{f}_e$, leaving us the following expression for $\tilde{f}_e$:

$$\tilde{f}_e(\vec{r}_o, \vec{v}_o) = \frac{n_e}{\pi^{3/2} w_c^3} e^{-\frac{1}{w_c^2}\left[(\vec{v}_o - \vec{V})^2 - 2u_o V_r K_1\right]} \tag{2.68}$$

The set of iso-contours for this $\tilde{f}_e$ are given in Figs. 27 and 28 for, respectively, $z_o = 0.1$ and 10.0. We will now confine our attention to regions where $w_n > 0$, which corresponds to electrons approaching the spacecraft without passing through it. Once this is done, one can see by comparing contours for $\phi_c = 0^o$ (observer at r_o looking at the sun) with those for $\phi_c = 180^o$ (observer at r_o looking away from the sun) that the electrons have an apparent drift back toward the sun. Another important feature to note is that at large angles of incidence near the forbidden zone boundaries, the deformations in $\tilde{f}_e$ are the largest. This is especially true for the short Debye length limit. For example, by referring to Fig. 28a ($\phi_c = 0^o$), the deformations at one thermal speed are significant for 0 as small as 63^o. You will also note that $\phi_c = 90^o$ the solid and dashed contours as expected are superimposed upon each other (solid contours become circles). We would also like to point out

that in the limit as $\lambda_D \rightarrow 0$, the forbidden zone boundary, which is football shaped for $z_o = 10$, will become two infinite planes in the transverse direction at $w_{n_o} = \pm u_o/w_c$.

These contours, Figs. 25-28, could be used for a variety of different purposes. One such example is where one could superimpose upon these contours the acceptance fan characteristic of the detector in order to get a visual picture of the effects of spacecraft charging on one's measurements.

As another example, one might want to see how $\tilde{f}_e$ would appear to a differential detector which is mounted on a spinning spacecraft (i.e., detector normal points in radial direction and is confined to the spin plane). To do this one has only to set $v_{t_o} = 0$ in Eq. (2.67) for $\tilde{f}_e$ and change ϕ_c continuously from 0^o to 360^o for a single contour. In Fig. 29 we have such a contour, where Eq. (2.67) is used for $\tilde{f}_e$. The horizontal and vertical axis in Fig. 29 are, respectively, the solar ecliptic x and y components of the electron velocity in units of most probable thermal speeds. Thus, the sun is to our left (positive x-direction), and downstream is to our right (negative x-direction). The detector may be imagined to be rotating around the center of the figure with its normal pointing in toward the origin. As pointed out in section 2.3, for $v_{ot} = 0$ "focusing" effects (convergence of electron trajectories) disappear, so that for these contours only the energy shift effect remains. A similar contour is shown in Fig. 30, where Eq. (2.68) was used for $\tilde{f}_e$ (i.e., normalization

correction term dropped). Referring to both figures, it is apparent that the electron will appear hotter. Furthermore, from Fig. 30 we see that the electrons appear to be drifting back toward the sun.

(b.) Velocity moments of $\tilde{f}_e(\vec{r}, \vec{v})$

Until now we have not presented any numerical estimates of the size of the effects introduced by the spacecraft potential upon the integral electron measurements. To do this, we will perform certain velocity moments (macroscopic averages) of $\tilde{f}_e$ that were first referred to in section 2.3. These macroscopic averages are not true moment integrations of $\tilde{f}_e$ over all velocity space, but are more representative of the way a detector may measure moments of $\tilde{f}_e$. For example, since one is unable to sample $\tilde{f}_e$ over all velocity space by looking in one direction (electrons subsonic), one must spin the spacecraft, thus allowing the detector to sample $\tilde{f}_e$ in different directions. Then, if one had a detector which had an angular width much larger than that for $\tilde{f}_e$ along the plane parallel to the spin axis and fairly narrow in the spin plane, such as the M.I.T. detector (see Fig. 2), one could obtain slices in velocity space of $\tilde{f}_e$ in different directions. Finally, by doing an appropriate sum of all these measurements, one could obtain, in principle, the various velocity moments of $\tilde{f}_e$ (hypothetical detector we are considering does sample

in the sunward direction). To simulate this, we use a 2π steradian detector which is designed to accept all allowed directions as defined in section 2.3 and all velocities in the v_{n_o} direction. With this model, only two separate integrations 180^o apart in angle are needed to produce one complete "moment" integration over $\tilde{f}_e$.

We define the following macroscopic averages (moments) of $\tilde{f}_e$:

$$M_o = \int R \tilde{f}_e \, d^3V_o \tag{2.69}$$

$$M_1 = \int R \tilde{f}_e V_{n_o} d^3V_o \tag{2.70}$$

$$M_2 = m_e \int R \tilde{f}_e (V_{n_o} - V_n)^2 d^3V_o \tag{2.71}$$

$$M_3 = \tfrac{1}{2} m_e \int R \tilde{f}_e (\vec{V}_o - \vec{V})^2 (V_{n_o} - V_n) d^3V_o \tag{2.72}$$

where R represents the response function of the detector, $\vec{v}_o$ is the electron velocity at the entrance aperture of the detector, and v_{n_o} is the normal component of the electron velocity v_n at the detector. In the case of our 2π detector, R is given by (using cylindrical coordinates):

$$R = \begin{cases} 1 \quad \text{for } 0 \le V_{n_o} \le \infty, \; 0 \le V_{t_o} \le \infty, \; 0 \le \phi_o < 2\pi \\ 0 \quad \text{for } -\infty \le V_{n_o} < 0, \; 0 \le V_{t_o} \le \infty, \; 0 \le \phi_o < 2\pi \end{cases} \tag{2.73}$$

Therefore, in one direction the detector integrates over $\tilde{f}_e$ in the "forward" half of velocity space as defined by Eq.

(2.73), while the "backward" or second half of velocity space is integrated over by first rotating the spacecraft 180^{o} and then performing the integrations as specified by Eq. (2.73) again. Then to get the complete "velocity" moment, we take the appropriate sum of the two separate integrations.

The form of the distribution function $\tilde{f}_e$ used in our calculations is the one derived in section 2.2, Eq. (2.29) [the convected bi-Maxwellian distribution function given by Eq. (1.26) at infinity]. We thus have the following for $\tilde{f}_e$ [see Eqs. (2.23), (2.29)]:

$$\tilde{f}_e(\vec{r}_o, \vec{V}_o) = \frac{n_e \beta_\perp \sqrt{\beta_\parallel}}{\pi^{3/2}} e^{-\left[\beta_\perp (\vec{V}_o - \vec{V})^2 + \Delta\beta (V_{\parallel_o} - V_\parallel)^2 + G(\vec{r}_o, \vec{V}_o)\right]} \tag{2.74}$$

where

$$G(r_o, \vec{V}_o) = -u_o^2 \beta_\perp \left[1 + \epsilon_B b_r^2 + \frac{(V_r + \epsilon_B b_r V_\parallel)}{u_o} K_1 - \frac{\epsilon_B b_r v_{t_o}}{u_o} \cos\chi \, K_2\right] \tag{2.75}$$

and K_1, K_2 are given by either Eqs. (2.39) or (2.40).

Referring to Fig. 24, the following definitions are used in the determination of the apparent electron density, wind velocity, temperature, and heat flow vector at various look directions (ϕ_c):

1) Apparent Density

$$n_o(\phi_c) = M_o(\phi_c) + M_o(\phi_c + \pi) \tag{2.76}$$

2) Component of apparent wind velocity along normal of detector

$$V_{n_o}(\phi_c) = (M_1(\phi_c) - M_1(\phi_c+\pi))/n_o \qquad (2.77)$$

3) Apparent Temperature

$$T_o(\phi_c) = (M_2(\phi_c) + M_2(\phi_c+\pi))/(n_o k) \qquad (2.78)$$

4) Component of apparent heat flow vector along normal of detector

$$Q_{n_o}(\phi_c) = M_3(\phi_c) - M_3(\phi_c+\pi) \qquad (2.79)$$

where the subscript "o" refers to the value of that quantity at the spacecraft $r = r_o$.

In doing our numerical integrations of Eqs. (2.69) to (2.72), the density, temperature, and wind velocity of the electrons far from the spacecraft were set equal to the following:

$$\begin{aligned} n_e &= 10\ cm^{-3} \\ T &= 1.2 \times 10^5\ ^\circ K \\ V &= 400\ km/sec \end{aligned} \qquad (2.80)$$

where the wind velocity is confined to the ecliptic plane and pointing in the anti-solar direction (see Figure 24). The anisotropy $T_{\parallel}/T_{\perp}$ was set equal to either 1.5 or 2.0; the magnetic field was oriented at 45° with respect to V and confined to the ecliptic plane [see Figures 24 and 11],

$$\begin{aligned} \phi_B &= 45^\circ \\ \theta_B &= 90^\circ \end{aligned} \qquad (2.81)$$

and the spacecraft potential at r_o was set equal to 4.5 volts,

$$\Phi_o = 4.5 \text{ volts} \tag{2.82}$$

Because of the lack of symmetry to the problem introduced by the magnetic field, the integrations over $\tilde{f}_e$ are three-dimensional. Then because the integrand is also an integral equation (K_1, K_2), Eqs. (2.69) to (2.72) are four-dimensional integrals. In order to reduce the computation time we constructed a two-dimensional array in u_z, u_t space for K_1 and K_2. The velocities u_z, u_t are, respectively, the normal, transverse velocity in units of u_o. Using a four point interpolation procedure, we were able to obtain values for K_1, K_2 for all u_z, u_t. The integrations were performed using an iterative procedure based on Simpson's rule. During the integration process, because of the presence of forbidden zones, the integral expressions K_1, K_2 were integrated numerically at the points in u_z, u_t space when any one of the four points used in the interpolation procedure fell inside the forbidden zone boundary. Finally, the forbidden zone boundary was determined from the parametric equations relating $(u_n)_c$ and $(u_t)_c$ given by Eq. (2.66).

The results of our numerical integrations for $z_o = 0.0$ and 10.0 are shown, respectively, in Tables 4 and 5. The reasons why we did the integrations for $z_o = 0.0$ instead of $z_o = 0.1$ are because, for one, they yield almost identical

results, as may be expected, and also because the integrals for the K_n's, where $z_o = 0$ (see Appendix B), can be evaluated; thus allowing for simplicity in the numerical integrations, faster computation time, while also allowing us to check our interpolation routine (i.e., compare numerical results for $z_o = 0.0$ and 0.1). The results of the integrations for $z_0 = 0.1$ and 1.0, respectively, are given in Tables 6 and 7 and, as may be seen, the differences between the integrations for $z_o = 0.0$, 0.1, and 1.0 do not differ significantly.

We will now discuss the results of our integrations for the large Debye length limit (i.e., $z_o = 0.0, \lambda_D \to \infty$). For no anisotropy ($T_{\parallel} / T_{\perp} = 1.0$), we find the average density $n_o \approx 12.86$ cm^{-3}, which is about the same result one gets with no convection ($\vec{V} = 0$, see Appendix B). Also, the electrons have an apparent drift velocity relative to the electron frame of reference back toward the sun, i.e., $\Delta V_o(0) \approx -45$ km/sec, where

$$\Delta V_o(\phi_c) \equiv V_{n_o}(\phi_c) - V \cos\phi_c \qquad (2.83)$$

is defined to be the apparent drift velocity. Also, the electrons have an apparent heat flow $\approx -3.3 \times 10^{-3}$ ergs/cm^2/sec, which is comparable to observed heat flow $\sim 8 \times 10^{-3}$ ergs/cm^2/sec. Both these effects are consistent with the backward drift of electrons suggested by the contours of $\tilde{f}_e$. The temperature $T_o \approx 1.4 \times 10^5$ ^{o}K is about 18% higher than

that for no spacecraft charging. The results of the integrations with anisotropy ($T_{\parallel}/T_{\perp}$ = 1.5, 2.0) yield qualitatively similar distortions in f_e that are found for no anisotropy. Some of the new affects introduced by the anisotropy are the following:

(1) At right angles to $\vec{B}$ the density is the largest with respect to all other directions, while the contrary is true along $\vec{B}$. This is consistent with previous discussions in section 2.2 concerning the correction term effecting the normalization in $\tilde{f}_e$ which is largest along directions where the temperature is coldest.

(2) The drift velocity vector is equal to 44 km/sec in magnitude where $\phi = -17^{o}$ (azimuthal direction drift velocity vector is pointing; ϕ has same definition as ϕ_c, see Fig. 24), and 47 km/sec in magnitude where $\phi = -31^{o}$ for $T_{\parallel}/T_{\perp}$ = 1.5 and 2.0, respectively. The directions indicated are such that the drift is toward the sun slightly rotated perpendicular to the magnetic field. A similar effect occurs for the apparent heat flow vector which is equal to 3.27 x 10^{-3} ergs/cm^2/sec in magnitude where $\phi = -8.2^{o}$, and 3.42 x 10^{-3} ergs/cm^2/sec in magnitude where $\phi = -12.5^{o}$ for $T_{\parallel}/T_{\perp}$ = 1.5 and 2.0, respectively. These results are consistent with the fact that the distortions introduced by convection ($\vec{V} \neq 0$) are greatest along those directions where the temperature is the smallest (i.e., transverse to the magnetic field for $T_{\parallel} > T_{\perp}$).

(3) The increase in temperature in all directions is about the same, $\sim 18\%$, so that the change in anistropy is small.

The results for $z_o = 10.0$, or short Debye length limit ($\lambda_D << r_o$), are markedly different from those for the long Debye length limit. One important result is that the density is less than the initial density by about 7%, contrary to that for the long Debye length limit, where the density is greater than the initial density by about 29%. This may be understood by considering the fact that for the short Debye length limit the geometry of the problem is becoming more plane parallel. For this geometry, trajectory convergence is not as important as the rarefraction experienced by the electrons as they enter the Debye sphere. This rarefraction comes about from the electrons being accelerated, so that in order to conserve particles their density becomes less (see Appendix B for more details). This rarefraction, as far as the numerical integrations are concerned, may be related to the extension of the forbidden zone out to higher energies, thus truncating significant portions of $\tilde{f}_e$ in the integrations (electrons coming in from the sides). Another important change is that the electrons appear to be drifting away from the sun rather than toward it, i.e., ($\Delta V_o = 35$ km/sec, $\phi = 180^o$), (43 km/sec, $\phi = 190^o$) for, respectively, $T_{\parallel}/T_{\perp} = 1.0$ and 2.0. Referring to Table 5, it appears that this flip in sign for $\Delta\vec{V}_o$ may to some degree be explained by the decrease

in density. Furthermore, the contours of $\tilde{f}_e$ suggest that the electrons are drifting toward the sun for $z_o = 10.0$. By looking at these contours, one can see that an appreciable part of $\tilde{f}_e$ is excluded by the forbidden zone in the backward direction (see Fig. 26) as is indicated in Table 5. Thus, it is the design of the detector that determines which way the electrons appear to be drifting (i.e., drift toward the sun for detectors differential in angle, drift away from sun for detectors integral in angle). The apparent heat flow vector is essentially the same as that for the large Debye length limit, though somewhat less.

We will now discuss the distortions introduced by spacecraft charging upon the temperature measurements for small λ_D. At this limit even though the potential is still 4.5 volts, the temperature has increased by as much as 55% for $T_{\parallel}/T_{\perp} = 1.0$ and 2.0. Thus, for the short Debye length limit the effects of spacecraft charging are not trivial. By referring to the contours of $\tilde{f}_e$ for $z_o = 10.0$, one may conclude that for this potential ($\Phi_o = 4.5$ volts) spacecraft charging effects will be important even out to a few thermal speeds. Furthermore, the apparent anisotropy for this limit ≈ 1.90 is somewhat less than the initial anisotropy $T_{\parallel}/T_{\perp} = 2.0$. This may in part be due to the fact that for small λ_D the integral K_2 becomes comparable to K_1.

In Table 8 we have tabulated the results of our "moment" integrations for $\lambda_D = 0$ ($z_o \to \infty$). For this limit, as pointed

out in section 2.2, the appropriate correction is a simple energy shift of the normal component of the velocity, (for details see Appendix B), i.e.,

$$v_n \rightarrow \sqrt{v_n^2 - u_o^2} \tag{2.84}$$

As a reminder, these integrations correspond to observations by detectors integral in angle. Here the density has decreased by almost a factor of two. Also, the wind velocity has almost doubled from 400 km/sec to 713 km/sec, while the heat flow has flipped in sign, so that it is now flowing away from the sun with a magnitude $\approx 2.95 \times 10^{-3}$ ergs/cm^2/sec. Furthermore, the temperatures have increased by more than a factor of 2, while for $T_{\parallel}/T_{\perp} = 2.0$ the apparent anistropy $(T_{\parallel}/T_{\perp})_o \approx 1.5$ has become less by about 50%.

In Table 9 we have displayed the results of calculations similar to the above, except that now they correspond to a detector differential in angle. This corresponds to the limit where $v_{t_o} = 0$, which is analogous to the plane parallel problem, though it holds for all λ_D. In this case the results are similar to those for the long Debye length limit, where the corrections for the temperature are, for example, only about 18% compared to 120% for the integral detector ($\lambda_D = 0$). This difference in results between the differential and integral detectors in angle may be attributed to the forbidden zone boundaries. For example, the integral detector must integrate along the forbidden zone boundary (infinite plane

in transverse direction at $v_n = u_o$), where the distortions in $\tilde{f}_e$ are large (critical trajectories); while for the differential detector, the forbidden zone, which only results from the energy shift experienced by the electrons (circle with radius u_o), only brings about moderate distortions in $\tilde{f}_e$. Thus, if one wishes to make electron measurements down to energies near the potential on the spacecraft, where the forbidden zone boundaries occur, it appears that only electron detectors differential in angle may be used, so that the corrections due to spacecraft charging be minimized, and the simple correction given by Eq. (2.84) be appropriate for all Debye lengths.

(5.) Closing Remarks

In order to by-pass the tremendous difficulties in solving the problem of a charged spacecraft, we assumed a highly simplified model for the spacecraft potential with spherical symmetry and simple Debye screening. The three parameters introduced by this potential are the potential at the spacecraft surface Φ_o, the radius of the spacecraft r_o, and the screening distance λ_D. In formulating the problem it was found that $e\Phi_o$ and $z_o = r_o/\lambda_D$ are the important parameters in the problem. The potential Φ_o determines over what energy range distortions of f_e are important, while the ratio z_o specifies the type of geometry involved, i.e., spherical for large λ_D, plane parallel for small λ_D. As is apparent throughout the discussion in this chapter, significantly different results are obtained depending upon the size of z_o and the type of detector used (i.e., detector differential in angle or integral in angle).

In conclusion, it is apparent from our calculations that the forbidden zone boundaries bring about considerable distortions to the observations made by detectors which integrate near these boundaries (2π steradian detector, energies near Φ_o). Furthermore, markedly different corrections result depending upon the size of the Debye length (e.g., convergence, rarefraction, ΔV_o = +300 km/sec, -50 km/sec, $Q_o = \pm 3 \times 10^{-3}$ ergs/cm^2/sec, $(\Delta T/T)_o$ = 20%, 120%). Since we

do not know the Debye length we are unable to know how properly to correct the data. In contrast, when spherical symmetry does hold, the differential detector appears not to have any of these difficulties, in that distortions do not get that large and the simple correction to the data given by Eq. (2.84) applies for all Debye lengths, i.e., simple energy shift correction for normal velocity into the detector. In general, spherical symmetry does not hold (e.g., λ_D is a function of angle around the spacecraft); therefore modifications will result, so that any electron measurements made near the spacecraft potential (i.e., U = 0) probably cannot be made. For instance, in the case where spherical symmetry does not hold, one could imagine cases where the distortions introduced by spacecraft charging upon measurements made by a detector differential in angle would be more severe than those for detectors integral in angle. Thus, in this case, the detectors integral in angle would be superior to those differential in angle. Therefore, in order to avoid these ambiguities, one must confine his measurements sufficiently above the spacecraft potential, (e.g., greater than 10 ev for Φ_o = 2 volts, see section 2.2), in order to ensure that the corrections due to spacecraft charging are only a small perturbation, so that the simple energy shift correction given by Eq. (2.84) will hold for all detectors (see section 2.2).

CHAPTER III

SEMI-EMPIRICAL DERIVATIONS OF THE WIND VELOCITY, EFFECTIVE TEMPERATURE, AND EFFECTIVE HEAT FLUX PROFILES

(1.) Opening Remarks

After having been acquainted with the experimental techniques involved in measurements of interplanetary electrons, we are now ready to turn our attention to the primary goal of our thesis. That is, the analysis of the physical processes involving interplanetary electrons. It is now well understood why most investigators in this field consider the importance of electrons from the fact that they are almost totally responsible for the conduction of heat. Before we embark on the models of the heat transport, it is essential that we understand the overall global pictures of the behavior of the macroscopic character of the solar wind. For example, of prime importance is that one understands how the heat flow vector due to electrons behaves as a function of distance from the sun.

At present, self-consistent solutions of the "fluid equations" describing the solar wind do not yet exist. Since they are very difficult to obtain, we decided to utilize a semi-empirical approach. To this end we have devised a certain systematic procedure of making use of the empirical knowledge of the interplanetary density and

phenomenological magnetic field topologies in conjunction with the three conservation laws for the interplanetary plasma as a whole. Before going into details of these calculations, we should like to review some of the observations pertaining to the solar corona and the interplanetary medium given in section 3.2 and the theoretical models of the solar wind given in section 3.3.

(2.) Review of Observations in the Solar Corona and Solar Wind

The solar corona, the outer envelope of the solar atmosphere and "source" of the solar wind, displays a complex structure composed of a number of different coronal forms. Three of the most prominent coronal features which give a more or less overall description of the solar corona are "quiet" regions (QR), coronal holes (CH), and active regions (AR). A brief description of each will now be given.

1. The quiet corona is defined to be those regions of the corona which are characteristic of the mean or normal corona. The magnetic topologies of the "quiet" corona are made up of a complex structure of closed and open field lines; the latter lines are believed to open with a more or less $1/r^2$ divergence. For reference, the electron density and coronal temperature characteristic of the lower "quiet" corona, as determined by Munroe and Whitbroe (1972)[17] from EUV data are, respectively, 5.5×10^8 cm^{-3}, and 1.66×10^6 ^oK. The large scale field strengths appear to be on the order of 10 gauss [Gurman et al. (1974)[18]].

2. Coronal holes, which appear as dark features on x-ray photographs of the solar corona display the following characteristics [see review article by Zirker (1977)[19]]:

(a) They display lack of emission in soft x-rays [Vaiana et al. (1973)[20]], reduced emission in certain EUV lines [Munroe and Withbroe (1972),[17] Neupert and Pizzo (1974,[21] Fisher and Musman (1975),[22] K-coronometer data

[Altshuler et al. (1972),[23] Munroe and Jackson (1977)[24]], and reduced emission in metric wavelengths [Dulk and Sheridan (1974)[25]]. This implies that they appear to be regions of low density and temperature relative to those found in the "quiet" corona. For example, Munroe and Withbroe (1972),[17] using EUV data, concluded that coronal holes were regions of reduced pressure by a factor of 3 relative to the quiet corona, with coronal temperatures about 6×10^5 ^oK lower than normal ($n_e \approx 10^8$ cm^{-3}, $T \approx 10^6$ ^oK).

(b) Temperature gradients at the transition level are about a factor of 2 less than that found in "quiet" regions, such that for coronal holes the conductive flux from the corona down to the transition layer was reduced by an order of magnitude.[17]

(c) Coronal holes coincide with large unipolar regions (or magnetic cells) [R. H. Levine (1977)[26]], where the magnetic field line topology is open with highly divergent field geometries near their boundaries.[20, 23, 24, 26]

(d) Coronal holes are found to be long lasting slowly evolving structures in the corona [Timothy et al. (1975),[27] Bohlin (1977),[28] Sheeley (1976)[29]] which have lifetimes on the order of many solar rotations (e.g., 3 to 10 solar rotations).

(e) Coronal holes appear to be less structured than that found in quiet regions.

(f) Polar coronal holes (PCH) appear to be present at all times (at least near solar minimum) and equatorial coronal holes are in general just extensions of polar coronal holes.[28]

(g) During solar minimum the coronal electron density inside polar coronal holes displays a latitudinal dependence such that the density is a minimum at the poles, and a maximum near the equator.[21]

(h) Coronal holes appear to rotate rigidly, showing no differential rotation with latitude as is found for most photospheric phenomena such as sun spots[27] [Wagner (1975)[30]].

(i) Outward streaming velocities of plasma in the range 16-20 km/sec have been observed within coronal holes from Doppler shifts of Si IX and Mg IX lines [Cushman and Rense (1976)[31]].

(j) Polar plumes are found to lie within the boundaries of polar coronal holes [I. A. Imad and G. L. Withbroe (1976)[32]]. Polar plumes are vertical columns of enhanced brightness relative to the weakly emitting polar coronal holes. They are about 3×10^4 km wide at about 1.1R [32] and extend out to distances on the order of a solar radius above the solar limb. They also tend to bend over as if to follow the large scale solar magnetic field which appears characteristically dipolar in these regions.

3. Active regions extending into the corona are large

bipolar magnetic features (closed field line topologies) where the underlying photospheric magnetic field strengths are very large relative to that found in "quiet" regions. They appear to form around the outer boundaries of coronal holes.[26] They are regions of enhanced emission in x-rays, EUV lines [Noyes et al. (1970)[33]], white light corona [Newkirk (1967)[34]], and metric wavelengths [Kundu (1967)[35]]. For typical active regions at the base of the corona the electron density $n_e \sim 10^9$ cm^{-3} is about a factor of 2-3 greater, coronal temperatures $T \sim 2.5 \times 10^6$ ^oK are slightly greater, and the temperature gradient at the transition layer is about a factor of 5 greater than that found in the "quiet" corona.[33] Without going into too much detail, active regions are associated with such features as helmet streamers (arch-like structures which form over "quiescent" prominences near the solar limb and extend out to several solar radii from the sun where they become thin streamers), streamers (extensions of enhancement which form over sunspot groups), sun spots (dark regions at the photospheric levels which are associated with very strong magnetic fields $\sim 10^3$ gauss), enhancements (regions of enhanced emission which form over sunspot groups), and condensations (small $\sim 10^4$ km, very bright emitters of radiation). Solar flares [Švestka (1976)[36]], which are eruptive phenomena on the sun and usually occur in sunspot groups, emit radiation in a broad spectral range from

γ- rays and hard x-rays all the way down to radio waves. Furthermore, in flare events some ions are accelerated up to very high energies on the order of 10Mev or in some cases 100 Mev.[36] Flares will produce hydromagnetic shock waves in the interplanetary plasma, resulting in considerable disruptions of the solar corona and the interplanetary medium for time periods on the order of hours. Also, there are the recently discovered x-ray bright points which are intense point-like sources of x-ray emission [Vaiana et al. (1970)[37]], and known to be associated with mini-flares.

As can be seen from this descriptive summary of the solar corona, it is an extremely complex structure spatially and temporally (Note: lack of structure (uniformity) seen within coronal holes may in part be due to our inability to see within them.) Furthermore, if one goes down to lower levels of the solar atmosphere where the photosphere and chromosphere reside, the structure gets even more complex (granulation, sunspots, plagues, spicules, etc.). Therefore, any attempt to describe the coronal expansion must consider the inherent complexities of the solar corona, at least in the interpretation of ones results.

The phenomenon of the coronal expansion and the interplanetary medium (solar wind) has been well-established and may be characterized in a qualitative way by a freely expanding fully ionized plasma which is moving in an approximately

radial direction away from the sun. Since the magnetic fields are constrained to move with the plasma which is moving radially away from the sun and because the sun is rotating, the photospheric magnetic fields of the sun become drawn out into interplanetary space with a form approximately described by an Archimedian spiral. The positive ion composition of this plasma mainly consists of protons $^{1}H^{+}$ with about a 5% contribution by # from alpha's $^{4}He^{++}$. Observationally the solar wind appears to be composed of two separate and distinct streams: high-speed streams (HSS), which are moving away from the sun at 1 AU with velocities V$\sim$700 km/sec, and low-speed streams (LSS), which in general reside between subsequent high-speed streams and have velocities V$\sim$300-325 km/sec. Superimposed upon this structure is the presence of shocks resulting from stream-stream interactions (e.g., high-speed streams overtake low-speed streams), flare-produced interplanetary shocks, discontinuities (abrupt changes in the plasma and field parameters), filaments (regions which reside between subsequent discontinuities, scale sizes $\sim$.01 AU), and waves, most notably Alfvén waves. Most of this structure may be attributed to azimuthal variations of the solar wind structure resulting from longitudinal variations of the solar wind sources on the sun. Then as the sun rotates (27 day synodic period) different streams will evolve along the sun-earth line

as a function of time, in such a way that the observed structure noted above is reproduced.

The low speed streams often referred to by the name "quiet solar wind" are characterized by relatively low wind velocities $\sim$300 km/sec which for a particular low-speed stream is not too variable, and the presence of microscale fluctuations (Alfvén waves, etc.) are at a relatively low level [see Tables 11 and 12 from A. J. Hundhausen (1972)[38] for a listing of average properties of low-speed streams]. Some of the other more important physical properties of low-speed streams are: (1) proton temperatures $T_p \approx 4 \times 10^4$ ^oK, (2) densities ~ 10 cm^{-3}, (3) electron heat flow vector $q_e >> q_p$ and is $\sim 10^{-2}$ ergs/cm^2/sec, (4) proton particle fluxes $\sim 2.4 \times 10^8$ cm^{-2} sec^{-1}, and (5) magnetic field strengths $B \sim 5\gamma$ ($\gamma = 10^{-5}$ gauss).

As pointed out by Hundhausen (1972),[38] the frequency distributions for the plasma parameters such as density, temperature, and magnetic field strength are very broad even for the narrow range of velocities between 300-325 km/sec. Thus, low speed streams do not appear to be representative of a well-defined, distinct state of the solar wind.[38] Furthermore, from auto-correlation studies by Gosling and Bame (1972),[39] the condition of steady state for low-speed streams only holds for periods less than 30 hours (3 hour averages of plasma parameters were used). A more complete

study by Gosling et al. (1976)[40] further shows this to be the case, especially for the year 1967 during solar maximum, when low-speed streams dominated the stream structure.

High speed streams which have very high wind velocities V $\sim$700 km/sec are characteristically very broad (140° in solar longitude), magnetic field is predominantly one polarity, microscale fluctuations are at a relatively high level and predominantly ($\sim$80%) composed of outwardly propogating Alfvén waves [Belcher (1976)[41]], plasma parameters such as density, temperature, and field strength are very stable (unchanging), and the lifespan of these streams may last for many solar rotations (refer to Table 13 and 14 from, respectively, Feldman et al. (1976)[12] and Bame et al. (1977)[42] for a listing of average properties of high-speed streams). Some of the other more important physical properties of high-speed streams other than those noted above are: (1) proton temperatures $T_p \approx 2.3 \times 10^5$ °K are about a factor of 2-3 greater than the electron temperatures $T_e \approx 10^5$ °K, (2) densities ~ 4 cm^{-3} and (3) electron heat flow vector $q_e \sim 3 \times 10^{-3}$ ergs/cm^2/sec are smaller than that found in low-speed streams, (4) proton particle fluxes $\sim 3 \times 10^8$ cm^{-2} - sec^{-1} are a little higher than that found in low-speed streams, (5) magnetic field strength $B \sim 5\gamma$, and (6) the Alfvén energy flux $E_A \approx 11 \times 10^{-3}$ ergs/cm^2/sec.

Gosling et al. (1976)[40] also showed from autocorrelation studies of the solar wind that high-speed streams appear to be more characteristic of the solar wind during solar minimum, especially the years 1973-1974, and are very long-lasting (up to 10 solar rotations). Furthermore, a study done by Bame et al. (1977)[42] showed that except for the wind velocity the plasma and field parameters within high-speed streams are more steady and more uniform than that found within low-speed streams. They also showed that the $^4He^{++}$ abundance within high-speed streams is very uniform (not true for low-speed streams) and its abundance relative to protons within high-speed streams is 4.8% (slightly higher than that found in low-speed streams $\sim$ 3.8%). Thus it appears that high-speed streams--and not low-speed streams--fulfill the requirement of being a well-defined state of the solar wind along with the conditions of steady state and uniformity.

The correlation studies by Krieger et al. (1973),[43] Neupert et al. (1974),[21] Krieger et al. (1974),[44] and Nolte et al. (1976)[45] show that coronal holes are highly correlated with high-speed streams (i.e., they are the "sources" of high-speed streams). As noted above, coronal holes and high-speed streams both satisfy the conditions of steady state and uniformity, contrary to that found for low-speed streams and their suspected source "quiet" regions. Thus, they appear to be more appropriate candidates for purposes of comparison

with theory. Furthermore, because of the high correlation between coronal holes and high-speed streams, we have the situation of cause and effect. This allows one to fix the boundary conditions, respectively, at the sun from coronal observations and at 1 AU from spacecraft observations, and thus allows for a better observational test of theory. Of course, from observations confined to the ecliptic plane there is the problem of evolutionary effects from stream-stream interactions. One could speculate that spacecraft observations made near the mid-points of very broad high-speed streams (the time it takes a high-speed stream to sweep past an observer at 1 AU is much longer than the propagation time of the stream from the sun to 1 AU) will closely approximate stream characteristics free from stream-stream interactions. This problem may also be bypassed by spacecraft observations out of the ecliptic plane when one considers the Pioneer 10 and 11 results along with solar magnetographic observations which suggest the presence of an interplanetary neutral sheet confined to the equatorial plane of the sun [E. J. Smith et al. (1977),[46] E. J. Smith et al. (1977)[47]]. This means there may only be one sector boundary which separates fields of opposite polarity in the northern and southern hemispheres. Thus with the concept of polar coronal holes one could imagine a single slowly evolving high-speed stream in each solar hemisphere (no

multiple stream structure) eminating continuously away from the sun and free from distortions due to stream-stream interactions. It is rather clear that spacecraft observations over the poles of the sun near solar minimum would offer a unique opportunity to test solar wind theories under nearly ideal conditions.

(3.) Present Status of the Theory of the Solar Wind

The basic equations governing the coronal expansion under steady state conditions are:

$$\nabla \cdot \vec{B} = 0 \tag{3.1}$$

$$\nabla \times (\vec{V} \times \vec{B}) = 0 \tag{3.2}$$

$$\nabla \cdot (\rho \vec{V}) = 0 \tag{3.3}$$

$$\nabla \cdot (\rho \vec{V}\vec{V} + (P + B^2/8\pi)\bar{\bar{I}} - \vec{B}\vec{B}/4\pi) = -\rho \nabla \Phi \tag{3.4}$$

$$\nabla \cdot ((\tfrac{1}{2}\rho V^2 + \tfrac{5}{2}P)\vec{V} + \vec{q} + \vec{S}) = -\rho \vec{V} \cdot \nabla \Phi \tag{3.5}$$

where ρ is the mass density, $\vec{V}$ is the wind flow velocity, P is the scalar pressure, $\vec{B}$ is the magnetic field vector, Φ is the gravitational potential, $\bar{\bar{I}}$ is the unit dyadic, $\vec{q}$ is the heat flow vector, and $\vec{S}$ is the Poynting vector. The approximations made in this formulation are: 1) the MHD approximation, stating that the electric field $\vec{E}$ is given by:

$$\vec{E} + \frac{\vec{V}}{c} \times \vec{B} = 0 \tag{3.6}$$

2) a scalar pressure is used for the tensorial pressure $\bar{\bar{P}}$ (viscosity effects), and 3) contributions due to waves (e.g., Alfven waves, etc.) are ignored.

It should be pointed out that the MHD approximation is the zeroth order approximation [given by Eq. (3.6)] of the generalized Ohm's law [see Rossi and Olbert (1970)[48]], where terms proportional to gradients in the plasma divided by the density are dropped, including a term due to collisions. In general it can be shown that if the proton gyroradius

$R_{T,P}$ is small compared to scale lengths L characteristic of the plasma (e.g., L is the distance over which the density changes appreciably) these higher order terms may be dropped. Furthermore, the collision term, which is inversely proportional to the so-called "magnetic Reynolds number" $R_{magn} >> 1$, may also be dropped. Therefore, under these conditions Eq. (3.6) for the electric field is a good approximation. Furthermore, observations in the interplanetary medium have given strong support to the validity of this approximation (e.g., presence of Alfvén waves, etc.). In fact it is generally believed that, with the possible exception of the thin layer of the chromosphere, the MHD approximation is true throughout the interplanetary medium of our concern, certainly above the lower corona.

(a.) "Classical" Parker model

We shall review some of the theoretical developments in solar wind theory. To start with, we present the "classical" physical picture due to E. N. Parker, used in the initial development of solar wind theory.

The high temperatures characteristic of the solar corona $T \sim 10^6$ ^oK are believed to be the result of convective motions at photospheric layers where temperatures are only on the order of 6000^oK. The convective motions generate MHD waves which propogate up along the sun's magnetic fields

to the base of the corona where they become strongly damped and deposit their energy. In doing so they heat up the lower corona to very high temperatures $T \sim 10^6$ °K, causing the gas to become fully ionized. For a collision-dominated gas (lower corona is collision dominated) the heat flow vector $\vec{q}$ is proportional to the negative gradient of the temperature, i.e.,

$$\vec{q} = -\kappa_c \nabla T \tag{3.7}$$

where κ_c is the thermal conductivity. For a fully ionized two component plasma (protons and electrons) the proportionality coefficient κ_c is [as determined from the Onsager relations, see Rossi and Olbert (1970)[48]]:

$$\kappa_c = \kappa_0 T^{5/2} = \frac{1.92 \times 10^{-5}}{\ln \Lambda} T^{5/2} \tag{3.8}$$

where the $\ln\Lambda$ is the Coulomb logarithm (see Chapter IV for details). For conditions typical of the lower corona we find:

$$\kappa_0 \approx 8 \times 10^{-7} \text{ ergs/cm/sec/deg}^{7/2} \tag{3.9}$$

As can be seen, the thermal conductivity κ_c is a strong function of the temperature and for $T = 10^6$ °K is about 20 times the conductivity of copper at room temperature. Because of the positive gradient in temperature across the transition layer from the chromosphere to lower corona, thermal energy will be conducted back down into the chromosphere. Then as the coronal temperature continues to rise, the energy conducted back will eventually become comparable to the wave

energy deposited into the corona, so that no further increase in temperature occurs. For quiet regions this temperature rise appears to take place in a very thin layer $\sim 10^3$ km wide and about .04 $r_\odot$ above the photosphere. Just above this transition layer, somewhere in the range $1\ r_\odot \leq r \leq 2r_\odot$, it was then felt that the temperature reached a maximum T_{max} at some distance r_{max} beyond which the temperature decreases with increasing r (no more wave deposition). (Note: r is the radial distance in a heliocentric coordinated system, $r_\odot = 7 \times 10^{10}$cm is the radius of the sun.) Since for $r > r_{max}$ the temperature gradient is negative and the plasma has a high thermal conductivity, a significant amount of thermal energy $q \sim 2 \times 10^4$ ergs/cm^2/sec is conducted away from the sun. The high temperatures characteristic of the lower corona extend out to many solar radii away from the sun (small thermal gradient) rendering the heart of the corona almost isothermal. Because of this the pressure gradients of the gas, mainly due to the sharp drop in density, remain greater for all r than the attracting force of gravity, which rapidly decreases with a $1/r^2$ dependence ("nozzle" effect). Thus, the plasma experiences a constant push away from the sun so that it eventually attains supersonic velocities away from the sun for $r > r_c$, where $r_c \sim 5\ r_\odot$ is the sonic critical point.

With the above picture in mind, Parker solved the equations (3.1) to (3.5) under the assumption of spherical

symmetry (monopole magnetic field). Assuming spherical symmetry, he was able to ignore the effects of the nonradial magnetic field in order to simplify the mathematics. This lead to the equations:

$$I = 4\pi n V r^2 \tag{3.10}$$

$$F = 4\pi n V r^2 \left[\tfrac{1}{2} m_H V^2 + 5kT - \frac{G M_\odot m_H}{r}\right] + 4\pi r^2 q \tag{3.11}$$

where I, which is a constant and equal to the particle flux, was derived from the conservation of mass equation, Eq. (3.3), while F, which is also a constant and equal to the energy flux, was derived from the conservation of energy equation, Eq. (3.5). We also have from the momentum equation the following:

$$\rho V \frac{dV}{dr} = \frac{dP}{dr} - \rho \frac{G M_\odot}{r^2} \tag{3.12}$$

where

$$\rho = n m_H \tag{3.13}$$

$$P = 2nkT \tag{3.14}$$

is the scalar pressure, n is the number density for electrons or protons, G = 6.67 x 10^{-8} dyne - cm^2/gm^2 is the gravitational constant, $M_\odot$ = 2 x 10^{33} gm is the mass of the sun, and m_H is the mass of the hydrogen atom. These equations are not yet closed since a separate equation specifying the heat flow vector q must be given. One could use the Onsager relations for q, using Eqs. (3.7) and (3.8), but this expression will hold only in the lower corona where the plasma is

collision dominated. Further out 5 r the plasma becomes collisionless. Realizing this, Parker (1958)[49] chose to approach the problem empirically by assuming a polytrope relation for the pressure

$$P = P_o \left(\frac{\rho}{\rho_o}\right)^{\gamma} \tag{3.15}$$

where γ is the polytrope index and P_o, ρ_o are, respectively, the pressure and mass density at the reference level. In order to avoid the theoretical difficulties related to the understanding of the heating mechanisms of the lower corona, the reference level r_o was confined to regions above the temperature maximum (i.e., $r_o > r_{max}$). Using Eq. (3.14) in conjunction with Eq. (3.15), one has

$$T = T_o \left(\frac{\rho}{\rho_o}\right)^{\gamma-1} \tag{3.16}$$

From Eqs. (3.10) to (3.12) and 3.15), one can show that q must have the following ad hoc form for this model

$$q = \left(\frac{\gamma}{\gamma-1} - \frac{5}{2}\right) PV \tag{3.17}$$

Thus the polytrope assumption closes the equations and allows their explicit solution. Furthermore, from Eqs. (3.16) and (3.17) it is evident that this replacement of the (unknown) q by Eq. (3.17) leads to the following consequences:

1) For the range $1 < \gamma < 5/3$ the heat flow vector is positive and finite. For large r, where free expansion is expected to take place (i.e., $\rho \propto 1/r^2$), the temperature will

have the following radial dependence:

$$T \propto r^{-\delta_T} \quad \text{where } 0 < \delta_T < \frac{4}{3} \text{ for } r >> r_0 \qquad (3.18)$$

and

$$\delta_T = 2(\gamma - 1)$$

2) $\gamma = 5/3$ (Adiabatic case)

$$T \propto r^{-4/3} \quad \text{for } r >> r_0 \qquad (3.19)$$

3) $\gamma = 1$ (Isothermal) has to be treated separately in that one must first take the divergence of Eq. (3.17) for q, then set $\gamma = 1$, and integrate the resulting expression for q. After doing this one gets

$$q = q_0 \left(\frac{r_0}{r}\right)^2 + P_0 V_0 \left(\frac{r_0}{r}\right)^2 \ln\left(\frac{n}{n_0}\right) \qquad (3.20)$$

where V_0 is the wind velocity at r_0, and $T = T_0$.

4) $\gamma < 1$ Here the temperature increases with radial distance, $q < 0$ (heat is being conducted back toward the sun) and for this solution the pressure is not zero at infinity. Thus they are not appropriate for wind solutions.

By using a polytrope, Parker in essence was assuming the form of the temperature profile (radial dependence of T). For instance, once solutions are obtained for ρ and V as functions of r, one can determine the temperature for all r by substituting the solutions for ρ into Eq. (3.16) (i.e., radial dependence of T implicitly given).

In solving Eqs. (3.10), (3.11), and (3.12) along with Eq. (3.15) for the pressure, one finds that there are four different classes or topologies of solutions depending upon the boundary conditions used. Separating these four

classes of solutions are two critical point solutions which pass through the sonic critical point r_c (coefficients in the equations becomes singular at r_c). Of all of these solutions only one of the two critical point solutions satisfies physically accpetable boundary conditions. As specified by Parker, they are:

1) Velocity V at lower corona r_o should be no more than a few km/sec since velocities significantly larger than this are not observed in the solar atmosphere (i.e., $V \ll C_s \sim 150$ km/sec in the lower corona, where $C_s^2 = \gamma (P/\rho)$ is the sound speed squared).

2) Pressure P at infinity is zero. This follows from the observation that pressures in the interstellar medium (outside the solar cavity) are known to be small. The condition of zero pressure does not necessarily rule out hydrostatic equilibrium. For example, $\gamma \leq 3/2$ implies a radial temperature gradient $\delta_T \geq 1$ and zero pressure at infinity under the condition of hydrostatic equilibrium (V = 0). But coronal observations at that time indicated that the coronal temperature profile was much flatter, in fact $(1 - \delta_T) \gtrsim 0$ at least out to a few solar radii. Under these conditions there is no hydrostatic equilibrium and there must be a free expansion in order to get zero pressure at infinity. Furthermore from Eq. (3.17), the condition $\lim_{r \to \infty} P = 0$ implies $\lim_{r \to \infty} q = 0$ if V = constant for $r \gg r_o$.

The isothermal case ($\gamma = 1$) gives the highest velocities at 1 AU but has a density profile steeper than that observed in the lower corona, and wind velocities which logarithmically diverge as $r \rightarrow \infty$ (i.e., thermal pressure force pushes on the gas out to infinity). For case 2, where $1 < \gamma < 3/2$, the velocities at infinity are finite and approach a constant value. $\gamma \approx 1.1$ ($\int_T \approx 0.9$ at 1.04 $r_\odot$ and $\int_T \approx 0.2$ for large r) gives solutions most characteristic of the observations in the lower corona and 1 AU [e.g., for $r_o \approx r_\odot$, $n_o = 3 \times 10^7$ cm^{-3}, T_o - 1.3×10^6 ^oK, one gets $n = 12$ cm^{-3}, $V = 290$ km/sec, and $T \sim 10^6$ ^oK (too high) at 1 AU].[50] In reality one value of the polytrope index will not hold for all r. For example, at 1 AU the observed temperatures $T \sim 10^5$ ^oK are an order of magnitude lower than coronal temperatures. This indicates the corona cannot be isothermal for all r. Furthermore, at 1 AU the observed heat flow vectors $q \sim 10^{-2}$ $ergs/cm^2/sec$ are much lower than that predicted by the $T^{5/2}$ law for the conductivity using observed densities and temperatures at 1 AU. Thus using these two facts, the flow must be more adiabatic at 1 AU than that in the lower corona. Parker (1963),[50] realizing the possibility for adiabatic flow for large r, computed solutions where $\gamma = 1$ (isothermal) for $r_o \leq r \leq b$, and $\gamma = 5/3$ (adiabatic) for $r > b$ where $b \sim 10 r_\odot > r_c$. For the boundary conditions $r_o \approx r_\odot$, $n = 3 \times 10^7$ cm^{-3} and $T_o = 10^6$ ^oK he computed solutions more typical of the solar wind

with wind velocities V = 300 km/sec, densities n - 10 cm^{-3}, and temperatures T ~ 7 x 10^5 ^oK (again too high) at 1 AU.[50] Thus, except for the high temperatures at 1 AU, which can easily be corrected for by introducing a more continuous change in γ with r, the polytrope model by Parker appears to be able to reproduce the overall characteristic of the "quiet" solar wind.

(b.) Other variants of thermally driven spherical winds

Single fluid models of the solar wind, where conduction is the only driving mechanism, have been developed by a number of different authors. These models assumed spherical symmetry and the $T^{5/2}$ law [see Eqs. (3.7) and (3.8)] for the heat flow vector in the energy equation. There are at least 3 sets of solutions which are known to exist. Each one has a different radial dependence for T. Briefly they are: 1.) $T \sim 1/r^{2/7}$ Parker (1964),[51] Noble and Scarf (1963)[52]; 2.) $T \sim 1/r^{2/5}$ Whang and Chang (1965)[53]; and 3.) $T \sim 1/r^{4/3}$ Durney (1971),[54] Roberts and Soward (1972)[55] As of now the one most quoted is that by Whang and Chang. Their results are given in Table 15 from Hundhausen (1972).[38]

One of the difficulties of these models is their inability to produce wind velocities greater than 400 km/sec at 1 AU, while having temperatures and densities characteristic of the lower corona, (i.e., require higher temperatures, lower densi-

ties at the coronal base than that observed). But the major difficulty, as previously mentioned, the expression for $\vec{q}$ is inappropriate in the interplanetary medium where for $r \gtrsim 5\text{-}10\ r_\odot$ it is collisionless. Furthermore, the thermal coupling between protons and electrons due to Coulomb collisions is very weak. Thus, a two-fluid picture should be more appropriate in describing the coronal expansion especially for distances outside 10 $r_\odot$. Such a calculation was performed by Sturrock and Hartle (1966)[56] where they used the classical heat conduction formula for a Coulomb collision dominated plasma appropriate for electrons and protons in their separate energy equations. Again, as in the single-fluid models, their solutions tended to have a need for higher temperatures, lower densities than normally found within the lower corona, for $V > 400$ km/sec at 1 AU (i.e., best fit to observations gave $V \sim 250$ km/sec). Another difficulty was that electron temperatures were a factor of 2-3 greater, proton temperatures were an order of magnitude lower and electron heat flow vector was an order of magnitude greater than that observed. The low proton, high electron temperatures can be understood since the thermal conduction for electrons is $\sim$40 times greater than that for protons, (i.e., electrons retain high coronal temperatures, protons cool adiabatically). But the observations indicate a stronger thermal coupling between electrons and protons.

This plus the overestimate for q_e is strong evidence that the $T^{5/2}$ relation for $\mathcal{K}_c$ is inappropriate in the interplanetary medium. One attempt to correct this problem of low proton temperatures while still keeping the $T^{5/2}$ law for q was to introduce viscosity effects, which are important for protons but not electrons, into the two-fluid model. This was done by Wolff, Brandt, and Southwick (1971)[57] where they were able to reproduce the observed temperatures for protons while retaining the same results for electrons computed by Sturrock and Hartle. In these calculations they included the effects of the spiral magnetic field upon the thermal conduction and viscosity expressions in the energy equations. Since thermal energy is constrained to move along the magnetic field, the heat conduction and viscosity in the radial direction are reduced by the factor:

$$\frac{1}{\left(1+\left(\frac{\Omega r}{V}\right)^2\right)} \qquad (3.21)$$

where Ω is the angular velocity of the sun. Thus as the magnetic fields wrap around, the flow becomes more adiabatic so that more thermal energy is converted into the kinetic energy of the flow (gets slightly higher wind velocities, $V \approx 310$ km/sec). Though the problem of low proton temperature may be accounted for, the high electron temperatures and heat flow vectors predicted by these models are still unacceptable.

(c.) The meridional models

With the recent discovery of coronal holes and their association with open highly divergent (non-radial) field lines and their correlation with high-speed streams, the assumption of spherical symmetry no longer seems appropriate. Near the sun the tension in the magnetic field lines dominates the dynamical and thermal pressures of the plasma, so that the flow is constrained to move along the magnetic field. It is thus apparent that when considering models of the solar wind, one must take into account the meridional flow (curvilinear) along the magnetic field lines.

A number of attempts have been made to solve for the non-spherical MHD solar wind flows where axial symmetry and a polytrope law for the pressure P are assumed. Examples are, G. W. Pneuman and R. A. Kopp (1971),[58] who developed numerical solutions for the isothermal case and no rotation in a dipole field; I. Okamoto (1975),[59] who did a more sophicated analysis compared to that done by Pneuman and Kopp, but in essence came to similar conclusions concerning the structure of the equations (elliptic) and therefore the numerical methods to be used; and Nerney and Suess (1975),[60] who did an expansion of the equations within the equatorial plane, where they solved for the flow far from the sun. M. A. Heinemann and S. Olbert (1978)[61] were able to show that none of these solutions were self-consistent.

Heinemann and Olbert were successful in developing a proper formulation of the problem by deriving a second order quasi-linear differential equation, called the transfield equation, for the magnetic stream function ψ defined by

$$\vec{B} = \nabla \times \hat{e}_\phi \psi \tag{3.22}$$

where $\hat{e}_\phi$ is a unit vector pointing in the azimuthal direction. It follows from this definition that ψ is a field line constant, i.e.,

$$\vec{B} \cdot \nabla \psi = 0 \tag{3.23}$$

They discovered the existence of four distinct domains separated by three critical surfaces (cusp, slow, and fast), where two of these domains were hyperbolic while the other two were elliptic. The transfield equation for ψ turned out to be exceedingly complicated, so much so that it appears an impossible task for obtaining self-consistent solutions which must simultaneously satisfy all boundary conditions, including those at the critical surfaces. When one realizes how idealized this model is in comparison to reality, the explicit self-consistent solutions of non-spherical models appear nearly impossible at present.

Along with the theoretical difficulties for nonspherical solar wind flow, there are the theoretical barriers in understanding the transport of energy in a plasma where Coulomb collisions are virtually absent. As previously

pointed out, the observations indicate that the $T^{5/2}$ law for the conductivity, or equivalently the Onsager relations, is inappropriate for the interplanetary medium. This result is not totally unexpected, and quite possibly wave-particle interactions are the appropriate mechanisms for regulating the transport of energy (see Chapter 4). Furthermore, in the case of coronal holes, where the densities within them are relatively low, the plasma becomes practically collisionless beyond one solar radius above the solar surface (see sections 3.5 and 3.6). Therefore, before any realistic model of the solar wind may be constructed, the correct transport coefficients derived from theory must be determined. As in the case for non-spherical flow, and probably more so, the theoretical difficulties in understanding the transport of energy in a plasma that is not collision dominated are formidable. Thus, there is a need for some empirical input in developing theories for the transport of energy in the interplanetary medium.

Except for the electron density and magnetic field line topologies (inferred from observed coronal topologies), all reliable observational information is absent between a few tenths of a solar radius above the sun's surface out to 1 AU. Since most of the expansion takes place within the range from 1 $r_\odot$ to 50 $r_\odot$, it is important that the

information pertaining to the radial dependence of the wind velocity, temperature, and heat flow vector of the expanding plasma within this range be as reliable as possible. Therefore, in order to fill this observational gap, we propose a semi-empirical approach based on the MHD conservation relations and empirically determined electron density distributions and magnetic field line topologies. By using the conservation laws one avoids the many pitfalls in making assumptions about the physical processes effecting the expansion which at present are poorly understood.

We would now like to make a few comments concerning the energy balance problem for the coronal expansion. As determined by Munroe and Jackson (1977),[24] the cross-sectional area of a polar coronal hole opens up to an area seven times greater than expected for $1/r^2$ expansion. Since particle fluxes for high-speed streams are about the same as those for low-speed streams, the particle flux eminating from within coronal holes must be a factor of seven greater than that for $1/r^2$ expansion, in order to conserve particles. Furthermore, temperatures $T \sim 10^6$ ^oK within coronal holes are colder than that within quiet regions $T \sim 1.6 \times 10^6$ ^oK.[17] This means the thermal conduction flux is reduced by a factor of ~ 5. Thus, there is a net effective reduction in energy by a factor of ~ 40 available to drive the coronal

expansion (see Figures 39 and 40 from section 3.5). Considering the problems that the heat conduction models already have in producing flows with wind velocities greater than 400 km/sec for coronal conditions characteristic of the "quiet" sun, the energy balance problem introduced by coronal holes seems to make the whole picture of a thermally driven wind questionable. One way to account for this problem, as pointed out by J. W. Belcher (1971)[62] is to allow for extended heating and momentum transfer via outwardly propagating MHD waves (preferably Alfvén waves). As demonstrated by Belcher, by introducing a wave pressure term due to Alfvén waves in the momentum and energy equations within the framework of a Parker type model for the solar wind (polytrope), he was able to account for the overall characteristics of high speed streams consistent with conditions in the lower corona. Therefore, it does not seem unreasonable to speculate that this may be the case, especially in the fact that high speed streams are associated with a predominant presence of outwardly propagating low frequency (periods $\sim$hours) Alfvén waves.[41] Moreover, it is known that within coronal holes the temperature gradients are not as steep as those found in "quiet" regions.[17] This suggests that within coronal holes, the waves are not strongly damped in the lower corona, so that a considerable portion of the wave energy can propagate upward.

Observations at 1 AU do indicate that the observed Alfvén wave energy fluxes $E_A \sim 10^{-2}$ ergs/cm^2/sec in high speed streams can only account for about 7% of the energy needed to accelerate high speed streams to their observed energy fluxes.[41] Thus, on its face value, it would seem that Alfvén waves alone would be insufficient to drive the solar wind. One could argue, since $\delta B/B \sim 1$ (δB is the wave amplitude) that the low Alfvén wave energy fluxes at 1 AU may be the result of the waves being damped by non-linear saturation effects during transit from the sun to 1 AU.[41] Since most of the power in Alfven waves at 1 AU occurs at time periods $\tau_A \sim$ hours, wavelengths for Alfven waves λ_A are on the order of a solar radius $r_\odot$. Then since the wave pressure term due to Alfven waves was derived by Belcher using the WKB approximation (i.e., $\lambda_A/L \ll 1$), it will not be applicable near the sun. At present, there is not a theory for MHD waves which applies in regions where the wavelengths of the waves are on the order of the scale size of the medium. It is hoped that progress in this area will be made in the near future.

(4.) Spherical Model

Let us begin with the calculations for a highly schematic spherical model of the solar wind. For this purpose let us use a composite of the radial density profile shown in Figure 32. In Figure 32 we have a log-log plot of the electron number density in cgs units versus the radial distance from the sun in units of solar radii r in a heliocentric coordinate system. (Note: all plots given in this chapter are log-log plots unless otherwise noted, where the abscissa is the same as that in Figure 32.) This figure represents a survey of the electron density measured over a wide variety of time periods, different periods of the solar cycle (solar minimum, maximum), while being predominantly confined to the equatorial plane. They were measured using various techniques: (1) white-light K-coronometer measurements [Newkirk (1967),[34] Van de Hulst (1953)[63]], radio frequency dispersion measurements for Pulsar NP 0532 (Crab Pulsar) [Counselman and Rankine (1972)[64]], satellite time-delay measurements [Muhleman et al. (1977)[65]], time delay measurements of radar pulses to Venus and back [Campbell and Muhleman (1969)[66]], and deep space plasma probe measurements [Neugebauer (1966),[67] Lazarus (1972)[68]].

The K-coronometer measurements [see review article by G. Newkirk, Jr., (1967)[34]] of the electron density n_e are determined from white light photographs of the sun taken during eclipses or more recently from coronagraph observations on Skylab.[24] Then from the observed radiances and polarization determined from these photographs and the assumption that the K corona is entirely due to Thomson scattering of the photospheric light by free electrons, it is possible to reconstruct the density distribution within the corona. Since the light intensity is proportional to the integrated electron density along the line of sight, it is possible to measure reliably n_e out to distances $\sim 10\ r_\odot$, and for extremely bright streamers $\sim 20\ r_\odot$. The limiting factor results from the K corona being only a small fraction of the F corona or zodiacal light which is unpolarized. Under such conditions only a minute polarization in the F corona will swamp the radiance from the K corona.[34]

Radio frequency dispersion measurements are based on the fact that the group delay of radio pulses propogating through an ionized plasma is inversely proportional to the frequency squared, where the proportionality constant is proportional to the integrated electron density along the ray path. By making simultaneous time delay measurements of radio pulses from the crab pulsar at different frequencies

taken at different impact parameters (different distances from the sun), while only making assumptions about the geometry and an empirical model for the density, it is possible to reconstruct the electron density distribution. This method gives reliable estimates of the electron density in the range from 5 $r_\odot$ to 20 $r_\odot$ where the major limiting factors result from multiple random scattering of the radio waves due to inhomogeneities in the density distribution near the sun $\sim$5 $r_\odot$ and the uncertainty in the interstellar dispersion baseline far from the sun $\sim$20 $r_\odot$.[64] The satellite time delay measurements simply measure the residual time delay resulting from the radio signal propagating at the group velocity of the medium between the spacecraft and the earth. In such measurements one must take into account the fluctuations of n_e which are on the order of 100%, for the purposes of computing the data weights (measurements must be confined for $r > 10\ r_\odot$).[65] Finally, the plasma probe measurements are direct measurements of the density with ion detectors on spacecraft (e.g., our own Imp 7 and 8 M.I.T. plasma detectors). In Figure 32 the X's and crosses "+" were determined via K-coronometer measurements and correspond, respectively, to the density distribution for a helmet streamer,[34] and regions characteristic of the "quiet" corona near solar maximum.[63] The boxes "□" were taken near solar maximum (1969, 1970) using radio dispersion measurements,[64] while the diamonds "◇" and

darkened boxes "■" were measured using, respectively, spacecraft time delay measurements (1970)[65] and time delay measurements of radar pulses to Venus (1969).[66] Finally, the circles "0" and traingles "△" were determined via plasma detectors on the spacecraft.[67, 68]

In order to compute radial profiles of V, T_{eff} and q_{eff} we must know the radial dependence of the density for all r. In order to do this we must fit a model to the empirical density profile displayed in Figure 32. The density model we chose is a very simple two parameter model which we find reproduces the data quite well, and may be written the following way:

$$n(z) = n_o e^{\sigma(z-1)} z^2 \qquad (3.24)$$

where $z = r_o/r$ is the inverse distance, $r_o = 1.04\ r_\odot$ is the reference level, the density n_o at the reference level and σ are adjustable parameters to be determined.

This model is characteristic of solutions for the density n within a gravitationally bound isothermal atmosphere in hydrostatic equilibrium for small r (z = 1) where the flow is expected to be highly subsonic. Under these conditions the parameter σ is given by the following relation:

$$\sigma = \frac{G M_\odot m_H}{2 k T_o r_o} \qquad (3.25)$$

where $T_o = T(r_o)$ is the temperature at the reference level. For large r ($z \to 0$) Eq. (3.24) approaches the solution for a freely expanding gas, where the density drops with a $1/r^2$

dependence. Spacecraft observations made by Mariner 2 between Venus and the earth suggest a $1/r^2$ dependence,[69] but because of time variation problems this has not yet been experimentally verified. The results by Muhlemann et al. (1977)[65] are strong evidence that the density does decrease with a $1/r^2$ dependence. A quick and simple way to make a fit to the data is simply to plot the log $((\frac{n}{n_o}) \times ^2)$ versus z ($z = 1/x$), which to a very good approximation is a straight line. Then by either reading off the slope or the intercept at $z = 1$, one may determine a reasonably accurate value for σ. The three curves shown in Figure 32 correspond to three separate fits to the data and are representative of lower, intermediate, and upper bounds of the density distribution. In Table 16 we have tabulated for the three profiles the values of the parameters n_o and σ and the predicted values of the density n at 1.04 $r_\odot$, 10 $r_\odot$, 215 $r_\odot$ = 1 AU, and the density index

$$\delta_r \equiv \frac{d(\ln n)}{d(\ln r)} = -(2+\sigma z) \qquad (3.26)$$

One should note that the logarithmic slope given at 10 $r_\odot$ is $\delta_r \approx -2.8$, which is about that given by Counselman and Rankine at this distance, i.e., $\delta_r \approx -2.9$, and the intermediate curve was fit so that $n_e \approx 10$ cm^{-3} at 1 AU.

The conservation relations used for this model are given by Eqs. (3.10), (3.11), and (3.12) and are rewritten

here for convenience, i.e.,

$$I = 4\pi n V r^2 \tag{3.27}$$

$$V\frac{dV}{dr} + \frac{1}{n m_H}\frac{dP_{eff}}{dr} + \frac{GM_\odot}{r^2} = 0 \tag{3.28}$$

$$F = 4\pi n V r^2\left[\frac{1}{2}m_H V^2 + 5kT_{eff} - \frac{GM_\odot m_H}{r}\right] + 4\pi r^2 q_{eff} \tag{3.29}$$

$$P_{eff} = 2nkT_{eff} \tag{3.30}$$

(Note: we added the subscript "effective" since waves may be important.)

Substituting Eq. (3.24) for n into the conservation of mass relation Eq. (3.27), it is an easy matter to solve for the velocity V for all r, i.e.,

$$V = V_\infty e^{-\sigma z} \tag{3.31}$$

where

$$V_\infty = V_{AU} e^{\sigma z_{AU}} \tag{3.32}$$

and V_{AU}, z_{AU} are the values of V and z at 1 AU. Thus, once the mass flux "V_{AU}" is specified, the velocity V is given for all r. From Eqs. (3.27), (3.28), and (3.30) and using the boundary condition $T_{eff} = 0$ at infinity ($z = 0$), it is possible to derive the following integral equation for T_{eff}:

$$T_{eff} = \frac{m_H}{2nk}\left[n_0^2 V_0^2 r_0^4\left[2\int_r^\infty \frac{dr}{n(r)r^5} - \frac{1}{n(r)r^5}\right] + GM_\odot \int_r^\infty \frac{n(r)dr}{r^2}\right] \tag{3.33}$$

where

$$V_0 = V_\infty e^{-\sigma} \tag{3.34}$$

is the value of the velocity at the reference level r_0. Note that once the density is given as a function of r the temperature T_{eff} can be determined for all r. Substituting Eq. (3.24) into

Eq. (3.33), it is found that the integrations can be evaluated in terms of known functions. The result is

$$T_{eff} = T_b \left\{ \xi^2 \left[1 - \frac{2}{(\sigma z)} + \frac{2}{(\sigma z)^2} \right] + 2\left[1 - \xi^2 \right] \frac{e^{-\sigma z}}{(\sigma z)^2} \right. \qquad (3.35)$$

$$\left. - \left[1 + \frac{2}{(\sigma z)} + \frac{2}{(\sigma z)^2} \right] e^{-2\sigma z} \right\}$$

where

$$k T_b \equiv \tfrac{1}{2} m_H V_\infty^2 \qquad (3.36)$$

$$\xi^2 \equiv \frac{1}{2\sigma} \left(\frac{v_{esc}}{V_\infty} \right)^2 \qquad (3.37)$$

$$v_{esc}^2 \equiv \frac{2GM_\odot}{r_o} \qquad (3.38)$$

where v_{esc} is the escape velocity at the reference level r_o. Again, once the mass flux is given, Eqs. (3.36) and (3.37), T_{eff} is determined for all r. Eq. (3.35) for T_{eff} has a few interesting limits. For small r, $z \sim 1$ and for typical values of σ (see Table 16), Eq. (3.35) reduces to the following simple form:

$$T_{eff} = \frac{1}{2\sigma} T_{esc} \left[1 - \frac{2}{(\sigma z)} + \frac{2}{(\sigma z)^2} \right] \qquad (3.39)$$

where

$$k T_{esc} = \tfrac{1}{2} m_H v_{esc}^2 \qquad (3.40)$$

If we ignore the second and third term in the brackets, Eq. (3.39) reduces to the form characteristic of a gravitationally bound isothermal static atmosphere where σ is given by Eq. (3.25). One may also note that the first order correction term $-2/(\sigma z)$ is a cooling factor arising from the expansion of the corona. For large r ($z \to 0$), Eq. (3.35)

for T_{eff} has the following asymptotic form

$$T_{eff} = T_b \left\{ \frac{1}{3}(1+\xi^2)(\sigma z) - \frac{1}{12}(7+\xi^2)(\sigma z)^2 + \cdots \right\} \quad (3.41)$$

Thus for large r, T_{eff} decreases with a radial dependence slightly less than 1/r and approaches a 1/r dependence as $r \to \infty$. One can see from Eqs. (3.39) and (3.41) that a larger σ gives colder temperatures for small r, and higher temperatures for large r and visa versa for smaller σ.

In order to determine an expression for q_{eff} we divided Eq. (3.29) for F by I and specified the boundary condition

$$\lim_{r \to \infty} \frac{q_{eff}}{nV} = 0 \quad (3.42)$$

By doing this we get the following expression for q_{eff}

$$q_{eff} = nV \left\{ \frac{1}{2} m_H (V_\infty^2 - V^2) - 5kT_{eff} + \frac{GM_\odot m_H}{r} \right\} \quad (3.43)$$

Thus, by knowing the radial dependence of n (given by empirical density distribution), V (given once the mass flux "V_{AU}" is specified), and T_{eff} [given by Eq. (3.35)], it is an easy exercise to compute the radial profiles of q_{eff} from Eq. (3.43). Furthermore, the radial dependence for q_{eff} can be shown to have the following asymptotic form for large r:

$$q_{eff} = \frac{1}{2} n m_H V_\infty^3 \left\{ \frac{1}{3}(1+\xi^2)(\sigma z) + \frac{1}{12}(11+5\xi^2)(\sigma z)^2 + \cdots \right\} \quad (3.44)$$

and since $n \sim 1/r^2$ for large r,

$$q_{eff} \propto \frac{1}{r^3} \quad \text{for large } r \quad (3.45)$$

(Note: radial gradient is slightly steeper than a $1/r^3$ drop off.) Also, as may be seen from looking at Eq. (3.44), q_{eff}

is proportional to the convective energy flux at infinity

$$\frac{1}{2} n m_H V_\infty^3 \qquad (3.46)$$

In Figures 33, 34, and 35 we have plotted radial profiles of the wind velocity, T_{eff}, and q_{eff} derived, respectively, from Eqs. (3.31), (3.35), and (3.43) using the three fits to the empirical density shown in Figure 32 and where the wind velocity at 1 AU was set equal to 425 km/sec (V_{AU} = 425 km/sec). The variation of the wind velocity with distance appears similar to a Parker type solution, where $\gamma \approx 1$ and $T_o \approx 10^6$ °K. The sonic critical point r_c determined using the temperature profile in Fig. 34 is about equal to 5r where

$$\left(\frac{1}{2} m_H V^2\right)_{r=r_c} = \zeta (kT)_{r=r_c} \qquad (3.47)$$

where ζ is close to unity.

The temperature profile displays a striking flat portion inside 10 $r_\odot$ (isothermal) where $T_o \approx 1.25 \times 10^6$ °K, a slight bulge at $10r_\odot$, and a nearly 1/r decrease for $r > 10\ r_\odot$. Also note that the temperature profiles are independent of the magnitude of the density. The temperature at 1 AU for the intermediate density profile is equal to 1.33×10^5 °K. Using the empirical relation by Burlaga and Ogilvie (1970)[69] for the proton temperature T_p, i.e.,

$$\sqrt{T_p} = .036\, V - 5.54 \qquad (3.48)$$

where V is in km/sec and T in 10^3 ^oK, and sets V = 425 km/sec, one gets $T_p = 9.5 \times 10^4$ ^oK. Then if one uses for the electron temperature T_e the average value quoted by Feldman et al. (1975),[9] i.e., $T_e = 1.6 \times 10^5$ ^oK and uses the relation

$$T = \frac{1}{2}(T_p + T_e) \qquad (3.49)$$

one gets for T the following:

$$T = 1.28 \times 10^5 \, ^oK$$

which happens to be only 4% different from that determined by our profiles. This result should not be thought as being an indication that our profiles can predict temperatures with such accuracy, but that it is an indication they may give a reasonable description of the temperature profile within the interplanetary medium. The temperature T_o at the reference level is smaller than it should be, since our simple model for n_e does not reproduce the data that well inside $1.2r_\odot$.

The radial profiles for q_{eff} are monatonic with a logarithmic slope approximately equal to -3. The slope inside 8 $r_\odot$ is less steep than that outside 8 $r_\odot$, indicating that the flow is more adiabatic outside 8 $r_\odot$, which is about the point where the temperature begins to decrease [see Fig. (34)]. One should also note that these profiles indicate a density dependence upon q, while the conduction law given by the Onsager relations is independent of the density [see Eq. (3.8)]. The values for q_{eff} (see Table 17)

at, respectively, r_o and 1 AU for the intermediate curve are equal to 7×10^4 ergs/cm^2/sec and 8.66×10^{-3} ergs/cm^2/sec. The value at r_o is about a factor of two to three greater than that expected from classical heat conduction [i.e., Eqs. (3.7) and (3.8)]. This is not necessarily an indication that conduction is not the dominant energy source when one considers the approximations and inaccuracies in our model. Furthermore, the value at 1 AU is about equal to the average value for the electron heat flow vector q_e = 7.8×10^{-3} ergs/cm^2/sec quoted by Feldman et al. (1975).[9] Again this result should only be thought of as an indication that our profiles give a reasonable representation of q in the interplanetary medium.

We would now like to address the issue of the mass flux "V_{AU}" and radial gradient of the density, which introduce the greatest uncertainty into our model predictions. By increasing V_{AU} above 425 km/sec, the bump at 10 $r_\odot$ in the T_{eff} profiles will move out and become more enhanced, while the contrary will occur if V_{AU} is reduced. Furthermore, the temperatures at 1 AU will increase with increasing velocity. For instance, a 40% increase in V_{AU} results in a factor of 2 increase in T_{eff}. Temperature profiles are insensitive to V_{AU} inside 1.5 $r_\odot$, as expected, since the flow is subsonic in this region. The q_{eff} profiles are also sensitive to V_{AU}, but this is expected since for larger V_{AU} we need more

energy to drive the expansion. Thus we may ask the question, what is the appropriate velocity or mass flux for our particular density profile. This issue can only be resolved by making spacecraft observations in a particular stream from which we know its source, measuring the density profile at that particular time along the line of sight between the source and the spacecraft; such problems as the time evolution of the source (steady state) and propogation distortions (stream-stream interaction) are minimal. As of now this has not yet been done. It is hoped that observational studies in the future will alleviate this deficiency. Uncertainties in the radial gradient of the density will also introduce considerable error, though for reasonable variations of the model parameters (uncertainties in the measured density profile) we find the overall shape of the T and q profiles to be preserved near the sun (e.g., bump at 10 $r_\odot$ in temperature profile will not go away). Far from the sun, where $n \propto 1/r^2$, the T and q profiles are very sensitive to the slope of the density. For instance a change in slope from $\delta_r = 2.04$ to $\delta_r = 2.07$ will produce an increase in the temperature at 1 AU by a factor of two. Thus, the observed temperature at 1 AU should be used to fix the slope in the density at 1 AU and not visa versa. The same strong dependence on δ_r at 1 AU is also found for q. Thus, the observed q at 1 AU may also be used as an added constraint upon the density profiles.

Even with the mass flux problem "V_{AU}" and the intrinsic uncertainties in the data, along with the approximations made and the simplicity of the model used, the results appear to be able to reproduce the observations quite well. Thus, we feel that this model does give a reasonable though crude description of the average or mean solar wind in the equatorial plane. Due to the reasonable success of this procedure we decided to tackle a more specific problem described in the next section.

(5.) MHD Model of a Polar Coronal Hole

(a.) Generalization of spherical model

We have chosen as a specific example the Polar Coronal Hole (PCH) studied by Munroe and Jackson (M & J).[24] As previously emphasized, empirically the density is by far the best known physical parameter, and in the case of the polar coronal hole studied by Monroe and Jackson we not only have available the three-dimensional distribution of the density, but the geometry of the hole boundary from which the magnetic field line topology can be inferred. In order to obtain numerical solutions we need models of the density and magnetic field, along with the assumption of axial symmetry. Since the polar coronal hole is approximately axisymmetric this will be a good approximation. In contrast to the spherical model, the topology of the magnetic field now enters in an important way (see Fig. 36); thus as previously emphasized one must self-consistantly take into account the meridional flow in order to obtain unambiguous estimates of such physical quantities as the wind velocity, temperature, and heat flow vector. This approach, where we use the MHD conservation relations along with density and magnetic field models, allows us to integrate along differential flux tubes rather than being forced to consider an integral areal divergence of the coronal hole, as done

by Munroe and Jackson.[24] As pointed out by Rosner and Vaiana (1976),[70] curvatures in the magnetic field lines below 2 $r_\odot$ can bring about considerable errors in calculations based on the integral areal divergence of the field lines. Furthermore, the rotation of the sun and its resulting spiral field were also included in the model calculations, thus allowing us to perform unambiguously our integrations along the field lines for all $\vec{r}$.

Because we take into account the rotation of the sun, we find it more convenient to write the equations, Eqs. (3.1) to (3.5), in the rotating frame. In the rotating frame the conservation of momentum and energy equations are

$$\nabla\cdot(\rho\vec{V}\vec{V} + (P+B^2/8\pi)\overleftrightarrow{I} - \vec{B}\vec{B}/4\pi) = -\rho\nabla\Psi + 2\vec{V}\times\vec{\Omega} \quad (3.50)$$

$$\nabla\cdot\left(\tfrac{1}{2}\rho V^2\vec{V} + \tfrac{5}{2}P\vec{V} + \vec{q} + \vec{S}\right) = -\rho\vec{V}\cdot\nabla\Psi \quad (3.51)$$

where, in particular, the gravitational energy Φ is replaced by

$$\Psi = \Phi - \tfrac{1}{2}\Omega^2R^2 \quad (3.52)$$

Ω is the angular velocity of the sun at a particular field line ($\Omega \approx 2.9 \times 10^{-6}$ rad/sec), and

$$R = r\sin\theta \quad (3.53)$$

where θ is the colatitude in a heliocentric coordinate system (r, θ, ϕ) aligned with the spin axis of the sun. The advantage of doing this is that $\vec{V}$ is parallel to $\vec{B}$, so that the electric field $\vec{E}$ is zero [see Eq. (3.6)]. It then follows that the Poynting vector $\vec{S}$ will also be zero.

In order to acquire our profiles of $\vec{q}$ we made the approximation that the heat flow vector $\vec{q}$ is aligned with the magnetic field, i.e.,

$$\vec{q} = q\,\hat{b} \tag{3.54}$$

where $\hat{b} = \vec{B}/B$.

The approximation that $\vec{q}$ is parallel to $\vec{B}$ should be a good one as long as the cyclotron frequency for electrons Ω_e is much larger than the electron-proton collision frequency $\nu_{e,p}$, i.e.,

$$\frac{\nu_{e,p}}{\Omega_e} << 1 \tag{3.55}$$

For all regions characteristic of the corona and interplanetary medium this can be shown to be the case.

In the case of axial symmetry, it is convenient to write the magnetic field $\vec{B}$ in the following way:

$$\vec{B} = \vec{B}_p + \vec{B}_t \tag{3.56}$$

where $\vec{B}_p$ is the poloidal component confined to the meridional plane, while $\vec{B}_t$ is the toroidal component which points in the azimuthal direction. Correspondingly, we do the same for the wind velocity in the inertial frame

$$\vec{V}_I = \vec{V}_{P_I} + \omega_I R\,\hat{e}_\phi \tag{3.57}$$

where $\vec{V}_{P_I}$ is the poloidal component and ω_I the angular velocity of the wind velocity in the inertial frame.

With axial symmetry, significant simplifications of the equations result. Most importantly, one can derive four field line constants [L. Mestel (1968),[71] Heinemann and Olbert

(1978)[61]. Defining them, respectively, by α, ω, L, and W, we have, (Note: for the convenience of the reader they are derived in Appendix C)

(1) $\alpha \vec{B} = \rho \vec{V}$ and $\vec{B} \cdot \nabla \alpha = 0$ (3.58)

(2) $\omega = \omega_I - \frac{\alpha B_t}{R\rho}$ and $\vec{B} \cdot \nabla \omega = 0$ (3.59)

(3) $L = \omega_I R^2 - \frac{B_t R}{4\pi\alpha}$ and $\vec{B} \cdot \nabla L = 0$ (3.60)

(4) $W = \frac{1}{2}V^2 + \frac{5}{2}\frac{P}{\rho} + \Psi + \frac{\mathcal{E}}{\rho V}$ and $\vec{B} \cdot \nabla W = 0$ (3.61)

The field line constant α replaces the particle flux I, which is a constant when spherical symmetry holds, as the conserved quantity derivable from the mass conservation equation. L is the total angular momentum per unit mass (plasma plus field), while W is the total energy per unit mass. The field line constant ω is the angular velocity of the rotating frame, where the electric field is zero, and will thus be equal to the angular velocity Ω at the footprints of the field lines at the solar surface, where the flow is field aligned. From Eq. (3.59) and (3.60) one can solve for B_t, and ω_I in terms of ρ and α, i.e.,

$$B_t = -\frac{\rho_A \Omega R_A^2}{\alpha R}\left(\frac{1 - R^2/R_A^2}{1 - \rho_A/\rho}\right) \tag{3.62}$$

$$\omega_I = \Omega\left(1 - \frac{\rho_A R_A^2}{\rho R^2}\right) \tag{3.63}$$

where

$$L = \Omega R_A^2 \tag{3.64}$$

is determined at the Alfven point $R_A = r_A \sin\Theta_A$ (i.e., denominators of Eqs. (3.62) and (3.63) are zero at R_A; therefore, in order for B_t and ω_I to be well-defined, the numerator must correspondingly be zero at this point). Furthermore, it can be shown from Eq. (3.58) that

$$\rho_A = 4\pi\alpha^2 \tag{3.65}$$

is the mass density at the Alfvén point. During our numerical integration we must deal with the singularity in B_t and ω_I at R_A. In order to handle this problem we applied L'Hospital's rule at R_A.

$$B_{tA} = \frac{\rho_A \Omega R_A}{\alpha}\left(\frac{2\left(\frac{\partial}{\partial \ell}\ln R\right)_A}{\left(\frac{\partial}{\partial \ell}\ln \rho\right)_A}\right) \tag{3.66a}$$

$$\omega_{I_A} = \Omega\left(1 + \frac{2\left(\frac{\partial}{\partial \ell}\ln R\right)_A}{\left(\frac{\partial}{\partial \ell}\ln \rho\right)_A}\right) \tag{3.66b}$$

where $\frac{\partial}{\partial \ell}$ means taking the derivative along the field line, ℓ is the arc length along the field line, i.e.,

$$\ell = r_o\left(1 + \left(\int_z^1 \frac{B}{B_r Z^2}\, dZ\right)_{\text{Along } B}\right) \tag{3.67}$$

For completeness we will now give the field line equation for the azimuthal angle ϕ

$$\phi - \phi_o = \left(\int_z^1 \frac{B_\phi}{B_r}\,\frac{dZ}{Z}\right)_{\text{Along } B} \tag{3.68}$$

where ϕ_o is the azimuthal angle of the field line at the reference level.

Thus, all in all, once α, the mass density ρ, and the poloidal magnetic field $\vec{B}_p$ are known, it is possible to reproduce the meridional flow for all $\vec{r}$.

(b.) Ad hoc model for the coronal magnetic field

The model for the poloidal component of the magnetic field $\vec{B}_p$ (component in meridion plane) is a simple multipole expansion (from monopole to octupole) which is independent of the ϕ component (axial symmetry). Its r and θ components may be written the following way:

$$B_r = B_0 Z^2 \left[\tfrac{1}{2} \eta_M \tanh(N_M \cos\theta) + \eta_D Z \cos\theta \right. \tag{3.69}$$
$$\left. + \eta_Q Z^2 \tfrac{1}{2} (3\cos^2\theta - 1) + Z^3 \tfrac{1}{2} (5\cos^2\theta - 3)\cos\theta \right]$$

$$B_\theta = \frac{B_0}{2} Z^3 \left[\eta_D \sin\theta + \eta_Q Z \sin 2\theta + Z^2 \tfrac{3}{4} (5\cos^2\theta - 1) \sin\theta \right] \tag{3.70}$$

where B_0 is the strength of the field at $(z,\theta) = (1, 0)$ and

$$\eta_M \equiv \frac{2 B_M}{B_0} \tag{3.71}$$

$$\eta_D \equiv B_D / B_0 \tag{3.72}$$

$$\eta_Q \equiv B_Q / B_0 \tag{3.73}$$

are the relative strengths, respectively, of the monopole, dipole, and quadropole terms with respect to the octupole term.

The theta dependence for the monopole term

$$h(\theta) = \tanh(N_M \cos\theta) \tag{3.74}$$

was used, since for large N_M this function approaches a step function at the equatorial plane where

$$h(\theta) = \begin{cases} +1 & 0 \leq \theta < 90^\circ \\ -1 & 90^\circ < \theta \leq 180^\circ \end{cases} \qquad (3.75)$$

This allows for the field lines to be radial for large r, since the areal divergence of the hole boundary appears radial beyond 3 $r_\odot$ (cf. Fig. 36)[24]; we reproduce the observed monopole term at 1 AU, and allow for the $\nabla \cdot \vec{B} = 0$ condition to be satisfied. Also, by doing this we get a current sheet in the equatorial plane which seems to be suggested by recent observations out of the equatorial plane [E. J. Smith et al. (1977)[47]]. The value we used for N_M was 86, so that the function $h(\theta)$ does not change significantly in the upper quadrant, for example, until $\theta > 89^\circ$. The parameters in the expansion η_M, η_D, and η_Q were adjusted in such a way that they reproduced the shape of the line studied by Munroe and Jackson (indicated by crosses shown in Fig. 36). The parameter B_o was determined by observations at 1 AU (e.g., B = 5γ). The way we did the fits was to plot the crosses on the Techtronix 4120 graphic system and then plot various field lines determined by a field line equation to be derived, for various values of the parameters η_M, η_D, and η_Q until the points passed through the crosses.

In order to plot the crosses shown in Fig. 36 we had to use the function

$$f(r) = \frac{f_{MAX}\, e^{(r-r_1)/\sigma} + f_1}{e^{(r-r_1)/\sigma} + 1} \qquad (3.76)$$

where $f_{MAX} = 7.26$ is the parameter which specifies by how much the areal divergence of the hole exceeds that for $1/r^2$ expansion, $r_1 = 1.31\ r_\odot$, $\sigma = 0.51\ r_\odot$, $r_o = 1\ r_\odot$, and $f_1 = -2.409$. The parameters in the model were determined by Munroe and Jackson fitting the areal function

$$A(r) = A_o \left(\frac{r}{r_o}\right)^2 f(r) \tag{3.77}$$

to the cross-sectional area of the hole, where $A_o = 0.51\ r_\odot^2$ is the area of the hole at the solar surface ($z = 1$). The hole boundary was determined by streamers lining the edge of the hole. Furthermore, by studying the streamers as the sun rotated over one solar rotation they found the hole to be approximately axisymmetric.

The relation

$$A(r,\theta) = 2\pi r^2 (1 - \cos\theta) \tag{3.78}$$

represents the area of a polar cap of radial and angular extent r,θ. Combining Eqs. (3.77) and (3.78) it is possible to derive the following relationship, which gives the colatitude of the hole boundary as a function of r,

$$\theta = \cos^{-1}\left(1 - \frac{A_o}{2\pi} f(r)\right) \tag{3.79}$$

where at the reference level (footprint of field line) the colatitude of the field line is $\theta_o \approx 23^o$ (i.e., $z = 1$, $r = r_o$, $f(r_o) = 1$). Eq. (3.79) was then used to plot our data points shown in Fig. 36.

In order to determine the parameters η_M, η_D, and η_Q along with being able to perform our integrations along the

field lines, we needed to determine the magnetic stream function $\psi(r,\theta)$ from which $\vec{B}$ may be expressed with the assumption of axial symmetry [see Eq. (3.22)]. The function ψ is related to the polar cap magnetic flux

$$\int B_r r^2 d\Omega = \int \frac{1}{R}\frac{1}{r}\frac{\partial \psi}{\partial \theta} r^2 \sin\theta \, d\theta \, d\phi = 2\pi\psi \tag{3.80}$$

and since ψ is a streamline constant [see Eq. (3.23)], then Eq. (3.80) is also a field line constant. Thus, by substituting Eq. (3.69) into Eq. (3.80) it is possible to determine the field line equation relating r and θ. We may write $\psi(r,\theta)$ in the following way

$$\psi(r,\theta) = \psi_M(r,\theta) + \psi_D(r,\theta) + \psi_Q(r,\theta) + \psi_O(r,\theta) \tag{3.81}$$

where

$$\psi_M = A_M g(\theta) \quad \text{where } A_M = B_M r_o^2 \tag{3.82a}$$

and

$$g(\theta) = \int_0^\theta h(\theta')\sin\theta' d\theta' = \frac{1}{N_M}\log\left[\frac{\cosh N_M}{\cosh(N_M\cos\theta)}\right] \tag{3.82b}$$

$$\psi_D = A_D Z \sin^2\theta \quad \text{where } A_D = \frac{B_D r_o^2}{2} \tag{3.83}$$

$$\psi_Q = A_Q Z^2 \sin^2\theta\cos\theta \quad \text{where } A_Q = \frac{B_Q r_o^2}{2} \tag{3.84}$$

$$\psi_O = A_O \frac{Z^3}{4}\left[(6-5\cos^2\theta)\cos^2\theta - 1\right] \quad \text{where } A_O = \frac{B_O r_o^2}{2} \tag{3.85}$$

By combining these terms in Eq. (3.81) and doing a little algebra we get the following quartic equation for $\cos\theta$:

$$\cos^4\theta + \frac{4}{5}X\eta_Q\cos^3\theta + \frac{4}{5}X^2\left(\eta_D - \frac{3}{2}Z^2\cos^2\theta\right) \tag{3.86a}$$

$$+\frac{4}{5}X^3\left(\eta_M - \eta_Q Z^2\right)\cos\theta + \frac{4}{5}X^3\left(\frac{1}{4}Z^3 - \eta_D Z + C_O - \eta_M\right) = 0$$

$$C_0 \equiv Z_0^3 \frac{1}{4}\left[(6-5\cos^2\theta_0)\cos^2\theta_0 - 1\right] + Z_0^2 \eta_Q \sin^2\theta_0 \cos\theta_0 \quad (3.86b)$$
$$+ Z_0 \eta_D \sin^2\theta_0 + \eta_M (1-\cos\theta_0)$$

where we used the simplifying limit for $g(\theta)$

$$\lim_{N_M \to \infty} g(\theta) = 1 - |\cos\theta| \quad (3.87)$$

Thus, Eq. (3.86) allows us to solve for θ in terms of Z once the field line constant C_0 is specified at (z_0, θ_0).

By setting $(z_0, \theta_0) = (1, 23^\circ)$ we can solve for the field line constant C_0 for the empirical field line indicated by crosses. Then for a particular set of values for the parameters η_M, η_D, η_Q we can plot a particular curve using Eq. (3.86) similar to that shown passing through the crosses. We then adjusted these parameters until we acquired the reasonable fit shown passing through the crosses. The results are

$$\eta_M = 0.25 \quad (3.88a)$$

$$\eta_D = 0.13 \quad (3.88b)$$

$$\eta_Q = 0.1 \quad (3.88c)$$

Once this was done we plotted the remaining field lines shown in the figure.

It is important to note that this magnetic field model is curl free, except for the current sheet mainly confined to the equatorial plane. In reality the field will not be curl free. The plasma will tend to bring about distortions in the field by generating currents which will introduce $\vec{j} \times \vec{B}$ corrections into our model calculations. Though such

corrections may in some regions introduce small corrections in the magnetic field topology, they may not be small compared to such quantities as gradients in the pressure which we are trying to determine.

Note the peculiar topology shown at lower latitudes. As may be seen, some of the field lines do not connect with the sun. Furthermore, at around 1.4 $r_\odot$, $\theta \approx 73^\circ$, the magnitude of the poloidal field strength B_p vanishes. Since this topology is similar to that characteristic of helmet streamers seen in coronal photographs, the zero in B_p could possibly correspond to the T cusp observed in streamers. Thus, we will refer to this point by using the term T cusp. This peculiar topology is probably a combination of our neglect of the plasma (fields curl free), and properties peculiar to the specific model used. Because of this, without considering the errors introduced by modeling, the correction currents will be large in these regions. For example, if one considers the equation for $\vec{j}_\perp$ (component of current perpendicular to $\vec{B}$) which is derivable from the momentum equation (neglecting rotation),

$$\vec{j}_\perp = c \frac{\vec{B}}{B^2} \times \left[\rho \frac{d\vec{V}}{dt} - \rho \frac{GM_\odot}{r^2} \hat{e}_r + \nabla P \right] \quad (3.89)$$

currents will be significant near the T cusp. In fact, right at the singular point where $B_p = 0$, the correction current $\vec{j}_\perp$ will be infinite unless the term in brackets is

zero. Thus, because of these limitations in our model for $\vec{B}_p$, we must confine our calculations to higher latitudes where this problem is not as severe, i.e., $\theta_o \leq 23^o$.

(c.) Density model for a polar coronal hole

In Figure 37 we have a log-log plot of the electron number density in cgs units characteristic of polar coronal holes. The Munroe and Jackson[24] data points, indicated by x's, and K. Saito (1970)[72] data points, indicated by circles "0", have an angular dependence and are shown along the radial line at 68^o latitude. The data from C. W. Allen (1973),[73] indicated by crosses "+", have no angular dependence and may be considered as a mean density for the polar coronal hole. It should be said that all this data was accumulated during solar minimum though for different cycles, and thus should correspond to regions characteristic of polar coronal holes. The data by Allen and Saito, which allow us to extend our profiles down to the solar surface, are from polarimetric observations taken during solar eclipses; while the data by Munroe and Jackson were acquired from coronagraph observations during the Skylab missions (all white light observations). Note: the densities are much steeper near the corona and lower in magnitude than that observed in equatorial regions or during solar maximum (see Fig. 32). Furthermore, there is an angular dependence where the density is lowest at the

poles. It is important to note that there is a large data gap between $5_{\odot}r$ and 1 AU. This gap results from the characteristically low densities of the polar corona during solar minimum, so that the light from the K corona becomes swamped by the F corona beyond 5 $r_{\odot}$. Because of this data gap our interpolated curves for the density must be treated as a tentative guess at best. The data points at 1 AU are densities typical of high speed streams. They were assumed to correspond to the 23° field line and were projected up to a latitude of 68° using the angular dependence given by Munroe and Jackson.[24] The density model we used is a generalization of that given for the spherical model and may be written the following way:

$$\rho(r,\theta) = \rho_o a_1 e^{a_2 Z} Z^2 P(z) f_{MJ}(\theta) \qquad (3.90a)$$

$$P(z) = 1 + a_3 Z + a_4 Z^2 + a_5 Z^3 \qquad (3.90b)$$

$$f_{MJ}(\theta) = 0.774\,(1 + 2.14 \sin^2\theta) \qquad (3.90c)$$

where a_1 through a_5 are adjustable parameters, ρ_o is the mass density at the reference level, and $f_{MJ}(\theta)$ is the angular dependence given by Munroe and Jackson. It should be pointed out that a variety of other functional forms were used, and that this model seemed to reproduce the data best. For purposes of reference the logarithmic derivatives of ρ with respect to x and θ are given

$$\delta_r = \frac{1}{\rho}\frac{d\rho}{dx} = -Z\left[2 + Z\left(a_2 + \left(a_3 + 2a_4 Z + 3a_5 Z^2\right)/P(z)\right)\right] \qquad (3.91a)$$

$$\delta_\theta = \frac{1}{\rho}\frac{d\rho}{d\theta} = \frac{2.14 \sin 2\theta}{1 + 2.14 \sin^2\theta} \qquad (3.91b)$$

The three separate curves shown in Figure 37 correspond to three separate fits of Eq. (3.90) to the data for the three density estimates at 1 AU. The numerical values for the parameters ρ_o, n_o, and a_1 through a_5 resulting from the fits are given in Table 18. Note: in computing the mass density at the reference level ρ_o, we assumed 5% of the positive ions were alphas. In Table 19 we have listed values of the electron density n_e and radial gradient δ_r for various (r, θ) along the 23^o field line. As may be seen, the slope of the density profile near the reference level $\delta_r \approx -13$ is much steeper than that for equatorial regions $\delta_r \approx -9$ [see Fig. 32]; while further out at 10 $r_\odot$, the radial gradient $\delta_r \approx -3.0$ is the same for both regions.

(d.) Derivation of pertinent expressions for $\vec{V}$, T_{eff}, and q_{eff}

We are now ready to derive the appropriate equation for the effective temperature T_{eff} and effective heat flow vector q_{eff} similar to that done for the spherical model. (Note: we have added the subscripts effective since waves may be important.) The component along the magnetic field of Eq. (3.50) (the momentum equation in the rotating frame) is

$$\rho V \frac{\partial V}{\partial \ell} + \frac{\partial}{\partial \ell} P_{eff} + \rho \frac{\partial \Psi}{\partial \ell} = 0 \qquad (3.92)$$

where $\vec{V} = V\hat{b}$ and

$$P_{eff} = \frac{\rho k T_{eff}}{\mu m_H} \tag{3.93}$$

is the effective pressure and

$$\mu = \frac{2}{1+3X+.5Y} \tag{3.94}$$

is the mean molecular weight (i.e., X and Y are the fraction of the gas by weight for protons and alphas). For our calculations, 5% of the positive ions are alphas, thus X = 0.826, Y - 1-X = 0.174, and μ = 0.561. From Eq. (3.58) and the fact that α is a field line constant, we find

$$\frac{\partial P_{eff}}{\partial \ell} + \rho \frac{\partial}{\partial \ell}\left(\frac{1}{2}\frac{\alpha^2 B^2}{\rho^2} + \Psi\right) = 0 \tag{3.95}$$

Then by using the boundary condition $T_{eff} \to 0$ as $\ell \to \infty$ and Eq. (3.93) for P_{eff} we get the following integral for T_{eff}

$$T_{eff} = \frac{\mu m_H}{2k\rho}\int_{\ell}^{\infty} \rho \frac{d}{ds}\left(\frac{\alpha^2 B^2}{2\rho^2} + \Psi\right) ds \tag{3.96}$$

where S is the arc length along the field line. We will now introduce the energy per unit mass W* which is related to the Bernoulli constant

$$W^* = \frac{\alpha^2 B^2}{2\rho^2} + \Psi = \frac{1}{2}V^2 + \Psi \tag{3.97}$$

Since T_{eff} is related to the derivative of W^*, the result will not be effected by adding a constant to it. Now if the integral is to be well-defined for purposes of doing numerical integrations we would like to integrand to approach zero at infinity. Thus we determined the asymptotic limit for W*

$$W_\infty^* = \tfrac{1}{2} V_{P\infty}^2 - \xi_\infty \Omega^2 R_A^2 \tag{3.98}$$

where $V_{P\infty}$ is the poloidal component of the wind velocity at infinity and

$$\xi_\infty = \lim_{r\to\infty} \left(1 - \frac{\rho}{\rho_A}\left(\frac{R}{R_A}\right)^2\right) \tag{3.99}$$

We may then define a new W

$$W' = W_\infty^* - W^* = \tfrac{1}{2}(V_{P\infty}^2 - V_P^2) + \tfrac{1}{2}\left(\Omega^2 R^2 - \frac{\alpha^2 B_t^2}{\rho^2}\right) + \tfrac{1}{2} v_{esc}^2 \Gamma - \Omega^2 R_A^2 \xi_\infty \tag{3.100}$$

Substituting Eq. (3.100) into Eq. (3.96) for W* and integrating by parts we get the following equation for T_{eff}:

$$T_{eff} = \frac{\mu m_H}{k}\left\{W' + \frac{1}{\rho}\int_\ell^\infty W' \frac{d\rho}{ds}\, ds\right\} \tag{3.101}$$

As a side remark, Eq. (3.101) for T_{eff} reduces to the form for the spherical model [see Eq. (3.33)] when we use a monopole for $\vec{B}$ and neglect rotation.

Using the following definition for q_{eff} (since waves may be present):

$$\vec{q}_{eff} = \vec{q} + \vec{S} - \tfrac{5}{2} P_w \vec{V} \tag{3.102}$$

where

$$P_{eff} = P + P_w \tag{3.103}$$

and P, P_w are, respectively, the gas pressure and the pressure due to waves. The energy equation [see Eq. (3.51)] then has the following form

$$\nabla\cdot\left(\tfrac{1}{2}\rho V^2 \vec{V} + \tfrac{5}{2} P_{eff}\vec{V} + \vec{q}_{eff}\right) = -\rho \vec{V}\cdot\nabla\Psi \tag{3.104}$$

It should also be pointed out that in the rotating frame the Poynting vector $\vec{S} = 0$, neglecting waves; thus $\vec{S}$ will only

contribute if there are waves. Since all the terms inside the parenthesis on the lefthand side of Eq. (3.104) are field aligned (note assumption that $\vec{q}_{eff} = q_{eff}\hat{b}$) then the identity

$$\nabla \cdot \vec{A} = B \frac{\partial}{\partial \ell}\left(\frac{A}{B}\right) \tag{3.105}$$

will apply where $\vec{A} = A\hat{b}$ is some field aligned vector. Eq. (3.104) then becomes

$$B \frac{\partial}{\partial \ell}\left\{\frac{1}{B}\left[\frac{1}{2}\rho V^3 + \frac{5}{2} P_{eff} V + q_{eff}\right]\right\} = -\rho V \frac{\partial \Psi}{\partial \ell} \tag{3.106}$$

Using the relations $\alpha \vec{B} = \rho \vec{V}$ and $\vec{B} \cdot \nabla \alpha = 0$, Eq. (3.106) reduces to

$$B \frac{\partial}{\partial \ell}\left\{\frac{1}{B}\left[\left(\frac{1}{2}\rho V^2 + \frac{5}{2} P_{eff} + \rho \Psi\right) V + q_{eff}\right]\right\} = 0 \tag{3.107}$$

This means that the quantity in braces is a field line constant, i.e.,

$$\frac{1}{B}\left[\left(\frac{1}{2}\rho V^2 + \frac{5}{2} P_{eff} + \rho \Psi\right) V + q_{eff}\right] = W_0 = \text{constant along the field line.} \tag{3.108}$$

If we divide Eq. (3.108) by α we get

$$W^* + \frac{5}{2}\frac{P_{eff}}{\rho} + \frac{q_{eff}}{\rho V} = W \tag{3.109}$$

Using the boundary conditions

$$\lim_{\ell \to \infty} \frac{q_{eff}}{\rho V} = 0 \tag{3.110a}$$

$$\lim_{\ell \to \infty} T_{eff} = 0 \tag{3.110b}$$

we get the following:

$$W = W^*_\infty \tag{3.111}$$

The expression for q_{eff} then reduces to the very simple relation

$$q_{eff} = \rho V \left[W' - \frac{5}{2} \frac{P_{eff}}{\rho} \right] \qquad (3.112)$$

In the case of no rotation, and monopole for the B field, Eq. (3.112) reduces to that for the spherical model [see Eq. (3.43)].

(e.) Some details of the procedure for evaluating solutions

The reader may omit reading this section, where we discuss for the record our method for evaluating solutions.

Using the method outlined in section 3.5b, we determined the parameters η_M, η_D, and η_Q from the Munroe and Jackson field line. Except for the field strength given by the parameter B_o, the poloidal component of the $\vec{B}$ field is completely determined. As will become apparent, because our observations are made at 1 AU we must first determine the toroidal component of the field at 1 AU before we can determine the parameter B_o. By knowing η_M, η_D, and η_Q, we do know the topology of the field, and since we know the position of the spacecraft

$$R_{s/c} = r_{s/c} \sin \theta_{s/c} \qquad (3.113)$$

we will know which field line we are situated upon (i.e., $r_{s/c} \sim 1$ AU). Note: in reality the determination of a field line and its origin is not possible except under certain ideal

conditions such as those outlined at the end of section 3.2, concerning polar coronal holes and spacecraft observations at high latitudes. Then by measuring the density, and assuming the positive ion composition (5% alphas in our case), we can determine the mass density at $R_{s/c}$ along a known field line. This will then allow us to project our density up to $(r_{s/c}, 22^{o})$ as pointed out in section 3.5c. Then by using some fitting procedure we determine the adjustable parameters ρ_o and a_1 through a_5 from the coronal densities and density point at 1 AU as shown in Fig. 37. By doing this, the mass density ρ is determined for all $\vec{r}$. (Note: in essence we are predicting what the density should be at different latitudes.) Furthermore, from spacecraft observations we can get the wind velocity in the inertial frame $V_{s/c}$, which is essentially equal to the poloidal component of V in the rotating frame. We also have available the magnetic field $\vec{B}_{s/c}$. In high speed streams the magnitude of the density, wind velocity, and magnetic field strength are fairly constant and less susceptable to fluctuations in comparison with their corresponding vector components (i.e., fluctuations and large amplitude Alfvén waves are at a high level in high speed streams). Using the magnitudes of $V_{s/c}$, $B_{s/c}$, and the already determined density model, we can solve for α for this particular field line at $R_{s/c}$

$$\alpha = \alpha_{s/c} = \frac{\rho_{s/c}\sqrt{V_{s/c}^2 + \Omega^2 R_{s/c}^2}}{B_{s/c}} \qquad (3.114)$$

once Ω is specified ($\rho_{s/c} = \rho(r_{s/c}, \theta_{s/c})$). As may be seen, α must be determined in the rotating frame. Since we are taking into account differential rotation, we must know the latitude of this field at the reference level. From Allen (1973) the angular velocity Ω as a function of latitude is given by the following relations

$$\Omega = \frac{2\pi}{T_{SID}(86,400)} \text{ rad/sec} \qquad (3.115)$$

where

$$T_{SID} = \frac{T_{SYN}}{T_{SYN}\Delta\Omega/360 + 1} \qquad (3.116)$$

is the sidereal rate in days,

$$T_{SYN} = 26.75 + 5.7 \sin^2\lambda \qquad (3.117)$$

is the synodic rotation period in days, λ is the latitude (i.e., $\lambda = \frac{\pi}{2} - \theta_o$), and $\Delta\Omega = 0.9856$. Since we know what field line we are situated upon, we can determine θ_o from the field line equation. To do this we simply substitute $(z_{s/c}, \theta_{s/c})$ in place of (z_o, θ_o) into Eq. (3.86b) for C_o, and then solve for θ_o by substituting z = 1 into Eq. (3.86a) for cos θ. (Note: $z_{s/c} = r_o/r_{s/c}$) We may then solve for Ω using Eqs. (3.115), (3.116), and (3.117) along with θ_o. Once this is done we will know α for this particular field line from Eq. (3.114).

As pointed out, we have not yet determined the field strength parameter B_o. To do this we need to know the poloidal component of the field strength at 1 AU, i.e.,

$$B_{P_{s/c}} = \sqrt{B_{s/c}^2 - B_{t\,s/c}^2} \tag{3.118}$$

For large r, it may be shown from Eq. (3.62) for B_t that

$$B_{t\,s/c} \approx -\Omega \rho_{s/c} R_{s/c} / \alpha_{s/c} \tag{3.119}$$

thus allowing us to solve for $B_{t\ s/c}$ since we know Ω, $\rho_{s/c}$, $R_{s/c}$ and $\alpha_{s/c}$. Therefore, from Eq. (3.118) we can solve for $B_{p\ s/c}$ from Eq. (3.119) and the observed field strength $B_{s/c}$. Futhermore, for large r only the monopole term will contribute significantly to $B_{p\ s/c}$. Thus, from Eq. (3.69) we have the following relation for B_o:

$$B_o = 2 B_{P_{s/c}} / \eta_M / Z_{s/c}^2 \tag{3.120}$$

which allows us to solve for B_o. Thus, the poloidal component of our magnetic field model $\vec{B}_p$ is known for all (r,θ). In our calculations we used $B_{s/c} = 5\gamma$ which is a typical value for high speed streams. Once this is done the field strength at the reference level is about 16 gauss, which is about that observed from photospheric magnetograph observations.[18, 26]

Referring to Eq. (3.62), one will note that the toroidal component of B will not be known for all (r,θ) until the Alfven point R_A is determined. From Eq. (3.65) we can solve for ρ_A since we know α. Then by solving along the

field line the equation

$$\rho(r_A, \theta_A) = \rho_A \tag{3.121}$$

where the density model for ρ given by Eq. (3.90) is substituted in place of $\rho(r_A, \theta_A)$, one can determine R_A. Next we substitute ρ_A and R_A into Eq. (3.62), B_t will be determined for all (r, θ) along this field line. Correspondingly, since we already know $\vec{B}_p$ for all (r, θ), the magnetic field $\vec{B}$ is known for all (r, θ) along this field line. We would like to point out that the above procedure may be duplicated for all the other field lines (different latitudes) by only knowing $V_{s/c}$ as a function of latitude, since $\rho(r, \theta)$, and $\vec{B}_p(r, \theta)$ are already known.

It is now possible from Eq. (3.58) relating $\vec{V}$ and $\vec{B}$ to solve for the wind velocity $\vec{V}$ in the rotating frame along this field line. Then by adding the angular velocity $\vec{\Omega} R$ of the rotating frame to $\vec{V}$, we can solve for the wind velocity in the inertial frame, i.e.,

$$\vec{V}_I = \vec{V} + \vec{\Omega} R \tag{3.122}$$

At this point it should be pointed out that the determination of α for a particular field line is equivalent to specify the mass flux for that field line. Then, as in the spherical case, once the mass flux is specified, the flow along a particular field line is completely determined, since we know ρ and $\vec{B}_p$. Furthermore, as in the spherical model, once we know $\vec{V}$ along the field line, the effective temperature

T_{eff} is determined along the field line by Eq. (3.101), and once T_{eff} is known, we can solve for q_{eff} along the field line by substituting V and T_{eff} into Eq. (3.112). Thus, we have demonstrated that once ρ and $\vec{B}_p$ are given along with the mass flux "$V_{s/c}$" for a particular field line, it is possible to compute radial profiles of $\vec{V}_I$, T_{eff}, and q_{eff} along that field line within the assumptions and approximations previously outlined.

(f.) Results

We will now give the results acquired for the 23° field line studied by Munroe and Jackson. As previously noted, there were three density profiles. The one we felt most characteristic of the data was density profile number one (top curve in Fig. 37). Furthermore, we used a field strength of 5 γ at 1 AU and two values for the wind velocity $V_{s/c}$ = 714 km/sec and 500 km/sec (i.e., solutions 1 and 2). This was mainly done because of the uncertainty in the wind velocity, and because we can see the differences between profiles characteristic of high speed streams and average velocity streams. For reference, the proton particle fluxes at 1 AU for the average and high speed streams are, respectively, 1.67×10^8 cm^{-2} $-sec^{-1}$ and 2.38×10^8 cm^{-2} $-sec^{-1}$.

In Figures 38, 39, and 40 we have plotted log-log plots, respectively, of V_I, T_{eff}, and q_{eff} along the 23°

field line for the conditions outlined above (also see Table 19). From looking at the profiles of the wind velocity, one should note the high velocities at the reference level $V_o \approx 4.0$ and 6.4 km/sec in comparison with those for the spherical model $V_o \approx 0.5$ km/sec shown in Fig. 33. Also, note the steep rise in velocity relative to that for equatorial regions (see Fig. 33). This steep rise is due to the initially sharp drop in density characteristic of polar coronal holes, which totally dominates the large divergence of the magnetic field. The temporary dip in velocity at around 1.5 $r_\odot$ to 2 $r_\odot$ is due to a temporary dip in the field strength (i.e., sort of a magnetic bottle) which is characteristic of the magnetic field model. Thus, one should take such results with a great deal of caution. In the 3 $r_\odot$ to 20 $r_\odot$ region there is a more gradual increase in the velocity, though it is still large. Finally, beyond 50 $r_\odot$ the acceleration of the plasma has essentially stopped. The sonic points r_s computed as in the spherical model occur at 5.18 $r_\odot$ and 4.58 $r_\odot$, respectively, for solutions one and two. Also, the Alfven points r_A for solutions one and two occurred, respectively, at 18.4 $r_\odot$ and 23 $r_\odot$. The reason why r_A moves out for smaller $V_{s/c}$ is because α is less for smaller $V_{s/c}$ [see Eq. (3.58)] and $\rho_A = 4\pi\alpha^2$ is quadratically related to . For all our solutions we find that the Alfven point occurs in the range from

$$18\, r_\odot \leq r_A \leq 30\, r_\odot$$

Note: this will not be true for the T cusp, since as $B \rightarrow 0$, $V_A \rightarrow 0$.

The T_{eff} profiles show an initial rise below 1.5 $r_\odot$, an extended isothermal region for solution #2, and a pronounced temperature rise of up to 3×10^6 ^oK reaching its peak at about 10 $r_\odot$ for solution #1. This temperature rise out to 10 $r_\odot$ was also indicated by Munroe and Jackson's calculations; however, it should be noted that our calculations are a further sophistication of theirs since we use the general MHD equations along the field lines. The high rise in temperature results solely from our requirement for higher velocities at 1 AU. This temperature rise is related to the necessity for extended acceleration far from the sun (see Fig. 38), and to the fact that this acceleration takes place over distances on the order of the Alfvénic critical distance, as would be predicted in Alfvénic wave pressure models (Belcher, (1971)).[62] Some other interesting points to note are the low temperatures near the lower corona $T_{eff} \sim 10^6$ ^oK and the initial rise in temperature inside 1.5 $r_\odot$. Note that this initial temperature rise, where the flow is subsonic, is independent of $V_{s/c}$. The low temperature, as observed by previous authors,[17] supports the notion that conduction is not sufficient to

drive the expansion from coronal holes. The initial rise in temperature cannot be explained by Alfvén waves since the wave pressure term due to Alfvén waves can be shown to be negligible this close to the sun. Thus, this is probably a real temperature rise in the gas. Finally, the temperature at 1 AU for solution #1 is $T_{eff} = 4.2 \times 10^5$ °K, which is about a factor of two greater than that observed. Using observed Alfven energy flues $E_A = 12 \times 10^{-3}$ ergs/cm^2/sec in high speed streams, this number reduces to 2.6×10^5 °K, which is still too high (i.e., $T = (T_p + T_e) = 1.6 \times 10^5$ °K for $T_p = 2.6 \times 10^5$ °K, $T_e = 9 \times 10^4$ °K). But, as pointed out for the spherical model, this may only be due to the strong dependence of the temperature at large r on the slope of the density profile (see section 3.4).

Figure 40 shows the emerging pattern of the effective heat flow. Note the large value for $q_{eff} \sim 7 \times 10^5$ ergs/cm^2/sec at the base of the corona. Note also that q_{eff} decreases throughout (even within the inner corona) in spite of the fact that the effective temperature rises. This obviously contradicts the canonical picture of the heat conduction in a collision dominated plasma; that is to say that q is proportional to the negative gradient of the temperature [see Eqs. (3.7) and (3.8)]. This picture definitely supports the notion of wave driven winds, which are probably due to the very low frequency transverse MHD waves, which on a

large scale downstream eventually become Alfvén waves. Furthermore, it clearly emphasizes the need for the subscript "effective" with the temperature and heat flow vector terms as previously noted. Some other points which need mentioning are the initially steep drop in q_{eff} indicating an enchanced energy deposition and the possibility for energy being conducted back to the lower corona because of the positive temperature gradient. At about 5 $r_\odot$ the energy deposition is a minimum and then increases beyond 8 $r_\odot$ (flow becomes more adiabatic). Beyond 8 $r_\odot$ the slope is -3 and then becomes less steep beyond 1 AU. This last effect is due to the spiraling of the magnetic field, and if one considers the radial component of q_{eff} it is decreasing with a slope equal to -3, as in the spherical model. Finally, $q_{eff} = 18 \times 10^{-3}$ ergs/cm^2/sec, 7×10^{-3} ergs/cm^2/sec for, respectively, solutions #1 and #2. As quoted by Feldman et al. (1976),[12] the observed heat flow vector due to electrons in high speed streams is only 2×10^{-3} ergs/cm^2/sec. If this discrepancy were due to Alfven waves, q_{eff} would only be reduced down to 16×10^{-3} ergs/cm^2/sec for $E_A = 12 \times 10^{-3}$ ergs/cm^2/sec (i.e., can be shown that $q_A \approx \frac{1}{6} E_A$, where q_A is the "heat flow" vector due to Alfvén waves). Again this discrepancy can be partially corrected by fixing the slope of the density profile at 1 AU. (Note: T_{eff} is also too high).

Finally, we would like to point out that since waves are important, one might question the original approximation that $\vec{q}$ is parallel to $\vec{B}$. In the case of Alfvén waves, one can show that in the rotating frame of reference the energy transport resulting from the Poynting vector due to Alfvén waves is also field aligned [J. V. Hollweg (1974)].[74]

Thus, with these facts in mind, the approximation that

$$\vec{q}_{eff} = q_{eff}\hat{b}$$

also seems to apply.

(6.) Possible Applications of the Results of Sections 4 and 5

One of the most apparent applications of these profiles is their direct comparison with profiles of the wind velocity, temperature, and heat flow vector predicted by various models of the solar wind based on different transport theories. Such comparisons allow for the discarding of some theories and probably the modifications of others. Another application is that we can now calculate at distance r a number of various physical parameters. Examples are the polytrope index:

$$\gamma = 1 + \frac{d(\ln T)}{d(\ln n)}$$

the Coulomb m.f.p. of a thermal electron $\bar{\lambda}_{ei}$ over the scale height H:

$$(\bar{\lambda}_{ei}/H)$$

the Alfvén velocity

$$V_A = \frac{B}{\sqrt{4\pi\rho}}$$

and the β parameter equal to the ratio of the gas pressure P over the magnetic field pressure

$$\beta = \frac{P}{(B^2/8\pi)}$$

For instance, in Figures 41 and 42 we have plotted radial profiles of the polytrope index γ derived from density and temperature profiles both from the spherical model and the polar coronal hole model.

Figure 41, which is characteristic of equatorial regions, shows γ to vary considerably around one with 10 $r_\odot$.

This brings into doubt the validity of a polytrope law near the sun (i.e., $\gamma < 1$ not applicable for expansion models). To some degree this variation could be model dependent, so that one could say that the temperature inside 10 $r_\odot$ is approximately isothermal ($\gamma \approx 1$); while beyond 10 $r_\odot$ the flow becomes more adiabatic and eventually approaches 3/2 at infinity. Thus, at least for equatorial regions the polytrope law may still apply. For polar coronal holes (Fig. 42) the polytrope law is definitely not applicable, where inside 10 $r_\odot$ the polytrope index is much less than one (i.e., large positive temperature gradient in this region).

In Figures 43 and 44 we have done the same for the ratio ($\bar{\lambda}_{coul}/r$) for core electrons (see Chapter IV for definition) as we did for γ. Using the following criteria:

$$\frac{\lambda_{ei}}{r} < 0.1 \qquad \text{collision dominated}$$

$$\frac{\lambda_{ei}}{r} >> 1.0 \qquad \text{collisionless}$$

and from these profiles one can determine those regions where the electron gas is collision dominated or collisionless. For instance, the intermediate curve shown in Fig. 43, which is characteristic of equatorial regions, shows the electrons to be collision dominated inside 5 $r_\odot$, to approach a collisionless state at 30 $r_\odot$, and then to become collision dominated beyond 2 AU (i.e., if T decreases faster than $r^{-1/2}$ the gas will eventually become collision dominated at large r). For

polar regions (see Fig. 44) the electrons become collisionless almost immediately $r > 2\ r_\odot$ and the ratio ($\bar{\lambda}_{coul}/r$) approaches values on the order of 10^2. Furthermore, the collisionless state extends far beyond 1 AU. Thus, fluid models of the solar wind which seem to give a reasonable description of the equatorial solar wind may not be applicable at polar regions.

Our model also allows us to predict the overall meridional flow for all latitudes and radial distances from spacecraft observations at 1 AU in the ecliptic plane and interplanetary scintillation measurements which give us empirical estimates of the solar wind velocity at higher latitudes. As an example, one may assume a sinusoidal variation of speed equator-to-pole from 450 km/sec to 800 km/sec similar to that suggested by interplanetary scintillation measurements by Coles and Rickett (1976).[75] Then by using the same method outlined in section 3.5e and applied in section 3.5f, along with the above empirical information, one is able to determine ρ and $\vec{B}_p$ for all (r, θ) and the profiles of V_I, T_{eff}, and q_{eff}, etc. along the $\theta_o = 23^o$ field line (i.e., this field line extends down to 17^o latitude far from the sun). Then from "empirical" wind velocities at higher latitudes, which allow us to determine α for the other field lines, we were able to determine B_t and thus $\vec{B}$ for all (r, θ). This then allows one to solve for V_I, T_{eff},

and q_{eff}, etc. along all field lines above 17^{o} latitude at 1 AU. Note: all calculations were confined above the $\theta_o = 23^{o}$ field line in order to avoid the problem with $\vec{B}_p$ at lower latitudes near the sun. Figure 45 is the result of such calculations [Courtesy of Out-of-Ecliptic Proposal (1977)[76]], which clearly demonstrates the usefulness of such a model calculation. Other than for the results previously noted to, one may readily see that the Alfvén velocities are extremely high near the sun, allowing for the possibility of great enhanced energy fluxes in MHD waves. The beta parameter, important for theoretical studies of waves in plasmas, decreases with increasing latitude, while beyond 1 AU it becomes much greater than one.

(7.) Closing Remarks

As pointed out in section 3.5c, the density profile for polar coronal holes has a large data gap between $5r_\odot$ and 1 AU. Furthermore, the latitudinal dependence used by Munroe and Jackson and in our calculations is probably not, realistically speaking, that simple and will not hold for all (r, θ). (Note: this angular dependence was suggested by the radio dispersion measurements of Counselman and Rankine (1972)[64] out to 20 $r_\odot$.) Thus the functional form for our density model [see Eq. (3.90)] and fit will therefore not be unique and quite possibly will not reproduce the data as well as it does for equatorial regions (spherical model). Since the profiles are sensitive to the shape of the density profile (see section 3.4), such model predictions as those presented here must be treated with extreme caution. This sensitivity upon the density profile is explicitly shown by Figures 46, 47 and 48 for, respectively, V_I, T_{eff}, and q_{eff}, where the three density profiles shown in Fig. 37 were used.

Another difficulty with our profiles is the problem with our simple magnetic field model noted to in section 3.5b. In order to remove such ambiguities or uncertainties, one should eventually use more sophisticated (realistic) models of the magnetic field topology as developed by R. H. Levine (1977).[26] Furthermore, because of the correction currents noted to in section 3.5b our model calculations will not be totally self-

consistant. At present there are unfortunately no clear solutions to this problem. It is hoped that such corrections are small and if large may possibly be reduced by using the more sophisticated models referred to above.

It should be emphasized that all the uncertainties in our model calculations previously referred to are predominantly due to limitations in the observations. As the observations get better the models for the density and magnetic field will correspondingly become more sophisticated and more accurate. Because of this, the "empirical" profiles of the wind velocity, T_{eff}, q_{eff}, etc. will also become more accurate. In the case of polar coronal holes, referring to the discussions near the end of section 3.2, the potential for such observational advances is the greatest. For instance, the mass flux problem discussed in section 3.4 and its effects explicitly shown in section 3.5f may be resolved by earth bound observations of the corona, more specifically near the poles near solar minimum, and simultaneous spacecraft observations at high latitudes. It is hoped that experiments of this sort will be performed, and that observational advances, especially the determination of electron densities over the sun's poles beyond 5 $r_\odot$, will become a reality in the near future. Finally, we would like to stress that the most important contribution of this endeavor is the introduction of the method, and not the results of our calculations, which should be thought of as the first generation of many to be performed in the future.

CHAPTER IV

REVIEW OF THE EXISTING TRANSPORT THEORIES FOR INTERPLANETARY ELECTRONS

(1.) Qualitative Remarks

At present there is no adequate theory for the heat transport in the solar wind. To begin, the physical entity describing the heat transport is the heat flow vector $\vec{q}$, defined by

$$\vec{q} = \frac{1}{2} m_e \int (\vec{v} - \vec{V})^2 (\vec{v} - \vec{V}) f_e \, d^3v \qquad (4.1)$$

The classical transport theory (conduction) states that

$$\vec{q} = - \varkappa_c \nabla T \qquad (4.2)$$

i.e., that $\vec{q}$ is proportional to the negative gradient of the temperature. According to the anzatz by Spitzer and Harm (1953)[77] or, equivalently, according to the Onsager relations, which predict an expression for $\vec{q}$ similar to that given by Eq. (4.2), the proportionality coefficient (thermal conductivity) is given by [see Eq. (4.4) for definitions].

$$\varkappa_c = \frac{1.92 \times 10^{-5}}{\ln \Lambda} T^{5/2} \qquad (4.3)$$

in cgs. units. This expression, which has a strong temperature dependence and predicts large thermal conductivities in the corona, is only applicable for the case of a fully ionized Coulomb collision dominated proton-electron

gas. That is, the characteristic scale lengths L and time scales T_s of the plasma must be large relative to their respective counterparts, i.e., mean free path (m.f.p.) λ_{coul} and collision time τ_{coul} for Coulomb collisions.

Our results obtained in Chapter III on the density and temperature as functions of radial distance from the sun, allow us to compute radial profiles of the Coulomb m.f.p. of a thermal electron λ_{coul} over the radial distance from the sun (see Figs. 43 and 44); this in turn allows us to determine when the core electrons become nearly collisionless. (Note: the radial distance r is used in the same sense as the scale height H, which is equal to r divided by the negative of the logarithmic derivative of the density with respect to r.) The exact expression used for Figures 43 and 44 is the following (m.f.p. for isotropization of electrons)[48]:

$$\left(\frac{\bar{\lambda}_{COUL}}{r}\right) = \frac{\left(\frac{2kT}{m_e c^2}\right)^2}{(4\pi r_e^2 n \eta \ln\Lambda\, r)} \qquad (4.4a)$$

where

$$\ln\Lambda = \frac{3kT}{m_e c^2}\,\frac{D}{r_e} \qquad (4.4b)$$

is the Coulomb logarithm, D = 9.76 $\sqrt{T/n}$ is the Debye length in cm, $r_e = 2.818 \times 10^{-13}$ cm is the "classical electron radius," and $\eta = 6/5\ \sqrt{3/\pi}\ (1 + \quad 2) = 2.83$.

As may be seen from Figures 43 and 44, the collision dominated condition for core electrons does not hold beyond a few solar radii above the solar surface, especially for

the case of coronal holes. Furthermore, since ($\bar{\lambda}_{coul}/r$) is proportional to T^2/n, the suprathermal electrons are not collision dominated at all as far as Coulomb collisions are concerned. Because of these facts, the classical transport theory for $\vec{q}$, Eqs. (4.2) and (4.3), gives an inadequate description of $\vec{q}$ for the interplanetary medium at large. At best, it may be applicable within the lower corona. It also follows that we must have a transport theory which is applicable to the case when $\bar{\lambda}_{coul} > H$. At present, such a theory based on sound physical arguments like those for a Coulomb collision dominated plasma (Onsager relations), has not yet been formulated. At present, some new theories are in the making concerning the heat transport by electrons in the interplanetary medium. In sections 4.3 and 4.4 we will review two of them.

(2.) Brief Summary of Published Observations Concerning Heat Flow

We would like to begin with a more detailed review of the electron observations than that given in the introduction to Chapter I. Montgomery et al. (1968)[3] was the first one to demonstrate that the interplanetary electrons had a non-Maxwellian suprathermal tail. More recently, Feldman et al. (1975)[9], using data derived from interplanetary electron measurements made by the Los Alamos Scientific Laboratory (LASL) plasma detector on the earth-orbiting Imps 6-8, derived electron plasma parameters from a much broader data base than that previously done.

In Figure 1 we have a plot of data representing the electron distribution for solar wind electrons determined by Feldman et al.,[9] while in Table 20 we have listed their average properties.[9] The electrons appear to be composed of two separate and distinct populations.

Below 60 ev are the core electrons with the distribution f_c, which are nearly Maxwellian and isotropic (i.e., $(T_{\parallel}/T_{\perp})_c \sim 1.1$) in the proper frame,[3,9] while at higher energies there are the "halo" (suprathermal) electrons with the distribution f_H, in agreement with the previous results by Montgomery et al.[3] and Ogilvie et al. (1971).[5] Furthermore, the suprathermal electrons are non-Maxwellian [3,5] and nearly isotropic ($T_{\parallel}/T_{\perp})_H \sim 1.25$) in a frame of reference moving with velocity $\Delta\vec{V}_H$ along $\vec{B}$ (see section 4.3

for definitions) relative to the proper frame.[9] They are shown to contribute to most of the heat flow.[9,5] The values for the heat flow vector determined by these authors[3,9,5] varies in the range from 4×10^{-3} ergs/cm^2/sec to 8×10^{-3} ergs/cm^2/sec, in a rough agreement within large experimental errors. Some other plasma parameters typical of electrons (refer to Table 20) are: (1) halo density $n_H \approx 0.065\ n_c$, (2) halo temperatures $T_H \approx 6T_c$, (3) core drift velocity $\Delta\vec{V}_c \sim -50$ km/sec, and (4) halo drift velocity $\Delta\vec{V}_H \sim 700$ km/sec. The core electrons are drifting back toward the sun along $\vec{B}$ and the halo electrons are moving away from the sun along $\vec{B}$ both relative to the proper frame. Furthermore, the electrons are found to be gyrotropic relative to $\vec{B}$.[9]

There are various observational difficulties concerning electron measurements. For instance, spacecraft observations of solar wind electrons, as pointed out by J.D. Scudder (1971)[78] and K.W. Ogilvie et al. (1971),[5] may become contaminated because of bow shock associated phenomena. This contamination, occuring when the magnetic field line at the spacecraft connects with the earth's bow shock, may introduce considerable distortion to the distribution of the suprathermal electrons, thus making estimates of the skewness of f_e at higher energies ambiguous[9,5] (e.g., the heat flow may appear to be flowing back toward the sun). Other difficulties arise because of spacecraft charging effects (see

Chapter II), which may introduce considerable distortions of f_e for energies $\lesssim$ 10-15 ev for typical values of the spacecraft potential $<$ 5 ev.[5] Because of this, the measurements of f_e below 10-15 ev are burdened with uncertain corrections that make accurate core density and temperature estimates difficult. Furthermore, because electrons are "subsonic," detectors are unable to sample total f_e; thus the calculations of q_e must rely on certain assumptions, which may or may not be justified.

Because of these observational difficulties, progress in making electron observations has been slow in comparison with positive ion measurements. However, some progress has been made, thus allowing for the development of two distinct models of the interplanetary electrons. They are the "convection" model by Feldman et al.,[9] discussed in section 4.3, and the "conduction" model by Scudder and Olbert,[14] discussed in section 4.4.

(3.) Feldman's Convection Model of Interplanetary Electrons

Because the solar wind electrons appear to be composed of two separate and distinct populations, Feldman et al.[9] proposed the following mathematical expression to fit the data:

$$f_e(\vec{v}) = \frac{n_c}{\pi^{3/2}} \beta_{\perp c} \sqrt{\beta_{\parallel c}}\, e^{-\beta_{\perp c}(\vec{v}-\vec{v}_c)^2 - \Delta\beta_c (v_\parallel - v_{\parallel c})^2} \tag{4.5a}$$

$$+ C_H(E) \frac{n_H}{\pi^{3/2}} \beta_{\perp H} \sqrt{\beta_{\parallel H}}\, e^{-\beta_{\perp H}(\vec{v}-\vec{v}_H)^2 - \Delta\beta_H (v_\parallel - v_{\parallel H})^2}$$

where either $C_H(E) = 1$ for all energies E (4.5b)

or

$$C_H(E) = \begin{cases} e^{-(E_{B_A} - E)/E_c} & E \leq E_{B_A} \\ 1 & E \geq E_{B_A} \end{cases} \tag{4.5c}$$

E_{B_A} is the breakpoint energy (i.e., point where $f_c = f_H$ after averaging overall angles), $E_c = k T_c$; n_c, n_H are, respectively, the core, halo electron density; $\beta_\perp$, $\beta_\parallel$, $\Delta\beta$ have the same definitions as those given by Eq. (1.26), except for the subscript "c" for core electrons and the subscript "H" for halo electrons; $\vec{V}_c$, $\vec{V}_H$ are, respectively, the velocity of the core, halo electrons relative to the satellite frame of reference; and $\vec{V}_\parallel = \vec{V} \cdot \hat{b}$ ($\hat{b} = \vec{B}/B$). In both these models both populations are moving relative to the proper frame, which is moving at velocity $\vec{V}$ relative to the satellite frame. Furthermore, in order

to satisfy the zero current condition, the following relation should hold

$$n_c \Delta \vec{V}_c + n_H \Delta \vec{V}_H = 0 \tag{4.6}$$

where n_c, n_H are, respectively, the number densities of the core, halo electrons and

$$\Delta \vec{V}_c = \vec{V}_c - \vec{V} \tag{4.7}$$

$$\Delta \vec{V}_H = \vec{V}_H - \vec{V} \tag{4.8}$$

are, respectively, the velocities of the core, halo populations relative to the proper frame. The relative velocities $\Delta \vec{V}_c$, $\Delta \vec{V}_H$ are both aligned along $\vec{B}$ in such a way that $\Delta \vec{V}_c$ points back toward the sun, and $\Delta \vec{V}_H$ points away from the sun. Superimposed upon the data points shown in Figure 1 is a fit by Feldman et al.,[9] using the truncated bi-Maxwellian for the halo electrons. As may be seen, this model does give a reasonable description of the data at low energies, while at higher energies (i.e., velocities greater than 10^4 km/sec), the Maxwellian fit does not follow the data points well. The authors argue that their model of two convected Maxwellians (convection model) may be characteristic of interplanetary electrons and that it may be consistent with exospheric theories [Eviatar and Schulz (1968),[79] Schulz and Eviatar (1972)[80]] of the solar wind. With this picture in mind, the break-point energy $E_{BA} \sim 60$ ev gives an approximate estimate of

the interplanetary potential Φ_I at 1 AU, the halo electrons are unbounded, collisionless, and moving away from the sun with velocities $\sim$700 km/sec relative to the plasma; while the core electrons are collision dominated, bound to the sun by the interplanetary potential, and are drifting back toward the sun relative to the plasma with velocities $\sim$-50 km/sec, in order to sustain charge neutrality within the plasma (zero current condition).

It is clear that in this model the halo electrons carry most of the heat even though they only compose 6% of the electrons in number.[9] The heat flow takes place via convection of halo electrons relative to core electrons. There is no contribution to $\vec{q}_e$ from stochastic conduction processes. From Eq. (4.1), we find from Eqs. (4.5) to (4.8) that

$$\vec{q}_e \cong (n_H \Delta \vec{V}_H) \frac{5}{2} k T_c \left(\frac{T_H}{T_c} - 1 \right) \qquad (4.9)$$

By using the previously given values for n_H, $\Delta \vec{V}_H$, T_H/T_c, along with typical core densities $n_c \approx 10$ cm^{-3} and temperatures $T_c \approx 1.2 \times 10^5$ ^oK, one gets

$$q_e \approx 9.4 \times 10^{-3} \text{ ergs/cm}^2\text{/sec}$$

about the value quoted previously.

As far as the comparison of Eq. (4.9) with our results in Chapter III, we note that Eq. (4.9) would be consistent for large r with our profiles of q if $\Delta \vec{V}_H$ and the ratio T_H/T_c are independent of r.

(4.) Scudder, Olbert Conduction Model of Interplanetary Electrons

The convection model described in the preceding section has been subjected to criticism by J.D. Scudder and S. Olbert (1977).[14] They point out that the LASL observations are not really consistent with exospheric theory of collisionless halo electrons, near isotropy of halo electrons in "convection" frame of reference. They propose that a conduction model, where collisions at least to some degree are important and there is no convection, must be first examined to see whether one obtains results similar to those of the LASL model. They claim that it is difficult to accept on physical grounds a picture of two pure Maxwellian distributions drifting relative to each other throughout the solar system. The only way that one can possibly visualize the LASL model to be valid is that these two populations have two completely different mechanisms of interaction. For example, if the core electrons interact among themselves via Coulomb collisions and the halo electrons interact via wave particle processes, both having very short mean free paths independent of each other. Until now, this has not been demonstrated.

Scudder and Olbert make suggestions as to how one may try to see the effects of stochastic processes and of gradients and forces upon the original distribution. At

the time of this writing, their approach was a semi-quantitative approach using Krook's approximation and the Chapman-Enskog Method. We give here a brief account of their findings.

(a.) Boltzmann equation in proper frame S* (S* moving with wind velocity $\vec{V}$)

In order to study the effects of collisions and the thermal gradients, etc., upon the electron distribution function f_e and the resulting energy flow in the proper frame S*, it is convenient to use the Boltzmann equation in the proper frame S*. [For reference, see Rossi and Olbert (1970)[48]]. The Boltzmann equation in the inertial frame S for arbitrary f is

$$\frac{df}{dt} = \left(\frac{\delta f}{\delta t}\right)_{coll} \tag{4.10a}$$

where

$$\frac{d}{dt} \equiv \frac{\partial}{\partial t} + \vec{v}\cdot\nabla + \frac{\vec{F}}{m}\cdot\nabla_v \tag{4.10b}$$

is the total phase space time derivative, v is the particle velocity,

$$\vec{F} = q(\vec{E} + \vec{v}\times\vec{B}) + m\vec{g} \tag{4.11}$$

is the Lorentz force plus gravitational force on a charged particle with charge q and mass m. In order to transform Eq. (4.10) into the proper frame, we may use the fact that f is invariant under the Lorentz transformation, i.e.,

$$f(t,\vec{r},\vec{v}) = f^*(t,\vec{r},\vec{w}) \tag{4.12}$$

where f* is the distribution function in the proper frame, and

$$\vec{w} = \vec{v} - \vec{V}(\vec{r},t) \tag{4.13}$$

is the particle velocity in the proper frame. Using Eqs. (4.12) and (4.13), one can readily show that

$$\frac{\partial f}{\partial t} = \frac{\partial f^*}{\partial t} - \frac{\partial V_i}{\partial t}\frac{\partial f^*}{\partial w_i} \tag{4.14a}$$

$$\frac{\partial f}{\partial x_i} = \frac{\partial f^*}{\partial x_i} - \frac{\partial V_j}{\partial x_i}\frac{\partial f^*}{\partial w_j} \tag{4.14b}$$

$$\frac{\partial f}{\partial v_i} = \frac{\partial f^*}{\partial w_i} \tag{4.14c}$$

Furthermore, since the collision term is invariant with respect to the transformation given by Eq. (4.12), we have

$$\left(\frac{\delta f}{\delta t}\right)_{coll} = \left(\frac{\delta f^*}{\delta t}\right)_{coll} \tag{4.15}$$

Then by using the non-relativistic transformation for $\vec{E}$ and $\vec{B}$, i.e.,

$$\vec{E}^* = \vec{E} + \vec{V} \times \vec{B} \tag{4.16a}$$

$$\vec{B}^* = \vec{B} \tag{4.16b}$$

along with Eqs. (4.14), (4.15), and (4.16), we get the following expression for Boltzmann's equation in the proper frame S*:

$$\frac{d^*}{dt} f^* = \left(\frac{\delta f^*}{\delta t}\right)_{coll} \tag{4.17a}$$

where

$$\frac{d^*}{dt} \equiv \frac{\partial}{\partial t} + \vec{V}\cdot\nabla + \vec{w}\cdot\nabla + \vec{a}^*\cdot\nabla_w \tag{4.17b}$$

If we introduce the following notation for the total time derivative in coordinate space

$$\frac{D}{Dt} \equiv \frac{\partial}{\partial t} + \vec{V}\cdot\nabla \tag{4.17c}$$

then the acceleration $\vec{a}^*$ has the following form

$$\vec{a}^* \equiv \frac{q\vec{E}^*}{m} + \frac{q}{m}(\vec{w}\times\vec{B}) + \vec{g} - \frac{D}{Dt}\vec{V} - (\vec{w}\cdot\nabla)\vec{V} \tag{4.17d}$$

The acceleration $\vec{a}^*$ contains all the external forces imposed upon the charged particles in the proper frame due to electric, magnetic, and gravitational fields, along with the inertial forces of the charged particles in the proper frame. The last term in Eq. (4.17d) contains the "viscous" forces of the plasma upon the particle.

(b.) Krook's anzatz

By using Krook's approximation, one avoids the tremendous complications introduced by more realistic expressions of the collision term (i.e., $(\partial f^*/\partial t)_{coll}$). In general, the collision term will be a function of all the distribution functions representing the different species in the plasma and terms describing the wave-particle interaction, so that one ends up with a series of coupled, inhomogeneous, non-linear integro-differential equations for f_1^*. In addition, the form of the wave-particle interaction term is generally not well-known.

Therefore, in order to study qualitatively the collisional effects upon f* under the influence of various gradients and forces in the plasma, Krook's approximation for the collision term is used, i.e.,

$$\left(\frac{\delta f^*}{\delta t}\right)_{coll} \cong -\frac{f^* - f_o^*}{\tau} \tag{4.18}$$

where τ is some phenomenological collision time yet to be given. The distribution function f* may be represented by:

$$f^* = f_o^* + f_1^* \tag{4.19}$$

where f_o^* is some known distribution function at some reference location $\vec{r}_o$, t_o and f_1^* is a correction term to f* resulting from the propagation of electrons through the gradients of the plasma and collisions. By substituting Eq. (4.19) into Eq. (4.18), which is then substituted into Eq. (4.17), we get

$$\frac{d^*}{dt} f_1^* + \frac{f_1^*}{\tau} = -\frac{d^*}{dt} f_o^* \tag{4.20}$$

It is interesting to note that this equation has a form similar to the radiative transfer equation, where $1/\tau$ would be the opacity and the term on the r.h.s. of the equation is the source term.

For conditions characteristic of the interplanetary medium, the gyro-frequency Ω of the various species will in general be many times larger than their corresponding collision frequencies ν_c, i.e.,

$$\frac{\nu_c}{\Omega} << 1 \tag{4.21}$$

Because of this, especially in the case of electrons, the charged particles will undergo many gyrations between collision. Therefore, they will in general have distributions which are gyrotropic with respect to the magnetic field. This allows us to make the following average of Eq. (4.20), where we take advantage of the fact that the particles undergo many gyrations between collisions

$$\overline{f^*} = \lim_{n\to\infty} \frac{1}{2n\pi} \int_0^{2\pi n} f^* \, d\phi^* \tag{4.22}$$

where

$$\vec{w} = \begin{cases} w_\perp \cos\phi^* \\ w_\perp \sin\phi^* \\ w_{\parallel} \end{cases} = w \begin{cases} \sin\theta^* \cos\phi^* \\ \sin\theta^* \sin\phi^* \\ \cos\theta^* \end{cases} \tag{4.23}$$

$w_{\parallel}$, $w_\perp$ are the components of $\vec{w}$, respectively, parallel and perpendicular to $\vec{B}$, θ^* is the polar angle of the velocity vector $\vec{w}$ relative to $\vec{B}$, and ϕ^* is the azimuthal angle of $\vec{w}$ around $\vec{B}$ (see Figure 11). The second term on the r.h.s. of Eq. (4.17d) may be written the following way by using (4.23) for $\vec{w}$ and the relation $\Omega = qB/m$

$$\frac{q}{m} (\vec{w} \times \vec{B}) \cdot \nabla_w f^* \equiv \Omega \frac{\partial f^*}{\partial \phi^*} \tag{4.24}$$

Then since

$$\frac{\partial f_o^*}{\partial \phi^*} = 0 \tag{4.25}$$

this term drops out. Furthermore, we have for $\overline{f^*}$, the following

$$\overline{f^*} = f_o^* + \overline{f_1^*} \tag{4.26}$$

if $f_o^* = \overline{f}_o^*$ is assumed to be initially gyrotropic.

In the Chapman-Enskog approximation, the correction term f_1^* is assumed to be a small perturbation of f_o^*, i.e.,

$$\overline{f_1^*} \ll f_o^* \tag{4.27}$$

Then by considering any gradients or time derivatives of any macroscopic parameter M to be first order small, i.e.,

$$|\lambda \nabla M| \ll 1 \tag{4.28a}$$

$$|\tau \frac{d}{dt} M| \ll 1 \tag{4.28b}$$

where λ is the m.f.p. for any stochastic process, so that any gradient or time derivatives of $\overline{f}_1^*$, which is first-order small, will be second-order small, while the corresponding gradients of f_o^* are first-order small. Furthermore, any product of $\overline{f}_1^*$ with gradients or time derivatives of any macroscopic parameter M will also be second-order small.

From this, one can show that

$$\overline{\frac{d^* f_1^*}{dt}} \ll \overline{\frac{d^*}{dt} f_o^*} \tag{4.29}$$

provided that the electric field in the proper frame along $\vec{B}$ is first-order small.

Assuming that Eq. (4.29) holds, one finds for an isotropic f_o^* in a steady state ($\frac{\partial}{\partial t} = 0$)

$$\overline{f_1^*} = -\tau \left[\vec{V} \cdot \nabla + \omega \cos\theta^* \nabla_{\parallel} + A_{\parallel} \cos\theta^* \frac{\partial}{\partial \omega} - \omega S \frac{\partial}{\partial \omega} \right] f_o^* \tag{4.30}$$

where

$$A_{\parallel} = \left(\frac{q\vec{E}^*}{m} + \vec{g} - \frac{D\vec{V}}{Dt} \right)_{\parallel} \tag{4.31}$$

$$\mathcal{S} = \frac{1}{2\omega^2}\, w_i \frac{\partial V_i}{\partial x_j}\, w_j \tag{4.32}$$

is the time averaged "viscosity" term, using the notation

$$\nu \equiv b_i \frac{\partial V_i}{\partial x_j} b_j \tag{4.33}$$

and introducing the Legendre polynomials of order one and two,

$$P_1 = \cos\theta^* \tag{4.34a}$$

$$P_2 = \tfrac{1}{2}(3\cos^2\theta^* - 1) \tag{4.34b}$$

one obtains after some algebra

$$\mathcal{S} = \tfrac{1}{3}\, div\vec{V} + P_2\left(\nu - \tfrac{1}{3}\, div\vec{V}\right) \tag{4.35}$$

One should note from Eq. (4.30), that if Eq. (4.28) is violated, $\overline{f}_1^*$ will no longer be first-order small.

We may now rewrite Eq. (4.30) for $\overline{f}_1^*$ in a more useful form

$$\overline{f_1^*} \cong -\tau\left[\Omega_0 + P_1\Omega_1 + P_2\Omega_2\right] f_0^* \tag{4.36}$$

where

$$\Omega_0 = \vec{V}\cdot\nabla + \tfrac{1}{3}\frac{D}{Dt}\ln\rho\; w\frac{\partial}{\partial w} \tag{4.37}$$

$$\Omega_1 = w\nabla_{\parallel} + A_{\parallel}\frac{\partial}{\partial w} \tag{4.38}$$

$$\Omega_2 = -\left(\nu + \tfrac{1}{3}\frac{D}{Dt}\ln\rho\right) w\frac{\partial}{\partial w} \tag{4.39}$$

where we made use of the continuity equation, viz,

$$div\vec{V} = -\frac{D}{Dt}\ln\rho \tag{4.40}$$

One of the nice features of Eq. (4.36) is that it is readily apparent which terms contribute to the different velocity moments of $\overline{f^*}$. For example, the first and third terms contribute to the even moments of $\overline{f^*}$, while the second term contributes to the odd moments of $\overline{f^*}$; in particular, the heat flow vector is given by the second term. In the case where MHD is valid, one can further show that Eq. (4.33) for ν reduces to [48]

$$\nu \cong \frac{D}{Dt}\left(\ln \frac{B}{\rho}\right) \tag{4.41}$$

Therefore, Ω_2 reduces to [see Eq. (4.39)]

$$\Omega_2 \cong -\frac{D}{Dt}\left(\ln \frac{B}{\rho^{2/3}}\right) w \frac{\partial}{\partial w} \tag{4.42}$$

(c.) An example of f_o^*

In the case of a collision dominated gas ($\lambda << H$), the form for f_o^* is known to be an isotropic Maxwellian f_M. For conditions characteristic of the interplanetary medium, which in general is not collision dominated, one is unable to predict a priori the form of f_o^*. Thus, the only alternative is either to guess at its form from qualitative physical arguments or from observations.

As an example, we will use the kappa distribution f_κ proposed by J.D. Scudder and S. Olbert (1977),[14] which at times seems to give a reasonable empirical description of

f_o^* for interplanetary electrons [Ogilvie et al. (1977)[81]]. Detailed descriptions of f_κ are given in Chapter I and Appendix A.

For convenience, we display it again here

$$f_o^* = f_\kappa = \frac{n C_\kappa}{\pi^{3/2} w_c^3} \frac{1}{\left(1 + \frac{w^2}{\kappa w_c^2}\right)^{\kappa+1}} \tag{4.43a}$$

where

$$C_\kappa \equiv \frac{\Gamma(\kappa+1)}{\Gamma(\kappa-\frac{1}{2})\kappa^{3/2}} \tag{4.43b}$$

$$kT_c = \tfrac{1}{2} m w_c^2 \tag{4.43c}$$

κ is the kappa parameter, Γ (z) is the gamma function, w_c is the most probable thermal speed, n is the number density, and T_c is the "core" temperature. Substituting Eq. (4.43) into Eq. (4.36), we get the following expression for $\bar{f}_1^*$:

$$\bar{f}_1^* = f_\kappa (P_{even} + P_{odd}) \tau \tag{4.44a}$$

where

$$P_{even} = -\frac{D}{Dt} \ln\left(\frac{n C_\kappa}{w_c^3}\right) + \frac{D}{Dt} \kappa \ln\left(1 + \frac{w^2}{\kappa w_c^2}\right) \tag{4.44b}$$
$$+ \eta u^2 \left[-\frac{D}{Dt}(\ln \kappa w_c^2) - 2\nu + (3\nu + \frac{D}{Dt}\ln\rho)\sin^2\theta^\alpha\right]$$

$$P_{odd} = w \cos\theta^* \left[-\nabla_{11} \ln\left(\frac{n C_\kappa}{w_c^3}\right) + \nabla_{11} \kappa \ln(1 + u^2/\kappa)\right. \tag{4.44c}$$
$$\left. + \eta u^2 \left[-\nabla_{11} \ln(\kappa w_c^2) + 2A_{11}/w^2\right]\right]$$

$$u^2 \equiv w^2/w_c^2 \tag{4.44d}$$

$$\eta \equiv \frac{\kappa+1}{\kappa} \frac{1}{1 + u^2/\kappa} \tag{4.44e}$$

Then by using the notation

$$\alpha_G \equiv r \frac{d}{dr} \ln G \tag{4.45}$$

where G = n, T_c, κ, and B, and

$$\vec{V} \cdot \nabla = V_r \frac{d}{dr} \tag{4.46}$$

$$\nabla_{\parallel} = \cos\chi \frac{d}{dr} \tag{4.47}$$

where χ is the garden hose angle, we get the more useful expressions for computational purposes for Eqs. (4.44b) and (4.44c),

$$P_{even} = \left(\frac{V_r}{r}\right)\left\{\frac{3}{2}\alpha_{T_c} - \alpha_n - [h(x) - x \ln(1+u^2/x)]\alpha_x \right. \tag{4.48a}$$
$$\left. - \eta u^2 [\alpha_{T_c} + \alpha_x + 2\nu - (3\nu + \alpha_n)\sin^2\theta^*]\right\}$$

$$P_{odd} = \frac{w\cos\theta^*}{r}\left\{\frac{3}{2}\alpha_{T_c} - \alpha_n - [h(x) - x \ln(1+u^2/x)]\alpha_x \right.$$
$$\left. - \eta u^2 [\alpha_{T_c} + \alpha_x + \frac{2A_r}{w^2}]\right\}\cos\chi \tag{4.48b}$$

where
$$h(x) = 2x\beta(2x-1) - 1/2 \tag{4.48c}$$

is positive definite for all $x > 2$, $\lim_{x\to\infty} h(x) = 0$, and no larger than ~ 0.25,

$$\beta(z) = \frac{1}{2}\left(\psi\left(\frac{z+1}{2}\right) - \psi\left(\frac{z}{2}\right)\right) \tag{4.48d}$$

is the beta function,

$$\psi(z) = \frac{d}{dz}\ln\Gamma(z) \tag{4.48e}$$

is the Psi-function, and

$$A_r = \vec{A} \cdot \hat{r} \tag{4.48f}$$

Let us discuss the values of the individual coefficients α_{T_c}, α_n, etc. For instance, in the case of a free expansion, the density will drop with a $1/r^2$ dependence so that $\alpha_n = -2$, while the temperature decreases adiabatically,

$\alpha_{T_c} = -4/3$. The coefficient $\alpha_\varkappa$ results from the fact that $\varkappa$ should be a function of distance away from the sun. Referring to Eq. (4.41) for the scalar quantity ν, one can see that under normal interplanetary conditions, $\nu \cong +1/2$ (i.e., $B \propto 1/r^{3/2}$, and $\rho \propto 1/r^2$). Note: if there were no spiral field, $B \propto 1/r^2$, the scalar quantity $\nu \cong 0$. The coefficient of the last term of Eq. (4.48a)

$$(3\nu + \alpha_n) \tag{4.49}$$

under normal conditions is negative, causing the electrons to be hotter along the $\vec{B}$ field while cooler perpendicular to it (i.e., $T_{\parallel}/T_{\perp} > 1$). But for certain conditions this term may be positive, so that $T_{\parallel}/T_{\perp} < 1$. For example, one can see that for regions where the density increases with r, $\alpha_n > 0$; while the magnetic field becomes compressed (increases with r), Eq. (4.49) may become greater than zero. Such regions may occur behind the leading edges of high speed streams.

The polynomial P_{odd}, which gives rise to the heat flow, is proportional to $w_{\parallel}$. The term proportional to A_r or equivalently to E_r^* tends to make the currents in the plasma small, i.e., quasi-neutrality condition. The term proportional to $w^3 \cos\theta^*$

$$-\eta u^2 w \cos\theta^* (\alpha_{T_c} + \alpha_n) \tag{4.50}$$

because of its strong velocity dependence relative to the other terms, contributes to most of the heat flow q

[see Eq. (4.1) for definition of $\vec{q}$]. Furthermore, these terms do not tend to cancel each other under normal expansion conditions (i.e., temperature and density decrease with r). By imposing the zero current condition [see Eq. (4.63) for definition of $j_{\parallel}$ *], where the current is mainly due to electrons, one finds $E_r^* > 0$. Because of this, the low energy portion of f_e^* will appear to be drifting back toward the sun, as in the convection model by Feldman et al.[9] The P_{even} term, which produces anisotropies in the pressure can be shown to be small relative to P_{odd} for electrons. For example, by noting that the leading factor outside the braces for P_{even} is proportional to the wind velocity V_r, while for P_{odd} the leading factor is proportional to w, one can see that since electrons are subsonic $(V_r/w_c) \ll 1$, $P_{even} \ll P_{odd}$. Furthermore, since the collision time $\tau \sim \lambda/w_c$, it follows that $P_{even} \sim \left(\frac{V_r}{\omega_c}\right)\left(\frac{\lambda}{r}\right)$ [see Eq. (4.44a)]. Then, if $(\lambda/r) \sim 1/10$ at 1 AU when considering both Coulomb collision and wave-particle interactions [see Fig. 43, Curve #2 from Chapter III which shows $(\bar{\lambda}_{coul}/r) \approx 1/5$ at 1 AU], P_{even} only introduces corrections $\sim 2\%$ to f_o^* for $V_r/w_c \sim 0.2$. Thus, one would expect the core electrons to be nearly isotropic in the proper frame, which is consistent with observations.[9] Finally, as previously noted concerning Eq. (4.49), because of the angular dependence displayed in

Eq. (4.48a) for P_{even}, the temperature is greater along $\vec{B}$ for normal interplanetary conditions.

It should be emphasized that this model does not represent a specific theory, but rather it is a tool which has close connections with theory. As a model it is incomplete, i.e., some empirical input is needed for completeness. As previously noted, it is not possible to predict f_o^* from theory; it must be determined from observations. Thus, f_o^* is one of the empirical inputs required by this model. In the case of electrons, where transport effects are expected to be small perpendicular to $\vec{B}$ ($\overline{f_e}^*$ nearly isotropic), it should be possible to determine f_o^* from measurements made in this direction (see Figure 1). Another empirical input is the collision time τ. As in the case for f_o^*, one must make a guess at its form.

An example for τ in the case of electrons will now be given. To begin with, one can write the following parameterization for the collision frequency due to Coulomb collisions

$$\nu_{COUL} = \overline{\nu}_{COUL} / w^3 \tag{4.51}$$

where

$$\overline{\nu}_{COUL} = \frac{6}{5}\sqrt{\frac{3}{\pi}}\,(1+\sqrt{2})\,\nu_{ep} \tag{4.52}$$

is the characteristic Coulomb collision frequency for the isotropization of electrons,[48] where

$$\nu_{ep} = 4\pi r_e^2 c \left(\frac{m_e c^2}{3kT_e}\right) n \ln\Lambda \qquad (4.53)$$

is the characteristic collision frequency for electron-proton collisions.

In the interplanetary medium, not only are there Coulomb collisions, but also wave-particle interactions due to collective phenomena. In order to take into account wave-particle interactions, the following expression for the collision frequency due to waves is introduced

$$\nu_w \equiv \frac{|\vec{w}|}{\lambda_w} = \frac{w_c}{\lambda_w} u \qquad (4.54)$$

where λ_w is the m.f.p. for wave-particle interactions. For simplicity, we assume λ_w is independent of $\vec{w}$; generalizations of this model can easily be taken into account by allowing for a velocity dependence in λ_w. Introducing the Coulomb m.f.p.

$$\bar{\lambda}_{coul} \equiv \frac{w_c}{\bar{\nu}_{coul}} \qquad (4.55)$$

and the definition for τ

$$\frac{1}{\tau} = \sum_i \frac{1}{\tau_i} \qquad (4.56)$$

where τ_i is the collision time for a particular type of interaction, we get the following for τ :

$$w_c \tau = \frac{\lambda_w u^3}{u^4 + \lambda_w / \bar{\lambda}_{coul}} \qquad (4.57)$$

Some interesting features of Eq. (4.57) are: 1) for velocities small compared to a thermal speed, $u << 1$,

Eq. (4.57) reduces to

$$\tau \cong \frac{\bar{\lambda}_{coul}}{w_c} u^3 \qquad (4.58)$$

the collision time for Coulomb collisions (note strong velocity dependences); 2) for velocities large compared to a thermal speed, $u >> 1$, Eq. (4.57) reduces to

$$\tau \cong \frac{\lambda_w}{w_c} \frac{1}{u} \qquad (4.59)$$

which has the property of approaching zero for large energies (i.e., electron run away does not occur).

Using this model for τ in conjunction with the empirically determined model for f_o^* and fitting the f^* given by Eqs. (4.26) and (4.36) to the data, one can in principle determine such parameters as λ_w, $\bar{\lambda}_{coul}$, etc. In addition, one may refer to the profiles determined in Chapter III and use them to perform a more global test of the model. These profiles give us an estimate of $\bar{\lambda}_{coul}$, thus allowing for a better determination of λ_w (i.e., more constraints). From this example, it should now be clear as to the usefulness of such an approach.

We will now give a numerical example showing the effects of the gradients upon $\bar{f}^*$. In Fig. 49 we have a plot (solid curves) of $\bar{f}^*$, where $f_o^* = f_{\mathcal{M}}$ and Eq. (4.57) is used for τ. The top curve corresponds to $\Theta^* = 0^o$ while the lower for $\Theta^* = 180^o$. (Note: $\vec{B}$ defined to be pointing away from the sun.) The values for the various parameters in this model were chosen to correspond to those

predicted by our radial profiles and observations at 1 AU ($\alpha_{T_c} = -1$, $\alpha_n = -2$, $\alpha_\varkappa$ arbitrarily set equal to zero, $\alpha_r = 2A_r/w_c^2 = 16/5$ [see Eq. (4.66)], $\nu = +\frac{1}{2}$, $\varkappa = 45^o$, $\mathcal{K} = 6.0$, $V_r = 400$ km/sec, $w_c = 1900$ km/sec, and $(\lambda/r) = 1/5$). The dashed curves correspond to the convection model by Feldman et al., where typical values of the parameters found at 1 AU and the simpler model of a convected bi-Maxwellian for the halo electrons were used. It should be emphasized that both these curves do not correspond to actual fits to real data. We would like to say that the data shown in Fig. 1, if plotted in the proper frame, follows a path similar to one intermediate between the solid and dashed curves. As may be seen, for both models we have the "core" electrons drifting back toward the sun, while the "halo" or suprathermal component appears to be moving away from the sun along $\vec{B}$. This last effect for the conduction model is due to a non-zero third moment in $\bar{f}^*$ and not due to a relative convection; it gives rise to similar values of the heat flow determined by the convection model. Because of this similarity (in doing an actual fit, they do not differ so markedly as that shown in Fig. 49), one is hard put to distinguish between the two models. Furthermore, since both models have similar angular dependences, i.e., see Eqs. (4.9) and (4.36) , this task should be even more difficult.

(d.) Estimates of the heat flow vector $\vec{q}_{\parallel}$ based on the Scudder, Olbert model

As in section 4.3, the kappa distribution f_κ is used for f_o^*, while the collision time τ is given by Eq. (4.57). Furthermore, the approximate form given by Eq. (4.41) has been substituted into Eq. (4.48a) for ν. Going one step further, the assumption that the parameter

$$b \equiv \frac{\lambda_w}{\lambda_{coul}\kappa^2} = 0 \tag{4.60}$$

was made (i.e., $\lambda_{coul} \to \infty$).

Introducing the constraint of particle conservation, viz,

$$\int f_{e_1}^* d^3w = 0 \tag{4.61}$$

we find the following relation for α_{Tc} and α_κ via Eqs. (4.44) and (4.61) for $\alpha_n = -2$:

$$\alpha_{Tc} = -\frac{4}{3} + 2\alpha_\kappa h(\kappa) \tag{4.62}$$

where $h(\kappa)$ is given by Eq. (4.48c). Eq. (4.62) for α_{Tc} says that the electrons will cool adiabatically (i.e., $\alpha_{Tc} = -4/3$) for $\kappa \to \infty$ or $\alpha_\kappa = 0$. For finite κ (e.g., $\kappa \sim 6$), $\alpha_{Tc} > -4/3$, the temperature drop is less than that for adiabatic cooling when $\alpha_\kappa > 0$ (i.e., electrons becoming collision dominated), while for $\alpha_\kappa < 0$ (i.e., electrons becoming accelerated up to higher energies), the contrary is true, $\alpha_{Tc} < -4/3$. Secondly, we imposed

the zero current condition

$$f_{\parallel}^{*} = -e \int \overline{f_{e_1}^{*}}\, w_{\parallel}\, d^3w \tag{4.63}$$

giving us the following for $\alpha_n = -2$ and α_{Tc} given by (4.62):

$$\alpha_r = \frac{\varkappa}{\varkappa-1}\left\{\frac{8}{3} + \alpha_\varkappa g(\varkappa)\right\}\cos\chi \tag{4.64}$$

where

$$g(\varkappa) \equiv \frac{\varkappa}{\varkappa-1} - 4\varkappa B(2\varkappa-1) \tag{4.65}$$

is positive definite for all $\varkappa > 2$, has the limit

$$\lim_{\varkappa\to\infty} g(\varkappa) = 0$$

and is no larger than $\sim$ 0.5, and

$$\alpha_r = \frac{e E_r^{*}}{k T_c}\, r \tag{4.66}$$

is the interplanetary potential in units of kT_c which results from our constraint that the current be zero. From (4.64), the electric field is enhanced for $\alpha_\varkappa > 0$. Setting $\alpha_\varkappa = 0$, we get

$$\alpha_r = \frac{8}{3}\,\frac{\varkappa}{\varkappa-1} \tag{4.67}$$

which gives us a potential $\sim$ 40 ev for $\varkappa = 4$ and $kT_c \approx 13$ ev.

The expression for the heat flow vector $q_{e_\parallel}$ is [see Eq. (4.1)]

$$q_{e_\parallel} = \tfrac{1}{2} m_e \int \overline{f_{e_1}^{*}}\, w^2 w_{\parallel}\, d^3w \tag{4.68}$$

which after performing the integrations, setting $\alpha_n = -2$, and Eqs. (4.62), (4.64) for, respectively, α_{Tc}, α_r, we get the following

$$q_{e_{\parallel}} = \frac{2}{3} n_e m_e w_c^3 \frac{\kappa^{3/2}}{\sqrt{\pi}} \frac{\Gamma(\kappa-2)}{\Gamma(\kappa-1/2)} \left(\frac{\lambda_w}{r}\right)\left(\frac{4}{3}\left(\frac{\kappa+1}{\kappa-1}\right) + \alpha_\kappa G(\kappa)\right)\cos\chi \quad (4.69)$$

where

$$G(\kappa) = \frac{\kappa}{\kappa-1}\left\{\frac{2\kappa-3}{(\kappa-1)(\kappa-2)} - h(\kappa)\right\}$$

is positive definite for $\kappa > 2$ and diverges for $\kappa = 2$, and has the limit

$$\lim_{\kappa\to\infty} G(\kappa) = 0$$

Thus, for $\kappa \to \infty$ (i.e., for a single Maxwellian), we get

$$q_{e_{\parallel}} = \frac{8}{9} \frac{n_e m_e w_c^3}{\sqrt{\pi}} \left(\frac{\lambda_w}{r}\right)\cos\chi > 0 \quad (4.70)$$

If we substitute $n_e = 10\ cm^{-3}$, and $w_c = 1900$ km/sec, ($T_c \approx 1.25 \times 10^5\ ^oK$) into Eq. (4.70), we get

$$q_{e_{\parallel}} = 3.12 \times 10^{-2} \left(\frac{\lambda_w}{r}\right)\cos\chi \quad (4.71)$$

while for $\kappa = 4$ and using the same parameters, we get from Eq. (4.69)

$$q_{e_{\parallel}} = 12.6 \times 10^{-2} \left(\frac{\lambda_w}{r}\right)\cos\chi \quad (4.72)$$

and by setting $(\lambda_w/r)\cos\chi = 0.1$, (4.71) and (4.72) reduce to, respectively,

$$q_{e_{\parallel}} = 3.12 \times 10^{-3}\ ergs/cm^2/sec \quad (4.73)$$

and

$$q_{e_{\parallel}} = 12.6 \times 10^{-3}\ ergs/cm^2/sec \quad (4.74)$$

which are about the values typically observed in the interplanetary medium. [3,5,9]

CHAPTER V

ANALYSIS OF M.I.T. IMP 8 DATA

(1.) Introductory Remarks--Constraints on our Data Analysis

The main objective of this chapter is to demonstrate how the formal results obtained in Chapters I and II may be applied to the electron measurements by the M.I.T. detector onboard the Imp 8 spacecraft. Ideally, the end product of our effort should be the determination of the detailed shape of the electron distribution function for a given period and location in space. The knowledge of this function would then allow us to compute a variety of macroscopic averages characterizing the interplanetary electron gas. Among those macroscopic parameters, the following are of primary interest: (1) the electron number density, n_e, (2) the mean streaming velocity of electrons, $\vec{V}_e$, (3) the scalar electron temperature, T_e, (4) the thermal anisotropy ratio, $T_{\parallel e}/T_{\perp e}$, and (5) the heat flow vector, $\vec{q}_e$. Unfortunately, there are a number of practical considerations that reduce the scope of such a comprehensive list. The operational limitations of the M.I.T. electron detector, especially the narrowness of the dynamic range, render any reliable determination of some of the above quantities nearly impossible. As it will become clear from the forthcoming discussion of the

data samples, any attempt to determine quantitatively $\vec{q}_e$ and $T_{\parallel e}/T_{\perp e}$ would be about futile. On the other hand, the determination of n_e, $\vec{V}_e$ and T_e should be possible at least in principle. The precision with which one can measure these quantities should vary widely from case to case. Since n_e can be ascertained from the measurements of the proton densities by the M.I.T. positive-ion detector on Imp 8, and, since $\vec{V}_e$ may be expected to be close or equal to the proton mean velocity $\vec{V}_p$, it is obvious that the most desirable quantity to be determined is the electron temperature, T_e. We shall demonstrate in the next section that T_e can, indeed, be measured quite accurately, inspite of the aforementioned limitations of the detector. In contrast, the accuracy of directly obtained values of n_e and $\vec{V}_e$ cannot be expected to be high. For this reason, we decided to adopt the following procedure: we make use of the available proton density and the proton mean velocity (the wind velocity) for each observational sample and thus treat n_e and V_e as given quantities putting

$$n_e = 1.1\, n_p \tag{5.1}$$

and

$$V_e \approx V_p \tag{5.2}$$

The factor 1.1 represents the correction due to the presence of α-particles (5% seems to be a reasonable

average abundance of α-particles by number, relative to protons). Equation (5.1) states simply the neutrality condition of ambient plasma, after appropriate corrections for a possible spacecraft charging were made. It represents a very severe constraint on the fitting procedures in electron data analysis. Equation (5.2) is an assumption, supported by strong physical arguments, and is verifiable a posteriori. The importance of the constraint given by Eq. (5.1), other than for the fact that we reduce the number of unknowns, can be seen by considering the following facts: First, the proton number density can be determined by the M.I.T. detector with an absolute accuracy $\sim$20%, while relative uncertainties between electron and proton current measurements should be less. Secondly, ion measurements are not hampered by spacecraft charging effects as are electron measurements. As shown in Chapter II, because of spacecraft charging, the normalization and temperature will acquire errors $\sim$ 20%, since one does not a priori know the potential Φ_o of the spacecraft. Thirdly, the total distribution of the ions are available for analysis, while for electrons only a portion of the distribution is sampled (bulk of f_e is available only at energies less than 20 ev).

In order to reduce the possibility of contamination of the data from bow shock related phenomena we have

confined our analysis to observations made on the dawn side of the solar wind, along with the constraint that the magnetic field does not connect to the earth's bow shock (i.e., $\phi_B \sim 135^o$ or 315^o).

Our final constraint is due to the unfortunate presence of noise $\sim$5 picoamp (1 picoamp = 10^{-12}amp) in the data for reasons that are not as yet understood. This noise confines our analysis to high density, low speed streams, where the electron currents are sufficiently above the 5 picoamp level for the first few energy channels in all eight angular sectors.

(2.) Examples of M.I.T. Imp 8 Electron Data

Due to the lack of dynamical range of the detector, we are forced to consider only the lowest energy channels. In this energy regime (i.e., energy channels 1 to 4), where transport effects are probably small, the electrons (core electrons) are expected to be Maxwellian. Because of this, we make the initial assumption to be verified by the data, that the electrons are Maxwellian in the proper frame of the plasma.

Before showing some samples of data, we should like to introduce the following quantity, which we found to be more useful in the analysis than the currents ΔI:

$$F \equiv \frac{\Delta I}{I_o \bar{R}(o)} \tag{5.3}$$

where $\bar{R}(o)$ is the mean response function of the detector defined by Eq. (1.22), evaluated at $\xi = v_x/\bar{v}_z = 0$, and I_o is the I_o defined in Eq. (1.27). Since we are assuming the core electrons to be Maxwellian, we will use Eq. (1.28) of Chapter I for the current ΔI. For simplicity we have dropped the second term in Eq. (1.28) for ΔI and set $\alpha_1^2 = 1.0$. The resulting expression, which gives the currents in a given channel to within 10% for $w_c \sim$ 1800 km/sec, is the following:

$$\Delta I = I_o \bar{R}(o) F_\infty \tag{5.4a}$$

where

$$F_\infty = \frac{U_o^3 e^{-U^2}}{\sqrt{1 + U_o^2}} \tag{5.4b}$$

Figures 50 and 51 show the plots of F versus the normal velocity $\overline{v}_z$ for two different spectra labeled, respectively, spectrum # 1 and spectrum # 2. Along the abscissa the circled numbers are the numbers of the first eight energy channels. The numerals on the graph symbolize the data points of the corresponding angular sector identified in Figure 2. The lines drawn through the data are not a fit but are shown only for the purpose of aiding the eye in following the data points. Figures 52 and 53 are identical plots of the data shown, respectively, in Figures 50 and 51, except now the curves shown are fits to the data where a Maxwellian was used for f_e. The two spectra were taken about two hours apart. For these spectra no significant time variations (less than 5%) in the data occurred for time periods less than 10 minutes (i.e., 5 TMS spectra). As may be seen, angular sectors 2 and 3 display an energy dependence characteristic of a Maxwellian, while for angular sector 8, which is aligned along B toward the sun, shows a non-Maxwellian tail at higher energies. This rise in f_e is probably due to the skewness in f_e, which contributes to the heat flow vector q_e. Angular sectors 2 and 3 do not display the presence of suprathermal electrons. The horizontal dashed line shown in Figures 50 to 53 represents the 5 picoamp level. Data points below this line may be subject to large

errors (on the order of a factor of two) due to the pickup problem mentioned. Thus, if suprathermal electrons were present we would not be able to see them. Because of this fact, we cannot measure q_e using this data, since we must have the suprathermal electrons in order to determine by how much f_e deviates from isotropy.

Figures 54 and 55 exhibit angular plots of F for spectra # 1 and # 2 shown in the previous figures. The numbers at the bottom of the figures correspond to the angular sectors indicated in Fig. 2, while the symbols used for the data points are the numbers of the energy channels for those data points. The arrow near the top center of the figure gives the direction of the wind velocity vector in the spacecraft frame. The vertical dashed lines indicate directions parallel and anti-parallel to the magnetic field. The horizontal dashed line indicates the 5 picoamp level. The wind velocities for these spectra are $\sim$ 340 km/sec, while the densities are $\sim$ 20 and 40 cm^{-3}, respectively. The solid curves were generated from Eq. (5.4b) for F with w_c = 1825 km/sec ($T_c = 1.1 \times 10^5$ ^oK) for Fig. 54 and w_c = 1840 km/sec ($T_c = 1.12 \times 10^5$ ^oK) for Fig. 55. As may be seen, the theoretical curves follow the data points quite well for energy channels 1 to 4 for spectra # 1 and energy channels 1 to 3 for spectra # 2. The problem at higher energies results from the noise problem and should thus be ignored.

The poor fit for angular sectors 7 and 8, which are aligned along the magnetic field direction and pointing toward the sun, results from transport effects along B. In both of these fits the spacecraft potential Φ_o was set equal to zero. Using the simple energy shift correction given by Eq. (2.34), we found no significant changes in the fit when the potential Φ_o was set equal to 1 volt. But when the potential was set equal to 2 volts, a significant change did result, in such a way that the fit became worse. Thus, it seems from this sample of data, where the currents are significantly above the noise, that the spacecraft potential on Imp 8 is less than 2 volts.

We should like to emphasize the fact that once n_e and $\vec{V}$ are given one can determine w_c from any data point from energy channel 1, where the currents are relatively large $\sim 10^{-10}$ amp, and transport effects are small. Then using this value of w_c, one can produce curves similar to those shown in Figures 54 and 55 with the help of Eq. (5.4b). We feel that we can say with confidence that the core electrons are Maxwellian and moving at the same velocity $\vec{V}$ as the protons. The above results also show that the instrument is operating properly within the uncertainties discussed above.

The data shown in the previous figures are not typical of the solar wind. They were shown because they contain an unusually high number of data points well above the noise.

Such fortunate circumstances occur when the plasma density is very high. Under average conditions the density is substantially lower (about a factor of 2 to 5). Fig. 56 shows an angular plot of F for a different time period where the wind velocities are higher $\sim$ 550 km/sec, and densities about 7 cm^{-3}. Note that an appreciable portion of the data is near the noise (the horizontal dashed line), thus producing the poor fit in the backward directions even for the first energy channel. Since the potential was shown to be small from the previous samples, we set the potential Φ_o = 0 volts. The curves shown in the figure correspond to a thermal speed w_c = 2000 km/sec (T_c = 1.3 x 10^5 ^oK). Except for the deviations along $\vec{B}$, where transport effects are present, the fit is good within the uncertainties mentioned above. For the largest currents in this spectrum, the uncertainties introduced by the noise are $\sim$ 10%.

Keeping in mind the conclusions reached from the previous spectra (i.e., instrument operating properly, core electrons are Maxwellian and moving at the same velocity $\vec{V}$ as the protons), this last example clearly demonstrates the fact that it is possible for us to get estimates of the temperature from electron data that on casual inspection appears to be unusable.

One sees from the angular response of the currents from the Imp 8 detector how serious the noise problem is as

far as the study of the suprathermal electrons, skewness of the distribution, and thus the determination of the heat flow is concerned. It is clear from these figures how much more information we would get if we were able to drop the noise level line by an order of magnitude. On the recently launched Voyager spacecrafts, there is an M.I.T. electron detector with a significantly lower noise level $\sim 10^{-14}$ amp (i.e., an improvement in sensitivity by a factor of 500). The date from this new detector are now being processed.

At this moment we have available only one partial preliminary sample. A quantity similar to the F defined by Eq. (5.3) for the Imp 8 detector and derived from Voyager 2 data taken at 1 AU is shown in Fig. 57. It is readily apparent from this figure that the better sensitivity of this instrument, permits us to see the suprathermal electrons, which appear at velocities greater than 4500 km/sec (58 ev). The data in Fig. 5.7 refer to one specific direction of the cup normal. The detector is mounted in such a way that its normal is pointing approximately at right angles to the sun-earth line, thus at 90^{o} with respect to the wind velocity. The angular dependence of the electron current is not available because the spacecraft does not spin. According to preliminary private communication from Goddard Space Flight Center,

the direction of the magnetic field is believed to be about 76^{o} to the normal of the cup. With this information in mind, we have attempted to fit the experimental points with an isotropic distribution. We have found that it was not possible to fit the data points by using a single kappa distribution given by Eq. (1.40). However, two non-convected Maxwellian distributions with different densities and temperatures (core, halo) were found to reproduce the data very well.

The solid curve in Fig. 57 represents these two Maxwellians, assuming that $n_c = 3.65\ cm^{-3}$, $n_H = 0.152\ cm^{-3}$, $w_c = 1650$ km/sec ($T_c = 9 \times 10^4\ ^{o}K$), $w_H = 3500$ km/sec ($T_H = 4.05 \times 10^5\ ^{o}K$) and $\Phi_o = 2$ volts. Using the relation

$$n\,T = n_c\,T_c + n_H\,T_H$$

we get a total temperature $T = 1.06 \times 10^5\ ^{o}K$. Note: the ratios for $n_H/n_c = .04$ and $T_H/T_c = 4.5$ are not the same as that typically found in the solar wind at 1 AU.

In conclusion, we can say that estimates of the core electron temperature can be acquired from the data on Imp 8 once the density and wind velocity of the protons are given. In cases where the electron currents are sufficiently high, the determination of n_e, $\vec{V}_e$, and w_c directly from the data should also be possible (see Figures 54 and 55). The core electrons were shown to be Maxwellian and moving at the same velocity as the protons. The presence of suprathermal electrons at high

energies could not be detected due to the presence of pickup of $\sim$ 5 picoamps. At present, this problem of pickup is not understood. Because we cannot see the suprathermal electrons, we are unable to determine by how much the electron distribution function deviates from fore-aft symmetry along the field lines (skewness in f_e); thus we cannot determine the heat flux vector from the data.

Preliminary results from the M.I.T. electron detector on Voyager 2 showed a significant improvement in the sensitivity over that on Imp 8.

APPENDIX A

For various models of f_e (v) evaluate the integral

$$H_\ell = \int_{-\infty}^{\infty} f_e(\xi, 0, \bar{v}_z)\, e^{-\alpha_\ell^2 \xi^2}\, d\xi \qquad (A.1)$$

where $\xi = v_x/\bar{v}_z$, and thus determine the current

$$\Delta I = 2 e A T_N \frac{D}{H} \Delta V_z \bar{V}_z^3 \sum_{\ell=1}^{2} a_\ell H_\ell \qquad (A.2)$$

(1) Bi-Maxwellian distribution function

$$f_{BM}(\vec{v}) = \frac{n_e \beta_\perp \sqrt{\beta_\parallel}}{\pi^{3/2}}\, e^{-[\beta_\perp w^2 + \Delta\beta w_\parallel^2]} \qquad (A.3)$$

where

$$\vec{w} = \vec{v} - \vec{V}$$

$$\beta_\parallel \equiv \frac{m_e}{2kT_\parallel}$$

$$\beta_\perp \equiv \frac{m_e}{2kT_\perp}$$

$$\Delta\beta \equiv \beta_\parallel - \beta_\perp$$

$w_\parallel = \vec{w} \cdot \hat{b}$, $\hat{b} = \vec{B}/B$, and $\vec{B}$ is the magnetic field vector. Refer to Figure 11 for definitions of the magnetic field vector with respect to the solar ecliptic coordinates system (SE), and the relationship between the cup coordinate system and the solar ecliptic coordinate system. From looking at Figure 11 it is straightforward to show that the rotation matrix which transforms a vector from the cup coordinate

system to the magnetic field coordinate system is the following:

$$\overleftrightarrow{R}_{C\to B} = \begin{pmatrix} -\sin\theta_B & \cos\theta_B \sin(\phi_B-\phi_c) & -\cos\theta_B\cos(\phi_B-\phi_c) \\ 0 & \cos(\phi_B-\phi_c) & \sin(\phi_B-\phi_c) \\ \cos\theta_B & \sin\theta_B \sin(\phi_B-\phi_c) & -\sin\theta_B\cos(\phi_B-\phi_c) \end{pmatrix} \quad (A.4)$$

where

$$\vec{V}_B = \overleftrightarrow{R}_{C\to B} \cdot \vec{V}$$

$$V_\perp^2 = V_{Bx}^2 + V_{By}^2$$

$$V_{11} = V_{Bz}$$

and $$\vec{V} = (V_x, 0, \bar{V}_z)$$

From (A.4) one can derive the following expression for w_{11} in terms of cup velocity coordinates:

$$w_{11} = V_x\cos\theta_B + [V_y \sin(\phi_B-\phi_c) - (\bar{V}_z - V_z)\cos(\phi_B-\phi_c)]\sin\theta_B$$

Introducing the following definitions:

$$U_o^2 \equiv \beta_\perp \bar{V}_z^2$$

$$U_{11} \equiv \sqrt{\beta_\perp}\,[V_y \sin(\phi_B-\phi_c) - (\bar{V}_z - V_z)\cos(\phi_B-\phi_c)]\sin\theta_B$$

the component of $\vec{U}$ along the $\vec{B}$ - field,

$$U^2 \equiv \beta_\perp [(\bar{V}_z - V_z)^2 + V_y^2]$$

$$\epsilon \equiv \Delta\beta / \beta_\perp$$

and

$$\xi \equiv V_x / \bar{V}_z$$

the expression for $f_e\ (v_x,\ o,\ \bar{v}_z)$ is:

$$f_e(v_x, 0, \bar{v}_z) = \frac{n_e \beta_\perp \sqrt{\beta_\parallel}}{\pi^{3/2}} e^{-[U_0^2(1+\epsilon\cos^2\theta_B)\xi^2 + U^2 + \epsilon U_\parallel^2 + 2\epsilon U_\parallel U_0 \cos\theta_B \xi]} \tag{A.5}$$

Substituting (A.5) into (A.1) and integrating gives the following for H:

$$H_\ell = \frac{n_e \beta_\perp \sqrt{\beta_\parallel}}{\pi} \frac{e^{-[U^2 + \epsilon U_\parallel^2/(1+\epsilon\cos^2\theta_B)]}}{\sqrt{\alpha_\ell^2 + U_0^2(1+\epsilon\cos^2\theta_B)}} \tag{A.6}$$

It then follows that the expression for ΔI is:

$$\Delta I = I_0 \sqrt{\frac{\beta_\parallel}{\beta_\perp}} U_0^3 e^{-[U^2 + \epsilon U_\parallel^2/(1+\epsilon\cos^2\theta_B)]} \sum_{\ell=1}^{2} \frac{a_\ell}{\sqrt{\alpha_\ell^2 + U_0^2(1+\epsilon\cos^2\theta_B)}} \tag{A.7}$$

where

$$I_0 \equiv \frac{2}{\pi} e A T_N \frac{D}{H} n_e \Delta V_z$$

For $\epsilon = 0$, (A.7) reduces to the simpler case of a Maxwellian for f_e, i.e.,

$$\Delta I = I_0 U_0^3 e^{-U^2} \sum_{\ell=1}^{2} \frac{a_\ell}{\sqrt{\alpha_\ell^2 + U_0^2}} \tag{A.8}$$

(2) Conduction model[14]

$$f_e(\vec{v}) = f_\kappa\left(1 + (P_e + P_0)\tau\right) \tag{A.9}$$

where f_κ is the kappa distribution function

$$f_\kappa = C_\kappa \frac{n_e}{\pi^{3/2} w_c^3} \frac{1}{(1+u^2/\kappa)^{\kappa+1}} \qquad \text{(A.10)}$$

where

$$C_\kappa = \frac{\Gamma(\kappa+1)}{\Gamma(\kappa-\frac{1}{2})\kappa^{3/2}}$$

$$\vec{w} \equiv \vec{v} - \vec{V}$$

$$\vec{u} \equiv \vec{w}/w_c$$

n_e is the electron density, $2 \leq \kappa \leq \infty$ is the kappa parameter, w_c is the "core" thermal speed,

$$w\tau \equiv \frac{\lambda_w u^3}{u^4 + \delta} \quad , \quad \delta \equiv \frac{\lambda_w}{\bar{\lambda}_{coul}}$$

τ is the effective collision time, λ_w is the effective m.f.p. for wave-particle interactions, $\bar{\lambda}_{coul}$ is the effective m.f.p. for Coulomb collisions, and P_e, P_o are polynomials in the velocity and look like the following (see Chapter 4):

$$P_e = -\left(\frac{V_r}{r}\right)\left\{\frac{3}{2}\alpha_\beta + \alpha_n + [S(\kappa) - \kappa \ln(1+u^2/\kappa)]\alpha_\kappa \right. \qquad \text{(A.11)}$$
$$\left. - \eta u^2 [\alpha_\beta - \alpha_\kappa - 2\cos^2\theta^* \alpha_n + (1-3\cos^2\theta^*)\alpha_B]\right\}$$

$$P_o = w_c \frac{u_\parallel}{r}\left\{-\left(\frac{3}{2}\alpha_\beta + \alpha_n + [S(\kappa) - \kappa \ln(1+u^2/\kappa)]\alpha_\kappa\right)\right. \qquad \text{(A.12)}$$
$$\left. + \eta[(\alpha_\beta - \alpha_\kappa)u^2 - \alpha_r]\right\}\cos\chi$$

where

$$\eta \equiv \frac{\kappa+1}{\kappa}\frac{1}{1+u^2/\kappa}$$

$$\cos\chi \equiv \hat{b}\cdot\hat{r}$$

$\vec{r}$ is the radius vector for the heliocentric coordinate system,

$$S(x) \equiv 2x\,B(2x-1) - 1/2$$

$$B(z) \equiv \tfrac{1}{2}\left[\psi\left(\tfrac{z+1}{2}\right) - \psi\left(\tfrac{z}{2}\right)\right]$$

$$\psi(z) = \frac{d}{dz}\ln\Gamma(z)$$

$$\alpha_r = \frac{e E_r}{k T_c}\, r$$

(E_r is the electric field along $\vec{r}$),

$$u_{\parallel} = u\cos\theta^*$$

$$\beta \equiv 1/\omega_c^2$$

and

$$\alpha_G \equiv r\frac{d}{dr}\ln G$$

where

$$G = \beta, n_e, |\vec{B}|, x, \text{etc.}$$

Before substituting (A.10), (A.11) into (A.9), the following definitions shall be made:

$$U_0^2 \equiv \bar{V}_z^2/\omega_c^2$$

$$U^2 \equiv \left[(\bar{V}_z - V_z)^2 + V_y^2\right]/\omega_c^2$$

$$U_{\parallel} \equiv \left[V_y \sin(\phi_B - \phi_c) - (\bar{V}_z - V_z)\cos(\phi_B - \phi_c)\right]\sin\theta_B/\omega_c$$

and

$$u^2 = U_0^2\beta^2 + U^2$$

$$u_{\parallel} = U_0\beta\cos\theta_B + U_{\parallel}$$

After substituting (A.10), (A.11) into (A.9), which is then substituted into (A.1) and integrated, one gets the following for H:

$$H_\ell = \frac{n_e C_\varkappa}{\pi^{3/2} w_c^3} h_{o\ell} \left\{ 1 + \left(\frac{\lambda_w}{r}\right)\left(\frac{V_r}{w_c}\right)\left[-\left(\tfrac{3}{2}\alpha_\beta + \alpha_n + \zeta(\varkappa)\alpha_\varkappa\right)\frac{h_{1\ell}}{h_{o\ell}} \right.\right.$$

$$+ \alpha_\varkappa \frac{h_{4\ell}}{h_{o\ell}} + \frac{\varkappa+1}{\varkappa}\left[(2\alpha_n + \alpha_B)(V_{\|}^2 - V^2\cos^2\theta_B)\frac{h_{2\ell}}{h_{o\ell}} \right.$$

$$\left.\left.\left. + (\alpha_\beta - \alpha_\varkappa + 2\alpha_n\cos^2\theta_B + \alpha_B \sin^2\theta_B)\frac{h_{3\ell}}{h_{o\ell}} \right]\right] \qquad \text{(A.13)}$$

$$+ \left(\frac{\lambda_w}{r}\right) V_{\|}\cos\chi\left[-\left(\tfrac{3}{2}\alpha_\beta + \alpha_n + \zeta(\varkappa)\alpha_\varkappa\right)\frac{h_{1\ell}}{h_{o\ell}} + \alpha_\varkappa \frac{h_{4\ell}}{h_{o\ell}} \right.$$

$$\left. \left. + \frac{\varkappa+1}{\varkappa}\left((\alpha_\beta - \alpha_\varkappa)\frac{h_{3\ell}}{h_{o\ell}} - \alpha_r \right)\frac{h_{2\ell}}{h_{o\ell}} \right)\right] \Bigg\}$$

where a.

$$h_{o\ell} \equiv 2\int_0^\infty \frac{e^{-\alpha_\ell^2 \xi^2}\, d\xi}{(1 + u^2/\varkappa)^{\varkappa+1}}$$

b.

$$h_{1\ell} \equiv 2\int_0^\infty \frac{u^3 e^{-\alpha_\ell^2 \xi^2}\, d\xi}{(u^4 + \delta)(1 + u^2/\varkappa)^{\varkappa+1}} \qquad \text{(A.14)}$$

c.

$$h_{2\ell} \equiv 2\int_0^\infty \frac{u^3}{u^4 + \delta} \frac{e^{-\alpha_\ell^2 \xi^2}\, d\xi}{(1 + u^2/\varkappa)^{\varkappa+2}}$$

d.

$$h_{3\ell} \equiv 2\int_0^\infty \frac{u^5}{u^4+\delta}\,\frac{e^{-\alpha_\ell^2 f^2}\,df}{(1+u^2/n)^{n+2}}$$

e.

$$h_{4\ell} \equiv 2\int_0^\infty \frac{u^3 \ln(1+u^2/n)\, e^{-\alpha_\ell^2 f^2}\,df}{(u^4+\delta)(1+u^2/n)^{n+1}}$$

In order to evaluate integrals a to e the saddle point method had to be used. A brief outline of this method will now be given. First consider the integral expression:

$$H = \int_{-\infty}^{\infty} g(x)\,dx \tag{A.15}$$

The function g(x) can be written like $e^{G(x)}$ where G(x) = ln g(x). One then writes a Taylor series expansion of G(x) up to the second derivative around some point x_o

$$G(x) = G(x_o) + \left[\frac{\partial G}{\partial x}\right]_{x_o}(x-x_o) + \frac{1}{2}\left[\frac{\partial^2 G}{\partial x^2}\right]_{x_o}(x-x_o)^2 \tag{A.16}$$

where the point x_o is determined by setting $\left[\frac{\partial G}{\partial x}\right]_{x_o} = 0$. Then, after defining the parameter

$$\gamma^2 \equiv -\frac{1}{2}\left[\frac{\partial^2 G}{\partial x^2}\right]_{x_o}$$

and substituting (A.16) for G(x) into (A.15), one gets the following for H:

$$H = g(x_o)\int_{-\infty}^{\infty} e^{-\gamma^2(x-x_o)^2}\,dx \tag{A.17}$$

This integration of (A.17) is straightforward and has the following result:

$$H = g(x_o)\,\frac{\sqrt{\pi}}{\gamma} \qquad \text{(A.18)}$$

The basic philosophy of this approach is to find the maximum of the integrand $\left[\frac{\partial G}{\partial x}\right]_{x_o} = 0$, where it is assumed that most of the contribution to the integral resides. Then the integrand is replaced by a Gaussian whose width is determined by the curvature of the integrand at its maximum; and because one knows the integral for a Gaussian, an analytical expression for the integral (A.15) can be determined, i.e., Equation (A.18). Since there is no way of estimating the accuracy of this approximation, one must check the answer by doing numerical integrations and comparing. As a final note, this method becomes exact for g(x) equal to a Gaussian.

Using this method, integrals a to e become the following:

a.

$$h_{o\ell} \approx \frac{1}{(1+U^2/\nu)^{\nu+1}}\,\frac{\sqrt{\pi}}{\gamma_{o\ell}}$$

where

$$\gamma_{o\ell}^2 = \alpha_\ell^2 + \eta_o U_o^2, \text{ and } \eta_o \equiv \frac{\nu+1}{\nu}\,\frac{1}{1+U^2/\nu}$$

b.

$$h_{1\ell} \approx \frac{U^3}{(U^4+\delta)(1+U^2/\nu)^{\nu+1}}\,\frac{\sqrt{\pi}}{\gamma_{1\ell}}$$

where $$\gamma_{1\ell}^2 = \gamma_{0\ell}^2 + \frac{U_0^2}{2U^2}\left[\frac{U^4-3\delta}{U^4+\delta}\right]$$

c. $$h_{2\ell} \approx \frac{U^3}{(U^4+\delta)(1+U^2/\kappa)^{\kappa+2}} \frac{\sqrt{\pi}}{\gamma_{2\ell}}$$

where $$\gamma_{2\ell}^2 = \gamma_{1\ell}^2 + \frac{\eta_0}{\kappa+1} U_0^2$$

(A.19)

d. $$h_{3\ell} \approx \frac{U^5}{U^4+\delta} \frac{1}{(1+U^2/\kappa)^{\kappa+2}} \frac{\sqrt{\pi}}{\gamma_{3\ell}}$$

where $$\gamma_{3\ell}^2 = \gamma_{2\ell}^2 - U_0^2/U^2$$

e. $$h_{4\ell} \approx \frac{U^3 \ln(1+U^2/\kappa)}{(U^4+\delta)(1+U^2/\kappa)^{\kappa+1}} \frac{\sqrt{\pi}}{\gamma_{4\ell}}$$

where $$\gamma_{4\ell}^2 = \gamma_{1\ell}^2 - \frac{\eta_0 U_0^2}{(\kappa+1)\ln(1+U^2/\kappa)}$$

The integrals were checked for all values of parameter space relevant to the physical parameters of the detector,

and the model parameters κ, w_c, δ, and $\vec{V}$. In general the accuracy was better than 5%. Inaccuracies $\sim 10\%$ for $h_{3\ell}$ and $h_{4\ell}$ do occur for specific combinations of the parameters at the lowest energy channel when electron core temperatures are $\gtrsim 2.5 \times 10^5$ °K (i.e., angular width of f_e becomes comparable to the angular width in R).

Substituting (A.13) into (A.2), one gets the following for I:

$$\Delta I = I_0 \sum_{\ell=1}^{2} q_\ell F_{\kappa\ell} M_{\kappa\ell} \qquad (A.20)$$

where

$$F_{\kappa\ell} \equiv C_\kappa \frac{U_0^3}{(1+U^2/\kappa)} \frac{1}{\sqrt{\alpha_\ell^2 + \eta_0 U_0^2}} \qquad (A.21)$$

and $M_{\kappa\ell}$ is equal to the term in braces $\{\ \}$ for H in (A.13). $M_{\kappa\ell}$ is equal to unity when there is no transport (i.e., all gradients in macroscopic parameters vanish). Then Eq. (A.20) reduces to the simpler case of an isotropic kappa distribution for f_e. For the special limiting case $\kappa \to \infty$, f_κ reduces to a Maxwellian, and Eq. (A.21) for $F_{\kappa\ell}$ becomes rigorously:

$$F_{\infty\ell} = \frac{U_0^3}{\sqrt{\alpha_\ell^2 + U_0^2}} e^{-U^2} \qquad (A.22)$$

where the following limits were used

$$\lim_{\kappa\to\infty} C_\kappa = 1$$

$$\lim_{\kappa\to\infty} \eta_0 = 1$$

$$\lim_{\kappa\to\infty} (1+U^2/\kappa)^{-(\kappa+1)} = e^{-U^2}$$

Equation (A.20) for the current ΔI when $M_{\kappa\ell} = 1$, and $\kappa = \infty$ is identical to (A.8) derived using a bi-Maxwellian for f_e and then setting $\epsilon = 0$.

APPENDIX B

(1) Numerical Checks of "Moment" Integrations in Section 2.4

To check the numerical procedures and approach, numerous checking procedures were developed. For example, in order to check the basic integration routine we computed estimates of the density, wind velocity, temperature, and heat flow vector for the special case of no potential (Φ_o = 0 volts), where the anisotropy parameter $T_{\parallel}/T_{\perp}$ was set equal to 1.5. The results of these integrations are quoted in Table 10, demonstrating that the integration routine is operating properly and that our definitions given by Eqs. (2.76) to (2.79) are appropriate. Note: for this check the interpolation routine was not needed.

We next considered the special case of normal incidence (i.e., differential detector, $v_{t_o} = 0$). At this limit the integrals K_1 and K_2 reduce to the following form:

$$K_1 = 2\left(u_n - \sqrt{u_n^2 - 1}\right) \tag{B.1}$$

and

$$K_2 = \sqrt{\frac{u}{e\Phi_o}} \int_0^{\frac{e\Phi_o}{u}} \left(\frac{r_o}{r}\right) \frac{dy}{\sqrt{1+y}} \tag{B.2}$$

As may be seen, both integrals are independent of λ_D and are well defined for all $U > 0$. By substituting Eq. (B.1) for K_1 in Eq. (2.23) for $G(\vec{r}_o, \vec{v}_o)$ and by noting that for $v_{t_o} = 0$, the K_2 term drops out, one gets the following for $\tilde{f}_e$ given by Eq. (2.29):

$$\tilde{f}_e(\vec{r}_o, \vec{v}_o) = \frac{n_e \beta_\perp \sqrt{\beta_n}}{\pi^{3/2}} e^{-H} \tag{B.3}$$

where

$$H = \beta_\perp \left[\left(\sqrt{v_{n_o}^2 - u_o^2} - v_n \right)^2 + v_t^2 \right] \tag{B.4}$$

$$+ \Delta\beta \left[b_r^2 \left(\sqrt{v_{n_o}^2 - u_o^2} - v_n \right)^2 + v_t^2 b_t^2 - 2 \left(\sqrt{v_{n_o}^2 - u_o^2} - v_n \right) b_r \vec{b}_t \cdot \vec{v}_t \right]$$

Eq. (B.4) is exactly the same expression one would get with no potential, except for the energy shift experienced by the normal component of the electron velocity v_{n_o}, i.e.,

$$v_{n_o} \longrightarrow \sqrt{v_{n_o}^2 - u_o^2} \tag{B.5}$$

Eqs. (B.3) and (B.4) are the expressions which we used in our numerical integrations for the special case of a detector differential in angle.

One can show that the solution given by Eqs. (B.3) and (B.4) are similar to that for the plane geometry analog of our spherical model. At this limit the potential may be written the following way (see Figure 31)

$$\Phi(z) = \Phi_0 \left(\frac{\lambda_D - |z|}{\lambda_D} \right) \tag{B.6}$$

Then if a convected bi-Maxwellian is assumed to be the initial f_e at $|z| = \lambda_D$ and using the same method outlined in section 2.2, one will get for $\tilde{f}_e$ at z = o a solution similar to that given by Eqs. (B.3) and (B.4), i.e.,

$$H = \beta_\perp \left[\left(\sqrt{V_{n_0}^2 - u_0^2} - V_n \right)^2 + V_t^2 \right] + \Delta\beta \left[b_r^2 \left(\sqrt{V_{n_0}^2 - u_0^2} - V_n \right)^2 \right. \tag{B.7}$$

$$\left. + \left(\vec{V}_{t_0} - \vec{V}_t \right)^2 b_t^2 + 2 \left(\sqrt{V_{n_0}^2 - u_0^2} - V_n \right) b_r \hat{b}_t \cdot \left(\vec{V}_{t_0} - \vec{V}_t \right) \right]$$

where the only difference is that the $-\vec{V}_t$ term in Eq. (B.4) is replaced by $(\vec{v}_{t_o} - \vec{V}_t)$. This is the expression we used in our numerical integrations for the $\lambda_D \to 0$ limit. We would like to note that for the one-dimensional problem the transverse velocity replaces the angular momentum as the conserved quantity. When this happens the r_o/r term in K_2, Eq. (B.2), is replaced by one, so that $K_2 = K_1$.

For the special case of no convection and no anisotropy, one may solve for the density at z = 0, i.e.,

$$n_0 = n_{\lambda_D} e^{u_0^2/w_c^2} \left(1 - \mathrm{erf}(u_0/w_c) \right) \tag{B.8}$$

where $n_{\lambda D}$ is the density at $|z| = \lambda_D$. For $T = 1.2 \times 10^5$ °K, and $\Phi_0 = 4.5$ volts, Eq. (B.8) gives us the following for n_0:

$$n_o = 0.545\, n_{\lambda_D} \tag{B.9}$$

Thus the density has decreased by almost a factor of two. This rarefraction comes about because the electrons are accelerated toward the origin when they enter the region of non-zero electric field, while at the same time the total number of electrons must be conserved. Using the same numbers, we check our numerical routine by using Eq. (B.7) for H and the appropriate forbidden zone boundary (i.e., two infinite planes in the transverse direction $w_n = \pm u_o/w_c$, see section 2.4). These results were the same as those in (B.9) within a few percent (see Table 8, $\phi_c = 90^o$, $V_r = 0$). For the same problem, but with the three-dimensional geometry of a sphere, one gets the following expression for the density:

$$n_o = n_\infty \left[\frac{2}{\sqrt{\pi}} \frac{u_o}{w_c} + e^{u_o^2/w_c^2} \left(1 - \mathrm{erf}(u_o/w_c)\right) \right] \tag{B.10}$$

where n_∞ is the density at infinity. Using the same numbers for Φ_o and T, one gets for n_o:

$$n_o = 1.29\, n_\infty \tag{B.11}$$

Here, contrary to the one-dimensional case, the density has experienced an increase by 29%. In this case, as in the one-dimensional problem, the electrons experience a rarefraction which is indicated by the second term in Eq. (B.10). But, because the electrons experience a convergence of their

trajectories from the larger area of the Debye sphere to the smaller sphere of the spacecraft [first term in Eq. (B.10)] the density increases. Eq. (B.11) is useful in that it allows us to check our numerical integrations for $\bar{\Phi}_o \neq 0$ for the case of no convection ($\vec{V} = 0$) and no anisotropy ($T_{\parallel}/T_{\perp} = 1$). The results of this calculation, which are shown in Table 10, gave a density about equal to that given by (B.11) with an error less than 1%.

For the special limit of infinite Debye length ($\lambda_D \to \infty$ $z_o = 0.0$) or Coulomb potential, the integrals K_1, K_2 given by Eqs. (2.39) or (2.40) may be evaluated in terms of known functions, i.e.,

$$K_1 = \sqrt{\frac{e\bar{\Phi}_o}{u}}\,\frac{1}{b_o}\left[\sin^{-1}\left(\frac{1}{\epsilon}\right) - \sin^{-1}\left(\frac{1-\frac{1}{2}\left(\frac{e\bar{\Phi}_o}{u}\right)(\epsilon^2-1)}{\epsilon}\right)\right] \tag{B.12}$$

$$K_2 = \sqrt{\frac{e\bar{\Phi}_o}{u}}\,\frac{1}{b_o^2}\left[1 - \sqrt{(b_o^2)_{max} - b_o^2} + \frac{1}{2b_o}\left(\frac{e\bar{\Phi}_o}{u}\right)K_1\right] \tag{B.13}$$

where

$$\epsilon = \sqrt{1+4\left(\frac{u}{e\bar{\Phi}_o}\right)^2 b_o^2} \tag{B.14}$$

is the eccentricity parameter

$$(b_o^2)_{max} = 1 + \frac{e\bar{\Phi}_o}{u} \tag{B.15}$$

is the maximum b_o (i.e., $\theta = 90^o$). These are the expressions we used in our numerical integrations for the large Debye length limit $\lambda_D >> r_o$ discussed in section 2.4. They were also used to check our four point interpolation scheme for $z_o \neq 0.0$.

(2) Proof that $\lambda_D \to 0$ Limit is Equivalent to the Plane Parallel Geometry Problem

If the notion of plane parallel geometry is correct, as suggested throughout Chapter II, then the integral expressions K_1, K_2 must reduce to the form given by Eq. (B.1) as $\lambda_D \to 0$. To show this is the case, we shall first rewrite Eq. (2.40) for K_1 in the following way:

$$K_1 = \sqrt{\frac{e\Phi_o}{u}} \int_{z_o}^{\infty} \frac{(1+z)}{z}\left(\frac{z_o}{z}\right) \frac{e^{-(z-z_o)}\, dz}{\sqrt{1 + \frac{2}{z_c - 1}\left(\frac{z_c}{z}\right) e^{-(z-z_o)} - \xi^2 \left(\frac{z_c}{z}\right)^2 \left(\frac{z_c+1}{z_c-1}\right)}} \tag{B.16}$$

where Eq. (2.50) for v_c was substituted for v, while the following was substituted for b_D^2:

$$b_D^2 = \xi^2 \frac{z_c^2 (z_c+1)}{z_c - 1} \tag{B.17}$$

where we used Eq. (2.49) for $(b_D^2)_c$ and

$$0 \leq \xi < 1 \tag{B.18}$$

As $\lambda_D \to 0$, the spacecraft radius in units of λ_D, $z_o \to \infty$. For this limit, the energy $(U_c)_{max}$ below which critical trajectories appear goes to infinity [see Eq. (2.57)]. Thus, for all finite energies U there are critical trajectories. Therefore, for

$$U << (U_c)_{max} \tag{B.19}$$

we have (see section 2.3)

$$z_c >> z_o \tag{B.20}$$

Then because of the exponential term in the numerator of the integrand for K_1, appreciable contributions to the integral occur only for

$$z \sim z_o \tag{B.21}$$

with possible exceptions to the critical points z_c. For $\xi << 1$ (no critical trajectories), the term proportional to ξ, Eq. (B.17), is small compared to

$$1 + \frac{2}{z_c - 1}\left(\frac{z_c}{z}\right) e^{-(z - z_c)} \tag{B.22}$$

for all z. For $\xi \sim 1$, Eq. (B.17) becomes comparable to Eq. (B.22) only for $z \sim z_c$, so that the denominator approaches zero. The singularity due to the denominator goes like $1/\delta$, where $\delta << 1$. This singularity due to the impact parameter b_D will only be important if

$$\frac{e^{-(z_c - z_o)}}{\delta} \sim 1 \tag{B.23}$$

As $z_o \to \infty$, z_c must also approach infinity. Then because the exponential term decreases faster than δ, (B.23) should tend to zero for all finite U as $z_o \to \infty$.

Therefore, the term given by (B.17) may be dropped compared to (B.22) as $z_o \to \infty$, so that

$$\lim_{z_o \to \infty} K_1 = 2\left(u_n - \sqrt{u_n^2 - 1}\right) \tag{B.24}$$

which is the solution for the plane parallel problem. Also, since contributions to the integral for K_2 occur only for $z \sim z_o$ ($r \sim r_o$), the term r_o/r in the integrand for K_2 [set Eq. (B.2)] may be set equal to 1 as $z_o \to \infty$. For example, for

$$r = r_o + \epsilon \quad \text{where} \quad \epsilon << 1$$

we have

$$z = z_o + \frac{\epsilon}{\lambda_D}$$

Then as $\lambda_D \to 0$, ϵ must also approach zero in order for $z \sim z_o$. Therefore,

$$\lim_{z \to \infty} k_2 = K_1 \tag{B.25}$$

which is the solution for K_2 in the plane parallel problem. Thus, we have indeed shown that as $\lambda_D \to 0$, the problem reduces to the one-dimensional (plane-parallel) case, so that the simple correction

$$V_{n_0} \rightarrow \sqrt{V_{n_0}^2 - u_0^2}$$

is appropriate to use in the short Debye length limit ($\lambda_D = 0$).

APPENDIX C

We will derive the vector relation given by Eq. (3.58), showing the flow to be field aligned in the rotating frame of reference. A more complete derivation may be found in L. Mestel (1968).[71] The magnetic field in terms of poloidal and toroidal components has the form

$$\vec{B} = \vec{B}_p + \vec{B}_t \tag{C.1}$$

where $\vec{B}_p$ the poloidal component is confined to the meridional plane, while B_t points in the azimuthal direction. The wind velocity in the inertial frame may be split up in a similar way

$$\vec{V}_I = \vec{V}_{P_I} + \omega_I R \hat{e}_\phi \tag{C.2}$$

where $\vec{V}_{pI}$ is the poloidal component and ω_I is the angular velocity of the flow. From the ideal Ohm's law Eq. (3.6) we may express the electric field $\vec{E}$ the following way:

$$\vec{E} = -\frac{1}{c}\vec{V}_I \times \vec{B} = -\frac{1}{c}\left[\vec{V}_{P_I} \times \vec{B}_p + \vec{V}_{t_I} \times \vec{B}_p - \vec{B}_t \times \vec{V}_{P_I}\right] \tag{C.3}$$

in terms of poloidal and toroidal parts. Because of steady state the electric field is expressable in terms of the negative gradient of a scalar potential [see Eq. (3.2)], i.e.,

$$\vec{E} = -\nabla \Phi_E \tag{C.4}$$

Then because of azimuthal symmetry the toroidal component of $\vec{E}$ must be zero.

$$\vec{E}_t = -\frac{1}{c}(\vec{V}_{P_I} \times \vec{B}_p) = 0 \tag{C.5}$$

Thus, the poloidal component of the magnetic field is parallel to the poloidal component of the wind velocity.

$$\alpha \vec{B}_p = \rho \vec{V}_p \tag{C.6}$$

Then with the assumption of axial symmetry the following is also true:

$$\nabla \cdot \vec{B} = \nabla \cdot \vec{B}_p = 0 \tag{C.7}$$

$$\nabla \cdot (\rho \vec{V}_I) = \nabla \cdot (\rho \vec{V}_{p_I}) = 0 \tag{C.8}$$

by referring to Eq. (C.6) it is then apparent that

$$\vec{B} \cdot \nabla \alpha = 0 \tag{C.9}$$

so that α is a field line constant. Furthermore, from Eq. (C.7) and Eq. (C.8) it is readily apparent that all field line constants are streamline constants. It can then be shown by taking the poloidal component of the ideal Ohm's law Eq. (C.3), Eq. (C.6), and azimuthal symmetry that

$$\vec{B} \cdot \nabla \left(\omega_I - \frac{\alpha B_t}{R\rho} \right) = \vec{B} \cdot \nabla \omega = 0 \tag{C.10}$$

so that

$$\omega_I - \frac{\alpha B_t}{R\rho} = \omega \qquad = \text{constant along the field line.} \tag{C.11}$$

From Eqs. (C.6) and (C.10) it can be shown that

$$\vec{V}_I = \frac{\alpha \vec{B}}{\rho} + \vec{\omega} \times \vec{R} \tag{C.12}$$

where $\vec{\omega} = \vec{\omega} e_z$ (i.e., e_z is a unit vector aligned along the axis of symmetry). It then follows from Eq. (C.12) and the ideal Ohm's law that in a rigidly rotating frame with angular velocity $\vec{\omega}$ the electic field is zero along a given field line. Thus,

for this frame the flow is field aligned. In the case of the sun, near the base of the corona or footprints of the magnetic field, the flow is constrained to move along $\vec{B}$ (i.e., tension in $\vec{B}$ field dominates all other forces in these regions). Then since the sun is rotating, the flow will be field aligned along field lines in the frame rotating at the angular velocity of the sun $\vec{\Omega}$ at the footprints of the field lines (i.e., because of differential rotation, field lines of a different latitude will have field aligned flow in frames with different angular velocity). We thus have the following from Eq. (C.12),

$$\alpha \vec{B} = \rho \vec{V} \tag{C.13}$$

which is the desired result, where $\vec{V}$ is the wind velocity in the rotating frame, and

$$\vec{\omega} = \vec{\Omega} \tag{C.14}$$

Then if ρ and $\vec{B}$ are known one may determine the wind velocity in the rotating frame along a given field line once α is known for that field line.

We will now derive expressions for the toroidal component of $\vec{B}$ and the angular velocity of the flow ω_I, which will allow us to extend our integration along the field lines in the rotating frame out into the interplanetary medium. From Eqs. (C.11) and (C.13) we can get the following relation for B_t:

$$B_t = \frac{\rho}{\alpha} R(\omega_I - \Omega) \tag{C.15}$$

Then from the toroidal equation of motion

$$R\left[\frac{(\nabla\times\vec{B})\times\vec{B}}{4\pi}\right]_t = \nabla\cdot(\rho\vec{V}\omega_I R^2) \tag{C.16}$$

in combination with Eq. (C.6) and (C.7) we get

$$-\frac{B_t R}{4\pi\alpha} + \omega_I R^2 = L \tag{C.17}$$

where L is the total angular momentum per unit mass of the field plus gas. From this and Eq. (C.15) we can get the following relation for ω_I

$$\omega_I = \frac{\Omega - \frac{4\pi\alpha^2 L}{\rho R^2}}{1 - \frac{4\pi\alpha^2}{\rho}} \tag{C.18}$$

We would now like to derive a useful relation between the field line constant α and the mass density at the Alfven point ρ_A. For instance, near the sun the flow will be subalfvenic $V<V_A$, while superalfvenic $V>V_A$ far from the sun, where

$$\vec{V}_A = \frac{\vec{B}}{\sqrt{4\pi\rho}} \tag{C.19}$$

is the Alfven velocity. Thus for some point (r_A,θ_A), called the Alfven point, along a given field line (i.e., confining our discussions in the rotating frame), the wind velocity will be equal to the local Alfven velocity

$$V = V_A \tag{C.20}$$

Then because

$$\alpha = \frac{\rho V}{B} \tag{C.21}$$

in the rotating frame we get the following relation for ρ_A from Eqs. (C.19), C.20), and (C.21):

$$\rho_A = 4\pi\alpha^2 \qquad \text{(C.22)}$$

Thus, once α is known for a field line, the mass density at the Alfvén point for that field line is known. Then since we know ρ and $\vec{B}_p$ for all $\vec{r}$ from our empirical models, it is possible to determine the Alfvén point (r_A, θ_A) for the field line. Combining Eqs. (C.15) and (C.18) we get the following relation for B_t

$$B_t = \frac{-\rho_A}{\alpha R}\,\frac{(L - \Omega R^2)}{1 - \rho_A/\rho} \qquad \text{(C.23)}$$

and rewriting Eq. (C.18)

$$\omega_I = \frac{\Omega - \dfrac{\rho_A L}{\rho R^2}}{1 - \rho_A/\rho} \qquad \text{(C.24)}$$

It is apparent from looking at Eqs. (C.23) and (C.24) that B_t and ω_I become undefined at the Alfvén point unless the numerator is simultaneously zero. By doing this we determine L, i.e.,

$$L = \Omega R_A^2 \qquad \text{where } R_A = r_A \sin\theta_A \qquad \text{(C.25)}$$

We thus have for B_t and ω_I the following:

$$B_t = -\frac{\rho_A \Omega R_A^2}{\alpha R}\left(\frac{1 - R^2/R_A^2}{1 - \rho_A/\rho}\right) \qquad \text{(C.26)}$$

$$\omega_I = \Omega\left(1 - \frac{\rho_A R_A^2}{\rho R^2}\right) \qquad \text{(C.27)}$$

REFERENCES

1. Wolfe, J.H., and D.D. McKibben, Pioneer 6 observations of a steady state magnetosheath, Planet. Space Sci., 16, 953, 1968.

2. Wolfe, J.H., R.W. Silva, and D.D. McKibben, Pioneer 6 observations of plasma ion and electron heating at the earth's bow shock (abstract), EOS.Trans. AGU, 48, 174, 1967.

3. Montgomery, M.D., S.J. Bame, and J.R. Asbridge, Solar wind electron Vela 4 measurements, J. Geophys. Res., 73, 4999, 1968.

4. Montgomery, M.D., J.R. Asbridge, and S.J. Bame, Vela 4 plasma observations near the earth's bow shock, J. Geophys. Res., 75, 1217, 1970.

5. Ogilvie, K.W., J.D. Scudder, and M. Sugiura, Electron energy flux in the solar wind, J. Geophys. Res.,76, 8165, 1971.

6. Montgomery, M.D., Average thermal characteristics of solar wind electrons, Solar Wind, NASA Spec. Publ., 308, 208, 1972.

7. Serbu, G.P., Explorer 35 observations of solar wind electron density, temperature, and anisotropy, J. Geophys. Res., 77, 1703, 1972.

8. Feldman, W.C., J.R. Asbridge, S.J. Bame, and M.D. Montgomery, Solar wind heat transport in the vicinity

of the earth's bow shock, J. Geophys. Res., 78. 3697, 1973.

9. Feldman, W.C., J.R. Asbridge, S.J. Bame, M.D. Montgomery, and S.P. Gary, Solar wind electrons, J. Geophys. Res., 80. 4181, 1975.
10. Scudder, J.D., D.L. Lind, K.W. Ogilvie, Electron observations in the solar wind and magnetosheath, J. Geophys. Res., 78, 6535, 1973.
11. Rosenbauer, H., H. Miggenrieder, M. Montgomery, and R. Schwenn, Preliminary results of the helios plasma measurements, in Physics of Solar Planetary Environment, edited by D. J. Willians, Proceedings of the International Symposium on Solar-Terrestrial Physics, Vol. I, AGU, p. 319, 1976.
12. Feldman, W.C., J.R. Asbridge, S.J. Bame, and J.T. Gosling, High-speed solar wind flow parameters at 1 AU, J. Geophys. Res., 81. 5054, 1976.
13. Vasyliunas, V.M., Deep space plasma measurement, Reprinted from Methods of Experimental Physics, 9B, 49, 1971.
14. Scudder, J.D., and S. Olbert, The problem of determining the heat transport mechanism of the electron component of the interplanetary medium, being prepared for publication, 1978.
15. Olbert, S., Summary of experimental results from M.I.T. detector on Imp-1, Physics of the Magnetosphere, edited

by R.L. Carovillano, John McClay, H.R. Radoski, p. 641, D. Reidel Publ., Drecht, Holland, 1968.

16. Bernstein, I.B., and I.N. Rabinowitz, Theory of electrostatic probes in a low-density plasma, Physics of Fluids, 2, 112, 1959.

17. Munroe, R.H., and G.L. Withbroe, Properties of a coronal hole derived from extreme ultraviolet observations, Astrophys. J., 176, 511, 1972.

18. Gurman, J.B., G.L. Withbroe, and J.W. Harvey, A Comparison of EUV spectroheliograms and photospheric magnetograms, Solar Phys., 34, 105, 1974.

19. Zirker, J.B., Coronal holes and high-speed wind streams, Rev., of Geophys. and Space Phys., 15, 257, 1977.

20. Vaiana, G.S., A.S. Krieger, and A.F. Timothy, Identification and analysis of structures in the corona from x-ray photography, Solar Phys., 32, 81, 1973.

21. Neupert, W.M., and V. Pizzo, Solar coronal holes as sources of geomagnetic disturbances, J. Geophys. Res., 79, 3701, 1974.

22. Fischer, R.R., and S. Musman, Detection of coronal holes from 5303 Fe XIV observations, Astrophys. J., 195, 801, 1975.

23. Altshuler, M.D., D.E. Trotter, and F.Q.Orrall, Coronal holes, Solar Phys., 26, 354, 1972.

24. Munroe, R.H., amd B.V. Jackson, Physical properties of a polar coronal hole from 2 to 5 r , Astrophys. J., 213, 874, 1977.

25. Dulk, G.A., and K.V. Sheridan, Structure of the middle corona from observations at 80 and 160 MHZ, Solar Phys., 36, 191, 1974.

26. Levine, R.H., Evolution of open magnetic structures on the sun: the Skylab period, Astrophys. J., 218, 291, 1977.

27. Timothy, A.F., A.S. Krieger, and G.S. Vaiana, The structure and evolution of coronal holes, Solar Phys., 42, 135, 1975.

28. Bohlin, J.D., Extreme ultraviolet observations of coronal holes, Solar Phys., 51, 377, 1977.

29. Sheeley, N.R., J.W. Harvey, and W. C. Feldman, Coronal holes, solar wind streams, and recurrent geomagnetic disturbances: 1973-1976, Solar Phys., 49, 271, 1976.

30. Wagner, W.J., Solar rotations as marked by EUV coronal holes, Astrophys. J., 198, L 141, 1975.

31. Cushman, G.W., amd W.A. Rense, Evidence for outward flow of plasma in a coronal hole, Astrophys. J., 207, L 61, 1976.

32. Imad, I.A., and G.L. Withbroe, EUV analysis of polar plumes, Center for Astrophys., Harv. Coll. Observ. and Smithson. Astrophys. Observ. preprint, 1976.

33. Noyes, R.W., G.L. Withbroe, and R.P. Kirshner, Extreme ultraviolet observations of active regions

in the chromosphere and the corona, Solar Phys., 11, 388, 1970.

34. Newkirk, G., Jr., Structure of the solar corona, Ann. Rev. Astron. Astrophys., 5, 213, 1967.

35. Kundu, M.R., Solar Radio Astronomy, Interscience, New York, 1965.

36. Švestka, Zdeněk, Solar Flares, Geophys. and Astrophys. Monographs, D. Reidel Pub., 1976.

37. Vaiana, G.S., A.S. Krieger, L.P. Van Speybroeck, and T. Zehnpfennig, Bull. Amer. Phys. Soc., 15, 611, 1970.

38. Hundhausen, A.J., Coronal Expansion and Solar Wind, Springer-Verlag, New York, 1972.

39. Gosling, J.T. and S. J. Bame, Solar wind speed variations 1964-1967: an autocorrelation analysis, J. Geophys. Res., 77, 12, 1972.

40. Gosling, J.T., J.R. Asbridge, S.J. Bame, and W.C. Feldman, Solar wind speed variations: 1962-1974, J. Geophys. Res., 81, 5061, 1976.

41. Belcher, J.W., J.D. Sullivan, and A.J. Lazarus, Alfvén wave fluxes in solar wind streams associated with coronal holes, EOS Trans. AGU, 57, 996, 1976.

42. Bame, S.J., J.R. Asbridge, W.C. Feldman, and J.T. Gosling, Evidence for a structure-free state at high solar wind speeds, J. Geophys. Res., 82, 1487, 1977.

43. Krieger, A.S., A.F. Timothy, and E.C. Roelof, A coronal hole as the source of a high velocity solar wind stream, Solar Phys., 29, 505, 1973.

44. Krieger, A.S., A.F. Timothy, G.S. Vaiana, A.J. Lazarus, and J.D. Sullivan, X-ray observations of coronal holes and their relation to high velocity solar wind streams, in Solar Wind Three, edited by C.T. Russell, p. 132, University of Calif. Press, Los Angeles, 1974.

45. Nolte, J.T., A.S. Krieger, A.F. Timothy, R.E. Gold, E.C. Roelop, G. Vaiana, A.J. Lazarus, J.D. Sullivan, and P.S. McIntosh, Coronal holes as sources of solar wind, Solar Phys., 46, 303, 1976.

46. Smith, E.J., B.T. Tsurutani, R.L. Rosenberg, Observations of the interplanetary sector structure up to heliographic latitudes of 16°: Pioneer 11, EOS Trans. AGU, 58, 484, 1977.

47. Smith, E.J., L. Davis Jr., B.T. Tsurutani, J.H. Wolfe, Observed properties of the interplanetary neutral sheet: Pioneers 10, 11, EOS, 58, 1226, 1977.

48. Rossi, B., and S. Olbert, Introduction to the Physics of Space, McGraw-Hill, New York, 1970.

49. Parker, E.N., Dynamics of the interplanetary gas and magnetic fields, Astrophys. J., 128, 664, 1958.

50. Parker, E.N., Interplanetary Dynamical Processes, Interscience, New York, 1963.

51. Parker, E.N., Dynamical properties of stellar coronas and stellar winds, II, Integrations of the heat-flow equation, Astrophys. J., 139, 93, 1964.

52. Noble, L.M., and F.L. Scarf, Conductive heating of the solar wind, I, Astrophys. J., 138, 1169, 1963.

53. Whang, Y.C., C.C. Chang, An inviscid model of the solar wind, J. Geophys. Res., 70, 4175, 1965.

54. Durney, B., A new type of supersonic solution for the inviscid equations of the solar wind, Astrophys. J., 166, 669, 1971.

55. Roberts, P.H. and A.M. Soward, Stellar winds and breezes, published in the proceedings of the Royal Society, 1972.

56. Sturrock, P.A., and R.E. Hartle, Two-fluid model of the solar wind, Phys. Rev. Letters, 16, 628, 1966.

57. Wolff, C.L., J.C. Brandt, and R.G. Southwick, A two-component model of the quiet solar wind iwth viscosity magnetic field, and reduced heat conduction, Astrophys. J., 165, 181, 1971.

58. Pneuman, G.W., and R.A. Kopp, Gas-magnetic field interactions in the solar corona, Solar Phys., 18, 258, 1971.

59. Okamoto, I., Magnetic braking by a stellar wind, V, Approximate determination of the poloidal field, Mon. Not.R. Astr. Soc., 173, 357, 1975.

60. Nerney, SF., and S.T. Suess, Restricted three-dimensional stellar wind modeling, I, Polytropic case, Astrophys. J., 196, 837, 1975.

61. Heinemann, M.A., and S. Olbert, Axisymmetric ideal MHD stellar wind flow, to be published in J. Geophys. Res., 1978.

62. Belcher, J.W., Alfvenic wave pressures and the solar wind, Astrophys. J., 168, 509, 1971.

63. Van deHulst, H.C., The chromosphere and the corona, in The Sun, edited by G.P. Kuiper, p. 255, University of Chicago Press, Chicago, 1953.

64. Counselman, C.C., and J.M. Rankine, Density of the solar corona from occultation of NP0532, Astrophys. J., 175, 843, 1972.

65. Muhleman, D.O., P. B. Esposito, and J.D. Anderson, The electron density profile of the outer corona and the interplanetary medium from Mariner-6 and Mariner-7 time-delay measurements, Astrophys. J., 211. 943, 1977.

66. Campbell, D.B., and D.O. Muhleman, Measurements of the electron content of the interplanetary medium between Earth and Venus, J. Geophys.Res, 74, 1138, 1969.

67. Neugebauer, M., and C.W. Snyder, Mariner-2 measurements of the solar wind, in The Solar Wind, edited

by Mackin and M. Neugebauer, p. 1, Pergamon, Oxford, 1966.

68. Lazarus, A.J., private communication referring to data from Mariner-5 flight to Venus, 1972.

69. Burlaga, L.F., and K.W. Ogilvie, Heating of the solar wind, Astrophys. J., 159, 659, 1970.

70. Rosner, R., and G.S. Vaiana, Comments on non-radial flows in the solar wind problem, Center for Astrophys., Harv. Coll. Observ. and Smithson. Astrophys. Observ. preprint, submitted to Solar Phys., 1976.

71. Mestel, L., Magnetic braking by a stellar wind-I, Mon. Not. R. Astro. Soc., 138, 359, 1968.

72. Saito, K., A non-spherical axisymmetric model of the solar K corona of the minimum type, Ann. Tokyo Astron. Observ., 12, 53, 1970.

73. Allen, C.W., Astrophysical Quantities, Third Edition,University of London, Athlone Press, p. 176, 1973.

74. Hollweg, J.V., Transverse Alfvén waves in the solar wind: arbitrary $\vec{k}$, $\vec{V}_o$, $\vec{B}_o$, and $|\delta\vec{B}|$, J. Geophys. Res., 79, 1539, 1974.

75. Coles, W.A., and B.J. Rickett, IPS observations of the solar wind speed out of the ecliptic, J. Geophys. Res., 81, 4797, 1976.

76. Solar wind plasma experiment on the NASA/ESA out-of-ecliptic mission, NASA proposal, Center for Space Res--M.I.T., Laboartory for Extraterres. Phys.--GSFC, JPL--Cal. Tech, and Laboratori per il Plasma nello Spazio--Consiglio Nazionale delle Richerche, 1977.

77. Spitzer, L., Jr., and R. Härm, Transport phenomena in a completely ionized gas, Phys. Rev., 89, 977, 1953.

78. Scudder, J.D., Solar Wind, edited by C.P. Sonnett, P.J. Coleman, Jr., and J.M. Wilcox, Proceedings of conference sponsored by NASA, p. 211, Mar. 21-26,1971.

79. Eviatar, A., and M. Schulz, Trans. Am. Geophys. Union, 49, 725, 1968.

80. Schulz, M., and A. Eviatar, Electron-temperature asymmetry and the structure of the solar wind, Cosmic Electrodynamics,2, 402, 1972.

81. Ogilvie, K.W., J.D. Scudder, and S. Olbert, A unifying picture of the interplanetary electron distribution function between 0.45-1.0 AU: Mariner 10, EOS Trans., Amer. Geophys. Un., 58, 1223, 1977.

BIOGRAPHICAL NOTE

The author was born in Freeport, Long Island, New York on October 4, 1947. He received his high school education in Massapaqua Park and Riverhead, Long Island. After earning an Associate in Applied Science degree in the field of Electrical Technology from Farmingdale Agricultural and Technical College in 1967, he worked as an Electronics Technician at Grumman Aerospace Corporation in Bethpage, Long Island on the F-111, F-14, and Lunar Excursion Module projects.

Returning to college in 1969, the author received a B.S. in Physics, graduating Magna Cum Laude with honors in Physics from Hofstra University (Hempstead, Long Island) in 1972. During his years at Hofstra, he was vice-president of the Physics Club, became a member of Sigma Pi Sigma National Physics Honor Society, and Kappa Mu Epsilon Mathematics Honor Society, and taught the observational lab of an Introduction to Astronomy course.

The author was admitted to the Masschusetts Institute of Technology as a graduate student in the Department of Physics and was awarded a Research Assistantship at the Center for Space Research. At M.I.T. he was involved in the testing, calibration, and integration of the M.I.T. plasma detectors on the SOLRAD 11A and 11B satellites. He presented a talk at the Spring, 1977 AGU meeting concerning semi-empirical radial profiles of the solar wind velocity, effective temperature, and effective heat

flow vector. In the same year he was nominated a full member of the M.I.T. Chapter of Sigma Xi:Scientific Research Society of North America.

Having accepted a Research Associateship from the National Research Council, the author will begin tenure at NASA's Goddard Space Flight Center in Greenbelt, Maryland, doing research related to heat transport by electrons in the interplanetary medium.

Fig. 1

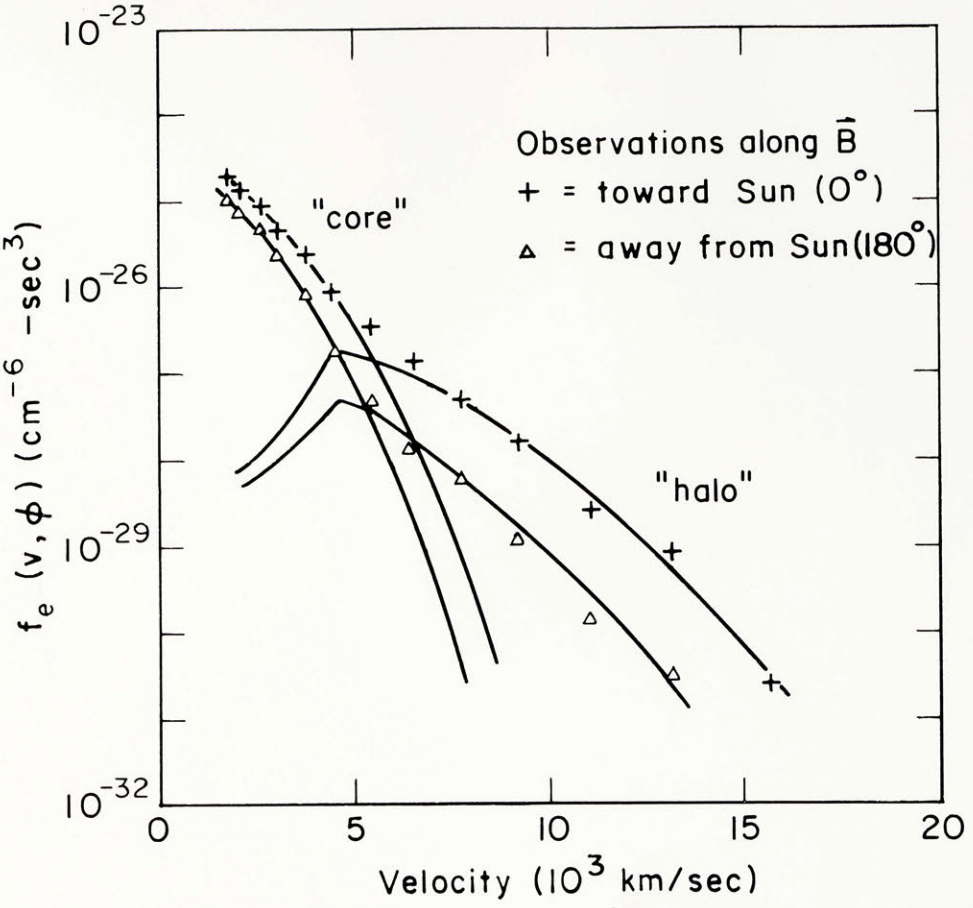
Observations along $\vec{B}$
+ = toward Sun (0°)
△ = away from Sun(180°)
"core"
"halo"
$f_e\ (v, \phi)\ (cm^{-6}-sec^3)$
10^{-23}
10^{-26}
10^{-29}
10^{-32}
0
5
10
15
20
Velocity (10^3 km/sec)

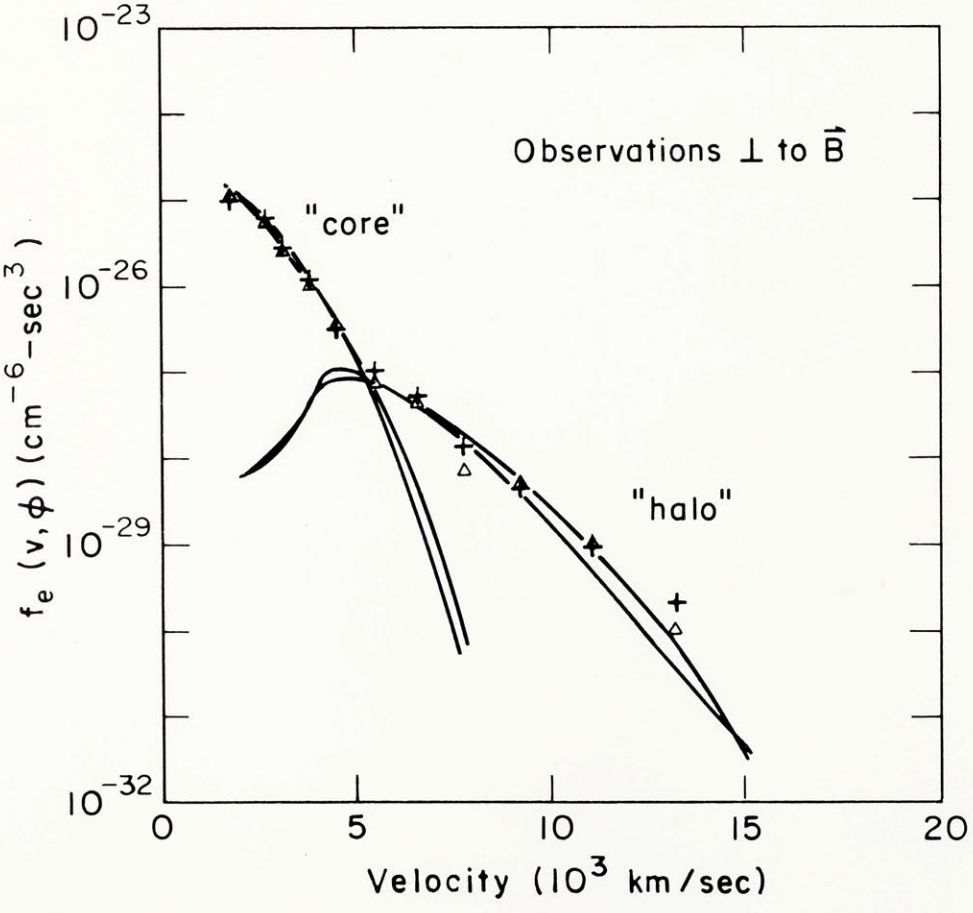
Observations ⊥ to $\vec{B}$
"core"
"halo"
$f_e\ (v, \phi)\ (cm^{-6}-sec^3)$
10^{-23}
10^{-26}
10^{-29}
10^{-32}
0
5
10
15
20
Velocity (10^3 km/sec)

Fig. 2

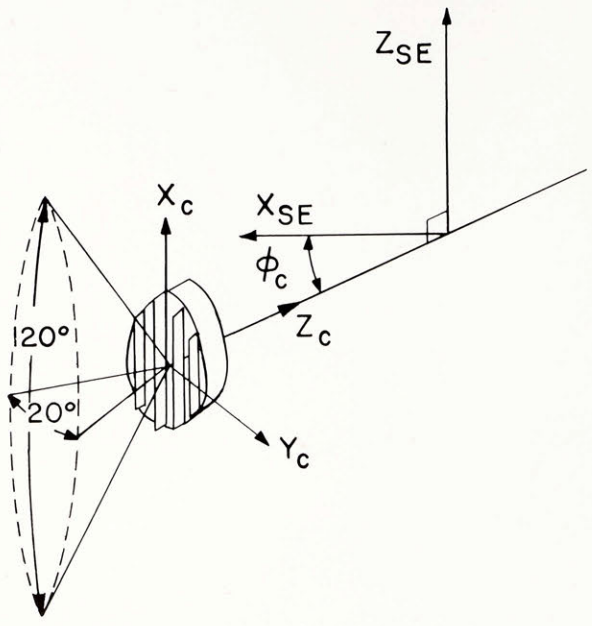
Z_{SE}
X_c
X_{SE}
ϕ_c
Z_c
120°
20°
Y_c

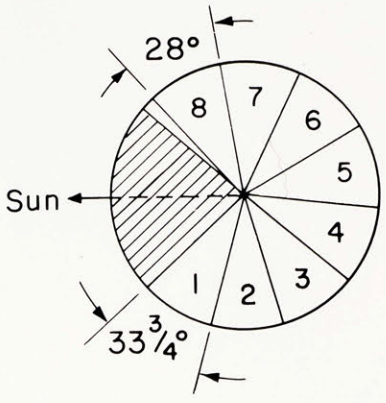
28°
8
7
6
5
Sun
4
1
2
3
33¾°

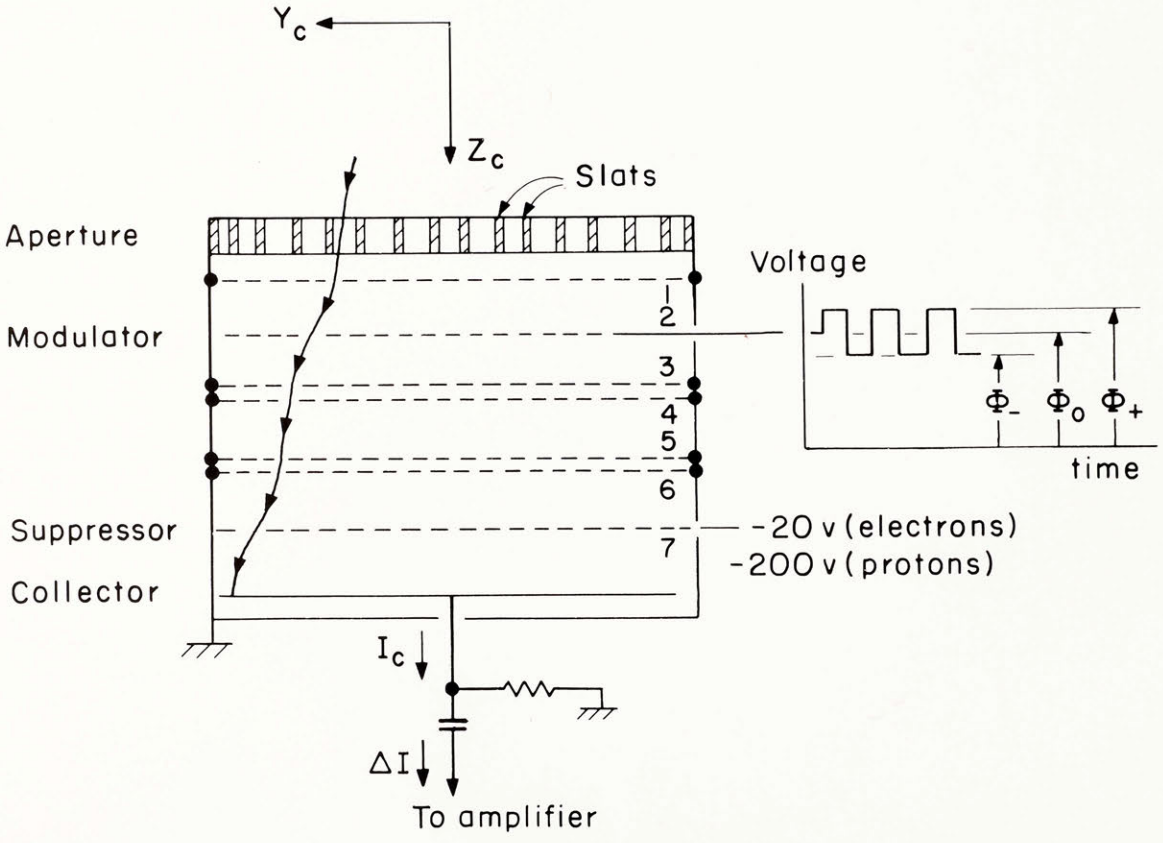
Y_c
Z_c
Slats
Aperture
Modulator
Suppressor
Collector
2
3
4
5
6
7
Voltage
Φ_-
Φ_0
Φ_+
time
-20 v (electrons)
-200 v (protons)
I_c
ΔI
To amplifier

Fig. 3a

Slats

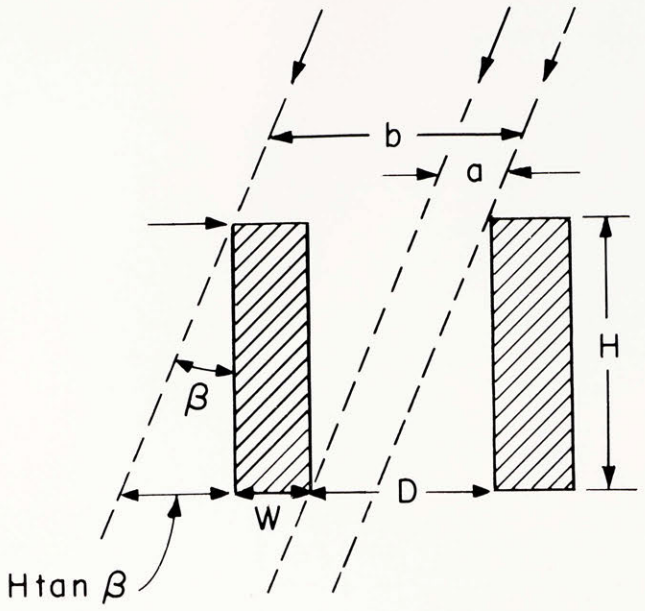

$$a = b - W - H\tan\beta$$

Fig. 3b

Grid Wires

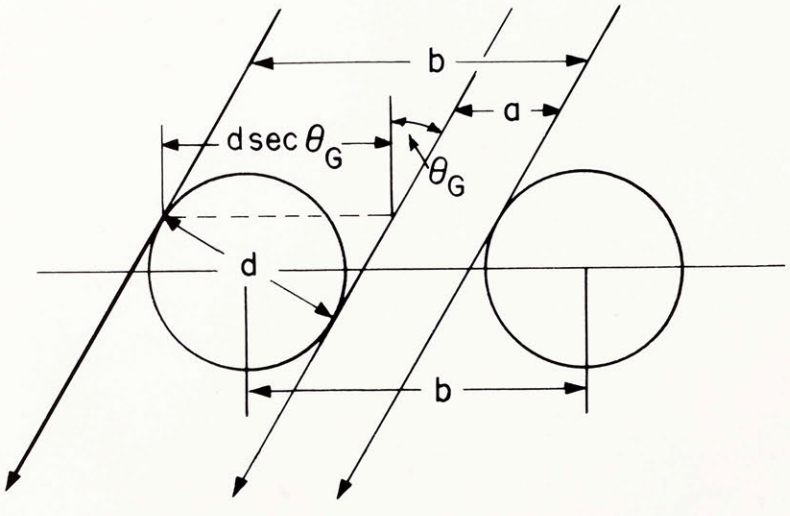

$$a = b - d\sec\theta_G$$

Fig. 4

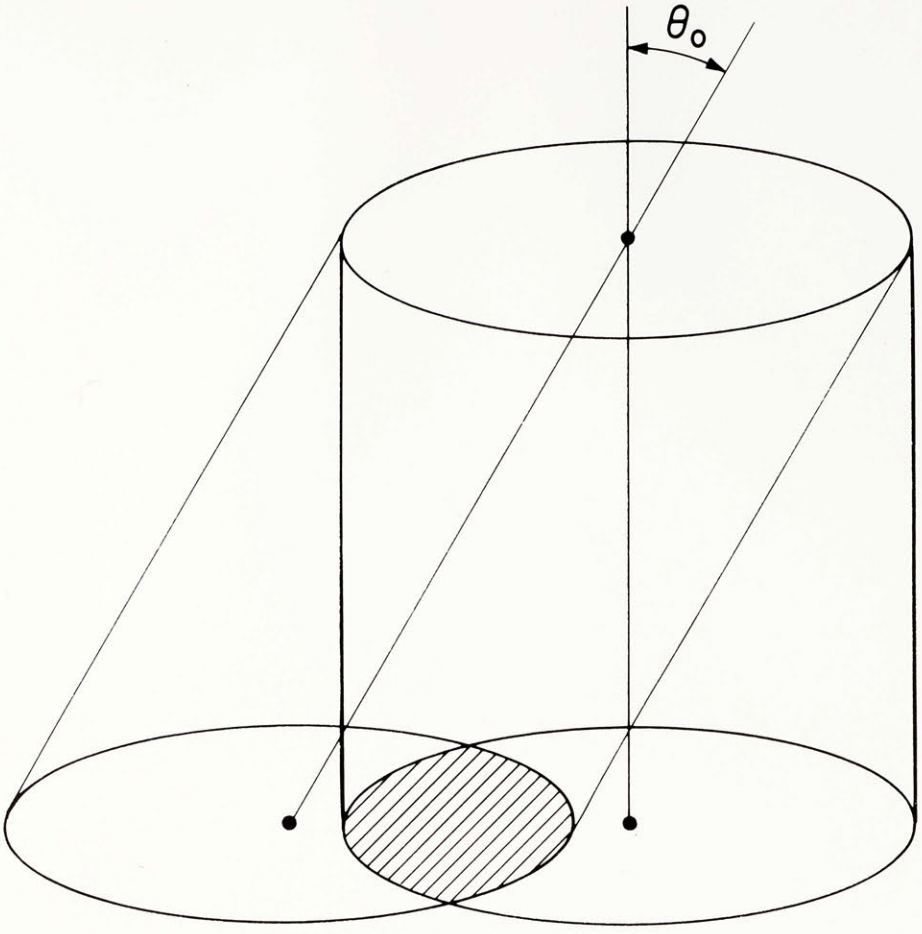

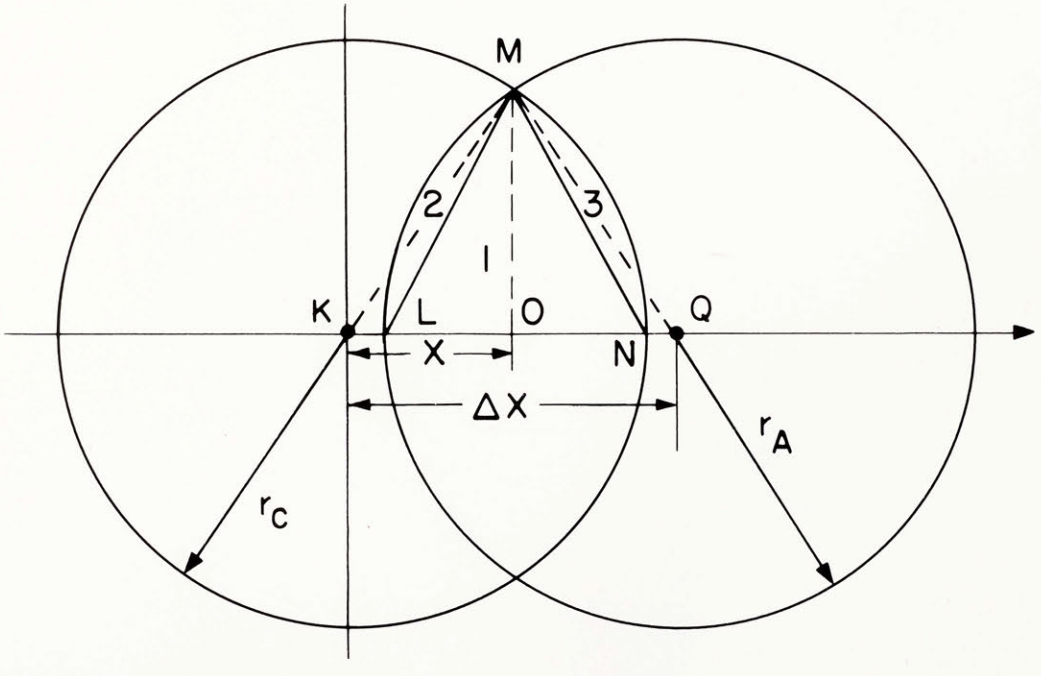

Fig. 5

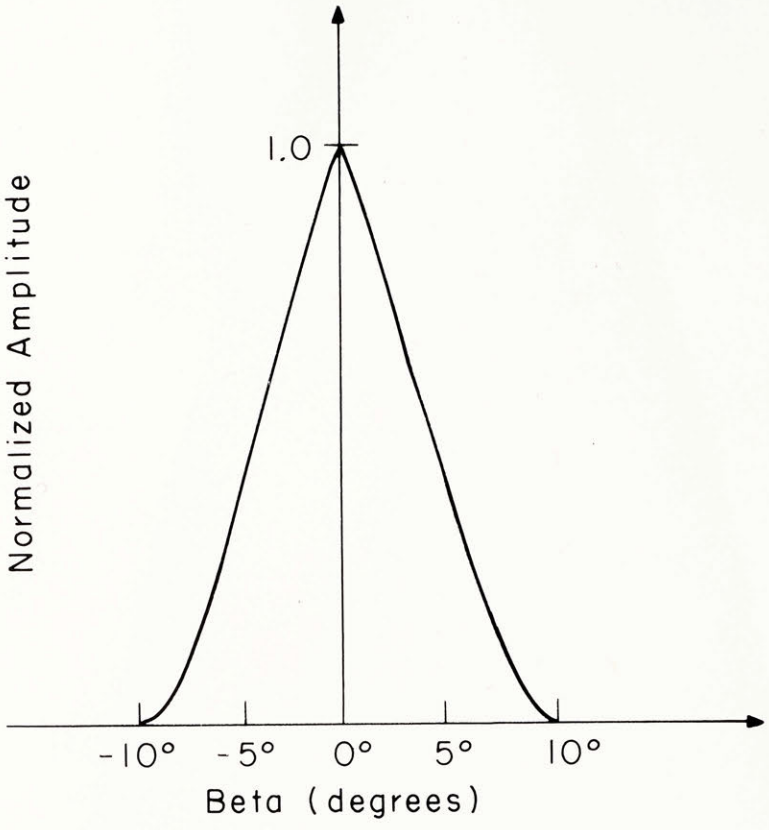

Fig. 6

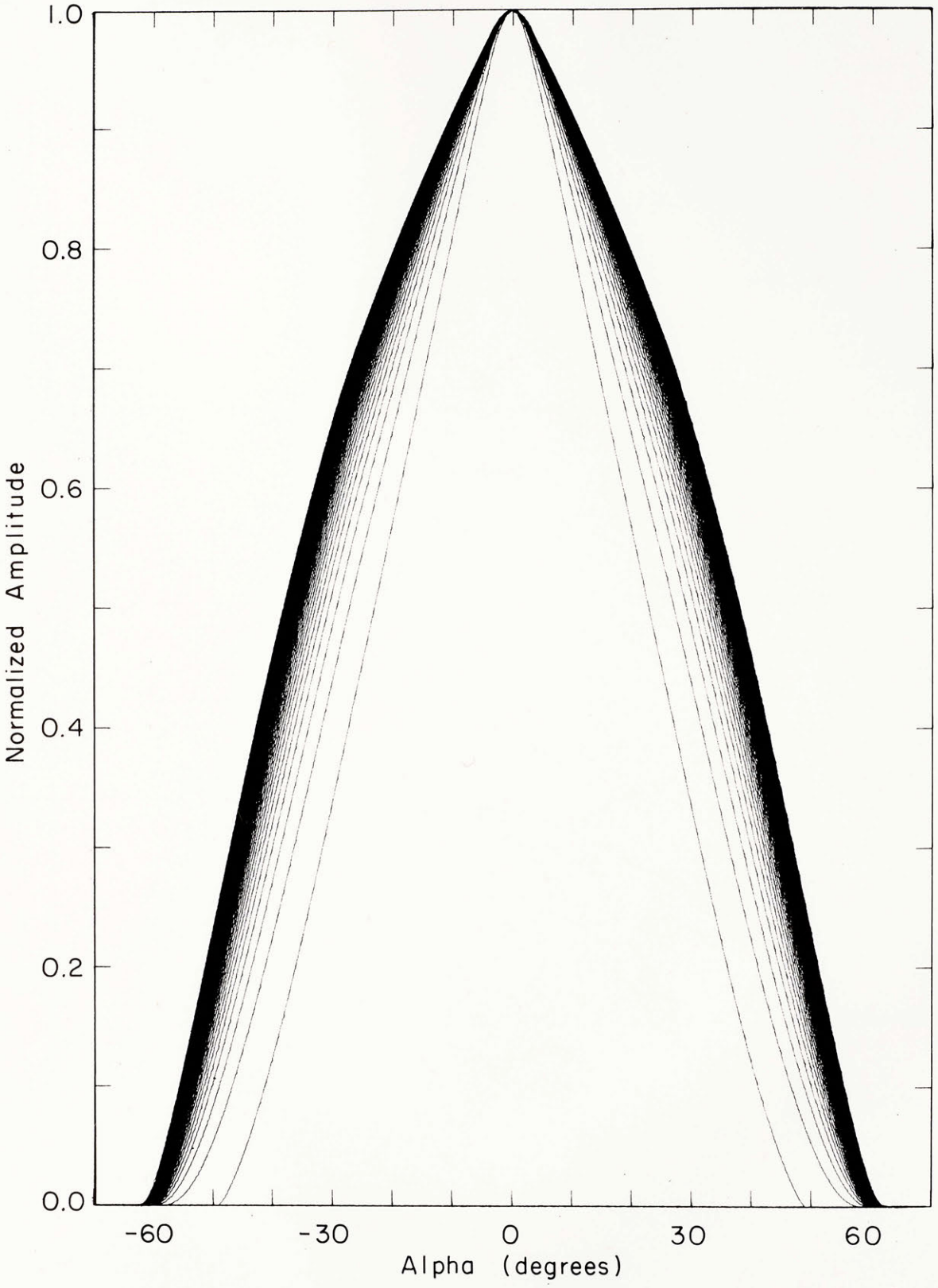
1.0
0.8
0.6
0.4
0.2
0.0
Normalized Amplitude
-60
-30
0
30
60
Alpha (degrees)

Fig. 7

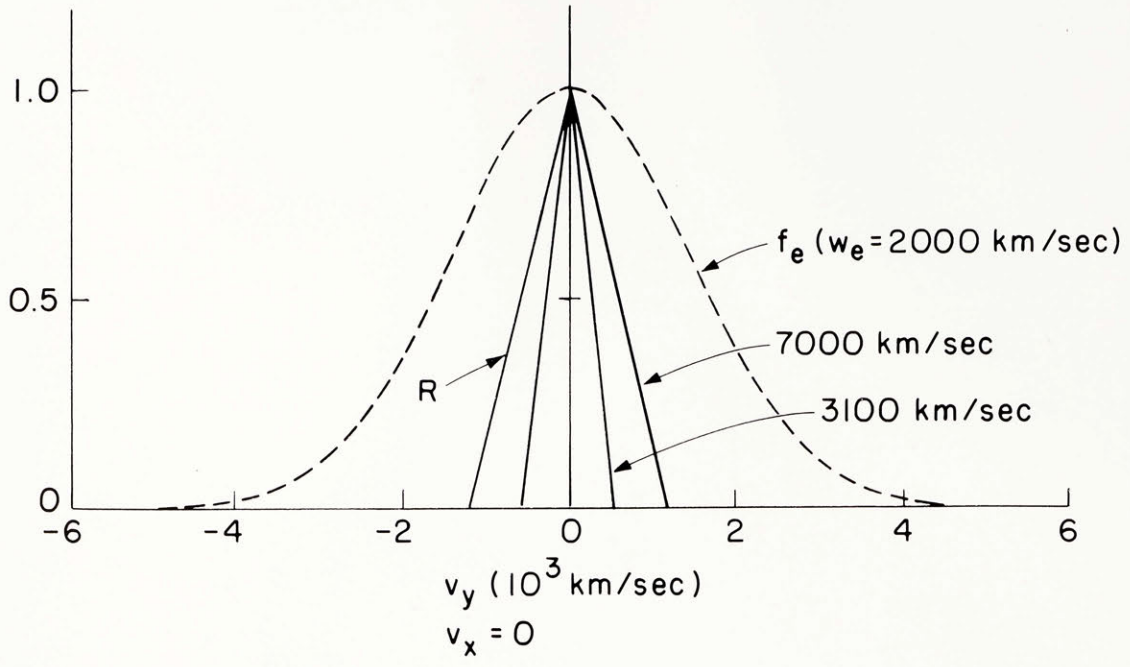
1.0
0.5
0
-6
-4
-2
0
2
4
6
f_e (w_e=2000 km/sec)
7000 km/sec
3100 km/sec
R
v_y (10^3 km/sec)
v_x = 0

Fig. 8

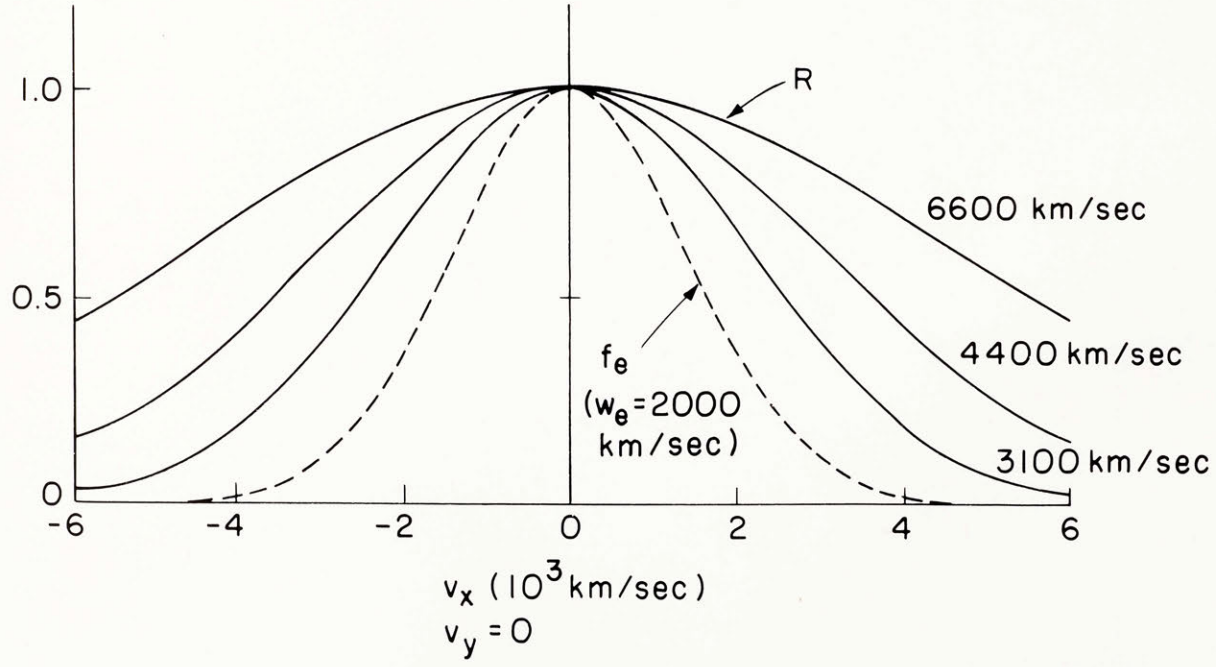
1.0
0.5
0
-6
-4
-2
0
2
4
6
R
6600 km/sec
4400 km/sec
3100 km/sec
f_e
(w_e=2000
km/sec)
v_x (10^3 km/sec)
v_y = 0

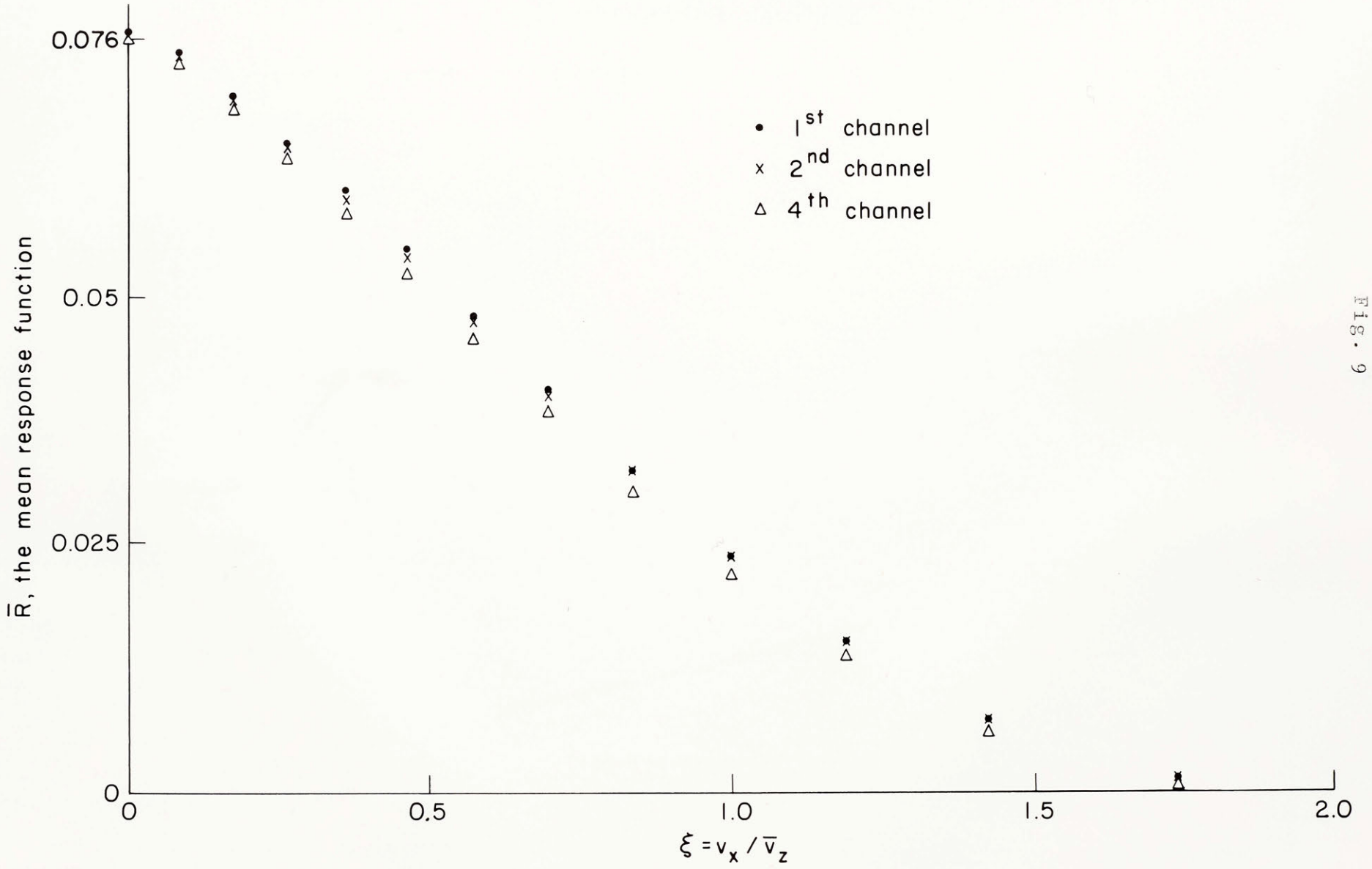
0.076
0.05
0.025
0
0
0.5
1.0
1.5
2.0
$\bar{R}$, the mean response function
$\xi = v_x / \bar{v}_z$
• 1st channel
x 2nd channel
△ 4th channel

Fig. 9

Fig. 10

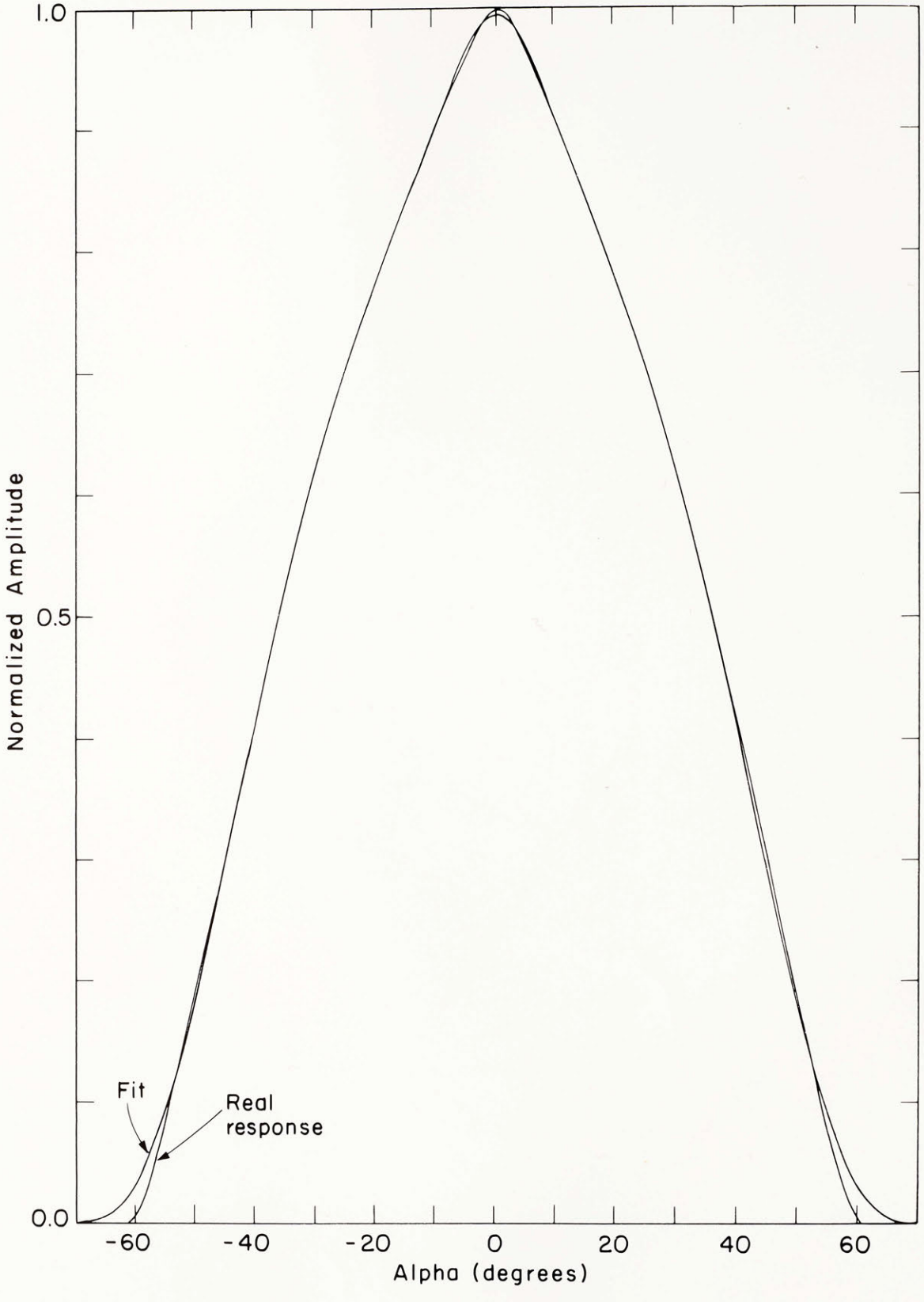
1.0
0.5
0.0
Normalized Amplitude
Fit
Real
response
-60
-40
-20
0
20
40
60
Alpha (degrees)

Fig. 11

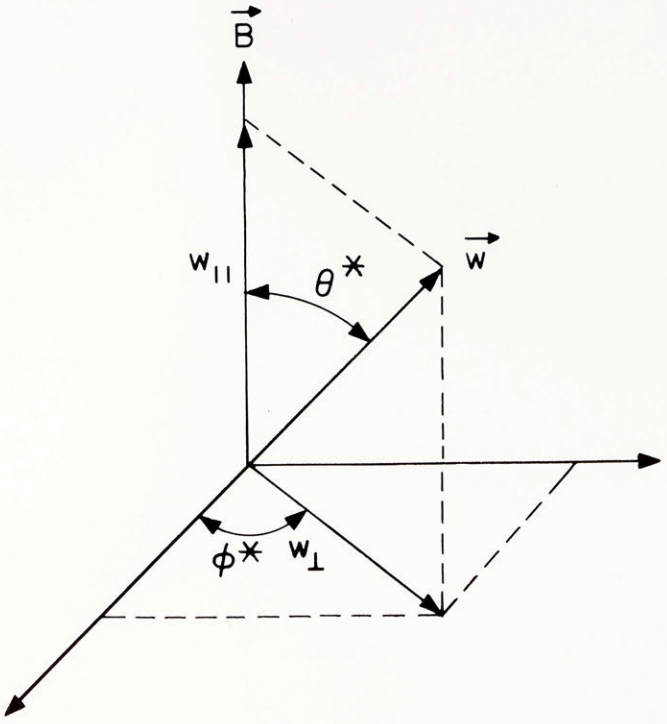

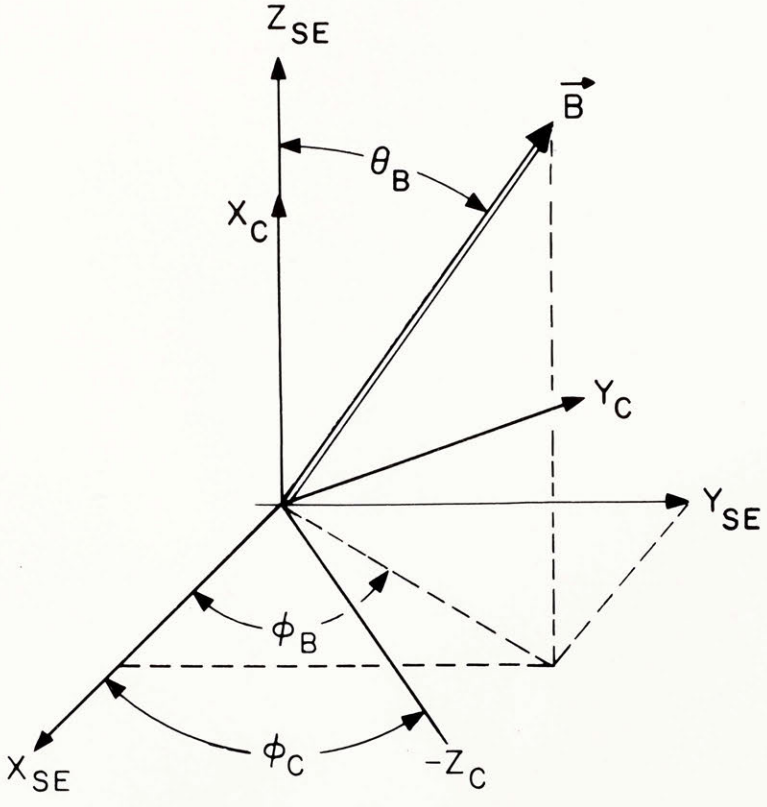

Fig. 12

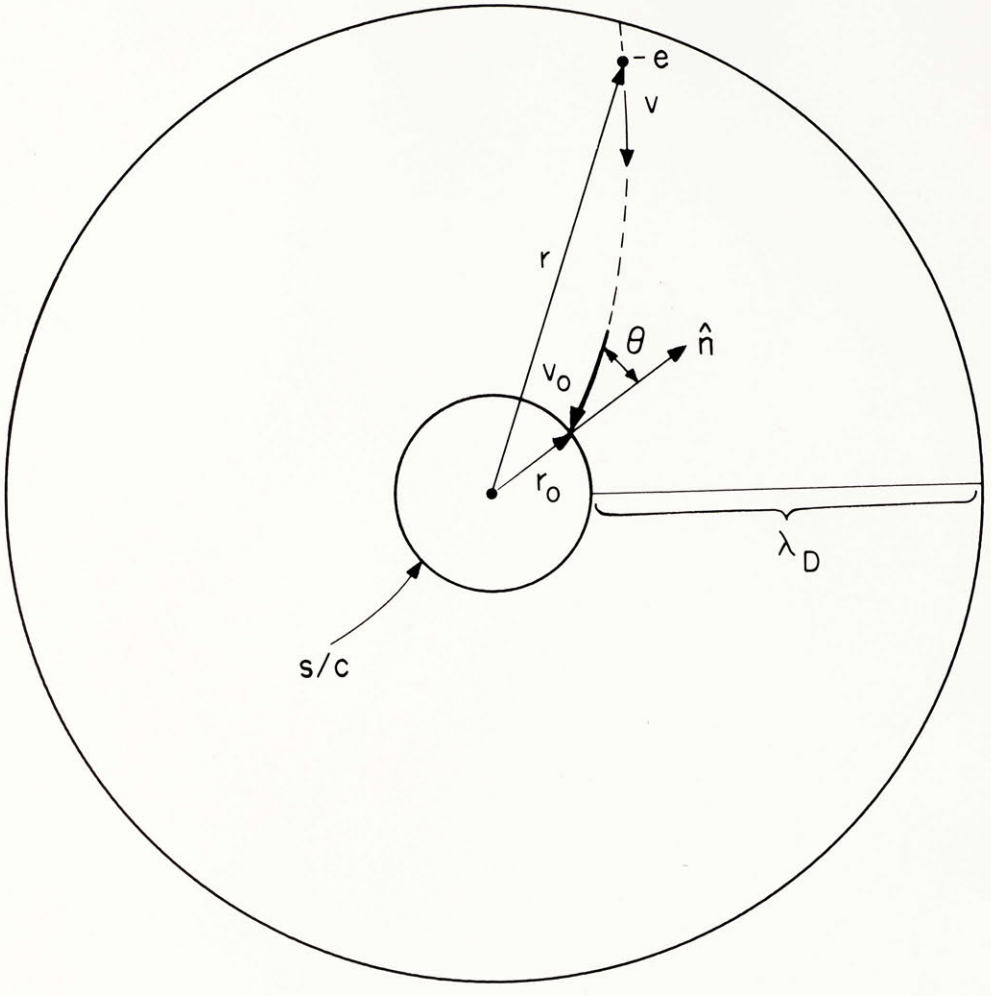

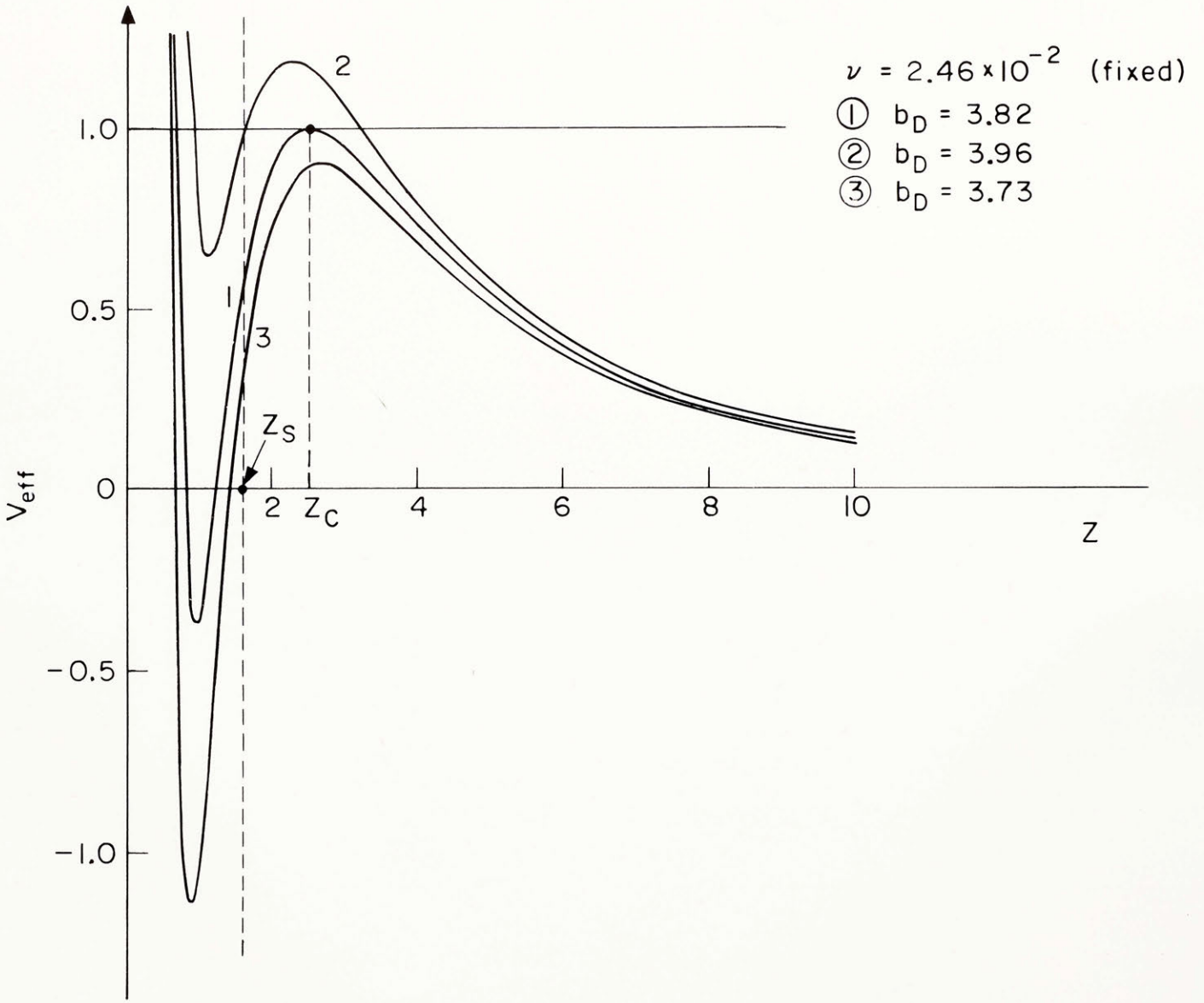
$\nu = 2.46 \times 10^{-2}$ (fixed)
① $b_D = 3.82$
② $b_D = 3.96$
③ $b_D = 3.73$
1.0
0.5
0
−0.5
−1.0
V_{eff}
2
1
3
Z_S
2
Z_C
4
6
8
10
Z

Fig. 13

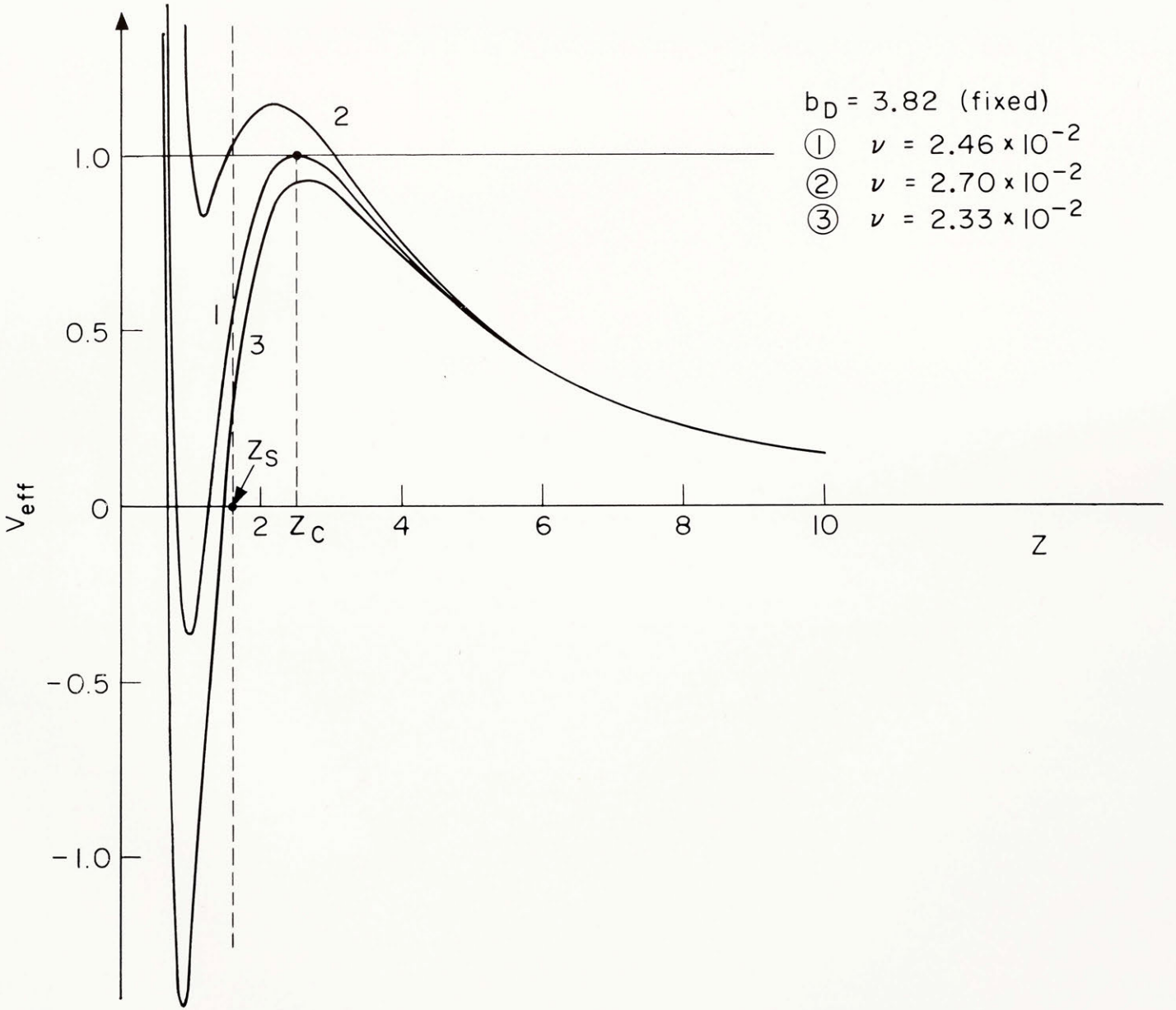
b_D = 3.82 (fixed)
① $\nu = 2.46 \times 10^{-2}$
② $\nu = 2.70 \times 10^{-2}$
③ $\nu = 2.33 \times 10^{-2}$
1.0
0.5
0
-0.5
-1.0
V_{eff}
2
1
3
Z_S
2
Z_C
4
6
8
10
Z

Fig. 14

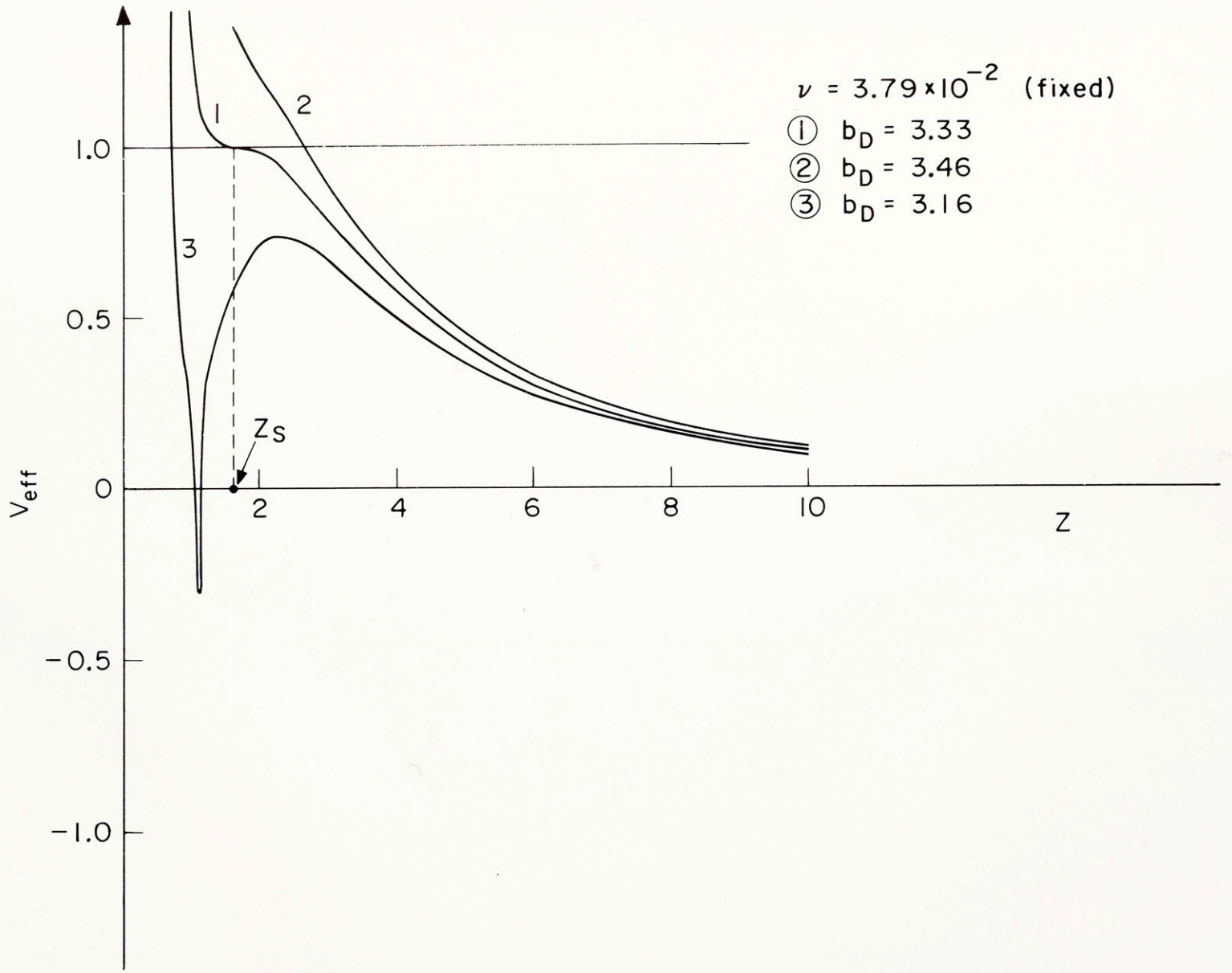
$\nu = 3.79 \times 10^{-2}$ (fixed)
① $b_D = 3.33$
② $b_D = 3.46$
③ $b_D = 3.16$
1
2
3
1.0
0.5
0
−0.5
−1.0
V_{eff}
Z_S
2
4
6
8
10
Z

Fig. 15

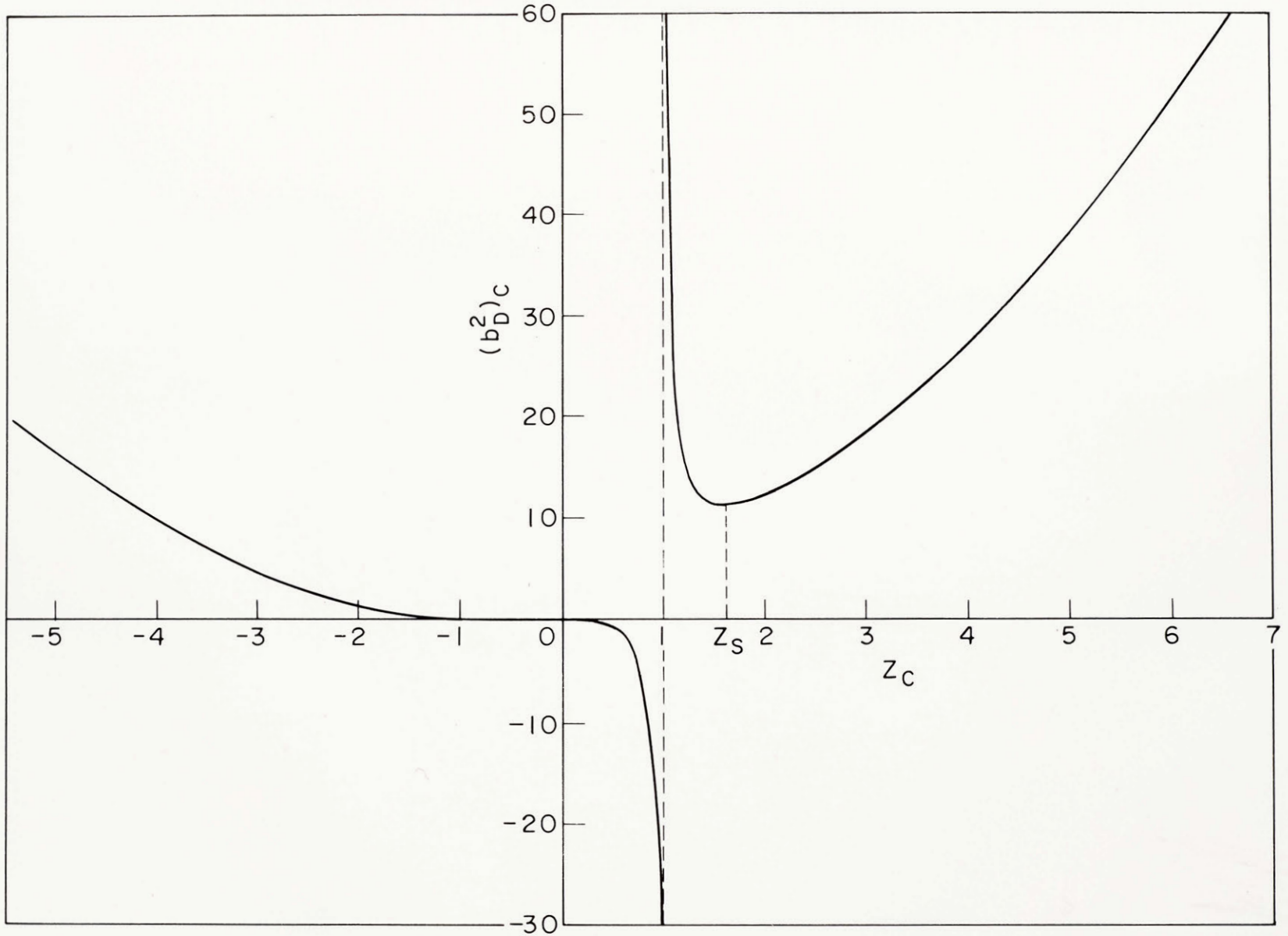

Fig. 16

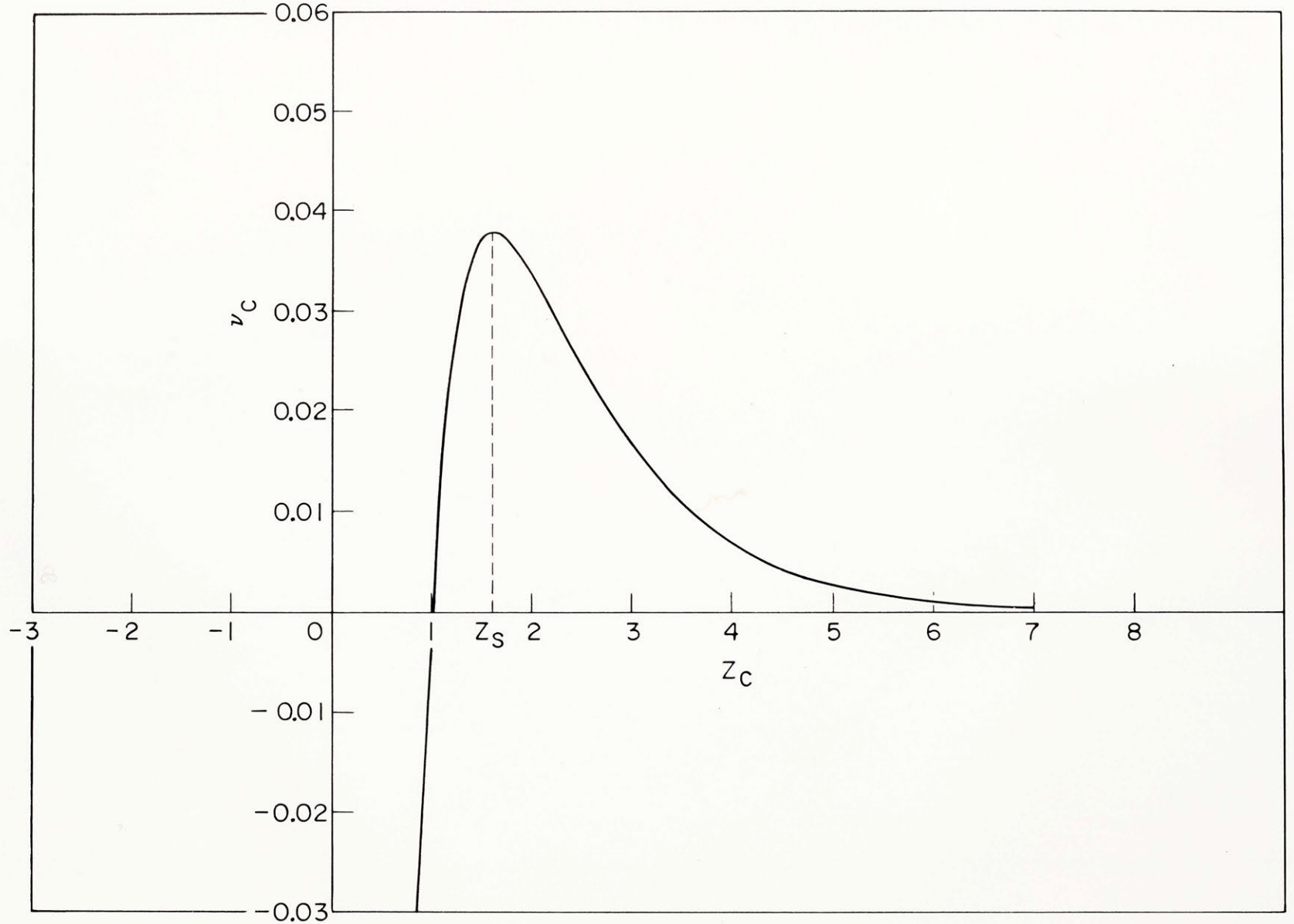

Fig. 17

Fig. 18

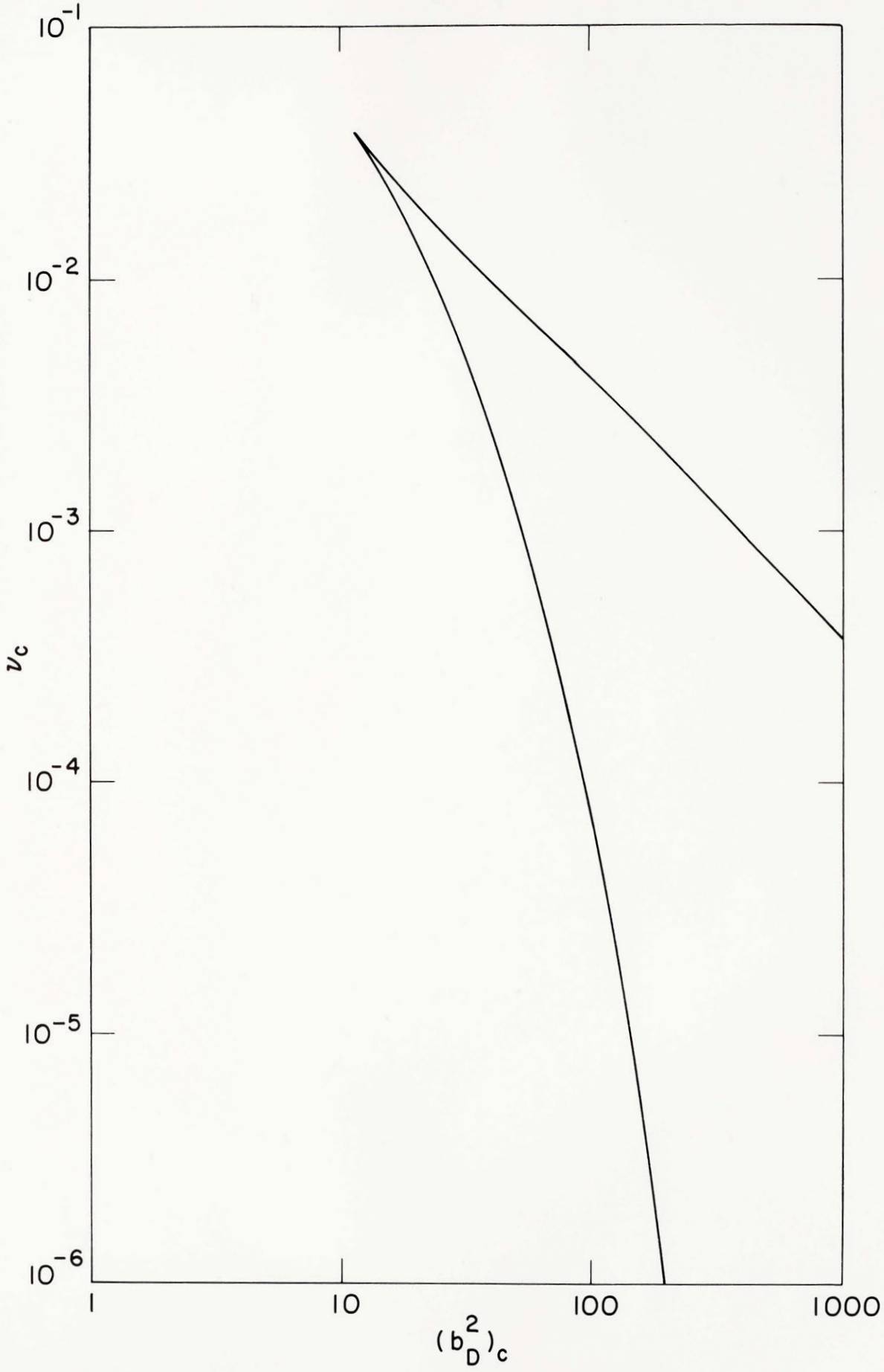

Fig. 19

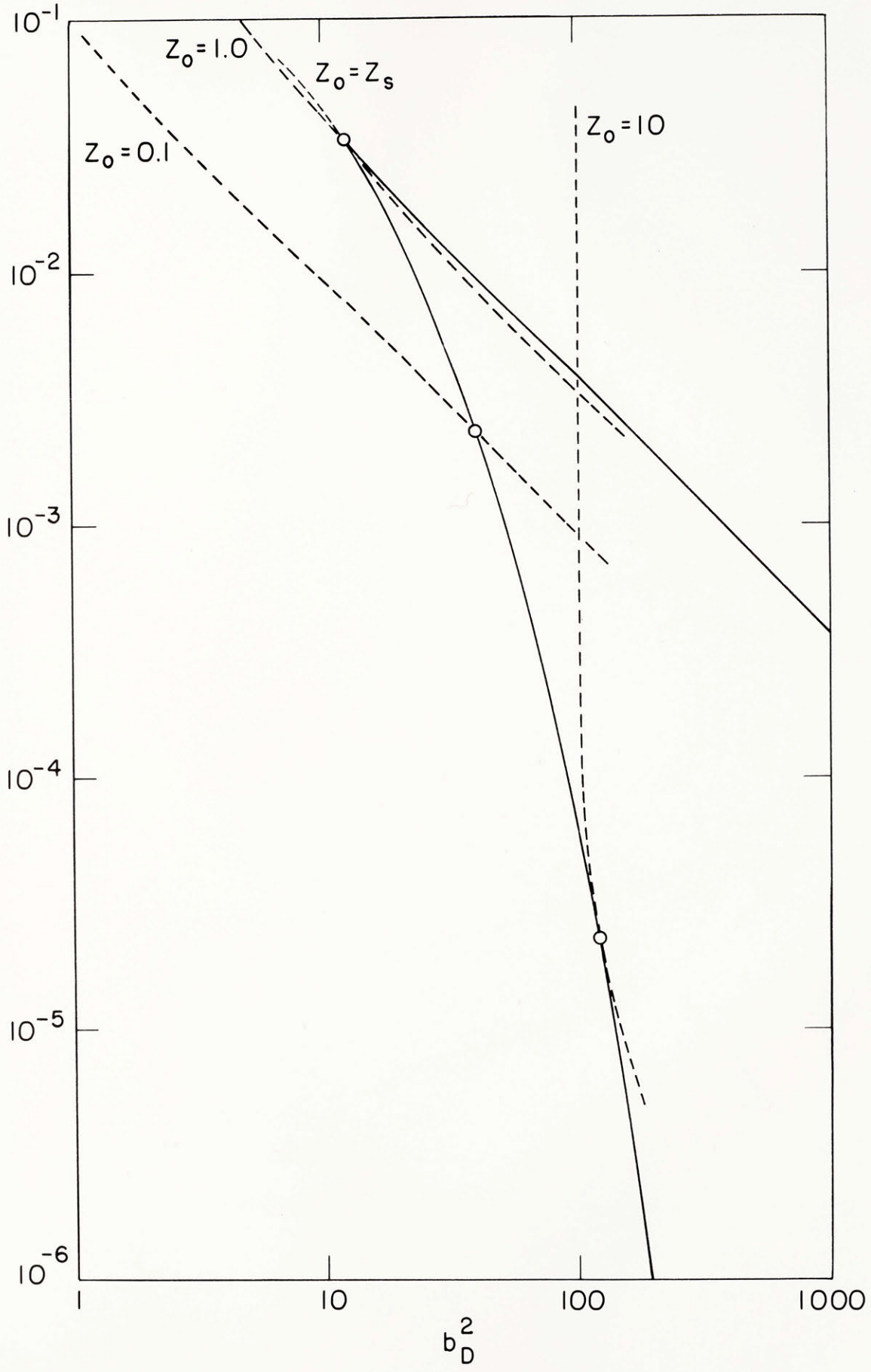

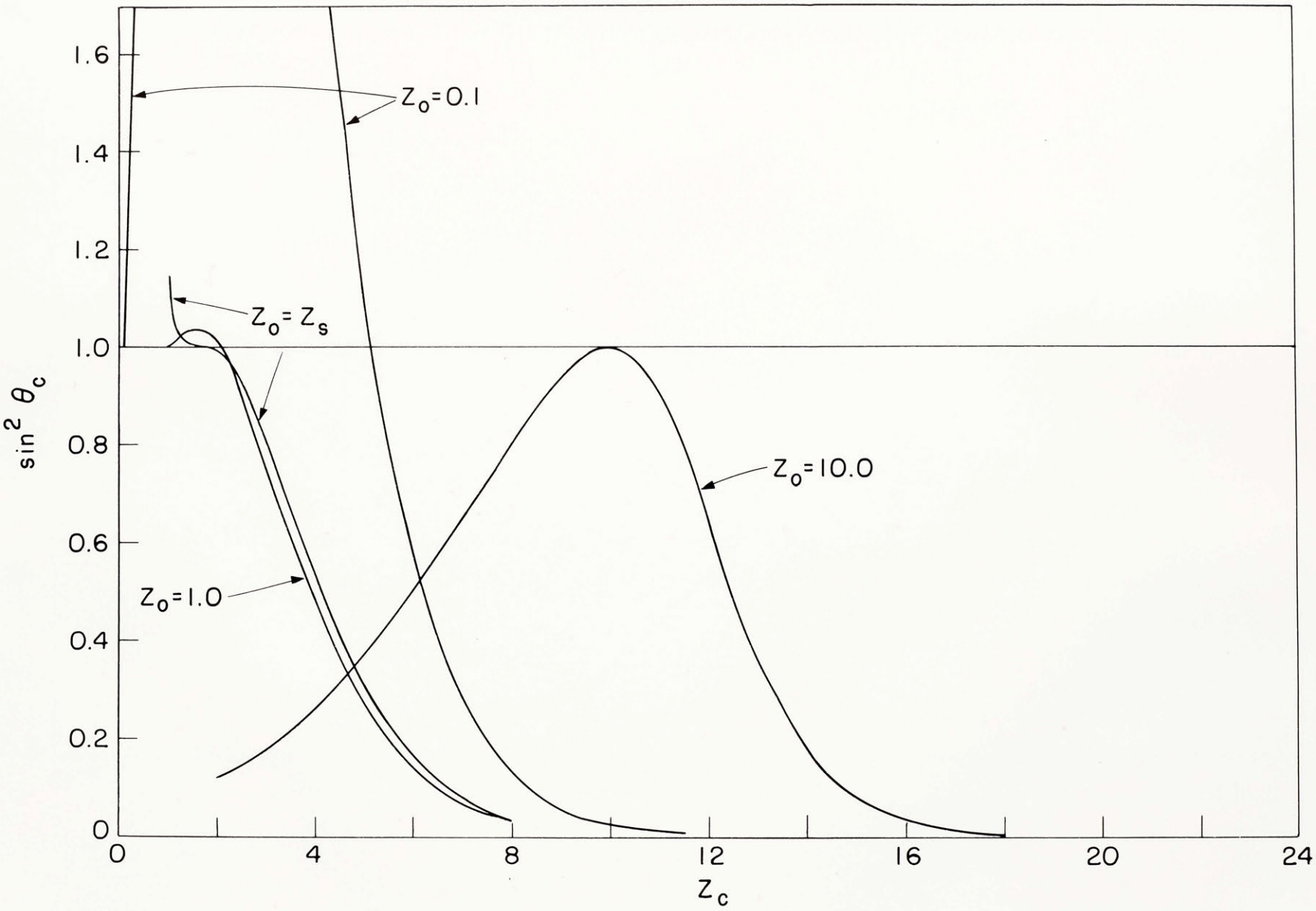
1.6
1.4
1.2
1.0
0.8
0.6
0.4
0.2
0
$\sin^2 \theta_c$
$Z_0 = 0.1$
$Z_0 = Z_s$
$Z_0 = 1.0$
$Z_0 = 10.0$
0
4
8
12
16
20
24
Z_c

Fig. 20

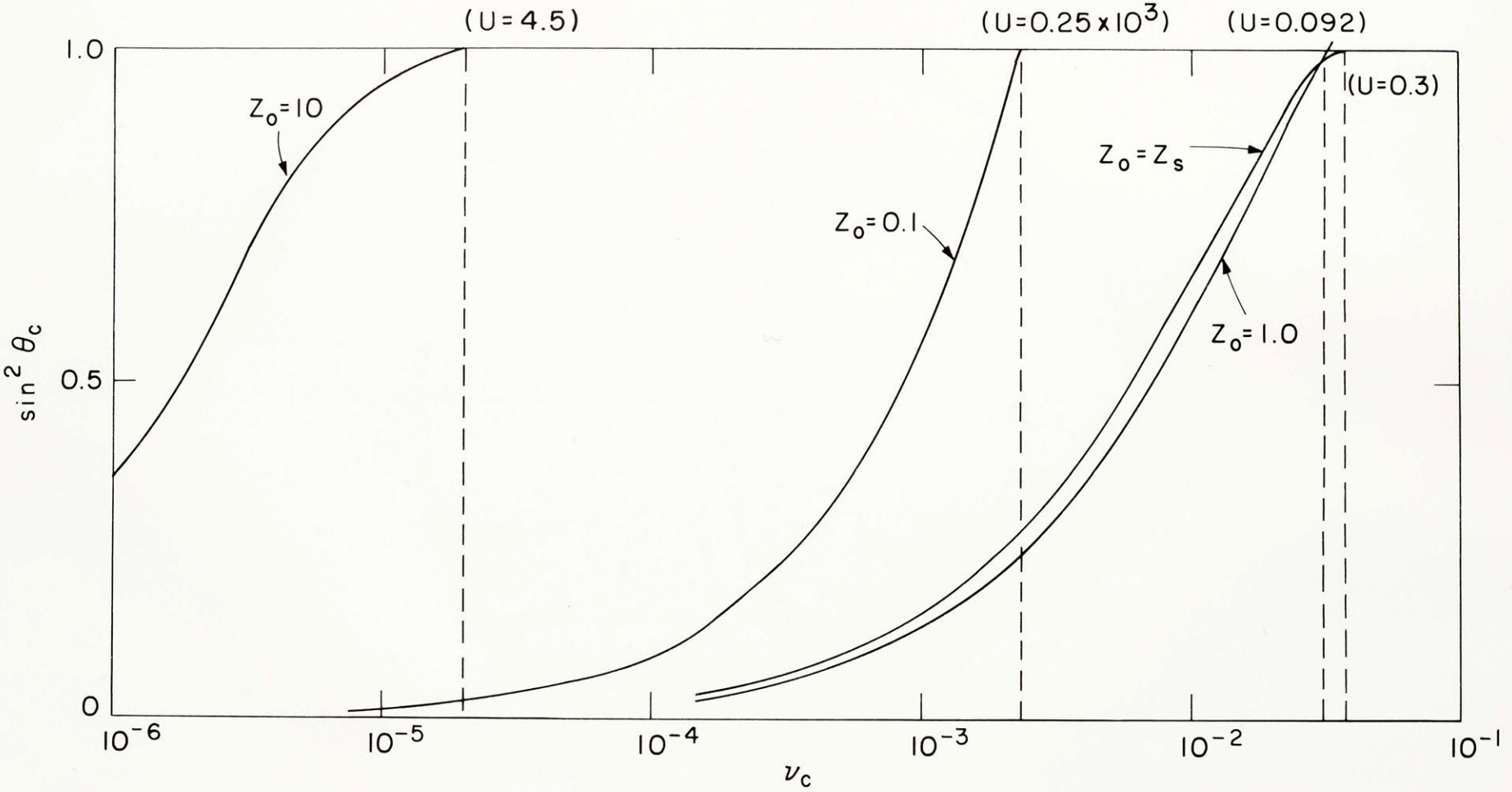
(U = 4.5)
(U=0.25 x 10^3)
(U=0.092)
(U=0.3)
1.0
0.5
0
sin^2 θc
Z0=10
Z0=0.1
Z0 = Zs
Z0=1.0
10^-6
10^-5
10^-4
10^-3
10^-2
10^-1
νc

Fig. 21

Fig. 22a

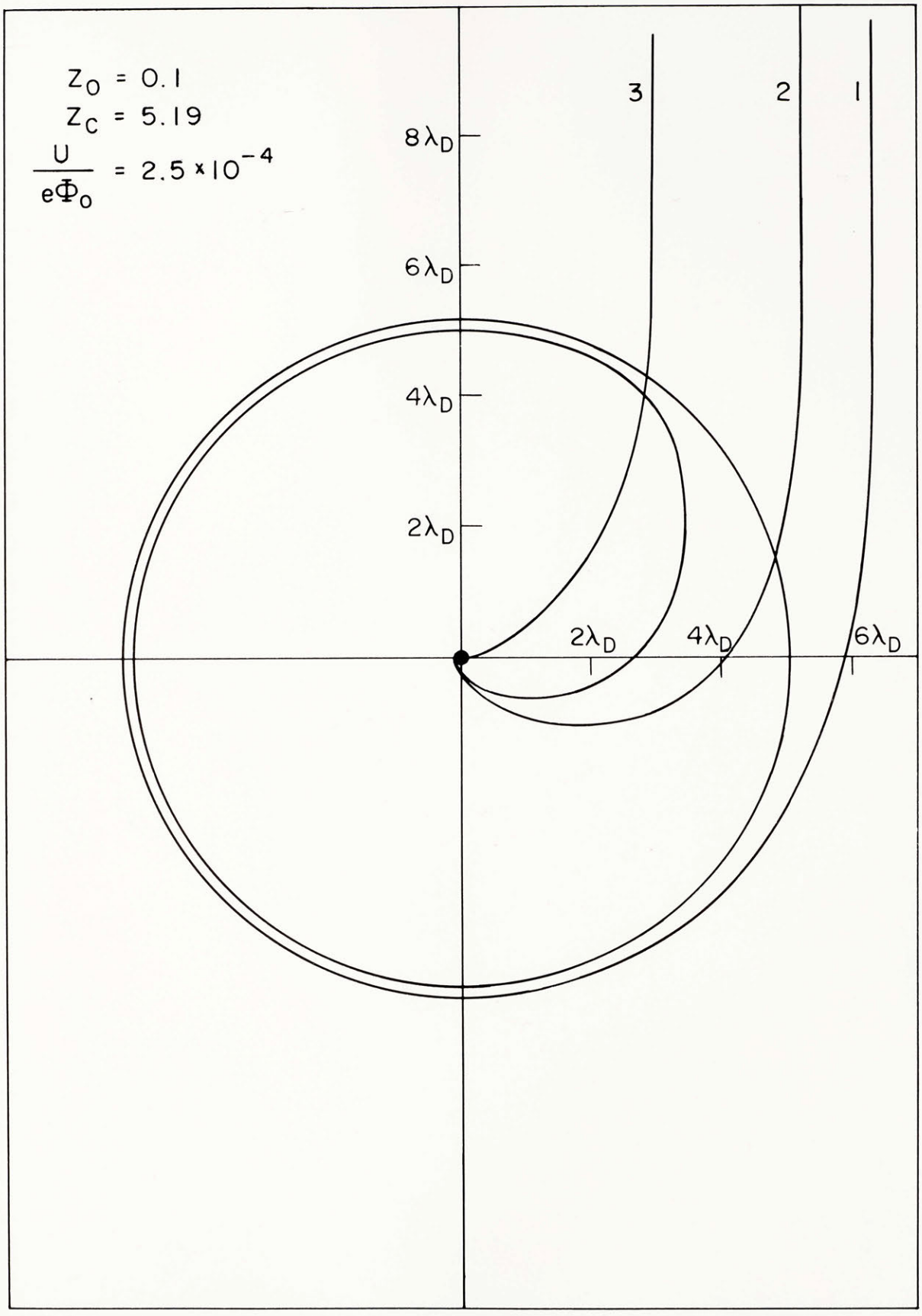
$Z_0 = 0.1$
$Z_C = 5.19$
$\frac{U}{e\Phi_0} = 2.5 \times 10^{-4}$
3
2
1
$8\lambda_D$
$6\lambda_D$
$4\lambda_D$
$2\lambda_D$
$2\lambda_D$
$4\lambda_D$
$6\lambda_D$

Fig. 22b

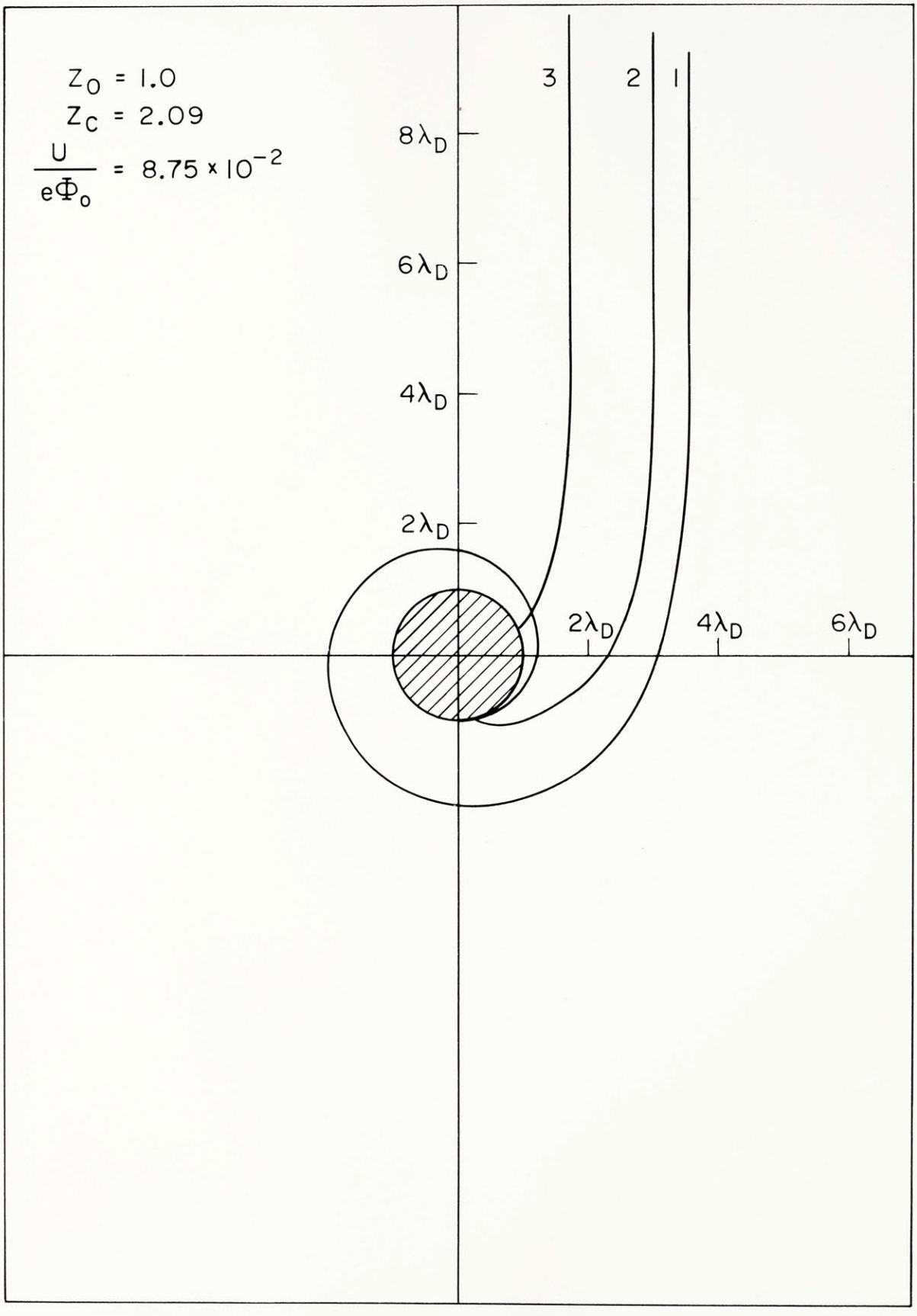
$Z_0 = 1.0$
$Z_C = 2.09$
$\frac{U}{e\Phi_0} = 8.75 \times 10^{-2}$
3
2
1
$8\lambda_D$
$6\lambda_D$
$4\lambda_D$
$2\lambda_D$
$2\lambda_D$
$4\lambda_D$
$6\lambda_D$

Fig. 22c

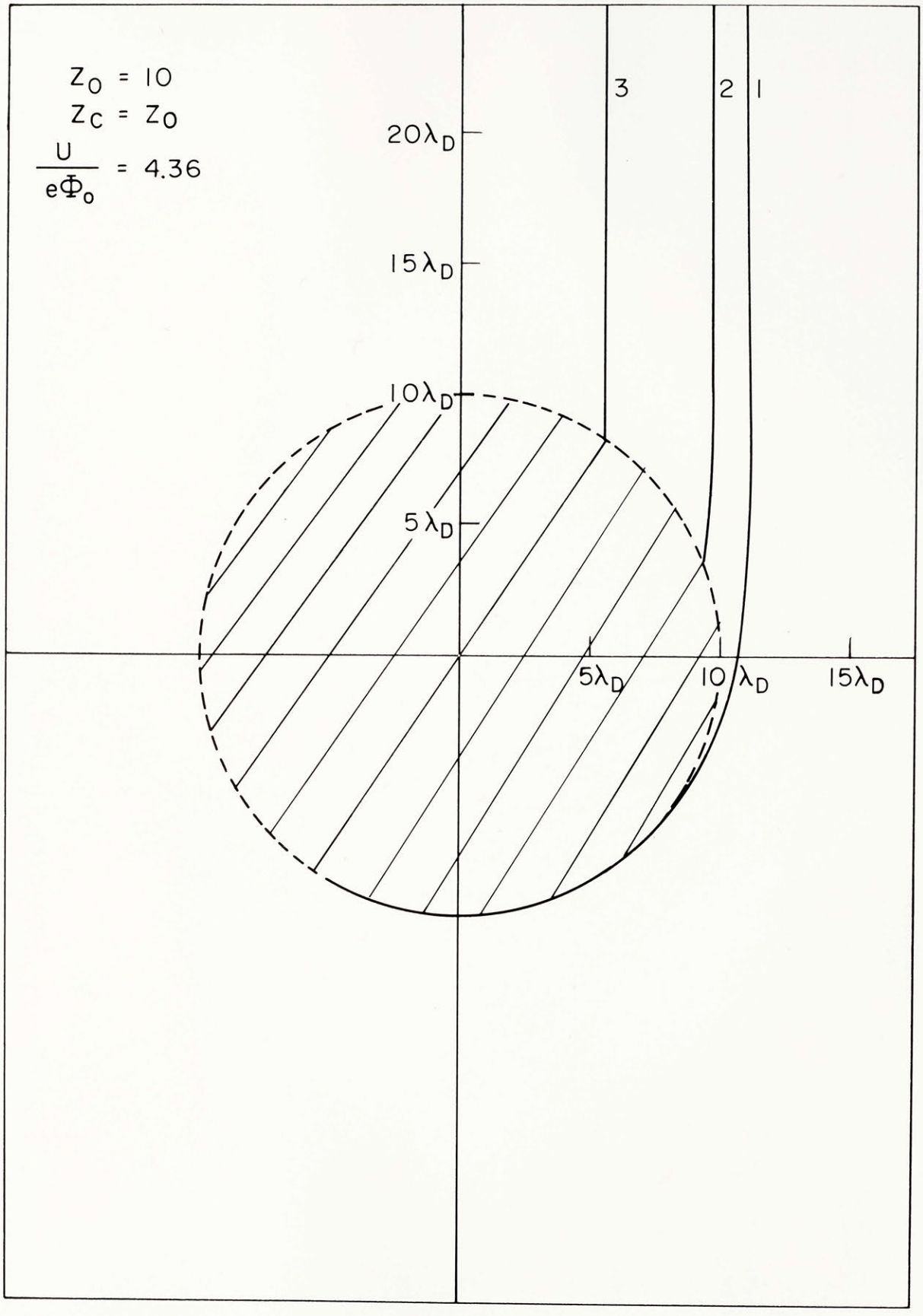
$Z_0 = 10$
$Z_c = Z_0$
$\frac{U}{e\Phi_0} = 4.36$
3
2
1
$20\lambda_D$
$15\lambda_D$
$10\lambda_D$
$5\lambda_D$
$5\lambda_D$
$10\lambda_D$
$15\lambda_D$

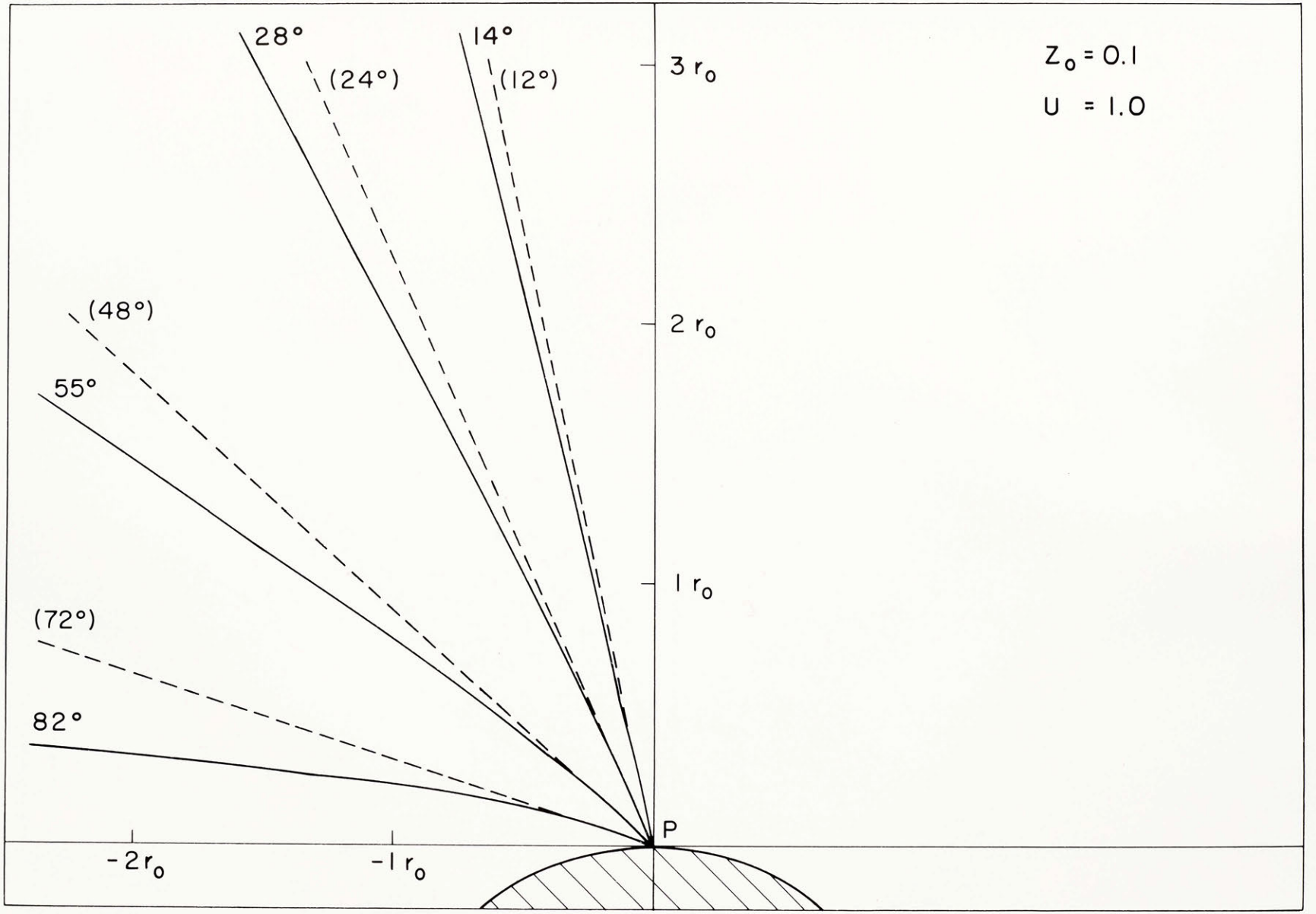

Fig. 23a

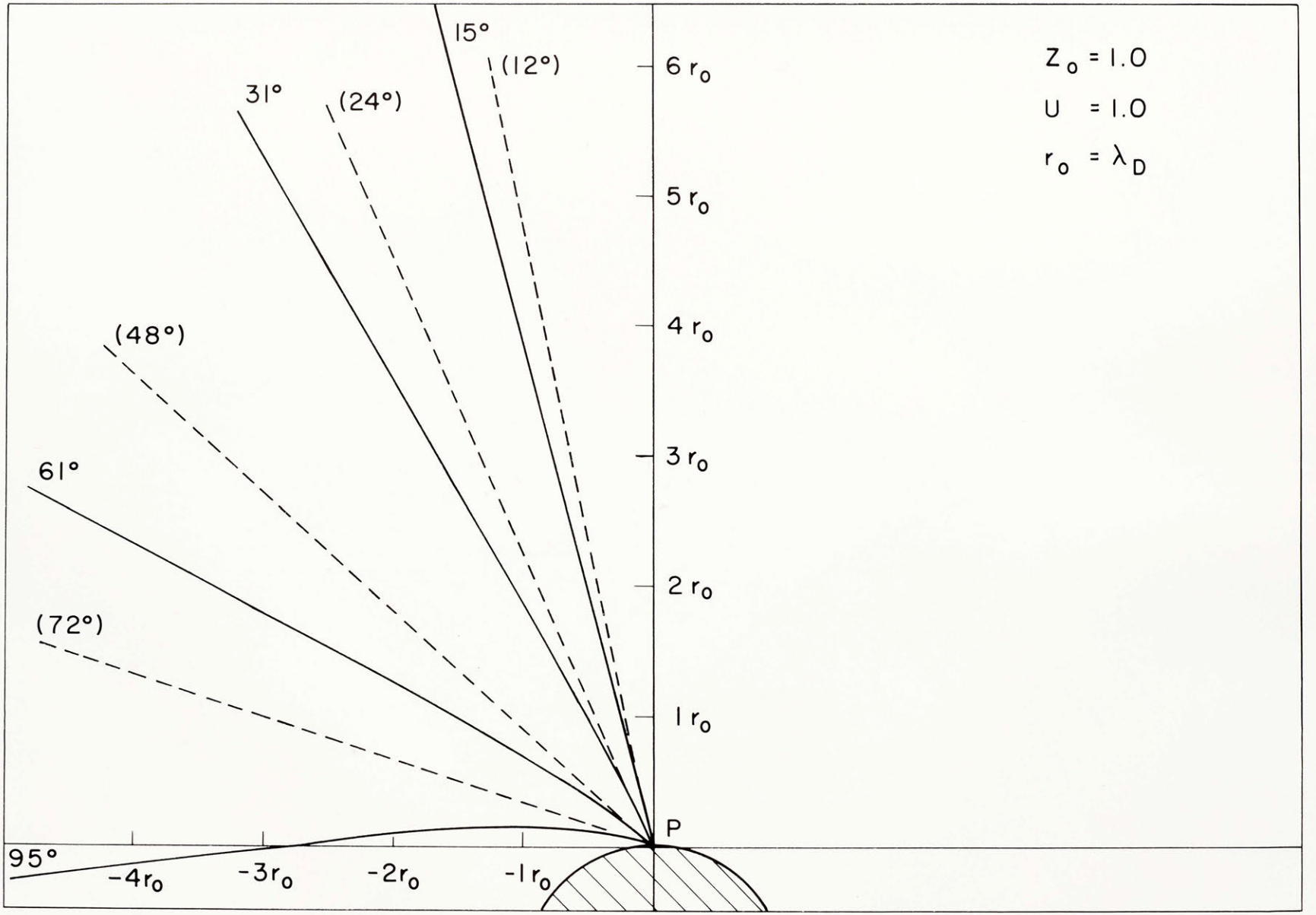
15°
(12°)
31°
(24°)
(48°)
61°
(72°)
95°
$Z_o = 1.0$
$U = 1.0$
$r_o = \lambda_D$
$6\,r_o$
$5\,r_o$
$4\,r_o$
$3\,r_o$
$2\,r_o$
$1\,r_o$
P
$-4r_o$
$-3r_o$
$-2r_o$
$-1\,r_o$

Fig. 23b

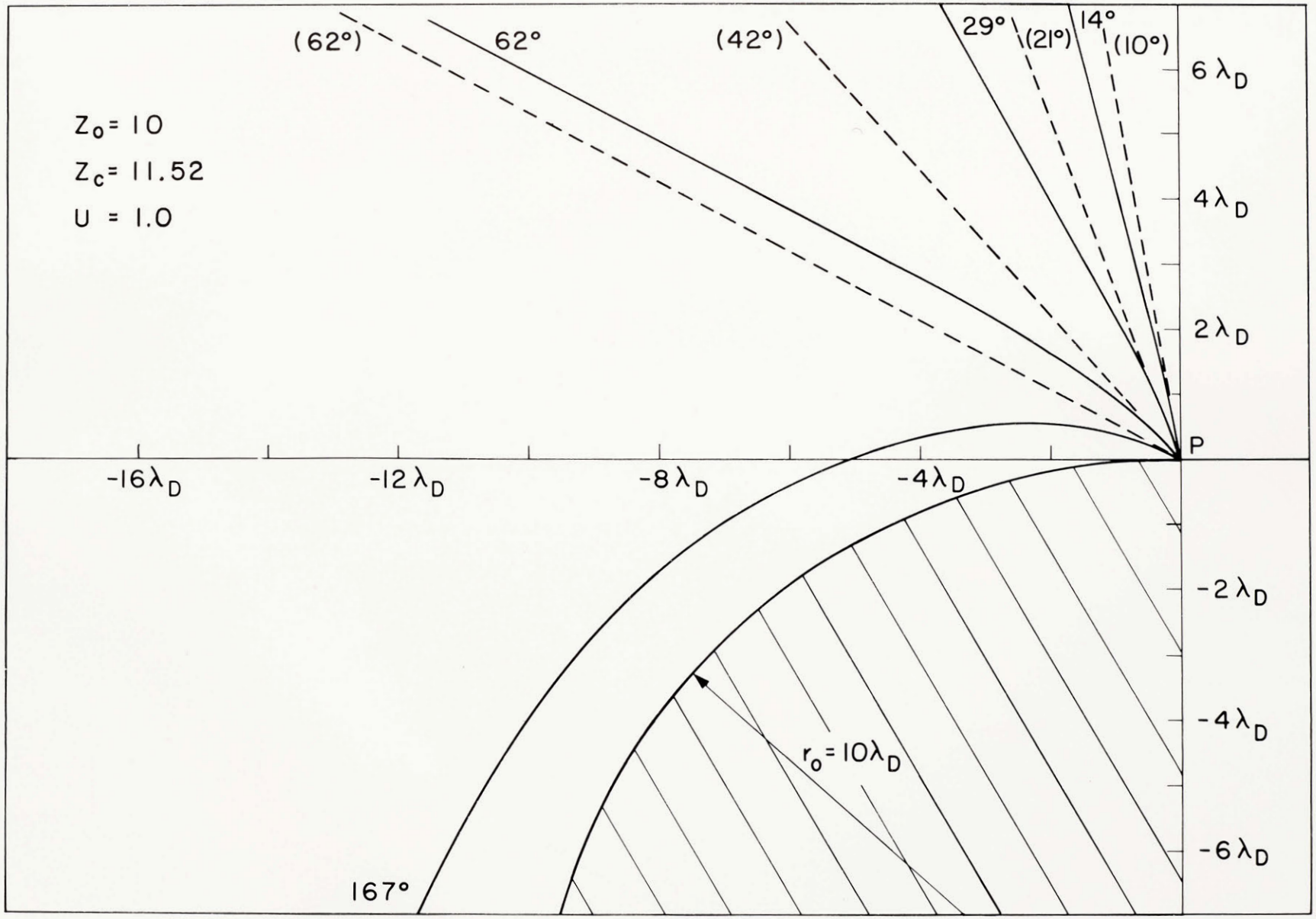
(62°)
62°
(42°)
29°
(21°)
14°
(10°)
$Z_o = 10$
$Z_c = 11.52$
U = 1.0
$6\lambda_D$
$4\lambda_D$
$2\lambda_D$
P
$-16\lambda_D$
$-12\lambda_D$
$-8\lambda_D$
$-4\lambda_D$
$-2\lambda_D$
$-4\lambda_D$
$-6\lambda_D$
$r_o = 10\lambda_D$
167°

Fig. 23c

Fig. 24

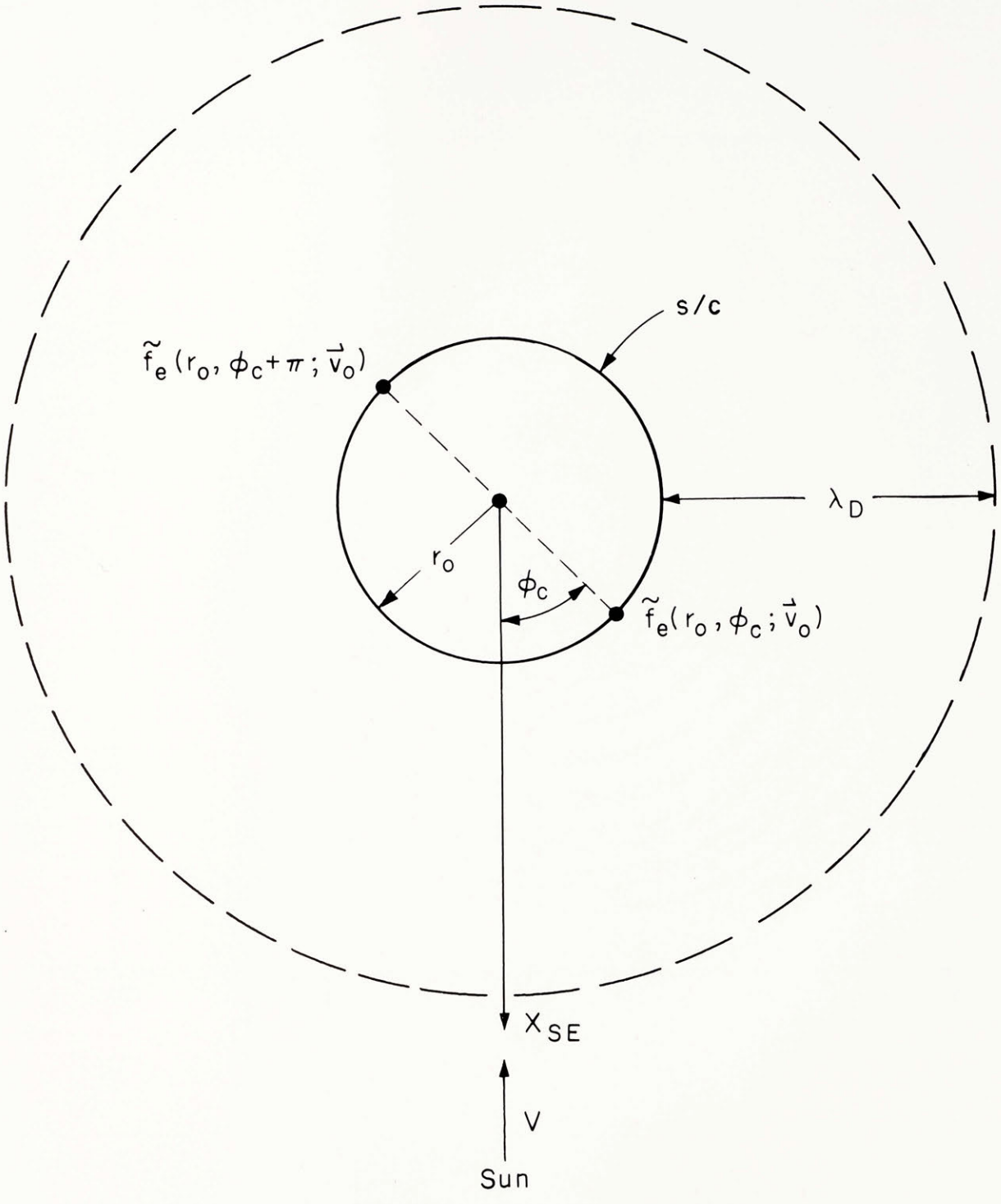
s/c
$\tilde{f}_e(r_o, \phi_c+\pi; \vec{v}_o)$
λ_D
r_o
ϕ_c
$\tilde{f}_e(r_o, \phi_c; \vec{v}_o)$
X_{SE}
V
Sun

Fig. 25a

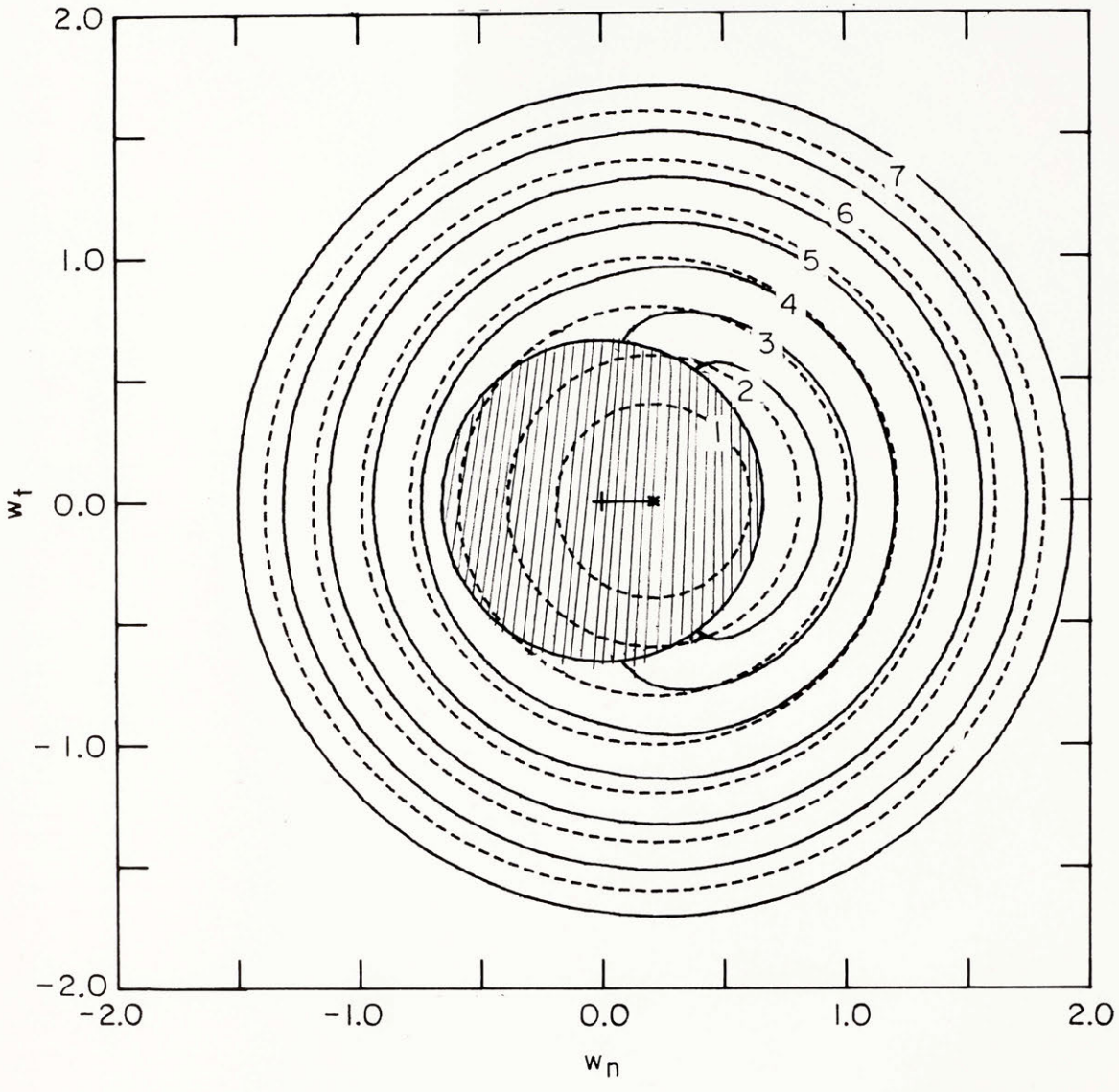

Fig. 25b

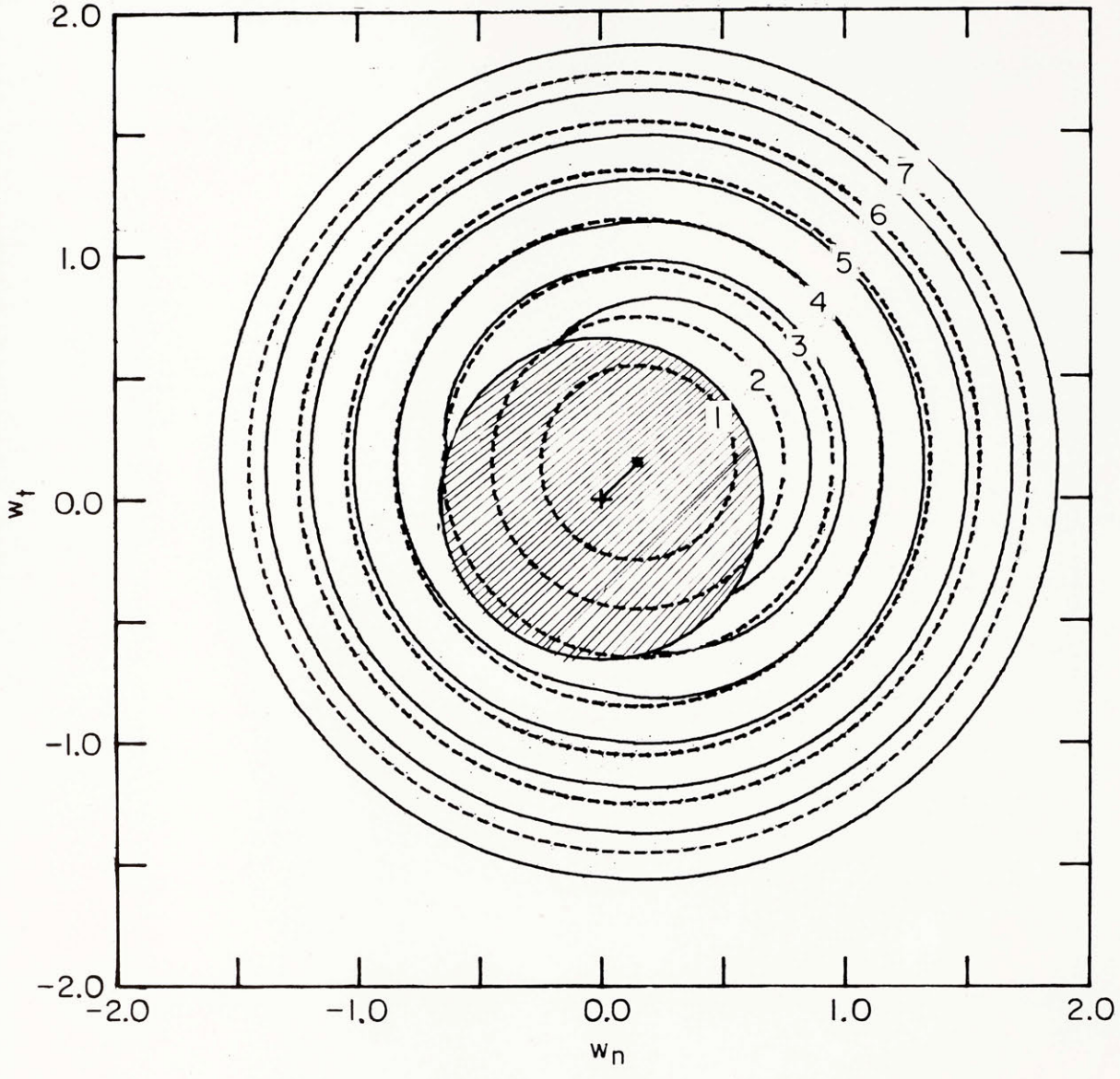

Fig. 25c

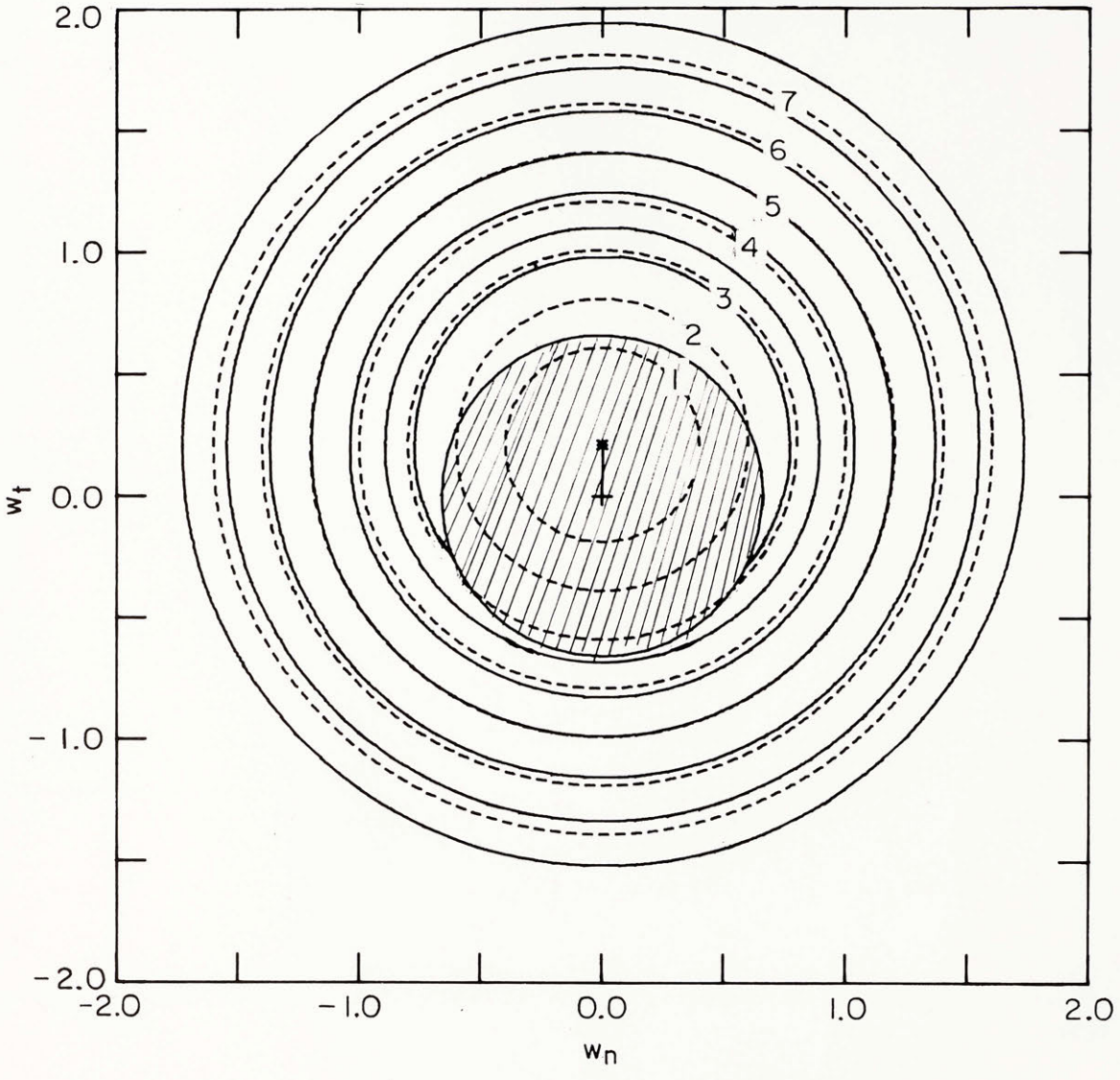

Fig. 25d

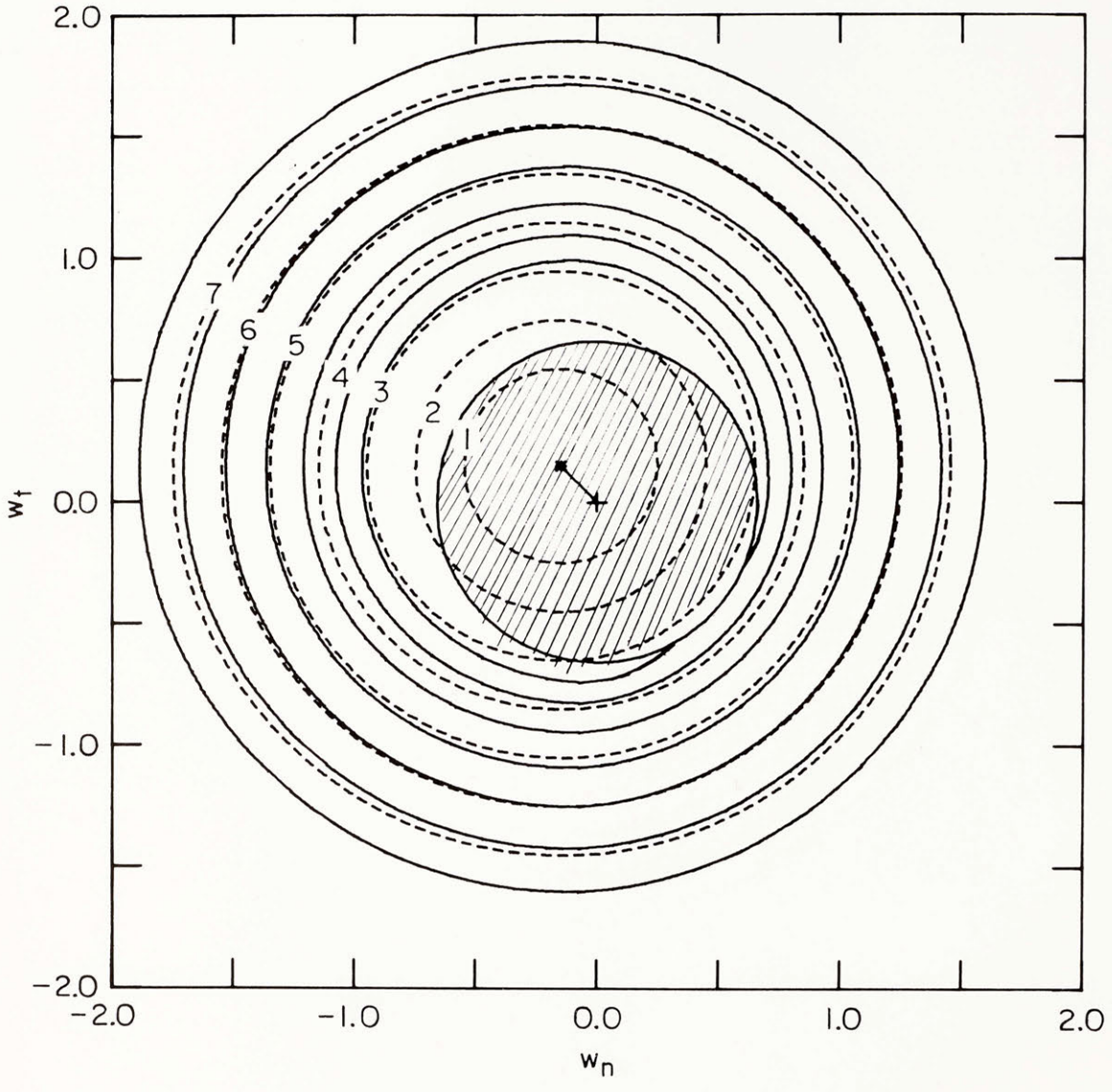

Fig. 25e

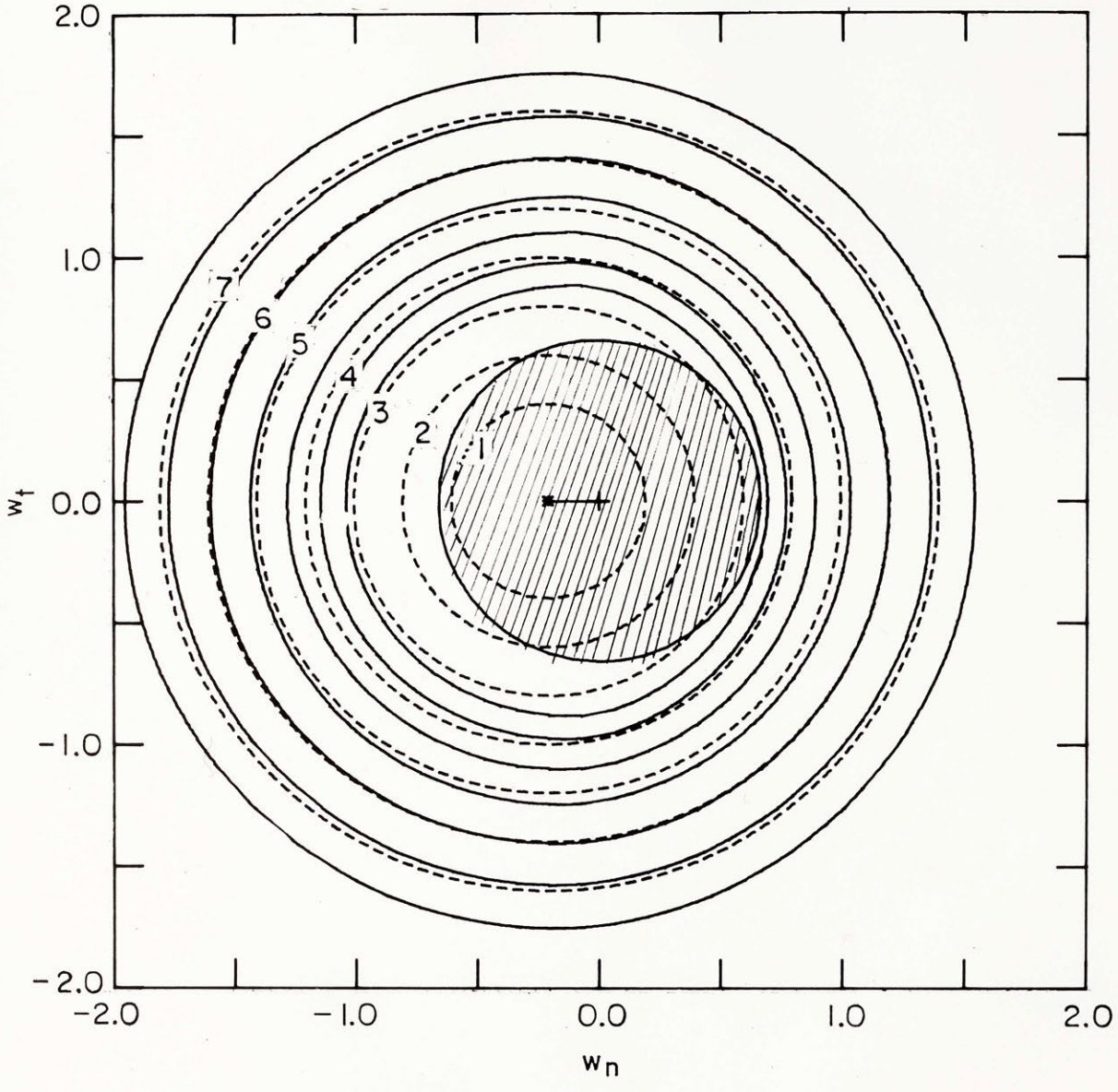

Fig. 26a

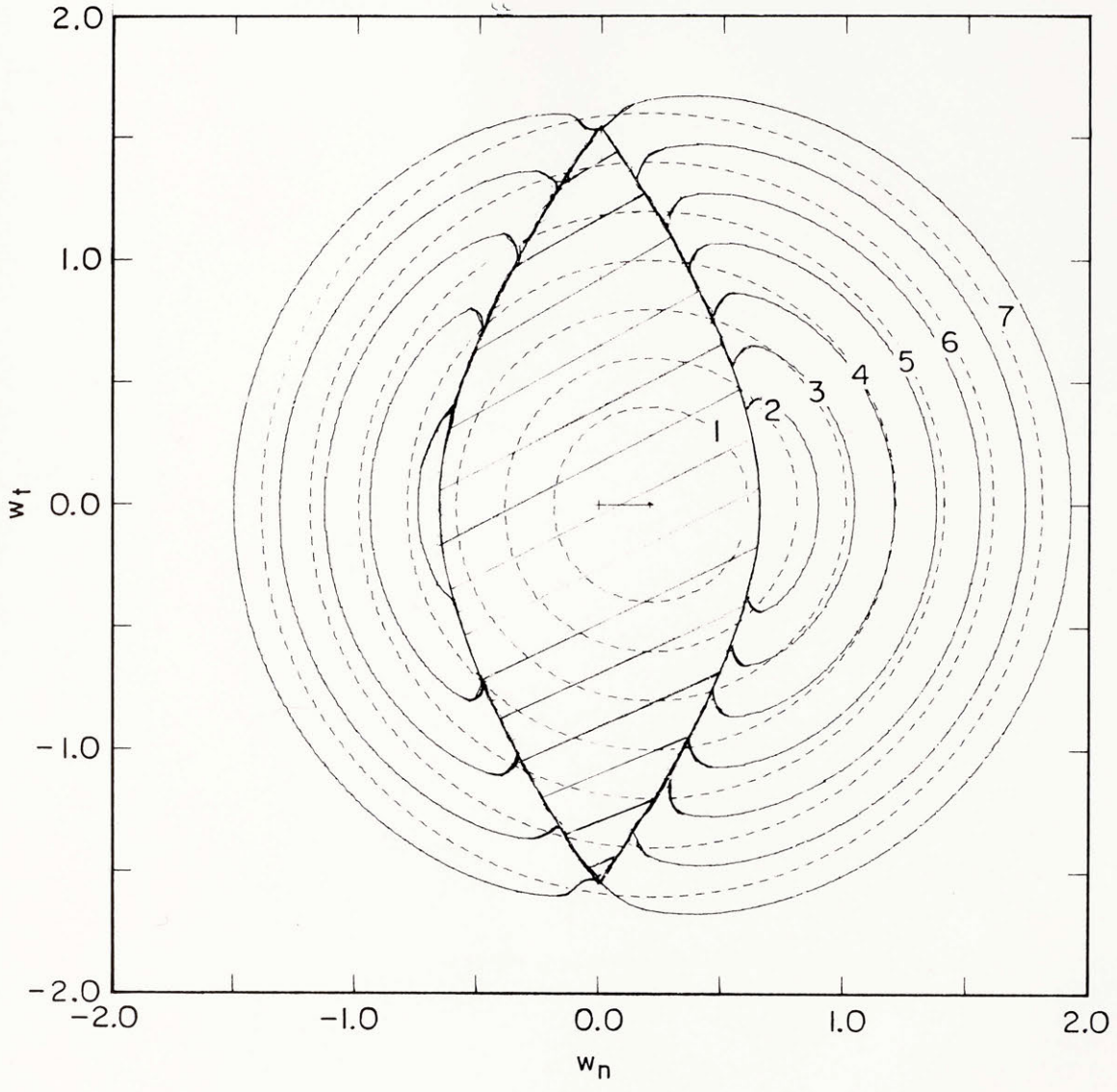

Fig.26b

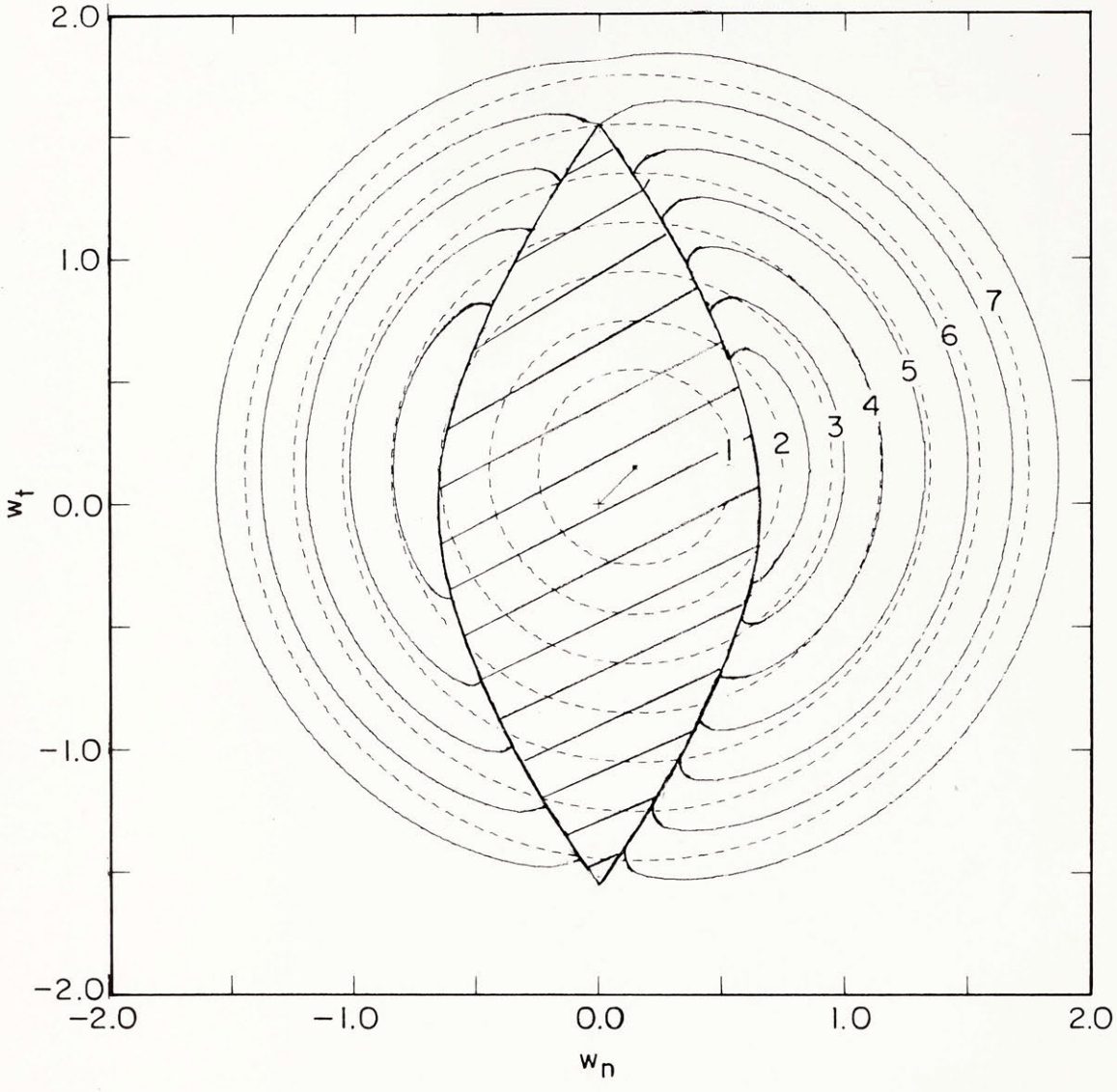

Fig. 26c

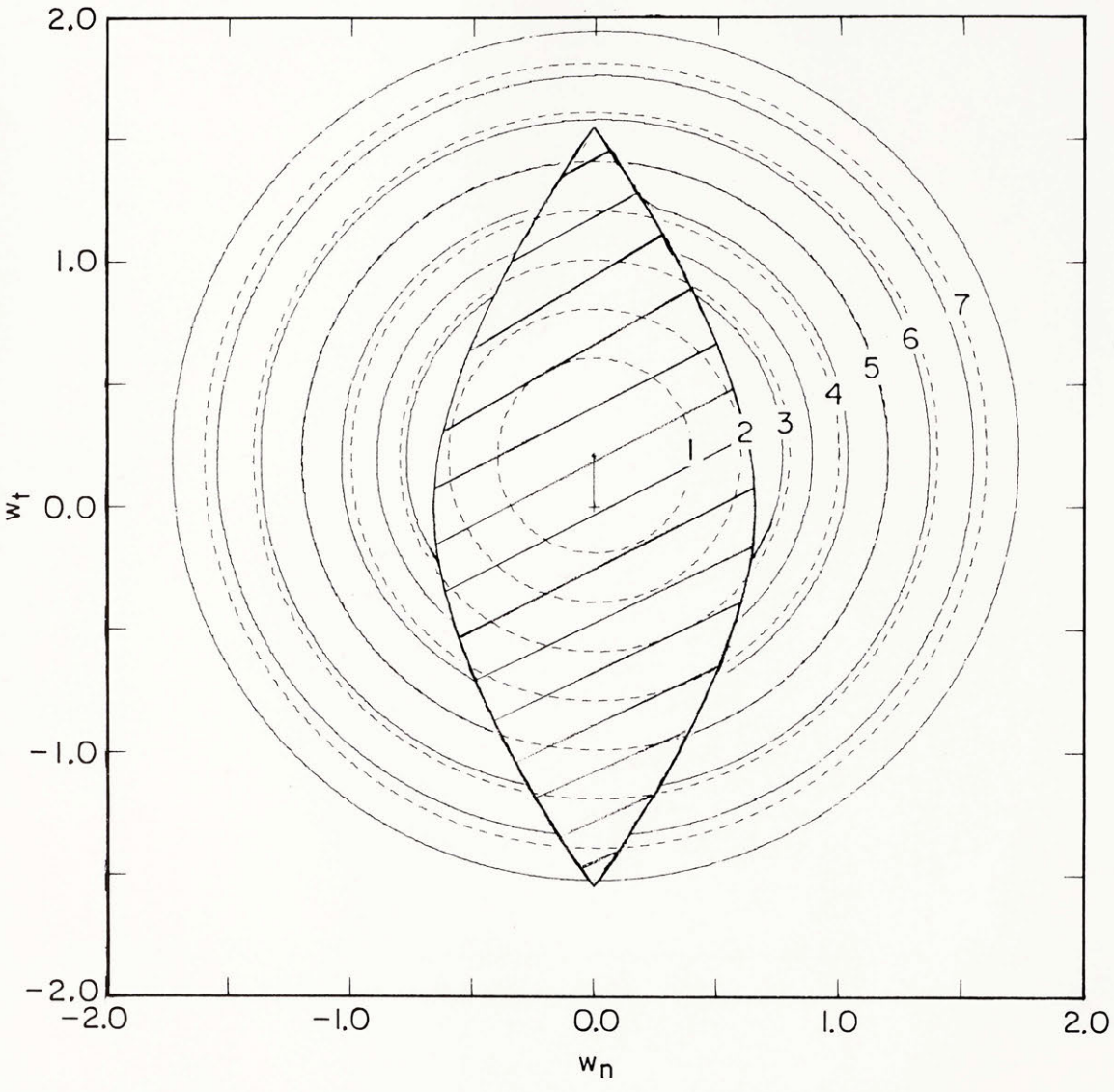

Fig.26d

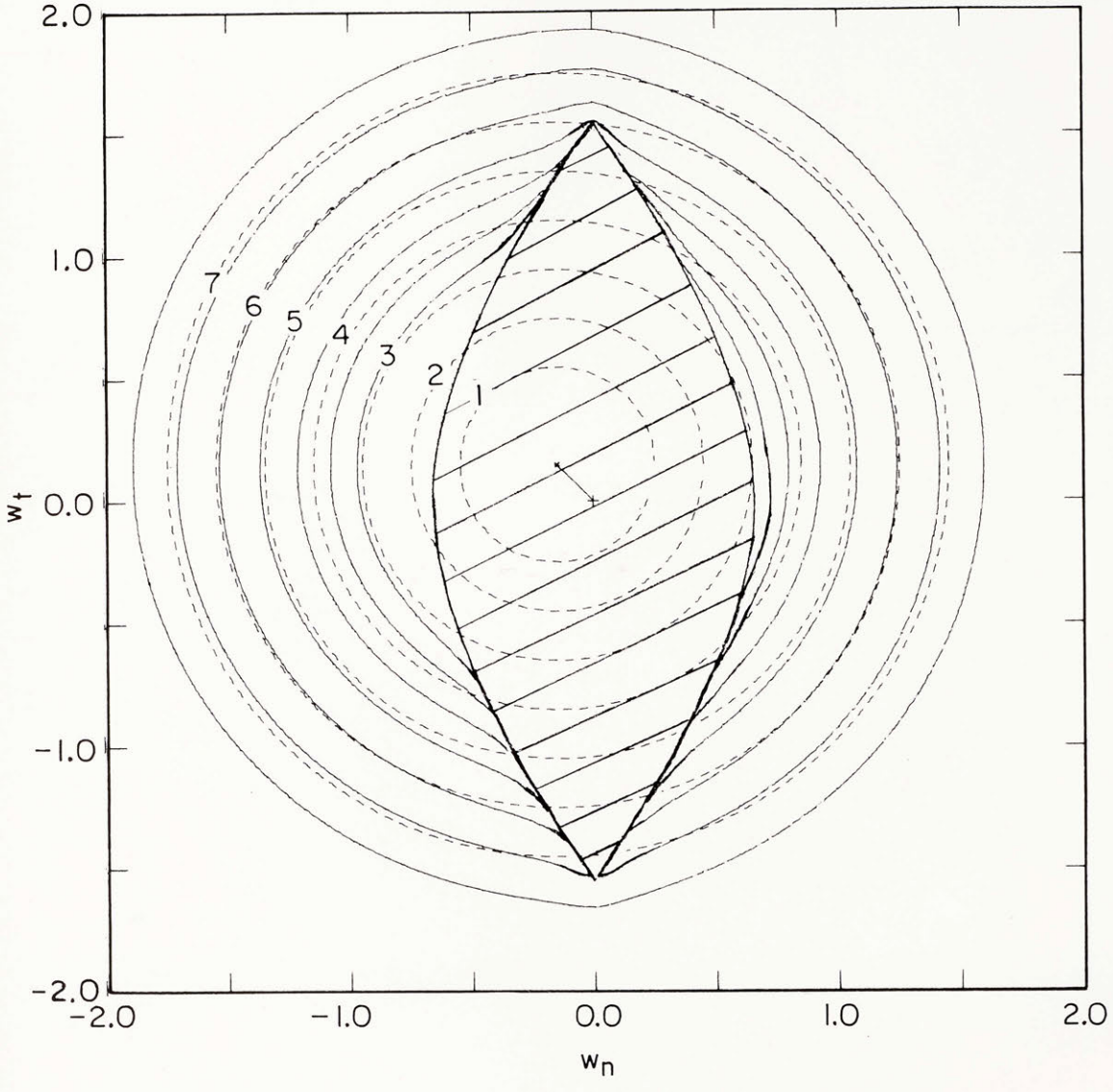

Fig. 26e

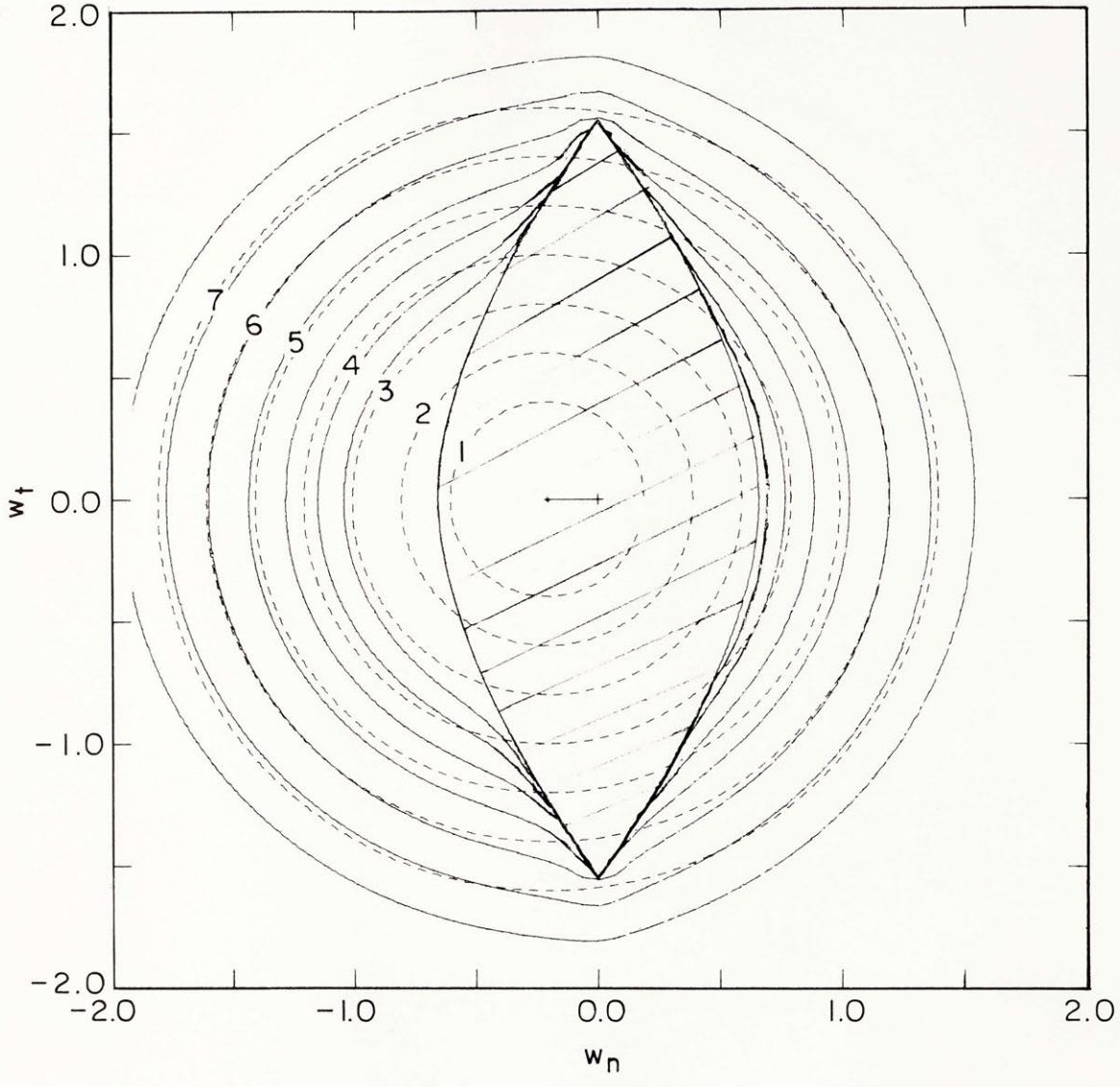

Fig.27a

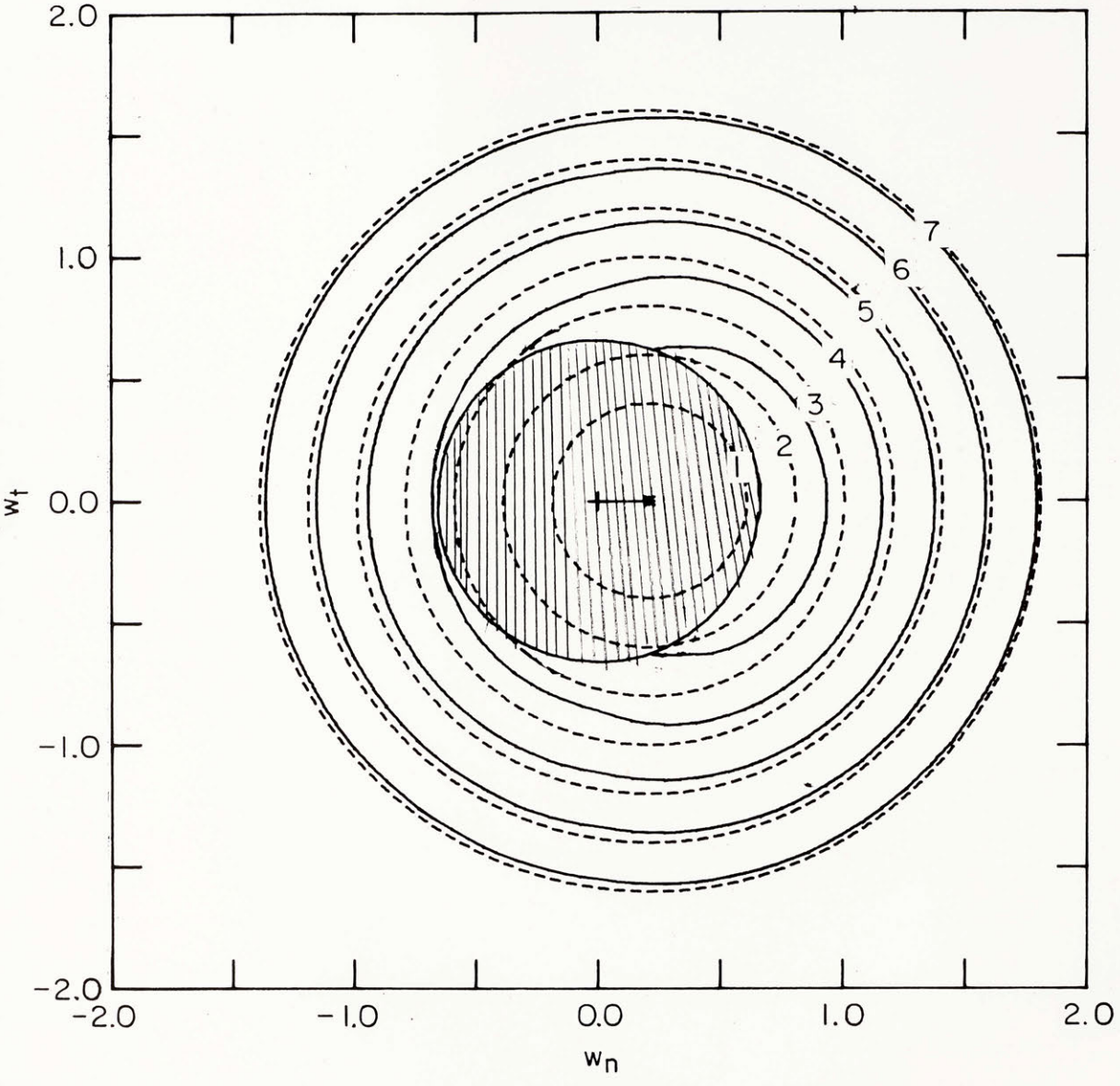

Fig. 27b

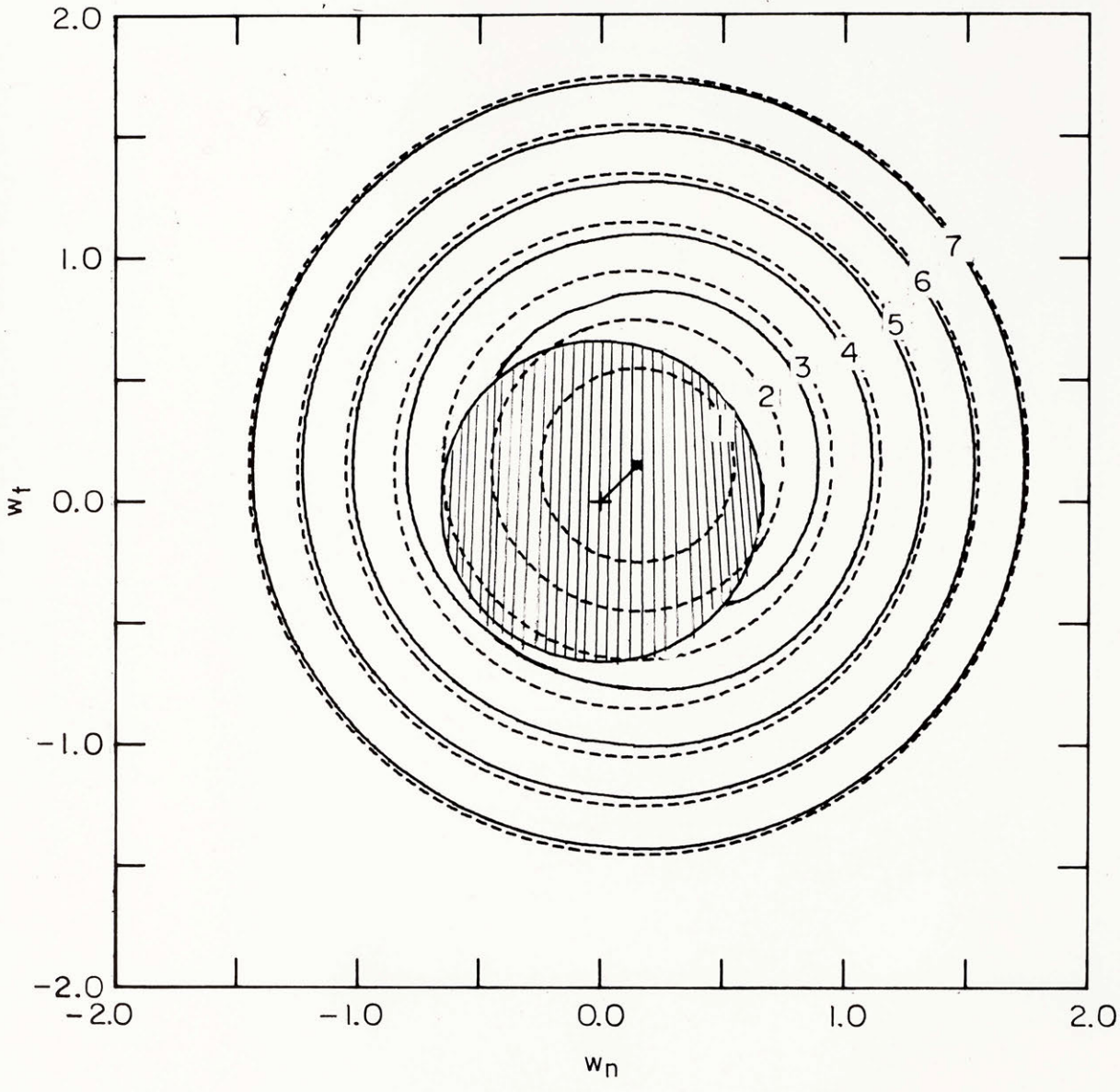

Fig. 27c

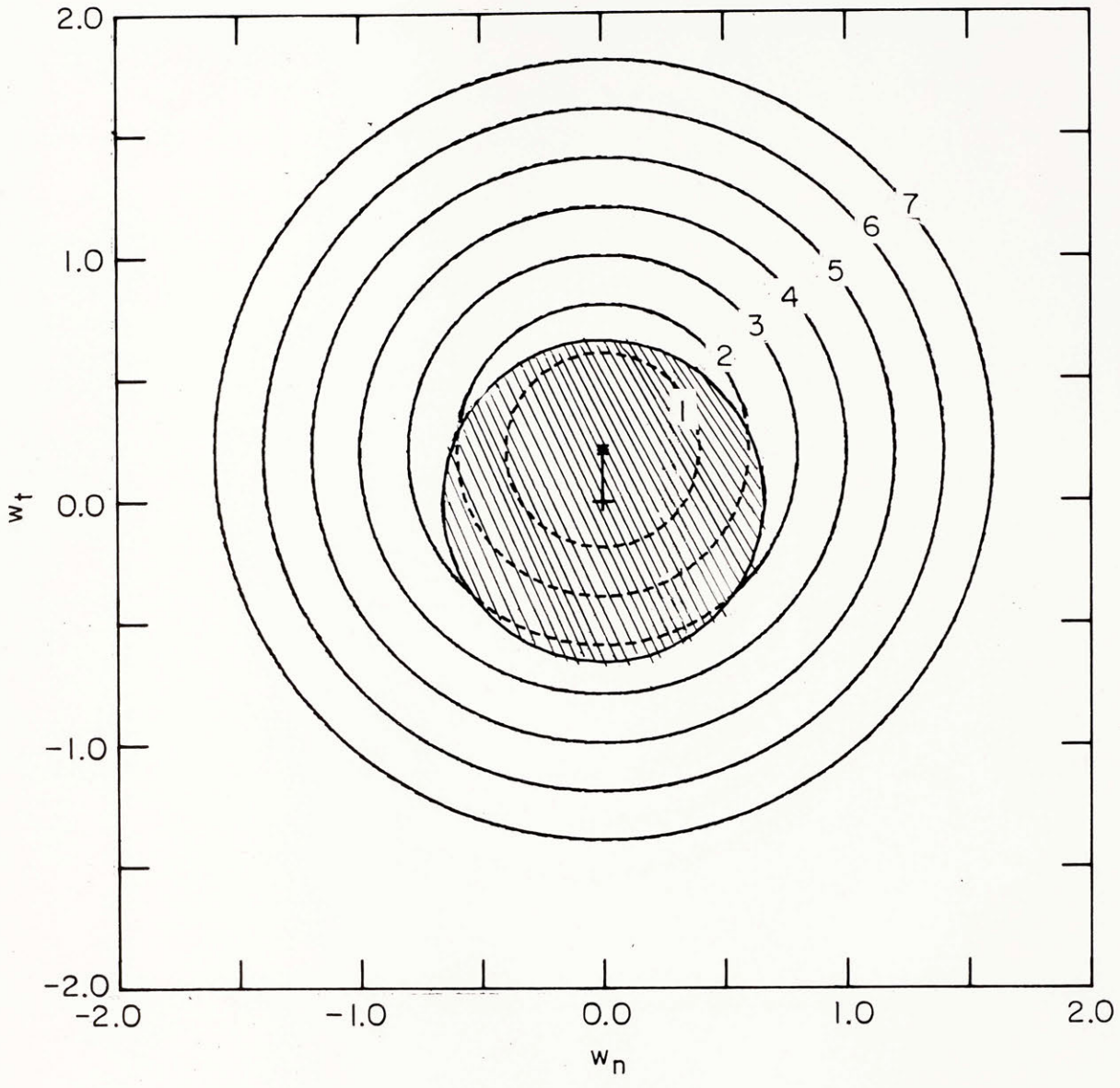

Fig. 27d

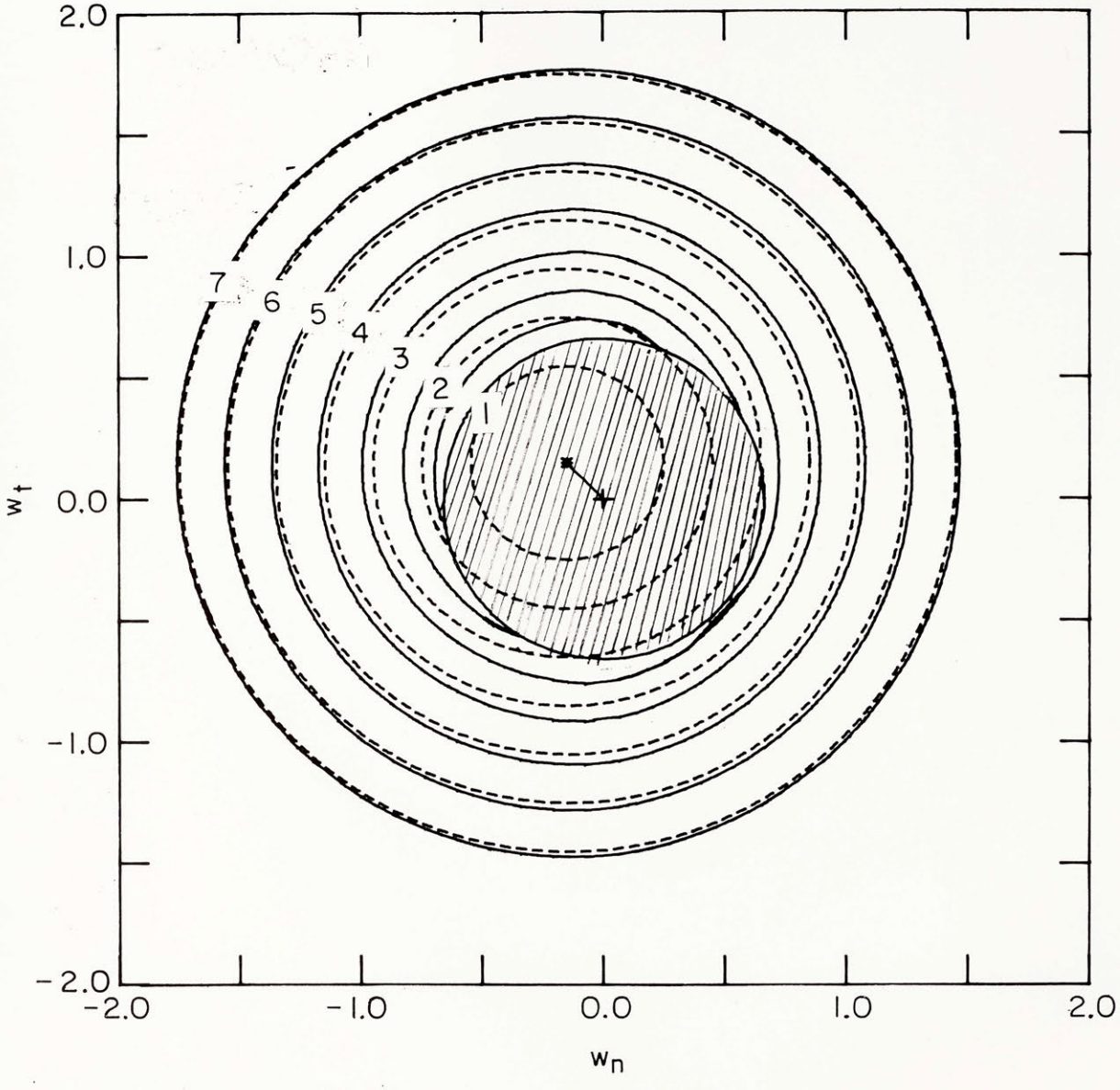

Fig. 27e

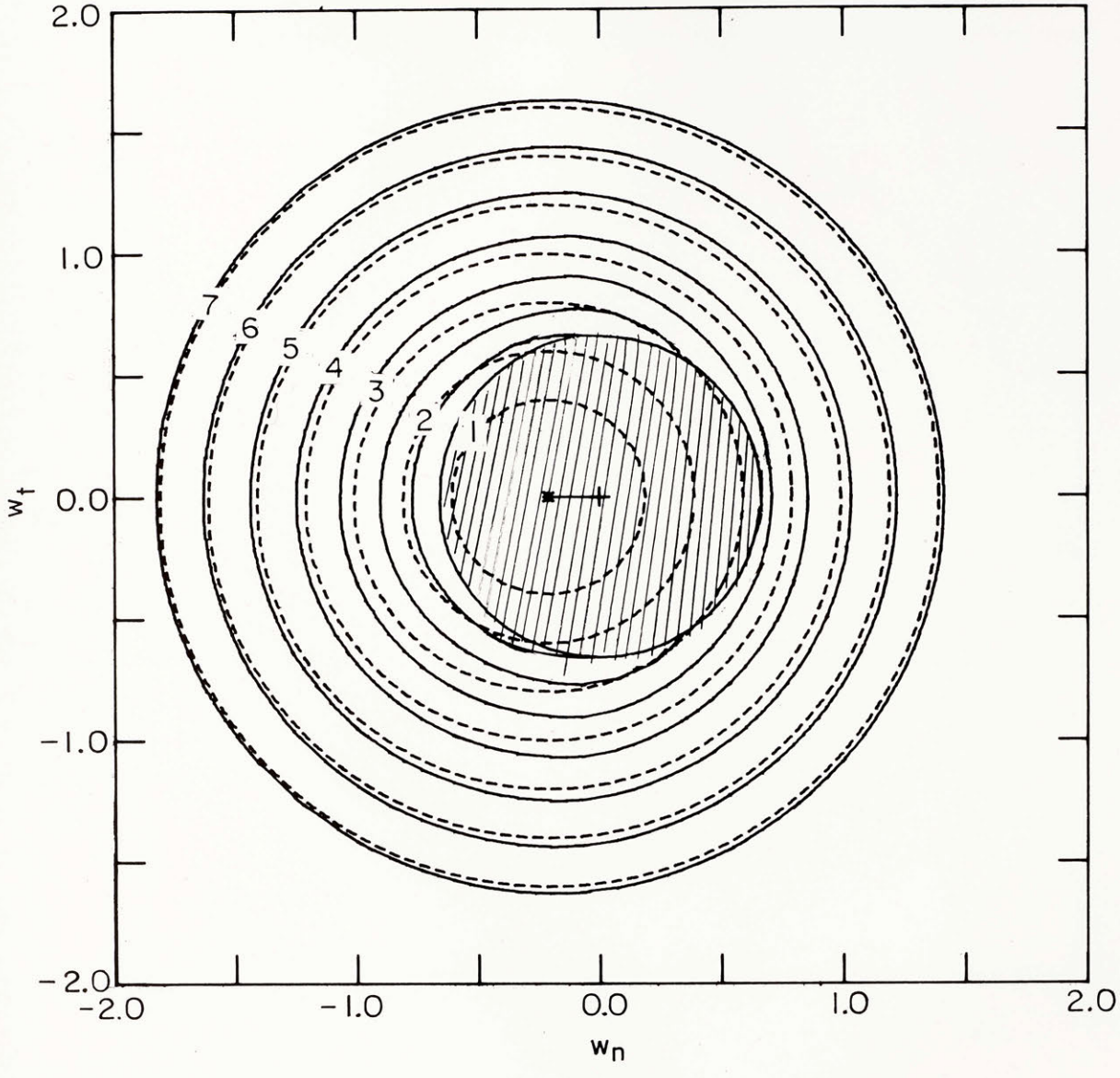

Fig. 28a

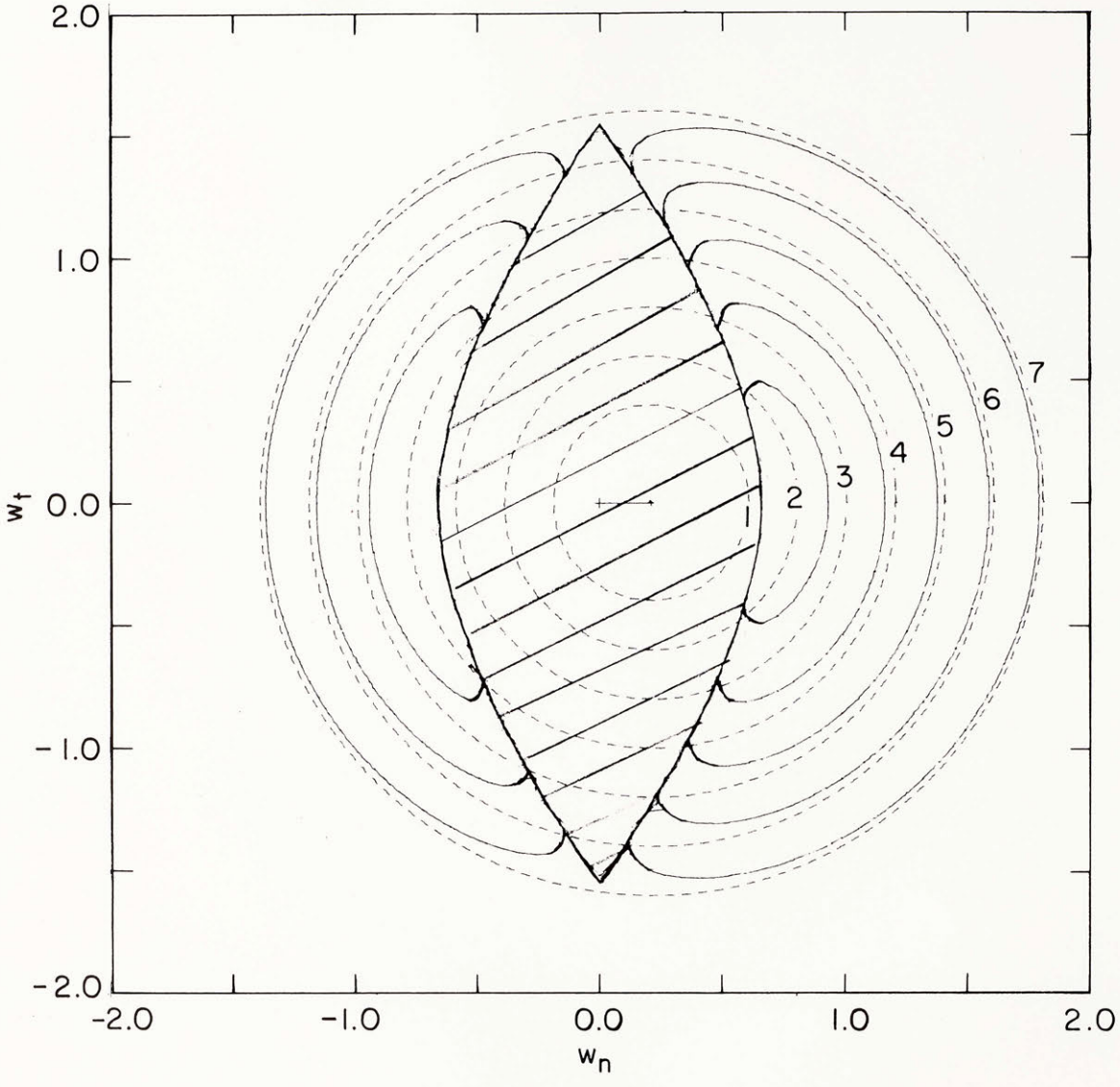

Fig. 28b

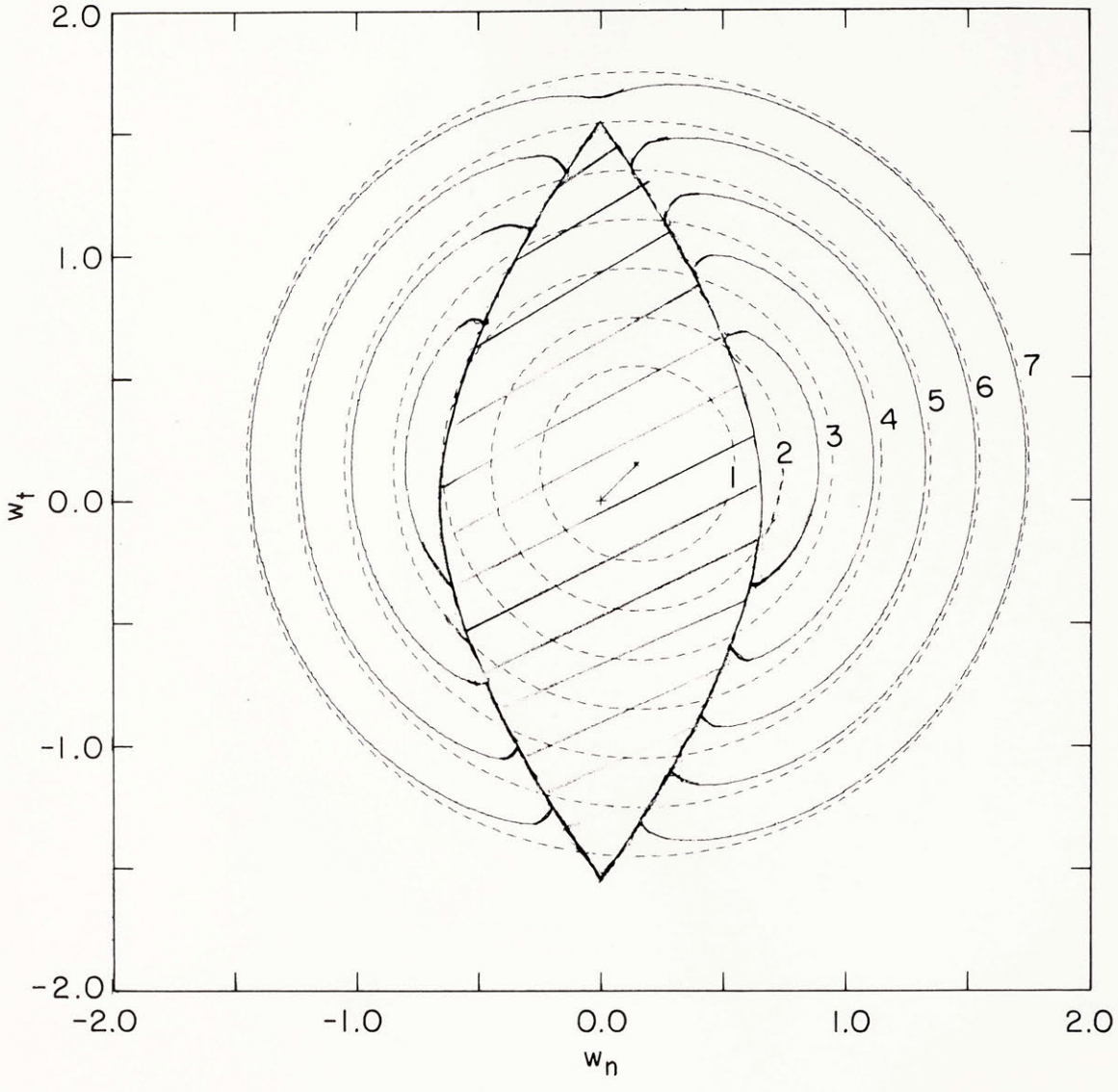

Fig. 28c

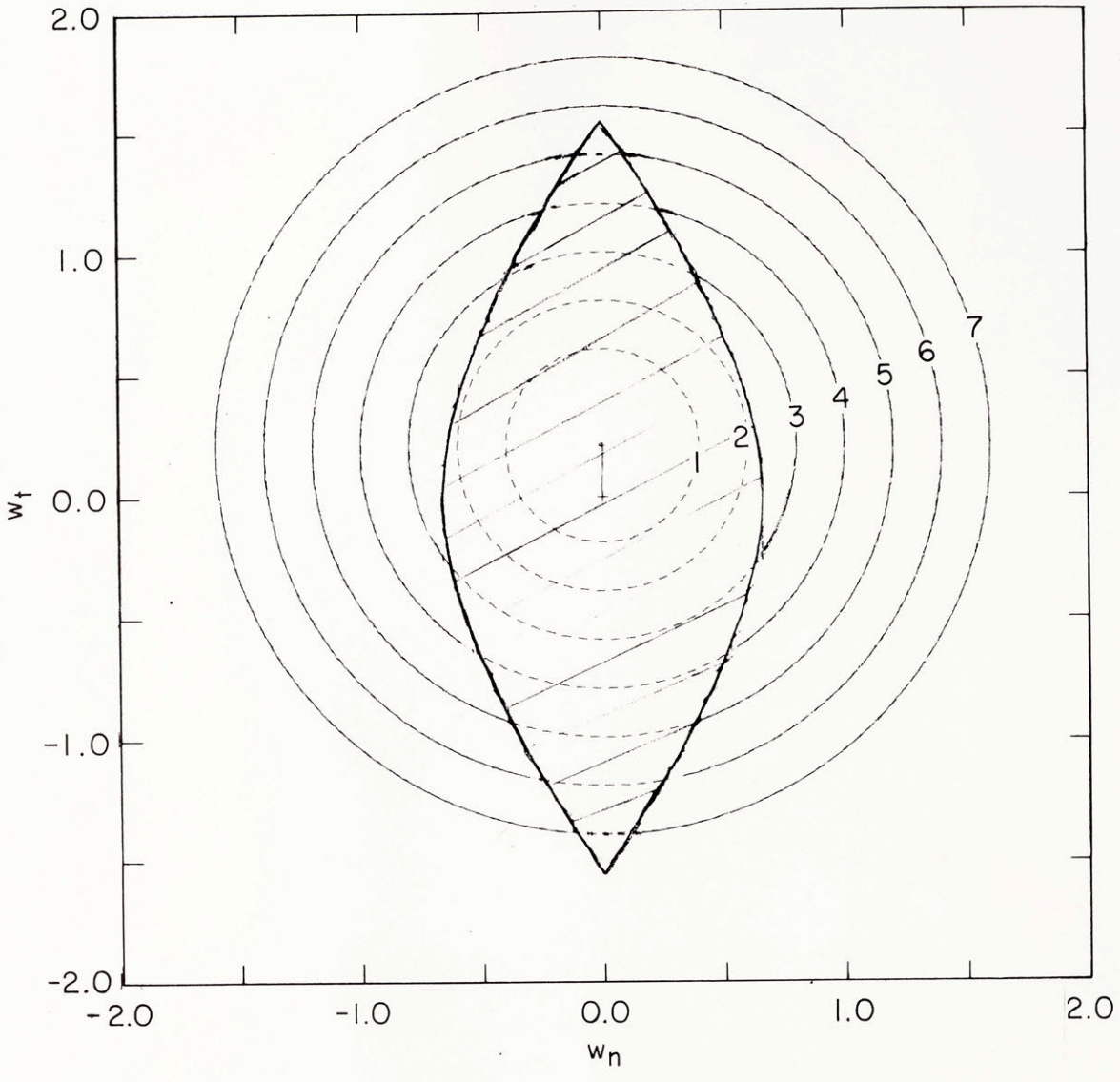

Fig. 28d

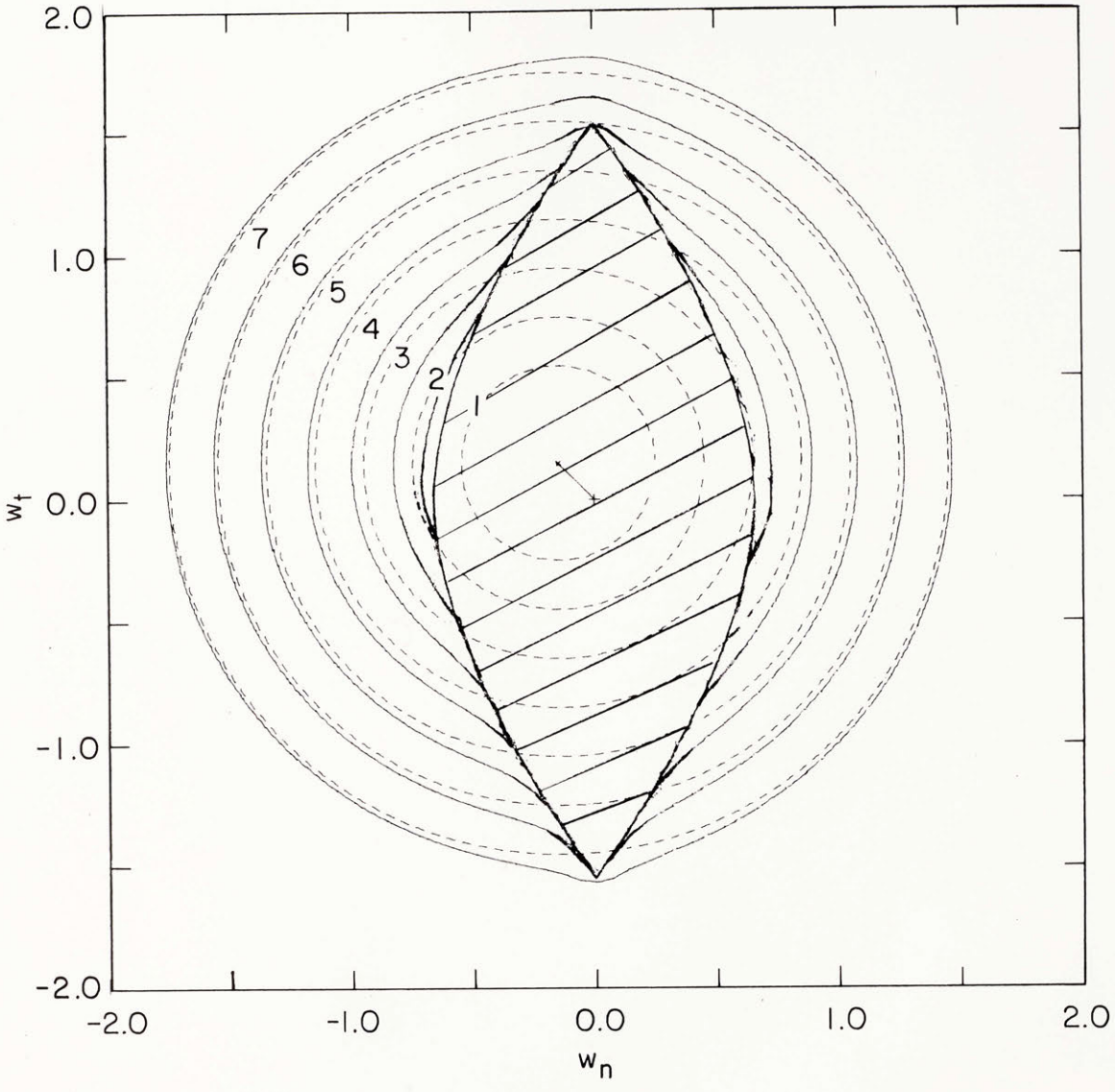

Fig. 28e

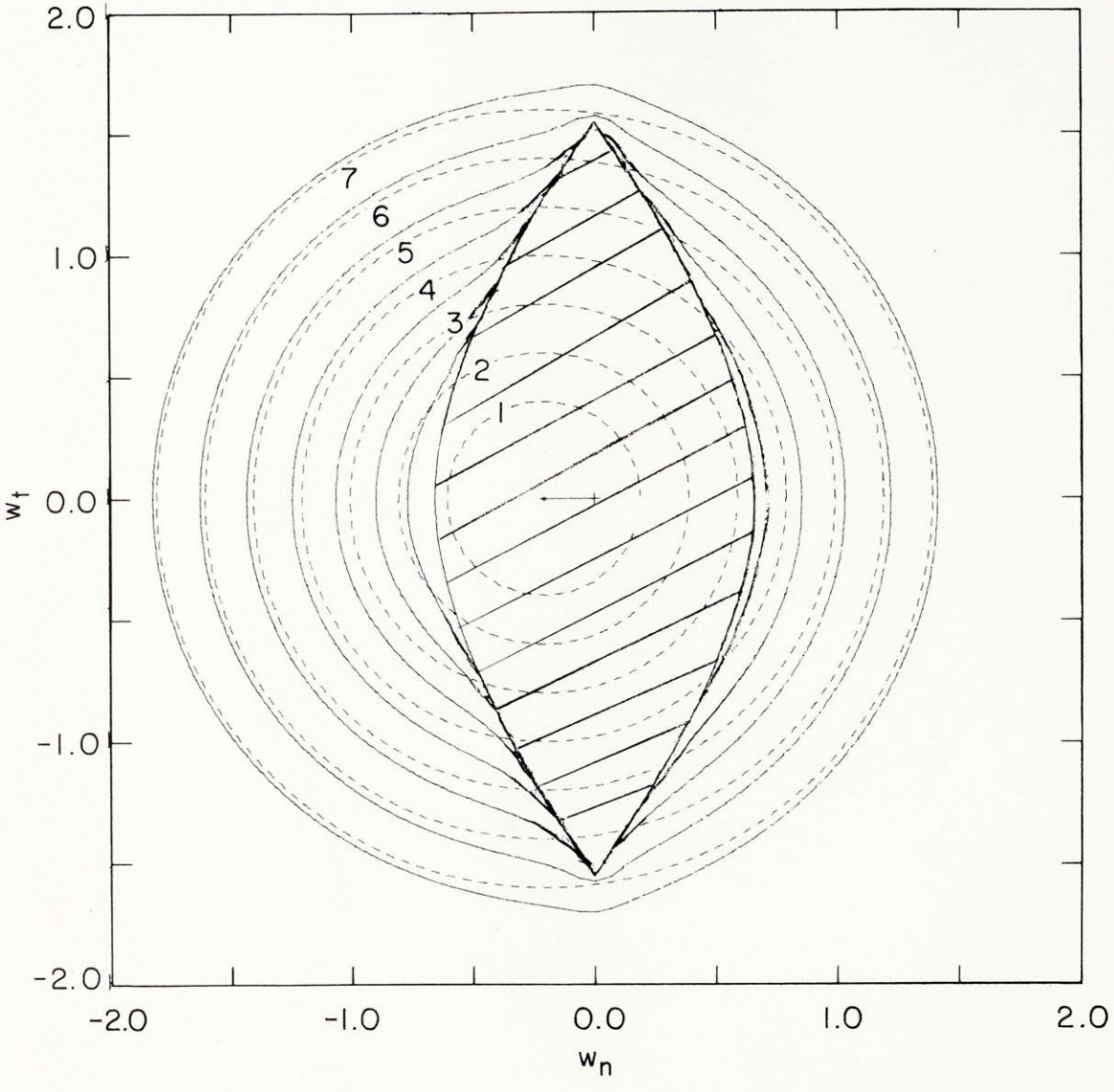

Fig. 29

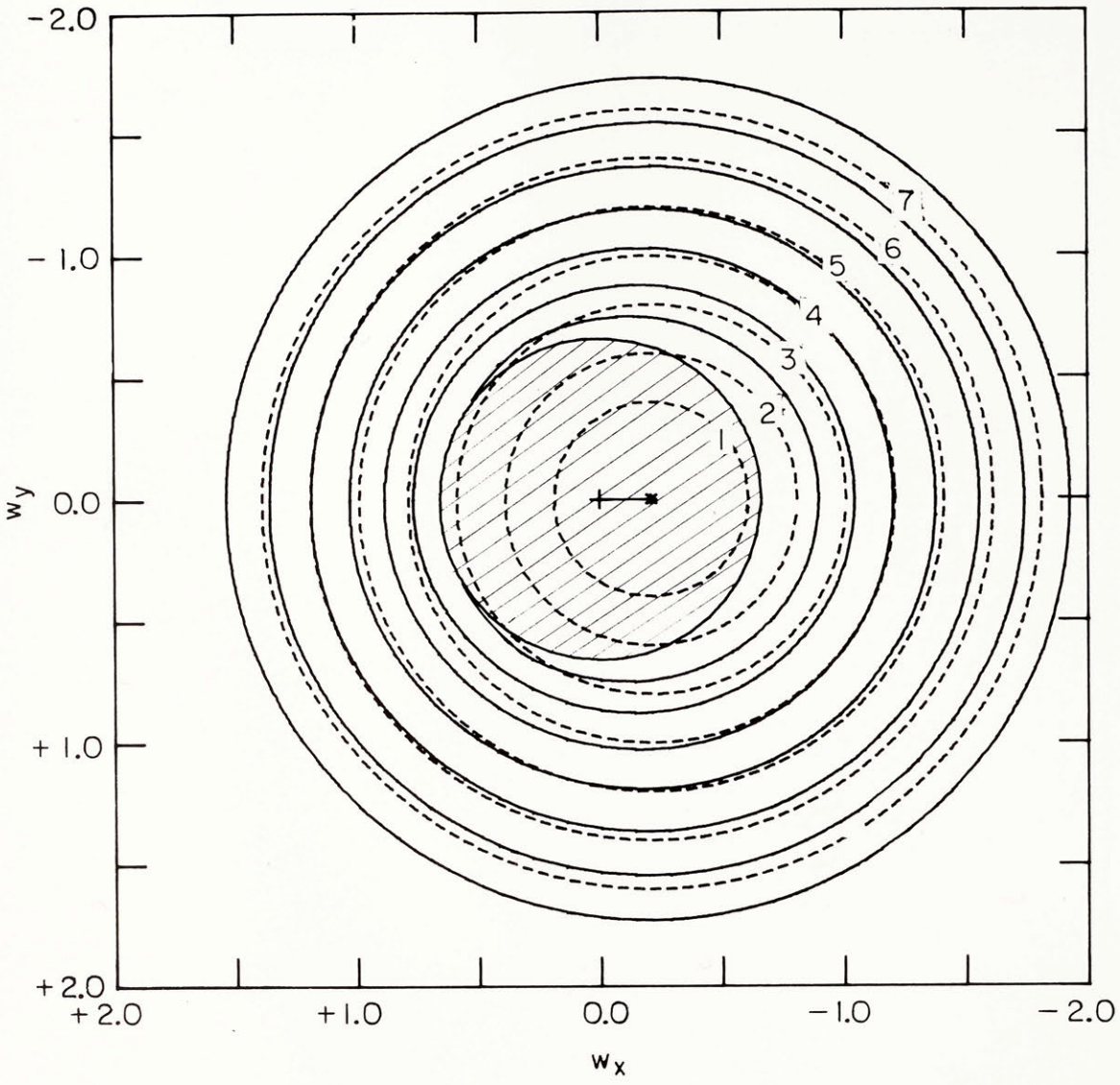

Fig.30

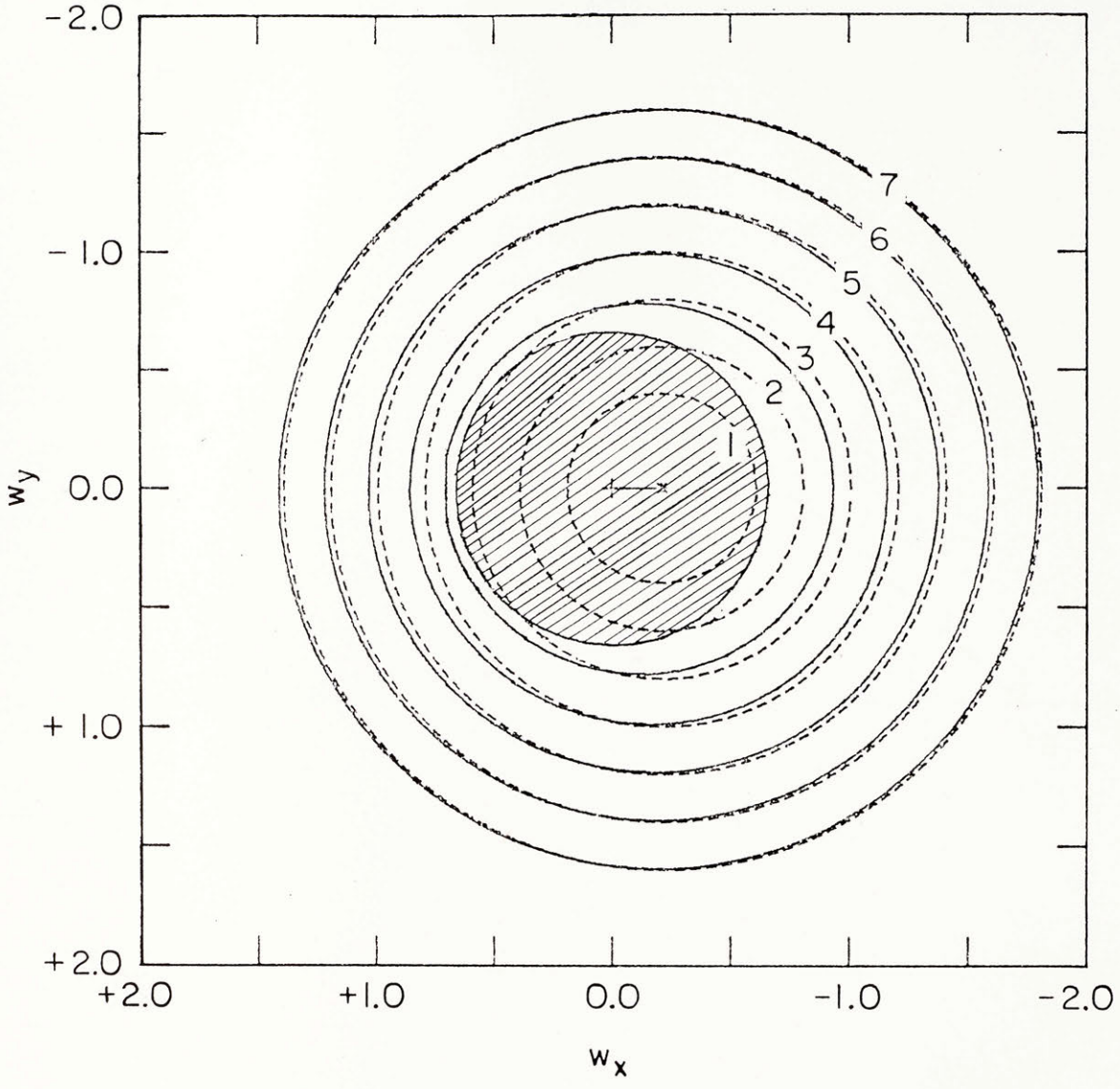

Fig. 31

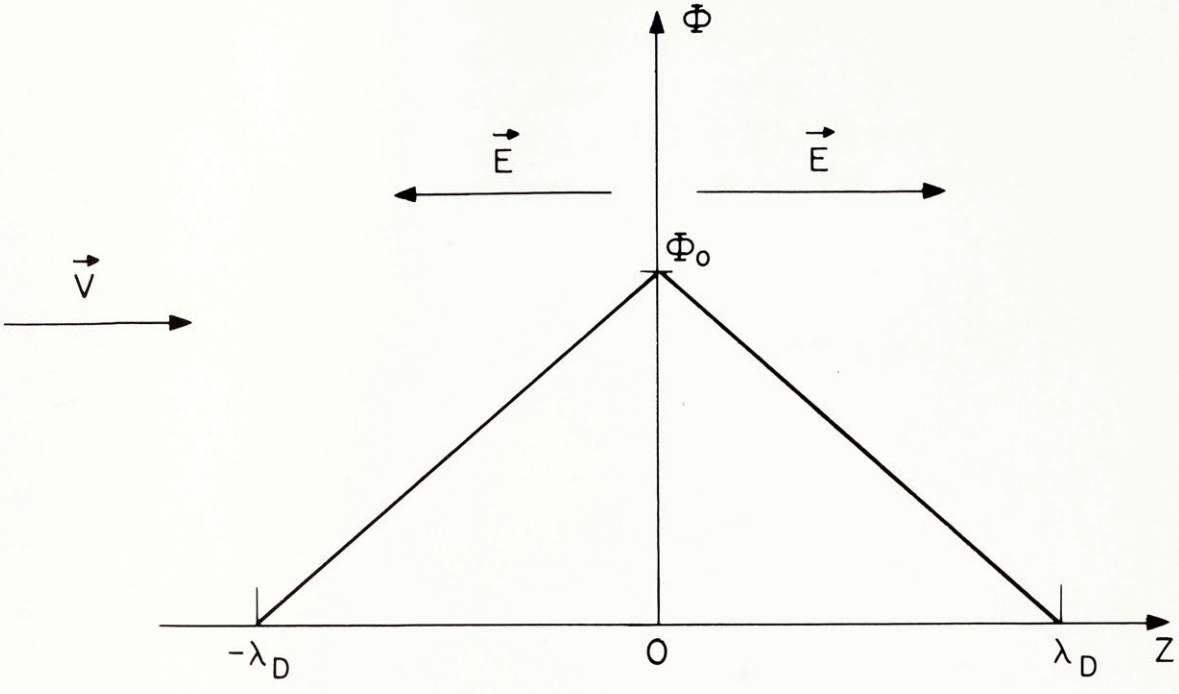

Fig. 32

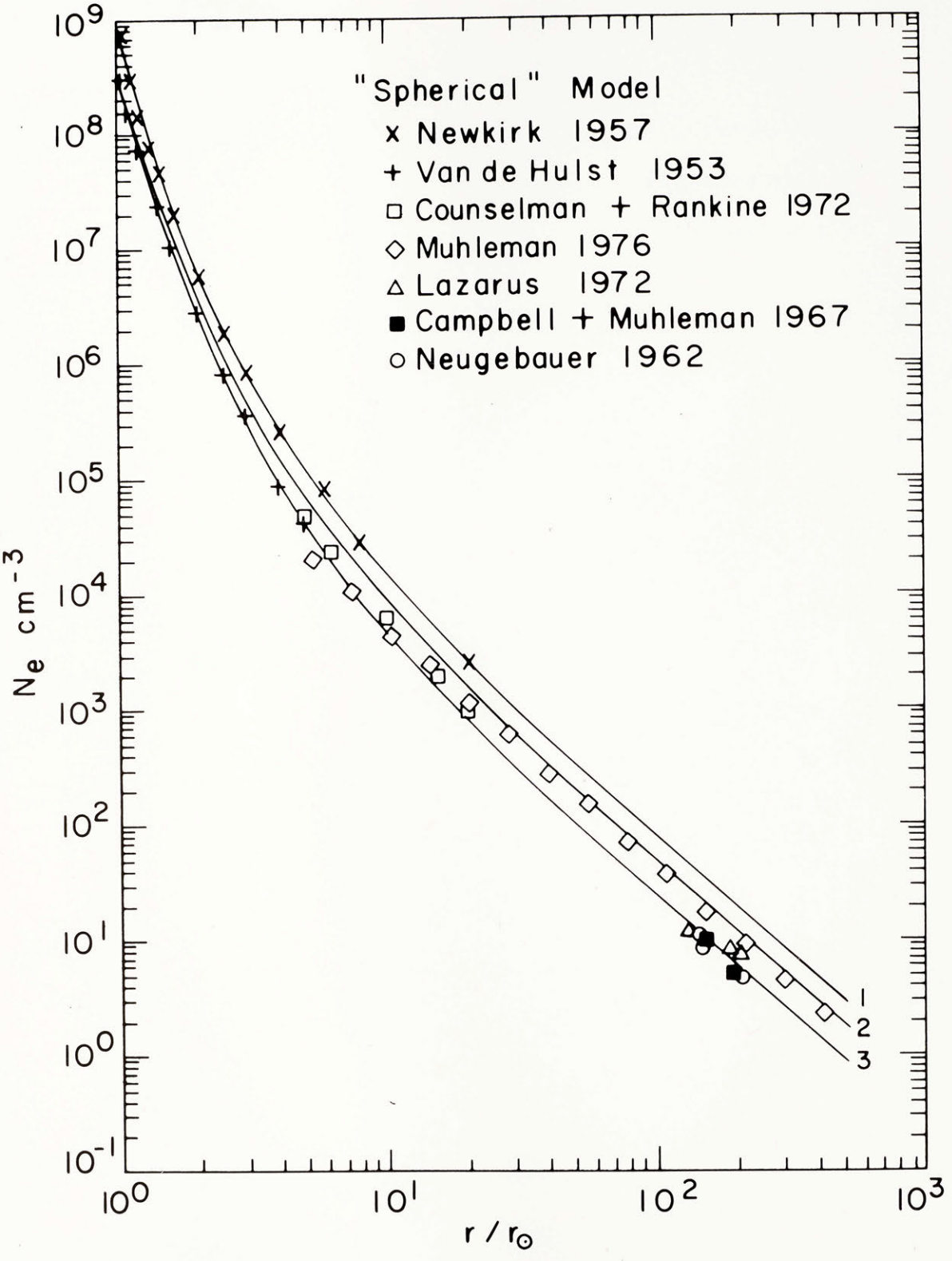
"Spherical" Model
x Newkirk 1957
+ Van de Hulst 1953
□ Counselman + Rankine 1972
◇ Muhleman 1976
△ Lazarus 1972
■ Campbell + Muhleman 1967
○ Neugebauer 1962
1
2
3
N_e cm^{-3}
$r / r_\odot$
10^9
10^8
10^7
10^6
10^5
10^4
10^3
10^2
10^1
10^0
10^{-1}
10^0
10^1
10^2
10^3

Fig.33

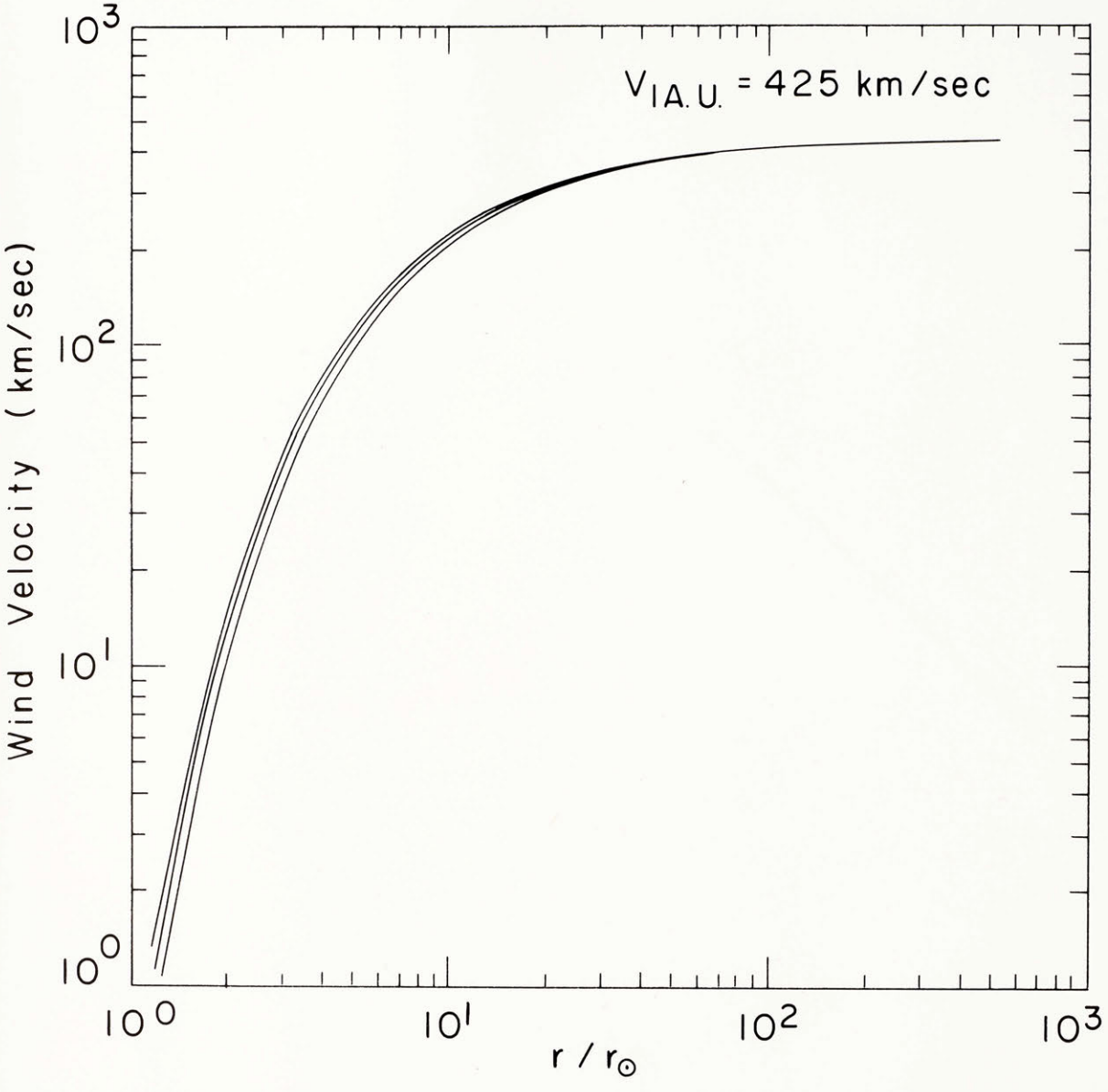
$V_{1A.U.}$ = 425 km/sec
Wind Velocity (km/sec)
10^3
10^2
10^1
10^0
10^0
10^1
10^2
10^3
$r / r_\odot$

Fig.34

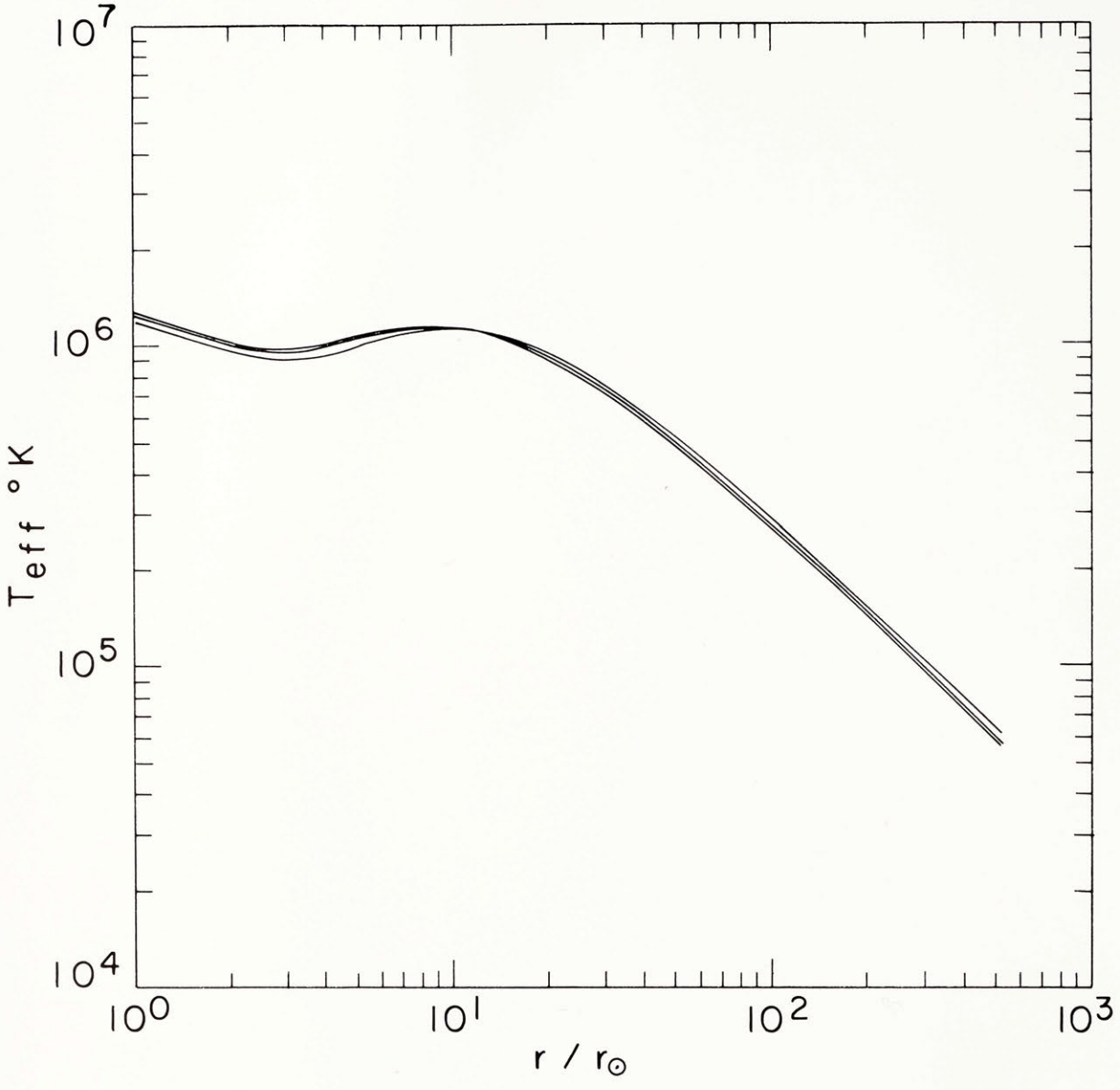

Fig.35

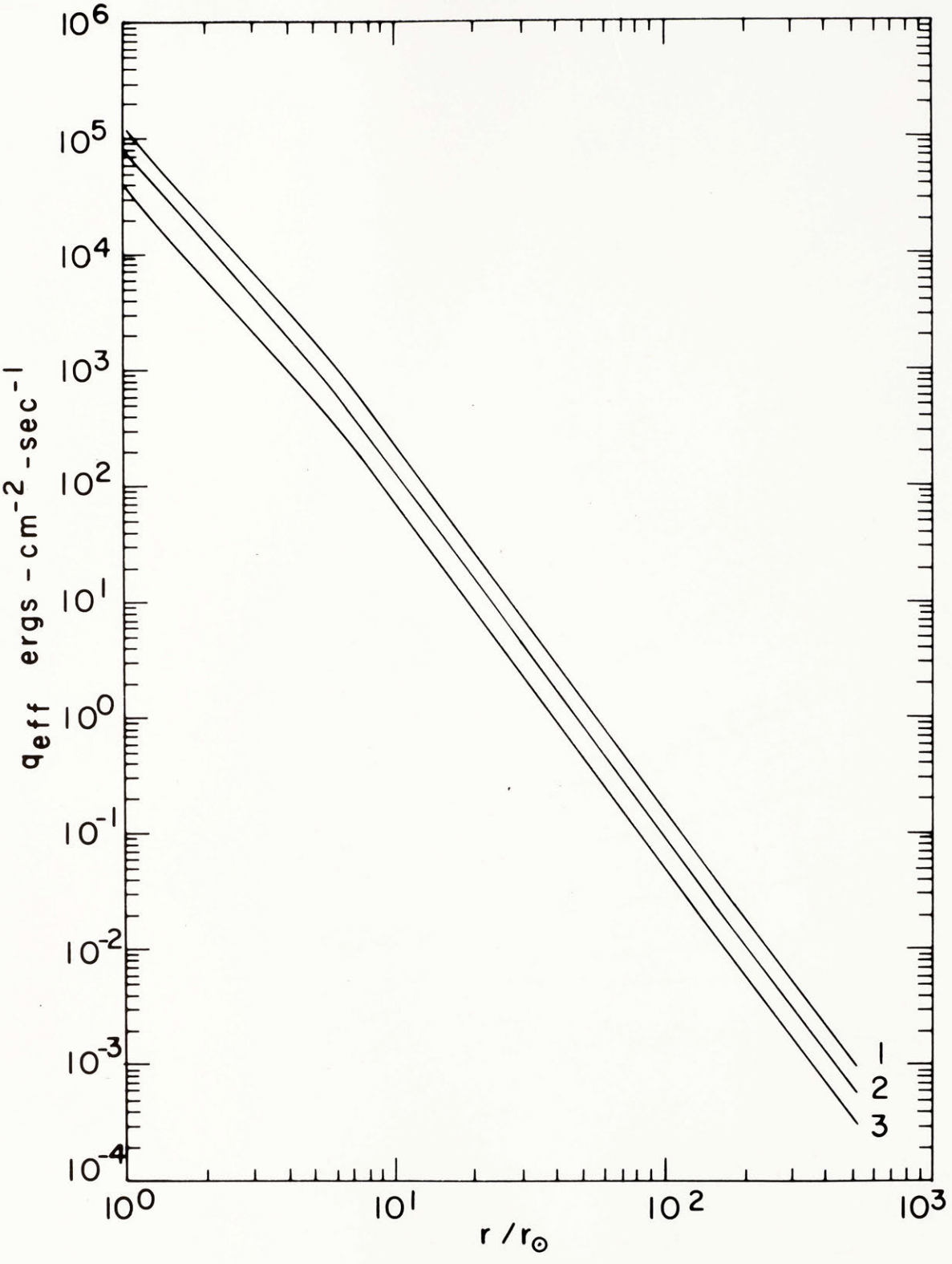
10^6
10^5
10^4
10^3
10^2
10^1
10^0
10^{-1}
10^{-2}
10^{-3}
10^{-4}
q_{eff} ergs - cm^{-2} - sec^{-1}
10^0
10^1
10^2
10^3
$r / r_\odot$
1
2
3

Fig.36

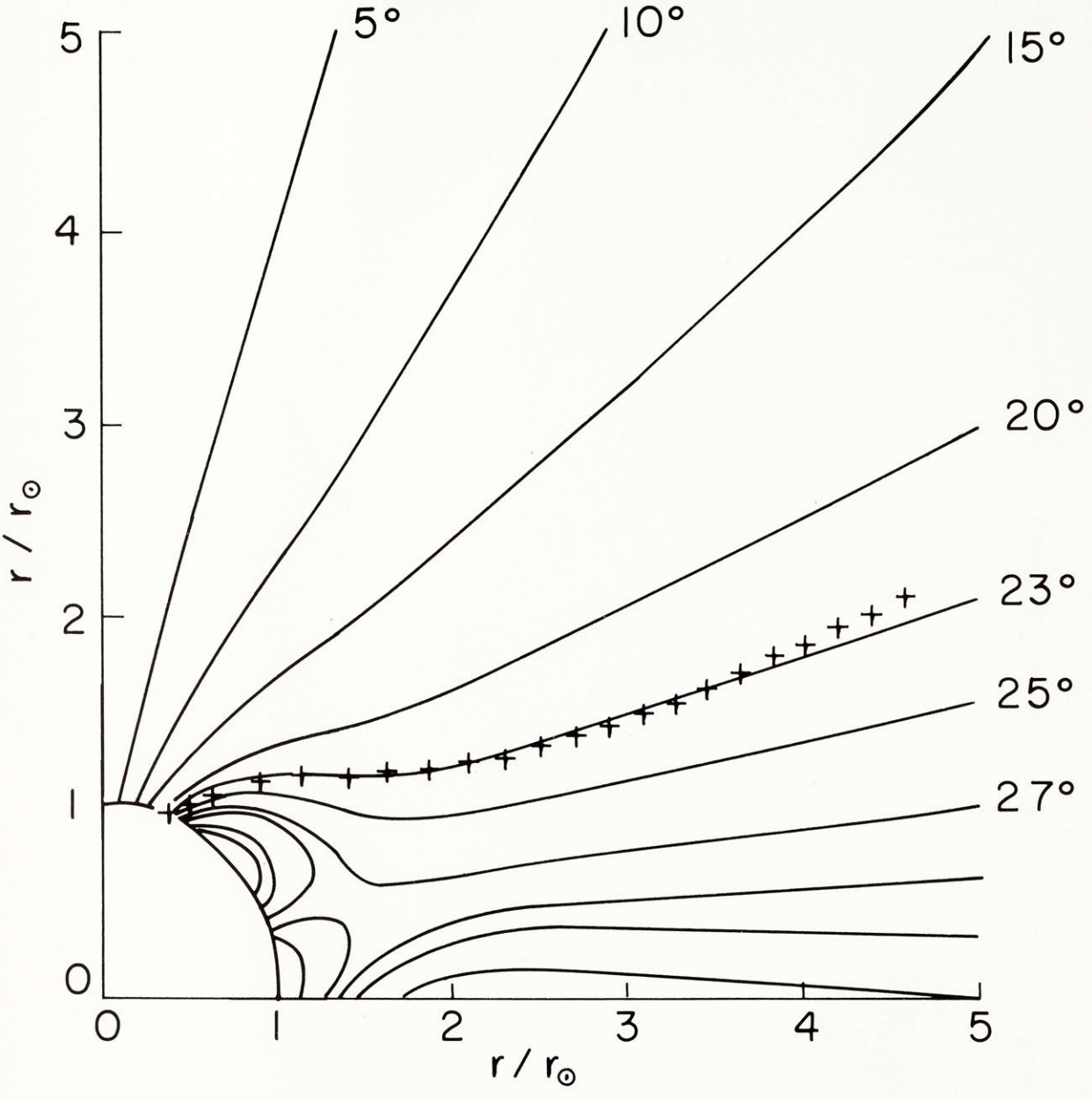

Fig. 37

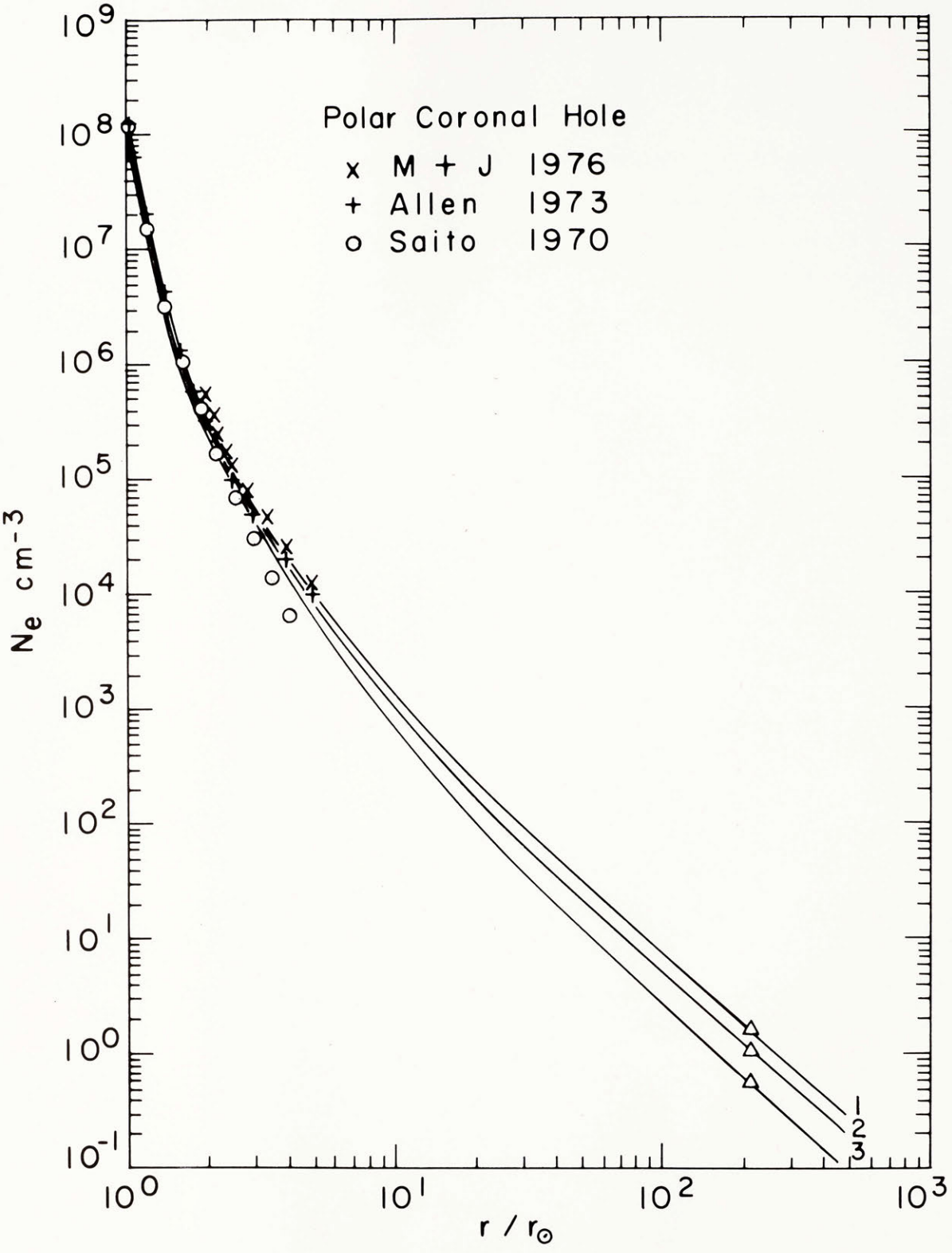
Polar Coronal Hole
x M + J 1976
+ Allen 1973
o Saito 1970
N_e cm^{-3}
$r / r_\odot$
1
2
3

Fig.38

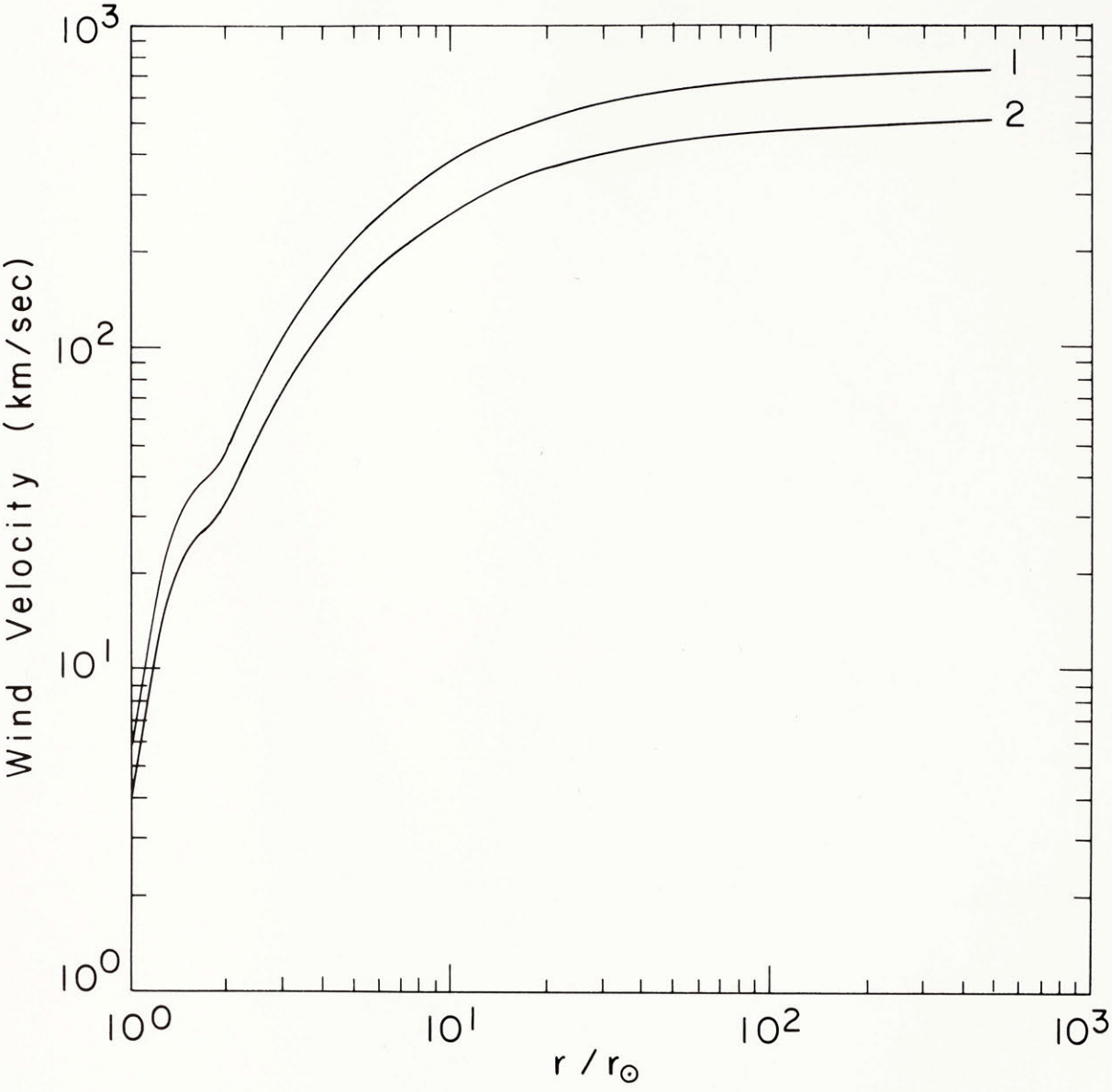

Fig. 39

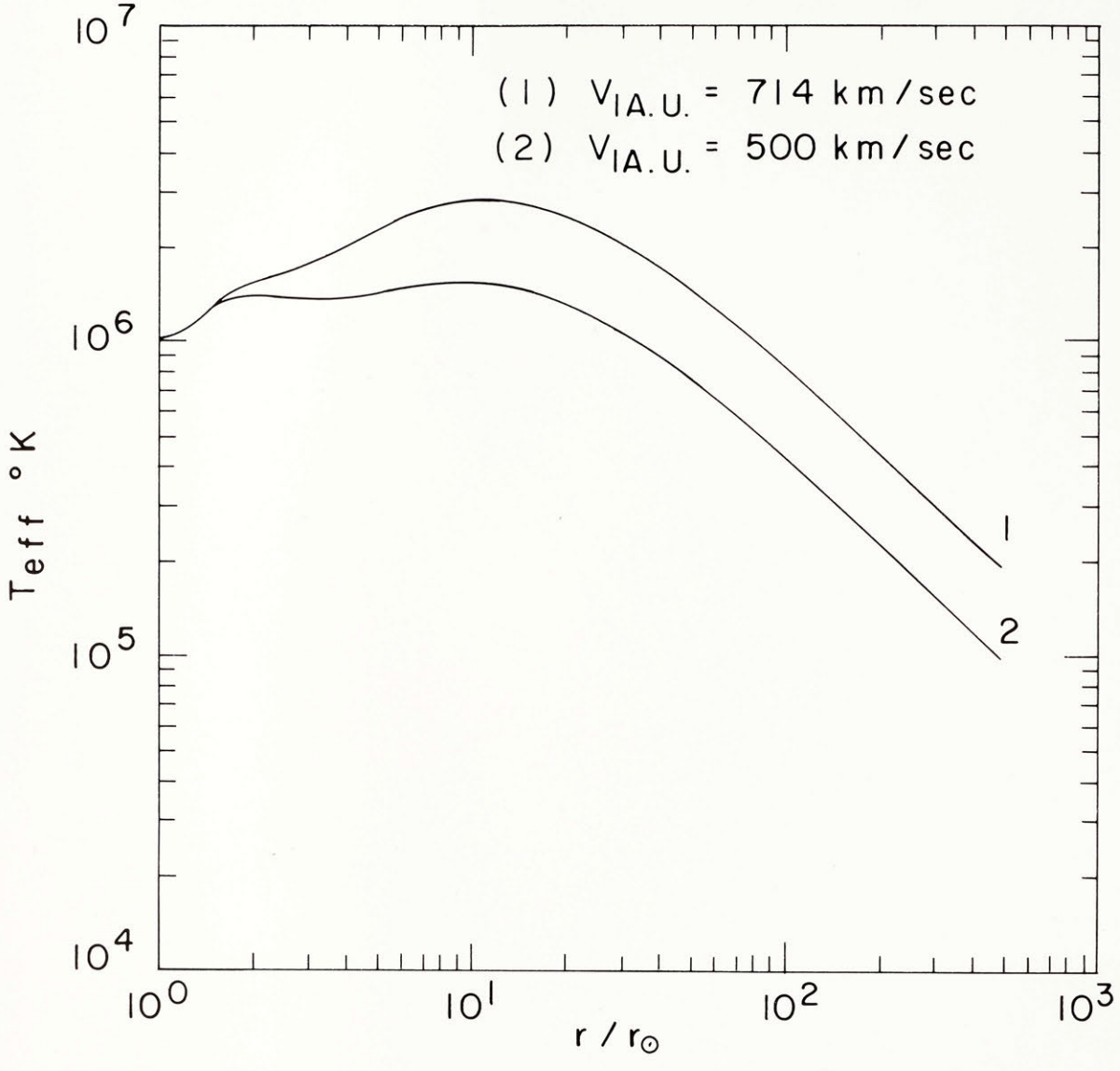
(1) $V_{1A.U.}$ = 714 km/sec
(2) $V_{1A.U.}$ = 500 km/sec
10^7
10^6
10^5
10^4
T_{eff} °K
10^0
10^1
10^2
10^3
$r / r_\odot$
1
2

Fig. 40

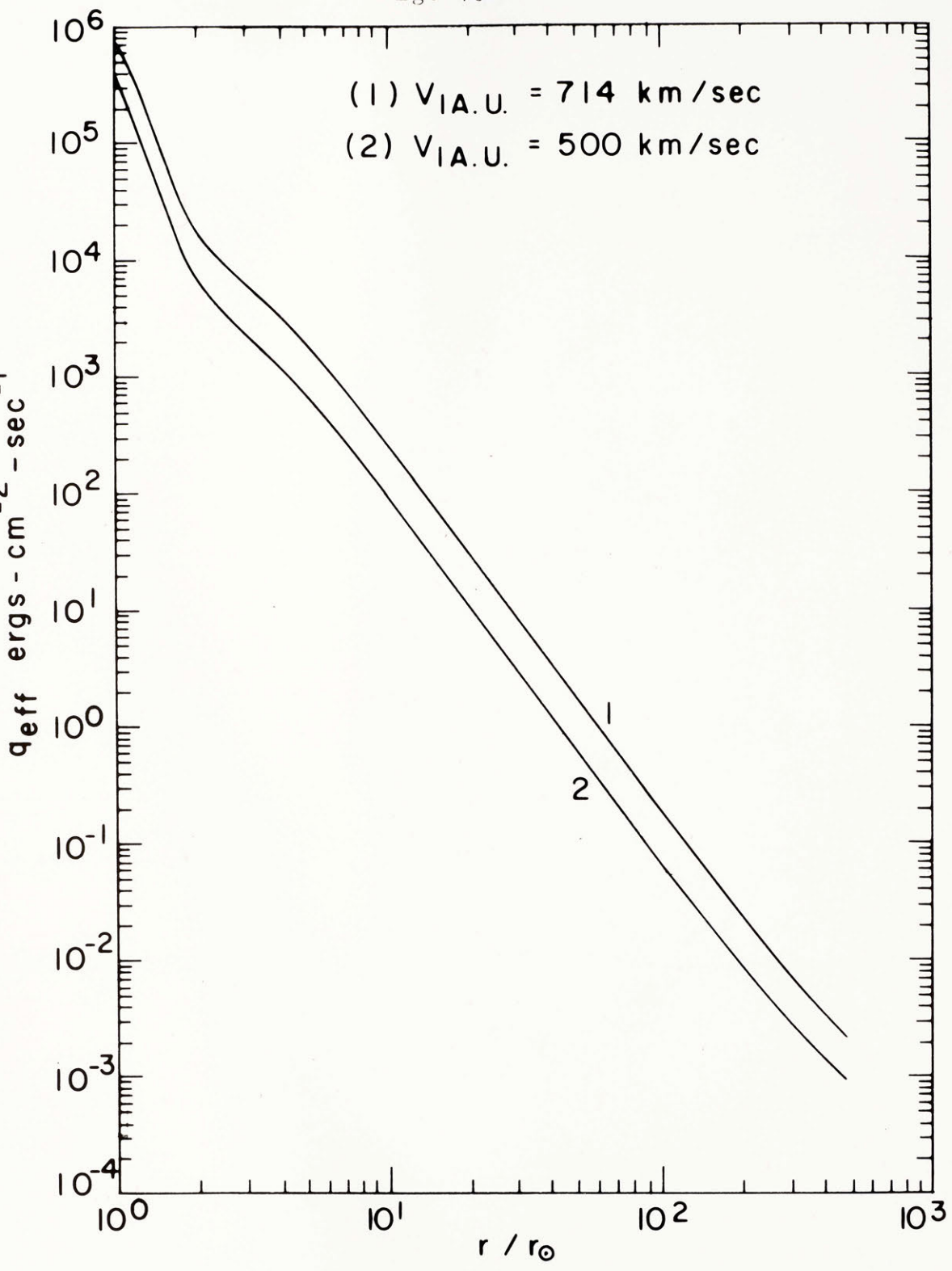
(1) $V_{I A.U.}$ = 714 km/sec
(2) $V_{I A.U.}$ = 500 km/sec
q_{eff} ergs - cm^{-2} - sec^{-1}
10^6
10^5
10^4
10^3
10^2
10^1
10^0
10^{-1}
10^{-2}
10^{-3}
10^{-4}
1
2
10^0
10^1
10^2
10^3
r / $r_\odot$

Fig. 41

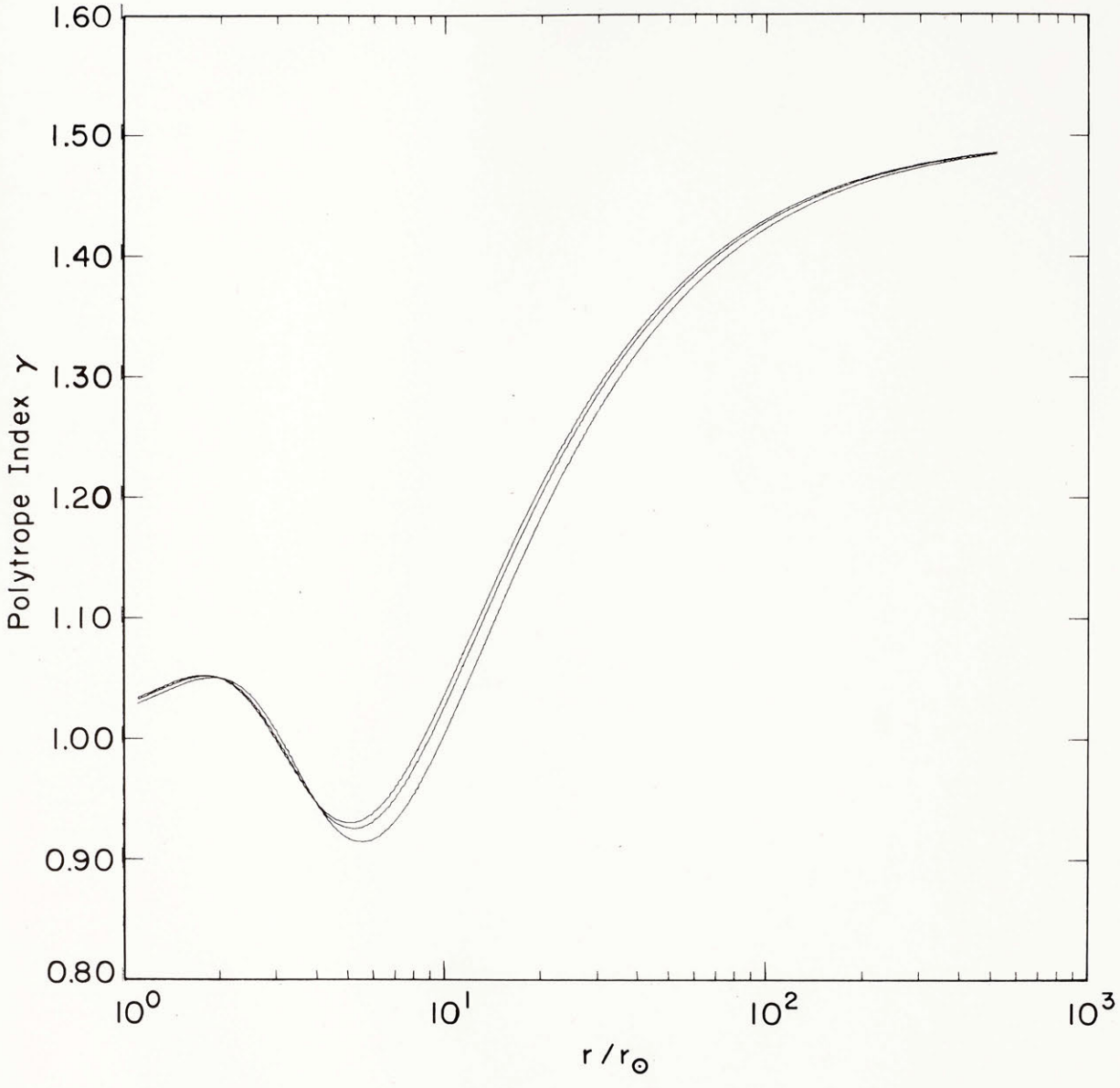
1.60
1.50
1.40
1.30
1.20
1.10
1.00
0.90
0.80
Polytrope Index γ
10^0
10^1
10^2
10^3
r/r⊙

Fig. 42

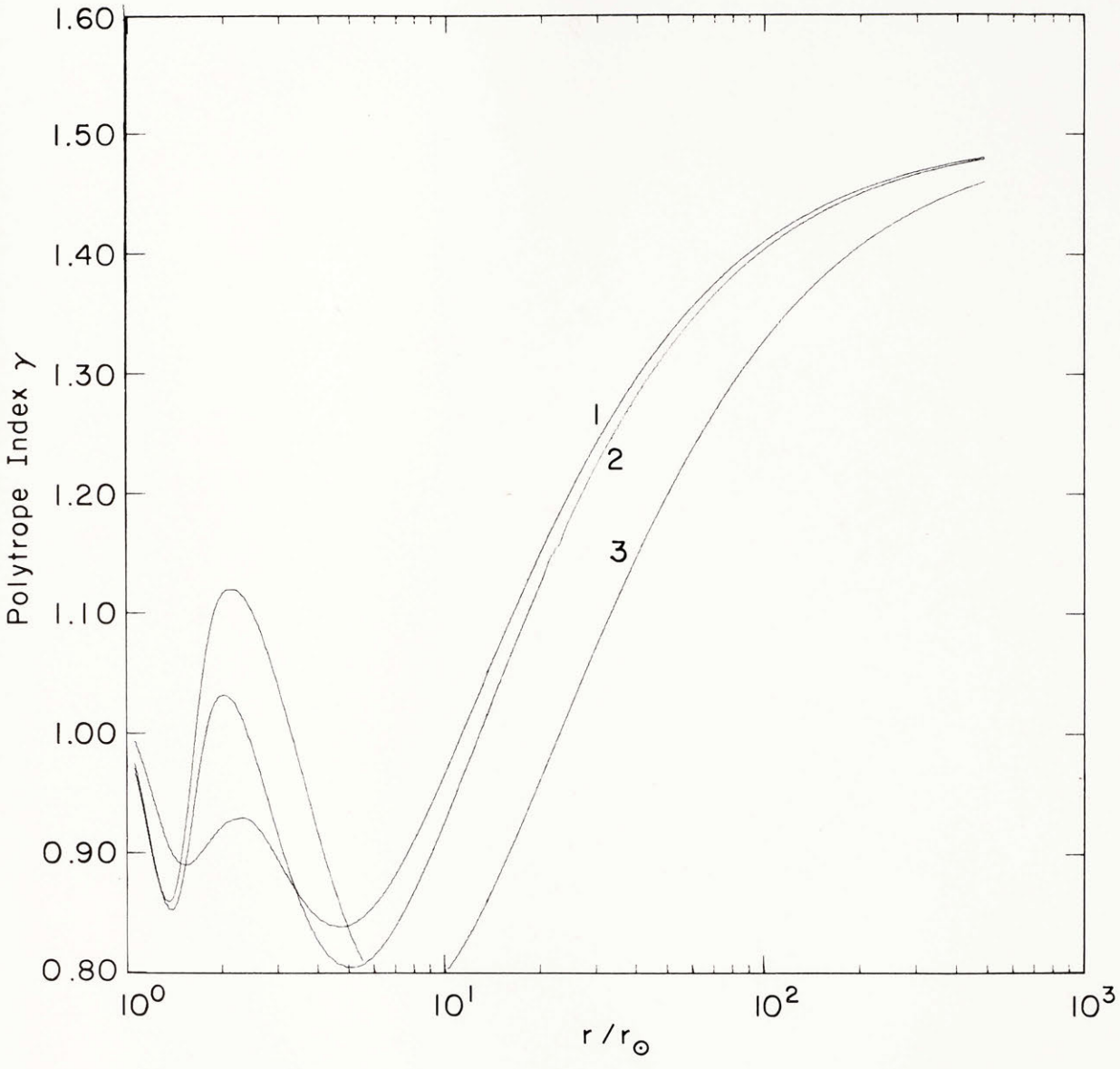
1.60
1.50
1.40
1.30
1.20
1.10
1.00
0.90
0.80
Polytrope Index γ
1
2
3
10^0
10^1
10^2
10^3
r / r⊙

Fig. 43

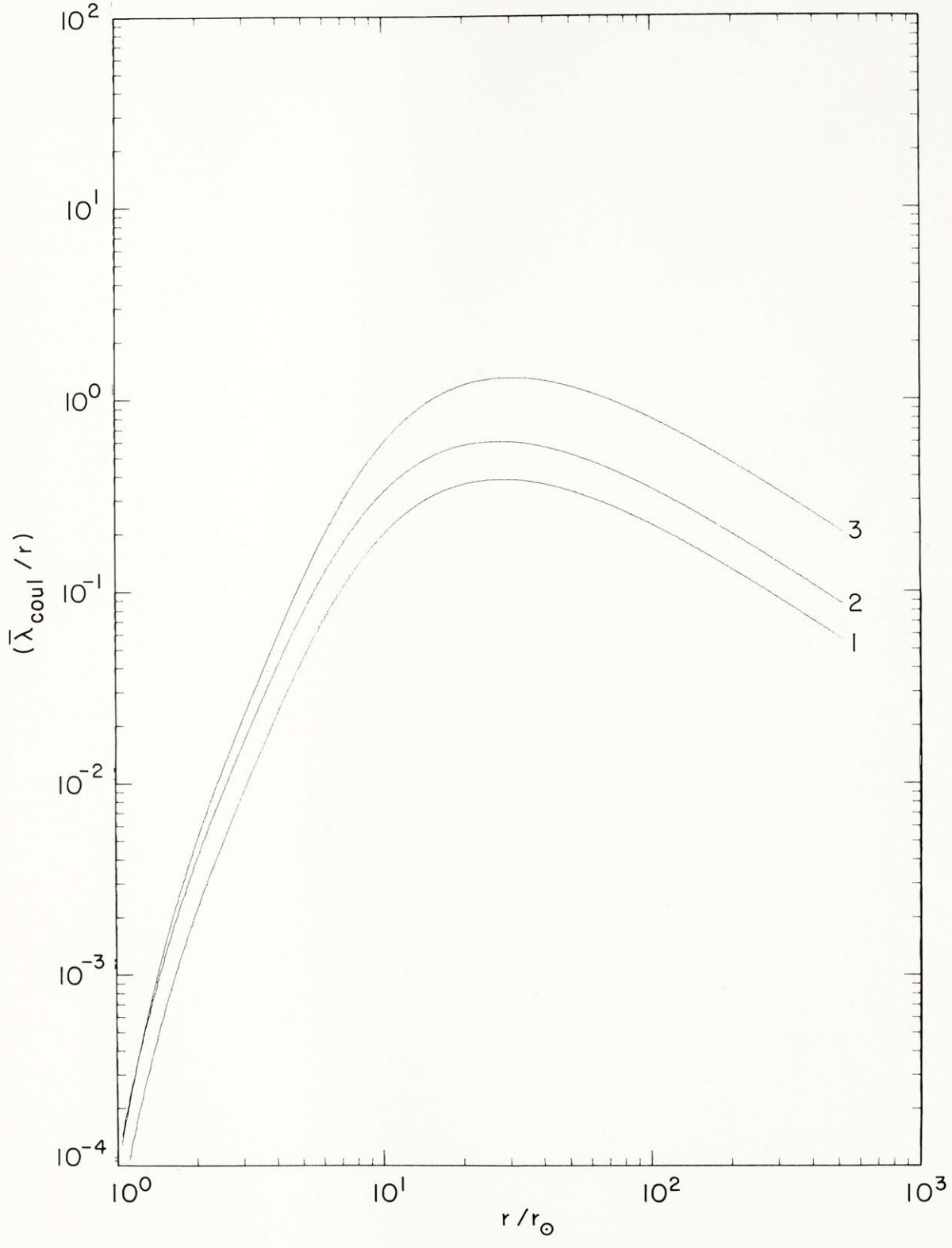
10^2
10^1
10^0
10^{-1}
10^{-2}
10^{-3}
10^{-4}
$(\bar{\lambda}_{coul}/r)$
3
2
1
10^0
10^1
10^2
10^3
$r/r_\odot$

Fig. 44

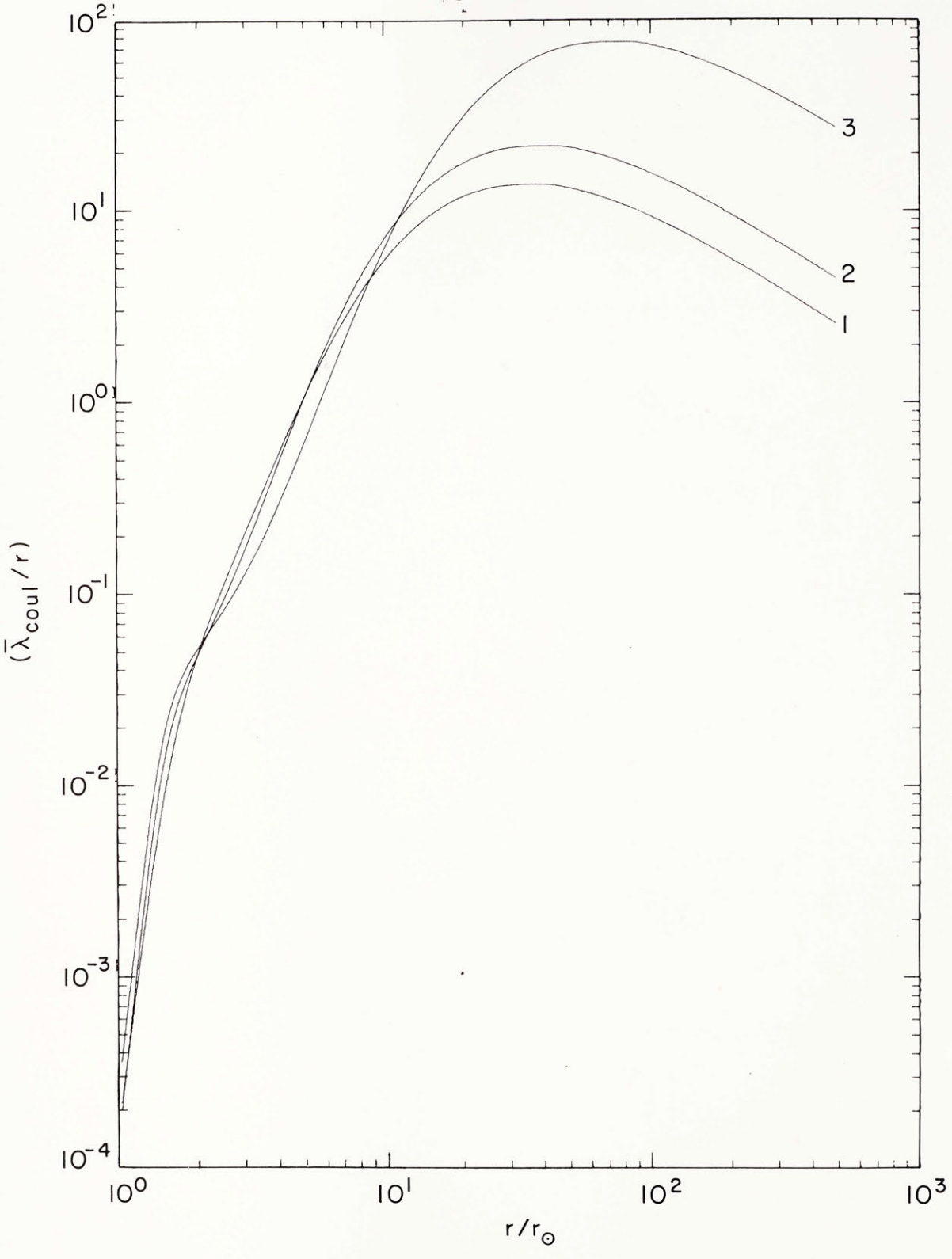
10^2
10^1
10^0
10^{-1}
10^{-2}
10^{-3}
10^{-4}
$(\bar{\lambda}_{coul}/r)$
10^0
10^1
10^2
10^3
$r/r_\odot$
3
2
1

Fig. 45

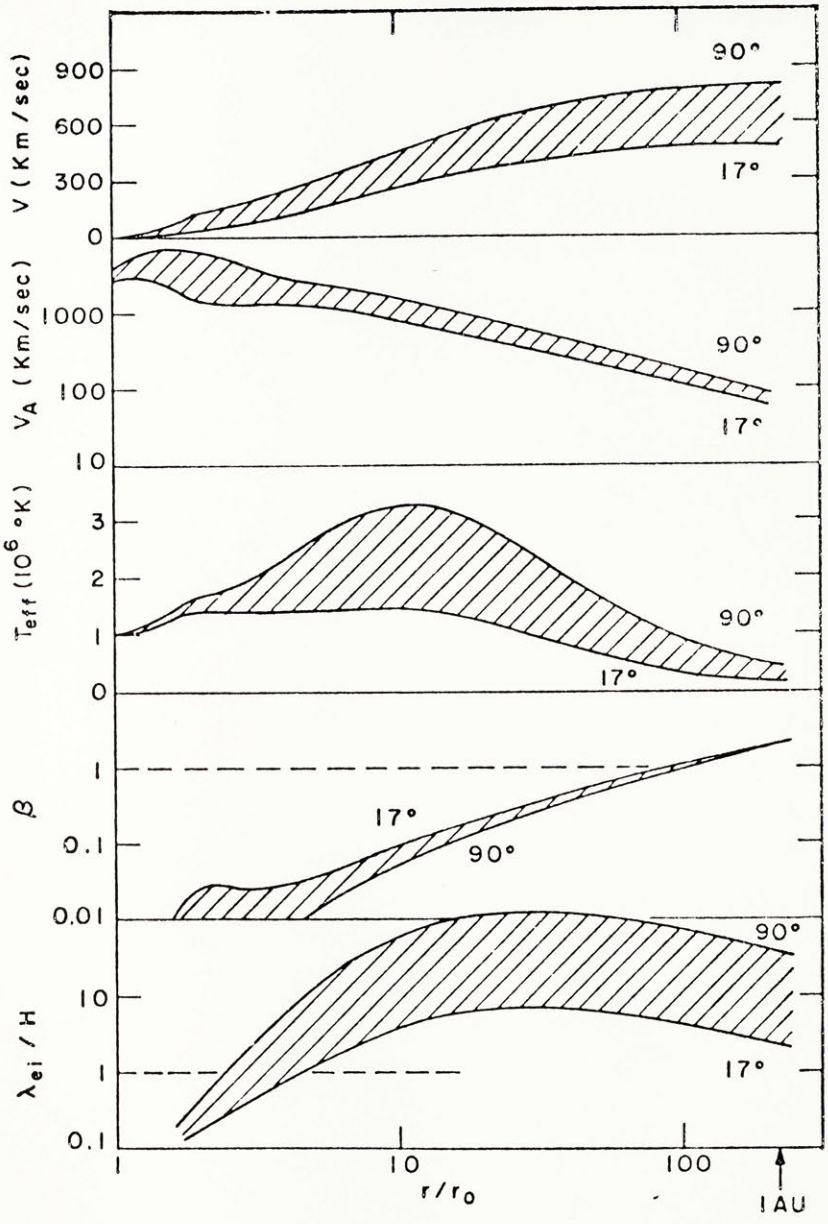
V (Km/sec)
900
600
300
0
90°
17°
V_A (Km/sec)
1000
100
10
90°
17°
T_{eff} (10^6 °K)
3
2
1
0
90°
17°
β
1
0.1
0.01
17°
90°
λ_{ei} / H
10
1
0.1
90°
17°
1
10
100
r/r_o
1AU

Fig. 46

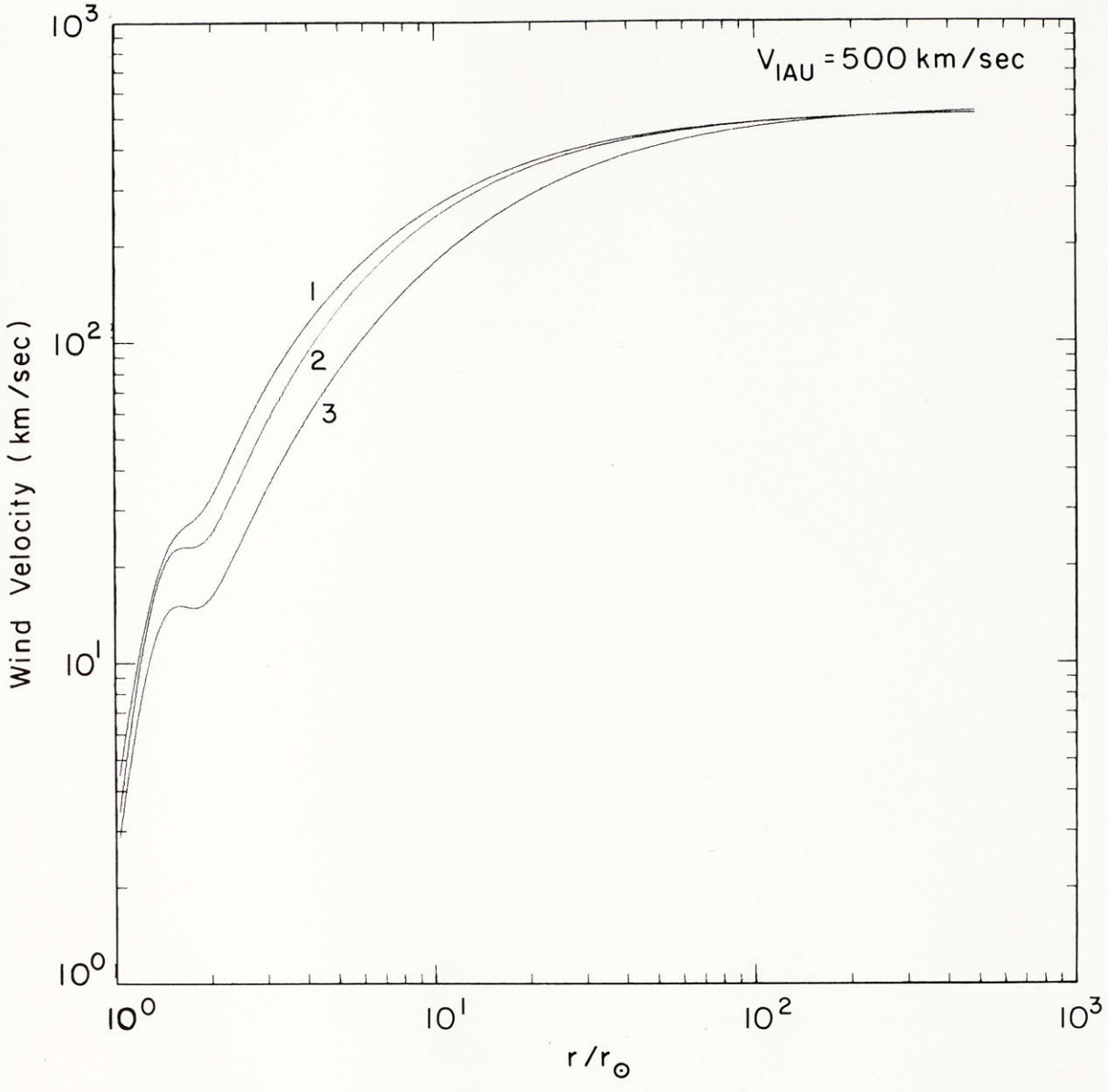
10^3
10^2
10^1
10^0
V_{IAU} = 500 km/sec
1
2
3
Wind Velocity (km/sec)
10^0
10^1
10^2
10^3
$r/r_\odot$

Fig. 47

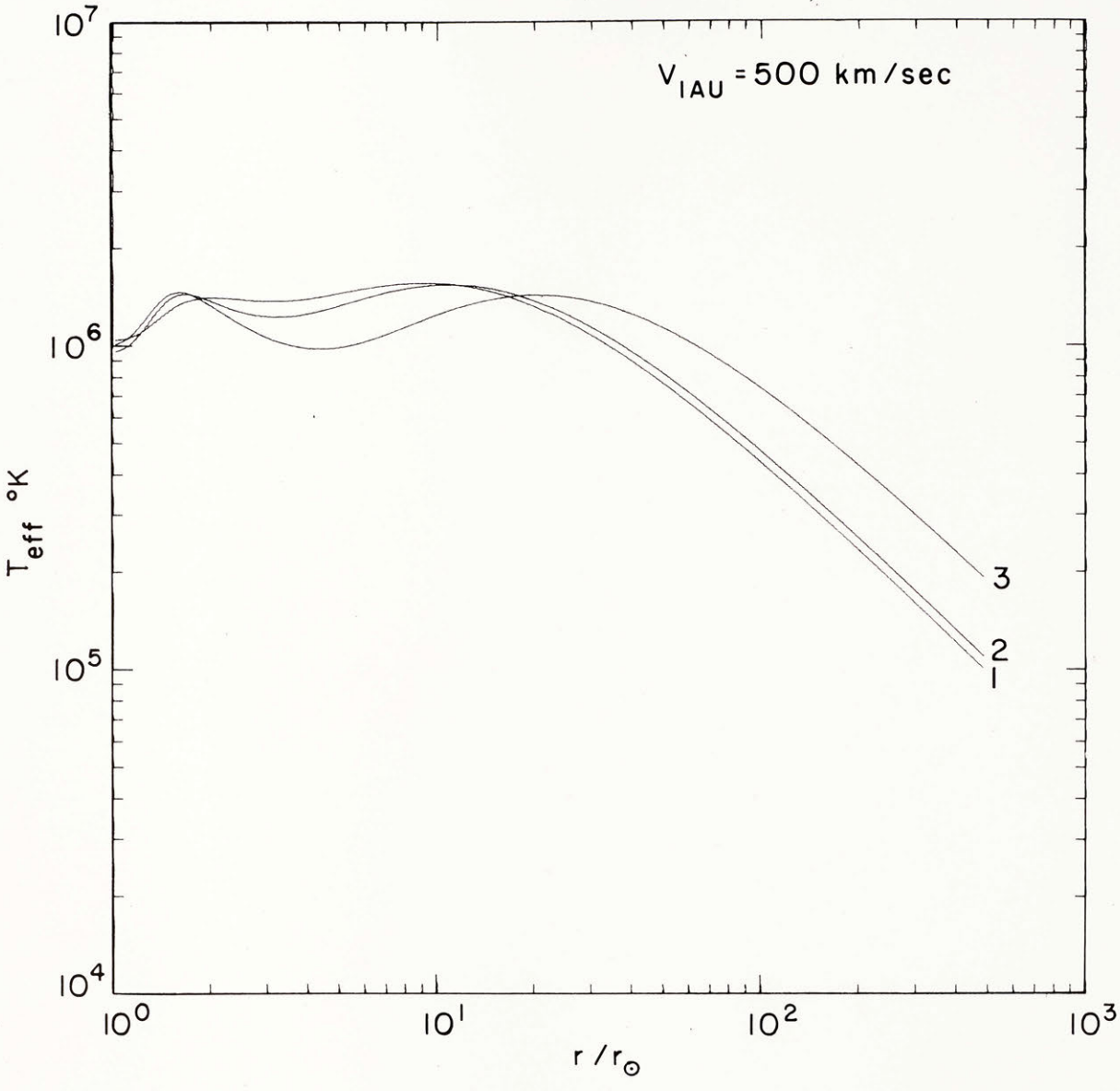
10^7
10^6
10^5
10^4
T_{eff} °K
V_{IAU} = 500 km/sec
3
2
1
10^0
10^1
10^2
10^3
$r/r_\odot$

Fig. 48

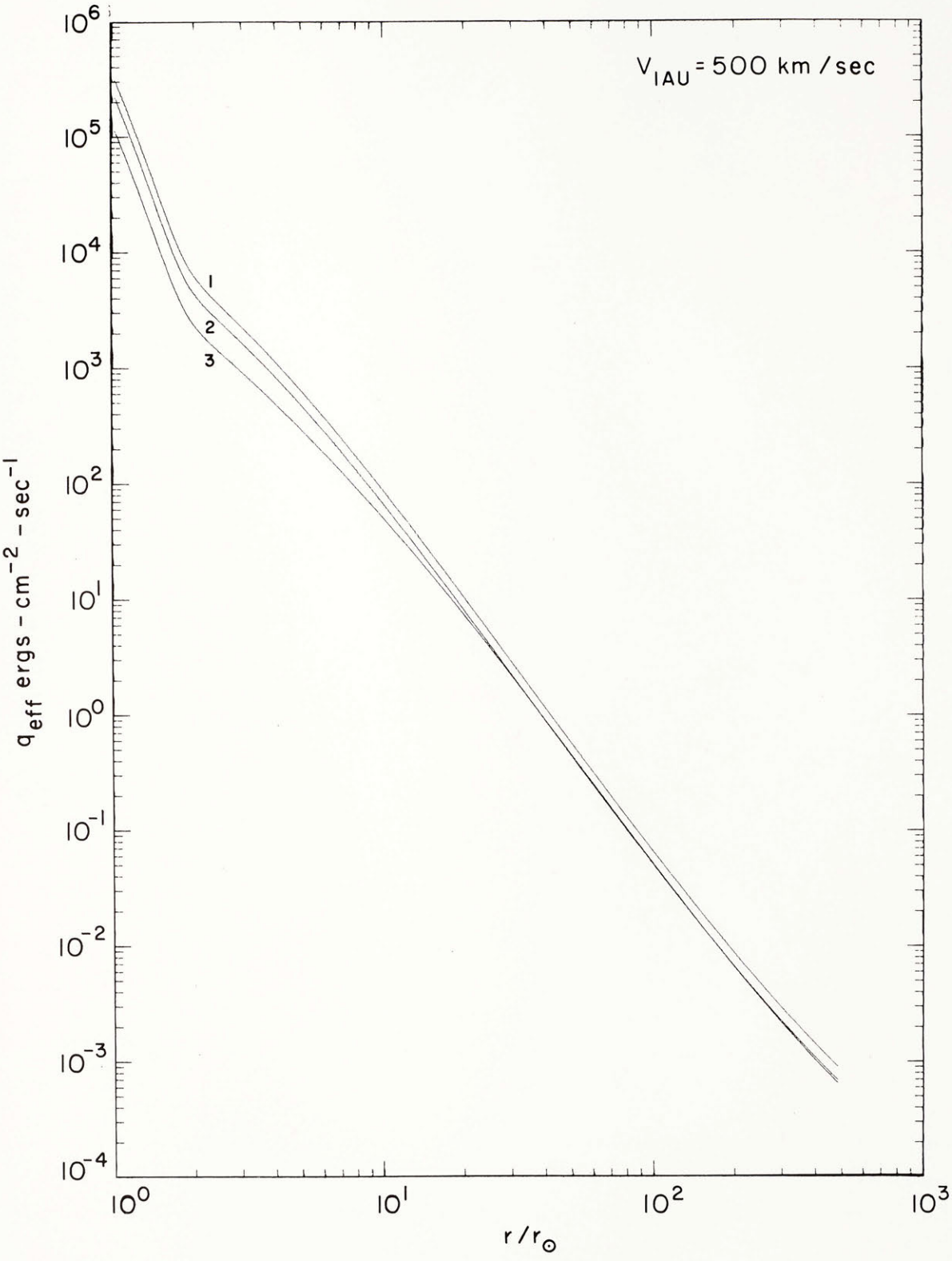
V_{1AU} = 500 km / sec
1
2
3
q_{eff} ergs - cm^{-2} - sec^{-1}
$r/r_\odot$
10^6
10^5
10^4
10^3
10^2
10^1
10^0
10^{-1}
10^{-2}
10^{-3}
10^{-4}
10^0
10^1
10^2
10^3

Fig. 49

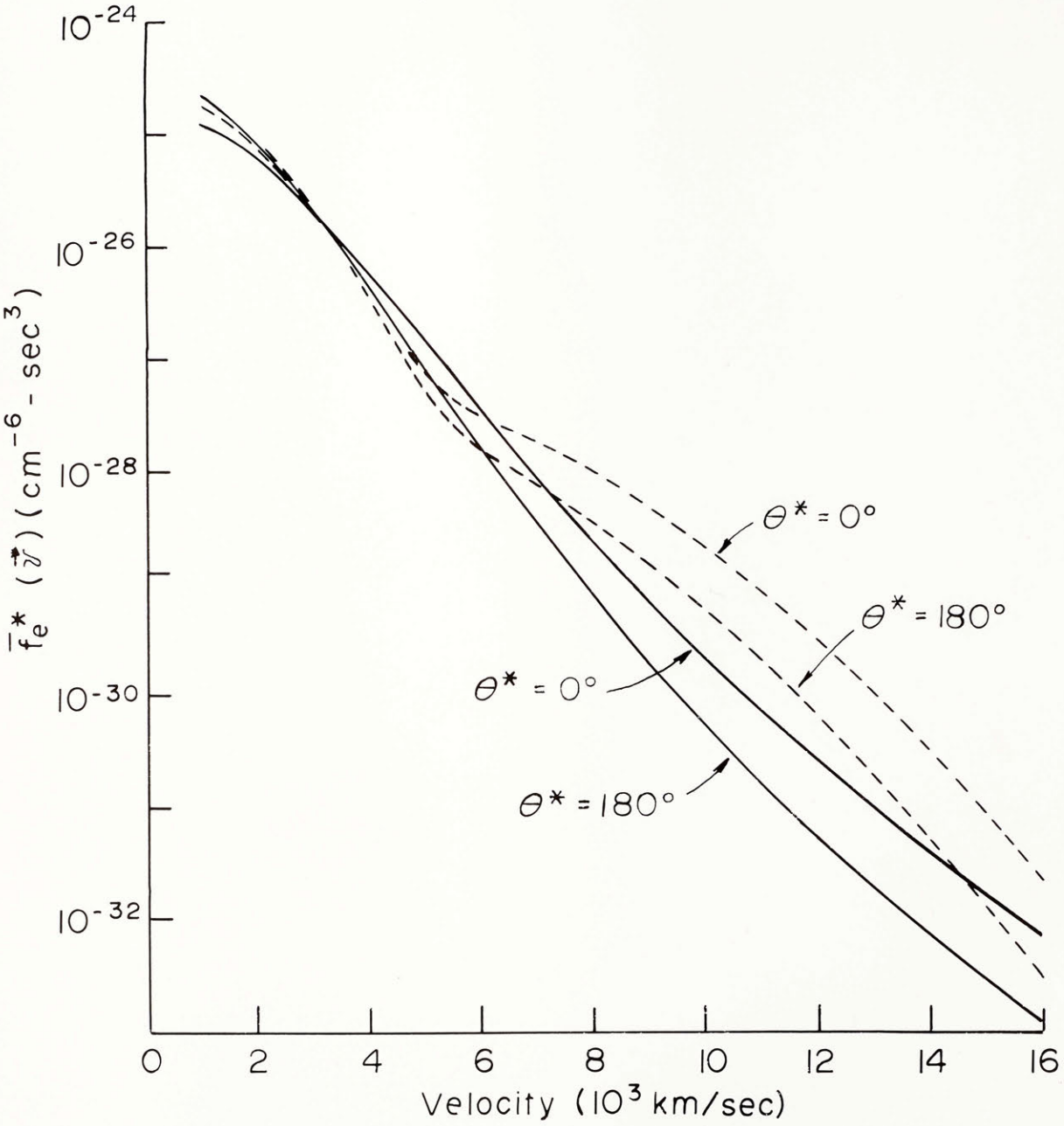
10^{-24}
10^{-26}
10^{-28}
10^{-30}
10^{-32}
$\bar{f}_e^*(\vec{v})$ (cm^{-6} - sec^3)
$\theta^* = 0°$
$\theta^* = 180°$
$\theta^* = 0°$
$\theta^* = 180°$
0
2
4
6
8
10
12
14
16
Velocity (10^3 km/sec)

Fig. 50

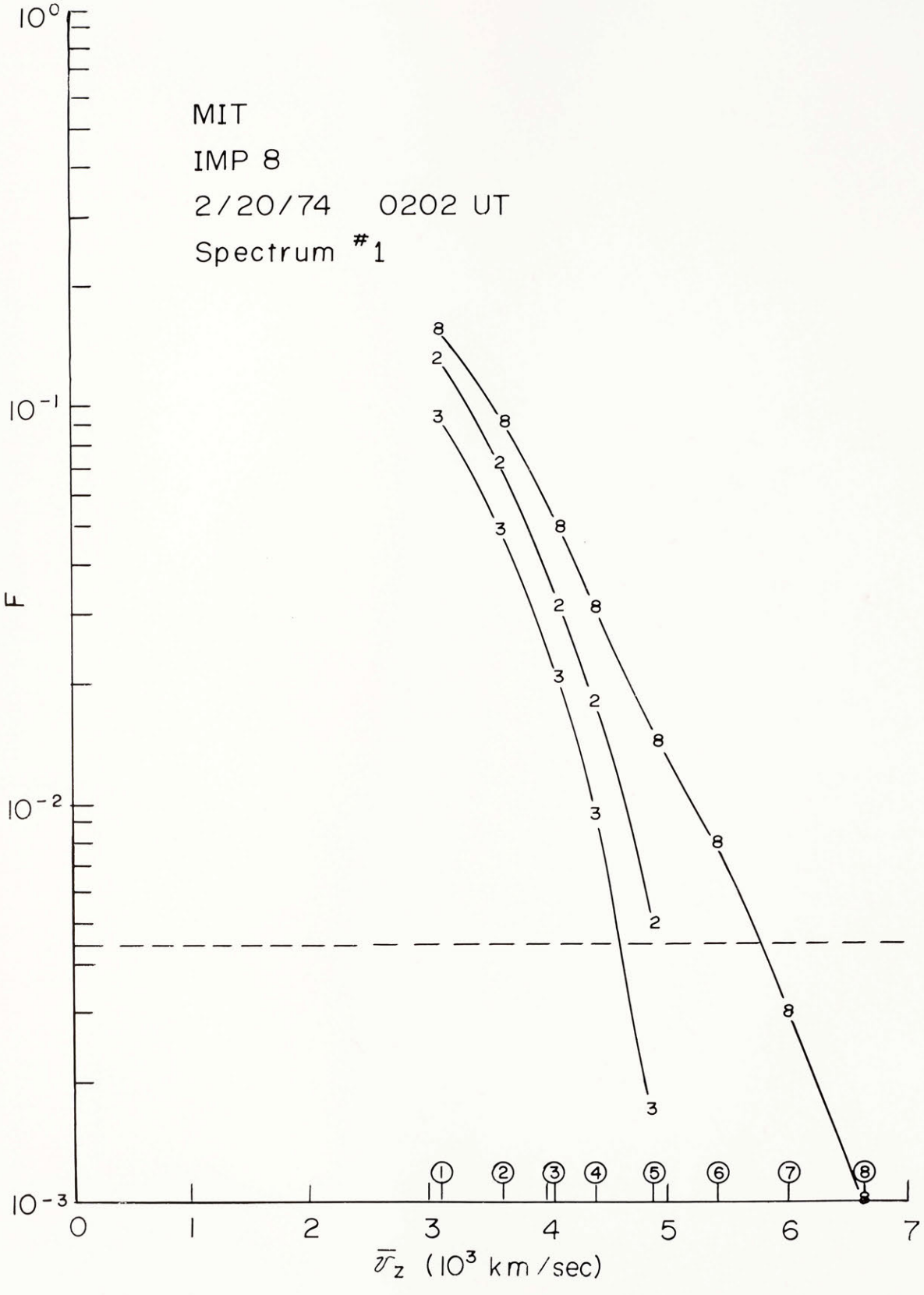
MIT
IMP 8
2/20/74 0202 UT
Spectrum #1
F
10^{0}
10^{-1}
10^{-2}
10^{-3}
0
1
2
3
4
5
6
7
$\bar{v}_z$ (10^3 km/sec)
①
②
③
④
⑤
⑥
⑦
⑧

Fig. 51

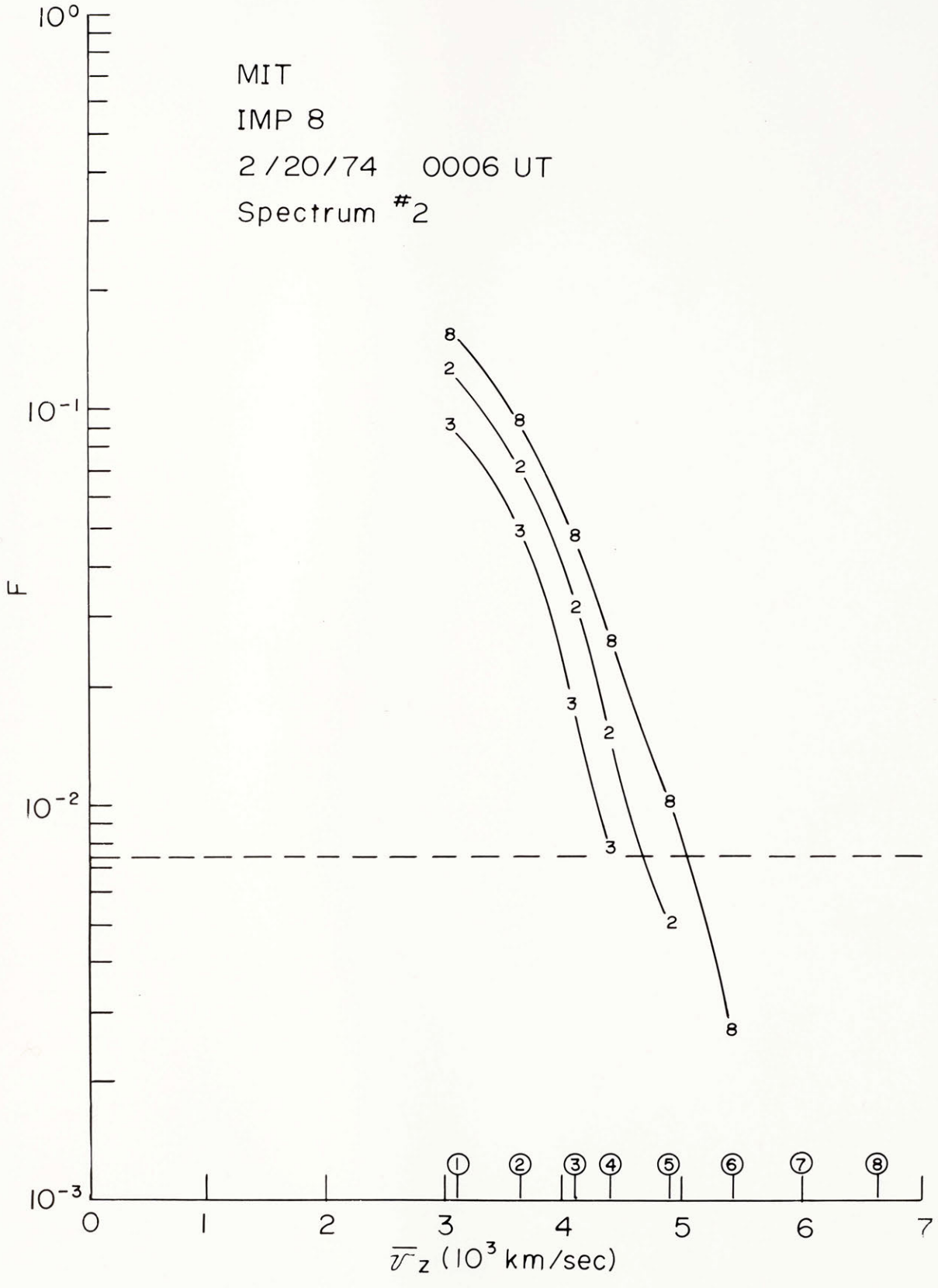
MIT
IMP 8
2/20/74 0006 UT
Spectrum #2
F
10^{0}
10^{-1}
10^{-2}
10^{-3}
0
1
2
3
4
5
6
7
$\overline{v}_z$ (10^3 km/sec)
①
②
③
④
⑤
⑥
⑦
⑧

Fig. 52

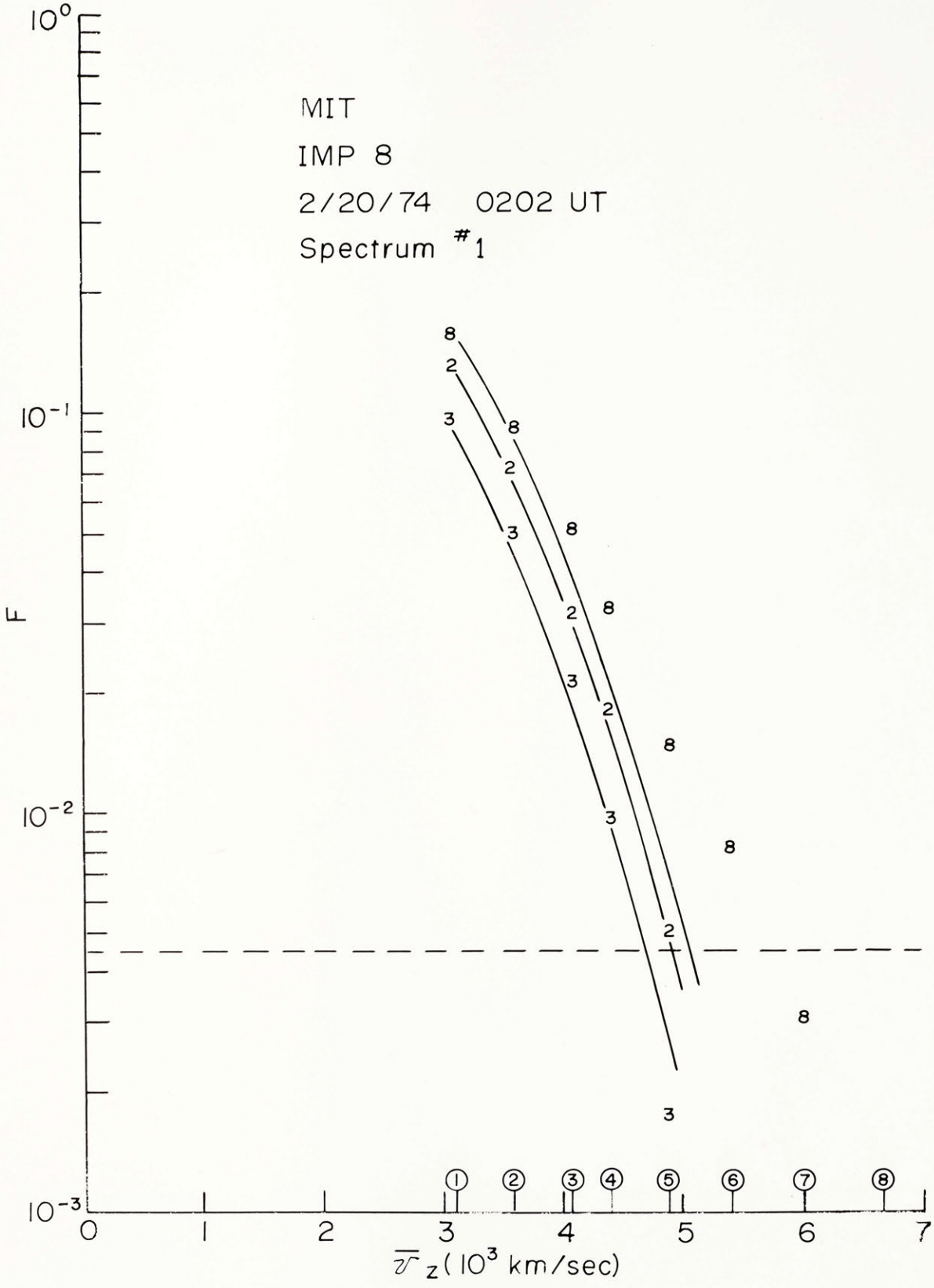
MIT
IMP 8
2/20/74 0202 UT
Spectrum #1
F
10^0
10^{-1}
10^{-2}
10^{-3}
0
1
2
3
4
5
6
7
$\overline{v}_z$ (10^3 km/sec)
①
②
③
④
⑤
⑥
⑦
⑧

Fig. 53

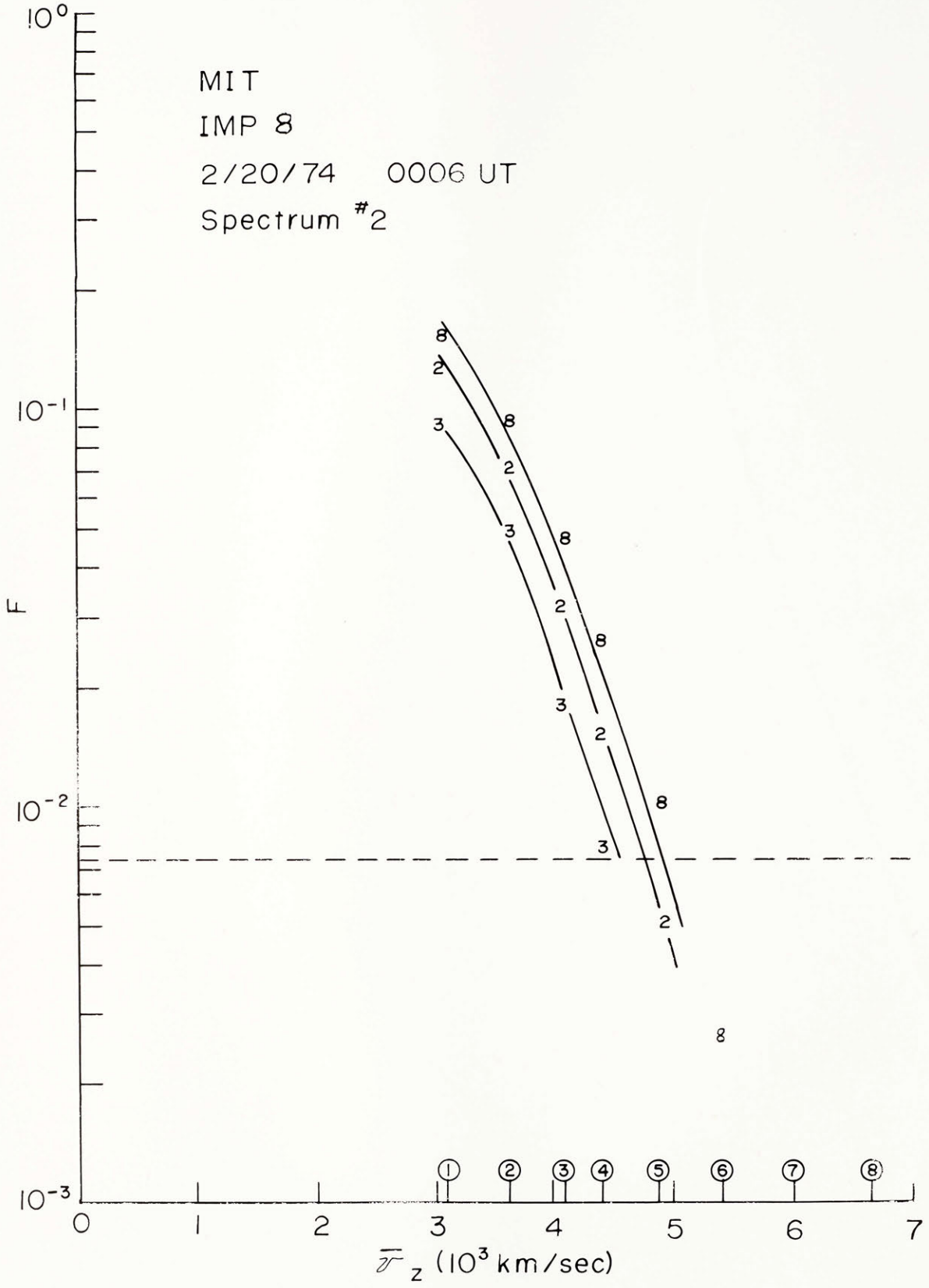
MIT
IMP 8
2/20/74 0006 UT
Spectrum #2
F
10^0
10^{-1}
10^{-2}
10^{-3}
0
1
2
3
4
5
6
7
$\bar{v}_z$ (10^3 km/sec)
①
②
③
④
⑤
⑥
⑦
⑧

Fig. 54

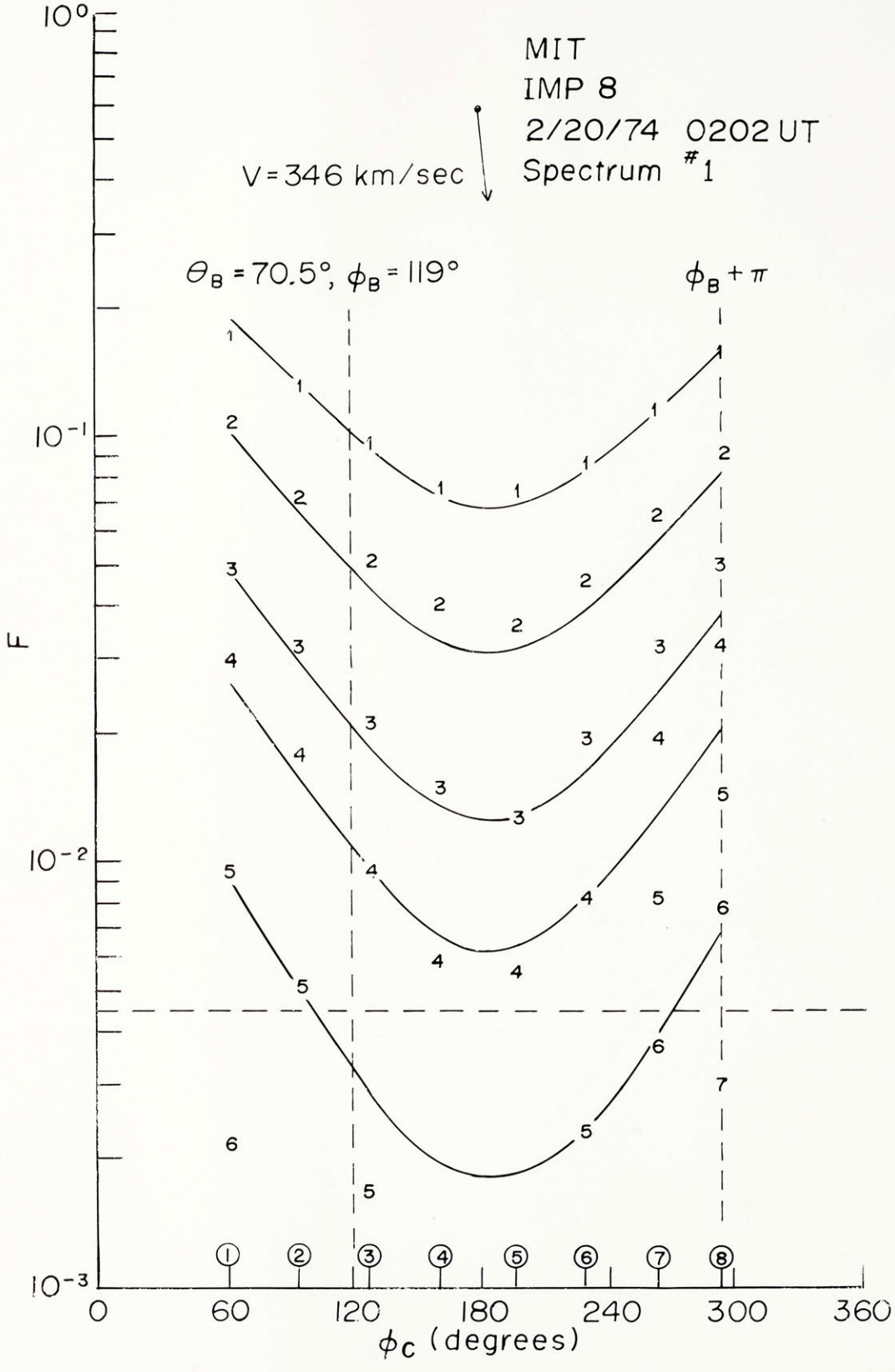
MIT
IMP 8
2/20/74 0202 UT
Spectrum #1
V = 346 km/sec
$\theta_B = 70.5°$, $\phi_B = 119°$
$\phi_B + \pi$
10^0
10^{-1}
10^{-2}
10^{-3}
F
0
60
120
180
240
300
360
ϕ_C (degrees)

Fig. 55

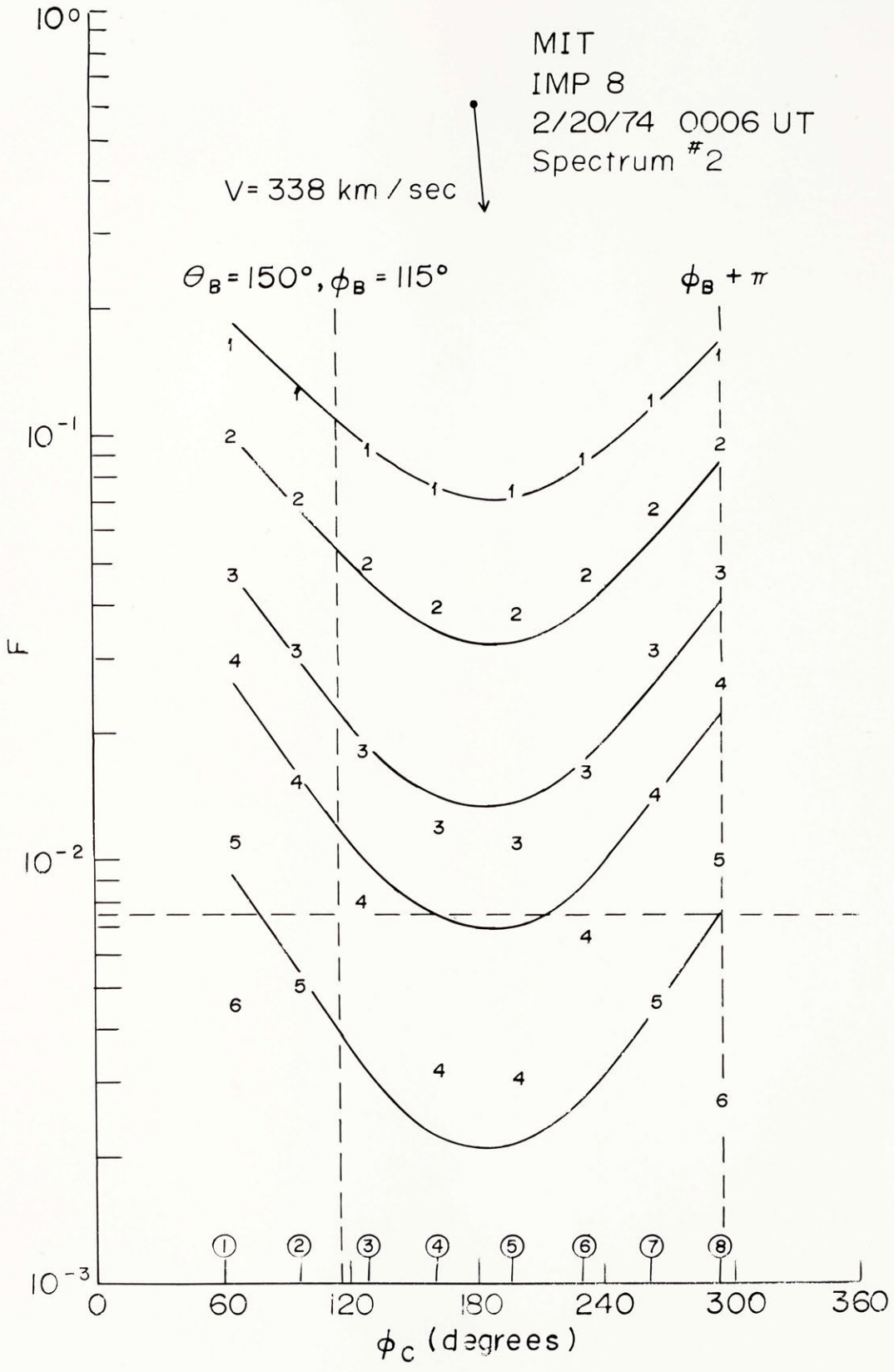
MIT
IMP 8
2/20/74 0006 UT
Spectrum #2
V = 338 km / sec
$\theta_B = 150°, \phi_B = 115°$
$\phi_B + \pi$
10°
10^{-1}
10^{-2}
10^{-3}
F
0
60
120
180
240
300
360
ϕ_C (degrees)

Fig.56

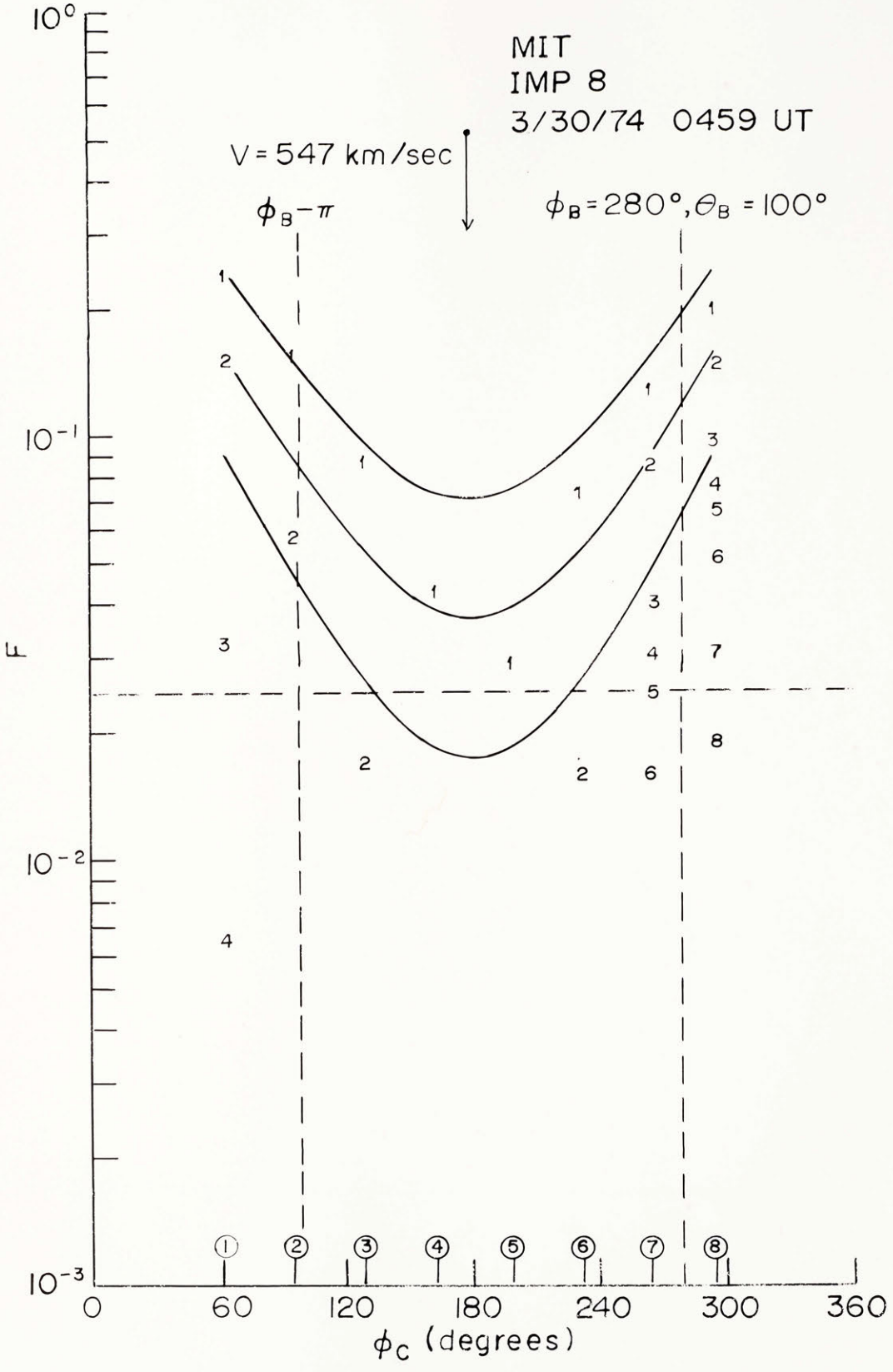
MIT
IMP 8
3/30/74 0459 UT
V = 547 km/sec
$\phi_B - \pi$
$\phi_B = 280°, \theta_B = 100°$
10^0
10^{-1}
10^{-2}
10^{-3}
F
0
60
120
180
240
300
360
ϕ_C (degrees)
① ② ③ ④ ⑤ ⑥ ⑦ ⑧

Fig. 57

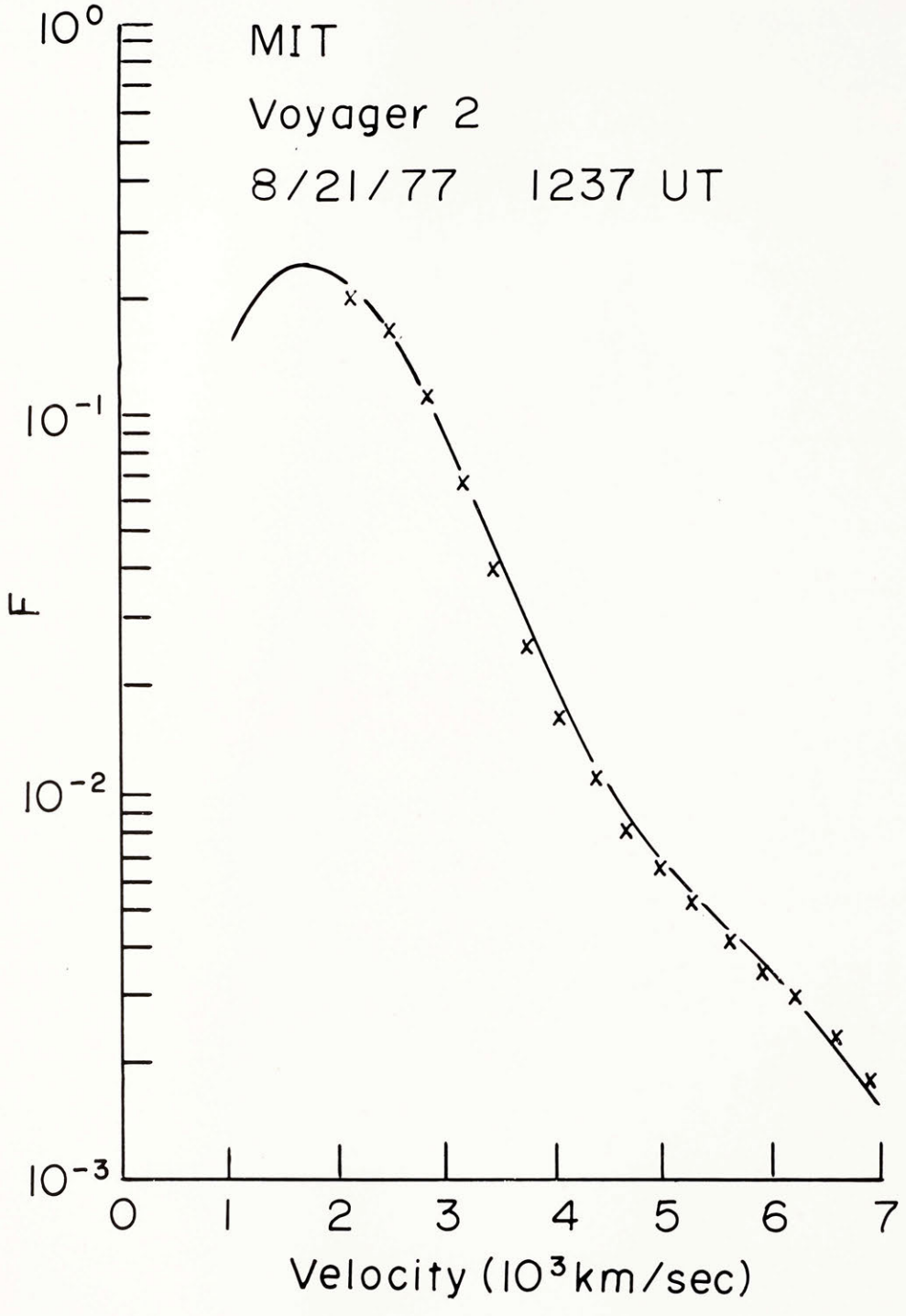
MIT
Voyager 2
8/21/77 1237 UT
10^0
10^{-1}
10^{-2}
10^{-3}
F
0
1
2
3
4
5
6
7
Velocity (10^3km/sec)

Table 1

			Electrons				Protons	
Channel #	Φ_o (volts)	$\Delta\Phi$ (volts)	v_{z+} (km/sec)	v_{z-} (km/sec)	v_z (km/sec)	v_z (km/sec)	v_z (km/sec)	v_z (km/sec)
1	28	11.0	3,432	2,808	3,120	624	-	-
2	38	11.0	3,889	3,355	3,622	534	-	-
3	48	11.0	4,317	3,843	4,080	474	-	-
4	55	11.4	4,620	4,164	4,392	456	102	10.6
5	68	14	5,136	4,631	4,884	505	114	11.7
6	83	17	5,672	5,118	5,395	554	125	12.9
7	102	21	6,290	5,672	5,981	618	139	14.4
8	126	26	6,991	6,304	6,648	687	155	16.0
9	155	32	7,754	6,991	7,373	763	171	17.7
10	190	39	8,583	7,743	8,163	840	190	19.5
11	235	48	9,543	8,614	9,079	929	211	21.6
12	280	59	10,432	9,386	9,909	1,046	230	24.3
13	354	73	11,718	10,566	11,142	1,152	259	26.8
14	437	90	13,019	11,741	12,380	1,278	288	29.7
15	531	110	14,355	12,938	13,650	1,417	317	33.0
16	659	136	15,989	14,416	15,200	1,573	353	37.0
17	813	166	17,750	16,022	16,886	1,728	393	40.0
18	995	204	19,641	17,721	18,680	1,920	434	45.0
19	1,219	251	21,744	19,610	20,677	2,134	481	50.0
20	1,503	310	24,146	21,772	22,960	2,374	534	55.0
21	1,849	378	26,771	24,161	25,466	2,610	592	61.0
22	2,266	467	-	-	-	-	673	69.0
23	2,793	573	-	-	-	-	747	77.0
24	3,436	705	-	-	-	-	829	85.0
25	4,216	866	-	-	-	-	918	95.0
26	5,183	1,068	-	-	-	-	1,018	105
27	6,368	1,304	-	-	-	-	1,128	116

Table 2

Height of Slats H	1.0"
Distance between Slats D	0.1735"
Width of Slats W	0.0265"
Normal Transparency of Slats T_{SN}	0.8675"
Modulator Grid d/b ratio	0.07
All other Grids d/b ratio	0.02647
Normal Transparency of Grid T_{GN}	0.627
$d_{12} = d_{23} = d_{45} = d_{76}$**	0.3"
d_{34}	0.125"
d_{56}	0.025"
d_{67}	0.25"
$H + \sum_{i=1}^{7} d_i$	2.6"
Radius of Aperture r_A	2.5"
Radius of Collector r_c	2.875"
Radius of Intermediate Ring r_R	2.45"
Normal Transparency T_N	0.5438
Angular Sector 1 - 7	33.75^o
Angular Sector 8	25.31^o
Spacecraft Spin Period	2.60 sec.
Integration Time Angular Sector 1-7	244 msec.

(Table 2 continued)

Integration Time Angular Sector 8	183 msec
TMS Spectrum Time	1 min. 44 sec.
NTMS Spectrum Time	55 sec.
AMS Spectrum Time	55 sec.

* " symbol means inches

** d_{nm} is the distance between grid planes n and m

Table 3

$n_e = 10\ cm^{-3}$ $V = 400$ km/sec*

$w_c = 1500$ km/sec

Energy Channel	ϕ_c (degrees	I_{Num} (picoamp)	I (picoamp)	$\frac{I_{Num} - I}{I_{Num}}$
1	62	25.18	24.12	.042
1	96	13.43	12.72	.053
1	129	7.628	7.149	.063
1	163	5.583	5.206	.068
1	197	5.853	5.464	.066
1	231	8.651	8.132	.060
1	264	15.79	15.01	.049
1	298	29.06	27.94	.039
2	62	7.075	6.713	.051
2	96	3.397	3.186	.062
2	129	1.754	1.630	.071
2	163	1.217	1.127	.070
2	197	1.286	1.192	.073
2	231	2.031	1.894	.067
2	264	4.104	3.864	.058
2	298	8.361	7.965	.047
3	62	1.790	1.698	.051
3	96	0.7818	0.7335	.060
3	129	0.3700	0.3448	.068
3	163	0.2449	0.2275	.071
3	197	0.2607	0.2424	.070
3	231	0.4368	0.4082	.065
3	264	0.9677	0.9116	.058
3	298	2.161	2.059	.047
4	62	0.6571	0.6210	.055
4	96	0.2692	0.2517	.065
4	129	0.1204	0.1117	.072
4	163	-	0.0714	-
4	197	-	0.0765	-
4	231	0.1440	0.1340	.069
4	264	0.3387	0.3180	.061
4	298	0.8049	0.7640	.051
5	62	0.1340	0.1221	.09
5	96	-	0.0448	-
5	129	-	0.0182	-
5	163	-	0.0111	-
5	197	-	0.0119	-
5	231	-	0.0222	-
5	264	-	0.0581	-
5	298	0.1678	0.1537	.084

* An aberration angle of 4.3° (wind appears to be coming from the west) resulting from the motion of the spacecraft was included in the calculations.

(Table 3 continued)

W_c = 2000 km/sec

1	62	72.65	70.69	.027
1	96	50.77	49.31	.029
1	129	36.78	35.67	.030
1	163	30.79	29.84	.031
1	197	31.63	30.66	.031
1	231	39.51	38.35	.029
1	264	55.68	54.13	.028
1	298	78.83	76.79	.026
2	62	38.91	37.87	.027
2	96	25.65	24.90	.029
2	129	17.63	17.08	.031
2	163	14.33	13.88	.031
2	197	14.79	14.33	.031
2	231	19.16	18.58	.030
2	264	28.56	27.76	.028
2	298	42.79	41.69	.026
3	62	19.22	18.77	.023
3	96	12.02	11.71	.026
3	129	7.872	7.657	.027
3	163	6.233	6.060	.028
3	197	6.457	6.280	.027
3	231	8.648	8.420	.026
3	264	13.56	13.23	.024
3	298	21.39	20.92	.022
4	62	11.55	11.31	.021
4	96	6.972	6.805	.024
4	129	4.423	4.309	.026
4	163	3.440	3.351	.026
4	197	3.574	3.482	.026
4	231	4.894	4.773	.025
4	264	7.940	7.762	.022
4	298	12.96	12.71	.019
5	62	5.371	5.239	.025
5	96	3.069	2.980	.029
5	129	1.853	1.794	.032
5	163	1.403	1.357	.033
5	197	1.463	1.416	.032
5	231	2.073	2.010	.030
5	264	3.545	3.449	.027
5	298	6.102	5.964	.023

Table 4 "Moment" Integrations. $z_o = 0.0$, $\Phi_o = 4.5$ volts

	#	ϕ_c deg	M_o cm^{-3}	$M_1 \times 10^{-8}$ cm^{-2} sec^{-1}	$M_2 \times 10^{10}$ dyne cm^{-2}	$M_3 \times 10^3$ erg-cm^{-2} sec^{-1}	n_o cm^{-3}	V_o km/sec	T_o 10^5 ^oK	$Q_o \times 10^3$ erg-cm^{-2} sec^{-1}	$V\cos\phi_c$ km/sec	ΔV_o km/sec	T 10^5 ^oK	$\Delta T/T$ %
$(\frac{T_{\shortparallel}}{T_{\perp}}) = 1.0$	1	0	7.336	10.17	1.192	25.284	12.776	355	1.42	-3.316	400	-45	1.2	18.3
	2	45	7.089	9.43	1.206	25.92	12.854	248	1.41	-2.37	283	-35	1.2	18.3
	3	90	6.479	7.75	1.246	27.26	12.958	0	1.39	0	0	0	1.2	18.3
	4	135	5.765	6.24	1.290	28.29								
	5	180	5.44	5.64	1.307	28.60								
	6	225												
	7	270												
	8	315												
$(\frac{T_{\shortparallel}}{T_{\perp}}) = 1.5$	1	0	7.146	10.28	1.258	26.552	12.51	358	1.52	-3.24	400	-42	1.286	18.2
	2	45	6.420	9.64	1.429	29.086	11.65	265	1.82	-1.83	283	-18	1.543	18.0
	3	90	6.438	7.96	1.323	28.681	12.70	13.4	1.50	0.471	0	13.4	1.286	16.6
	4	135	6.166	6.09	1.195	27.322	13.74	-241	1.21	2.77	-283	42	1.028	17.7
	5	180	5.360	5.80	1.371	29.788								
	6	225	5.229	6.55	1.495	30.916								
	7	270	6.257	7.79	1.30	28.21								
	8	315	7.573	9.40	1.098	24.55								
$(\frac{T_{\shortparallel}}{T_{\perp}}) = 2.0$	1	0	7.063	10.48	1.322	28.10	12.48	360	1.6	-3.34	400	-40	1.35	18.5
	2	45	6.052	9.88	1.60	31.68	11.03	276	2.14	-1.57	283	-7	1.8	19
	3	90	6.50	8.22	1.402	30.42	12.67	23.7	1.58	0.74	0	23.7	1.35	17
	4	135	6.623	6.05	1.131	26.88	14.69	-229	1.06	3.17	-283	54	0.9	18
	5	180	5.418	5.99	1.441	31.44								
	6	225	4.98	6.84	1.66	33.25								
	7	270	6.166	7.92	1.359	29.68								
	8	315	8.066	9.42	1.019	23.71								

Table 5 "Moment" Integrations. Z_o = 10.0, Φ_o = 4.5 volts

	#	ϕ_c deg	M_o cm^{-3}	$M_1 \times 10^{-8}$ cm^{-2} sec^{-1}	$M_2 \times 10^{10}$ dyne cm^{-2}	$M_3 \times 10^{3}$ ergs-cm^{-2} sec^{-1}	n_o cm^{-3}	V_o km/sec	T_o 10^5 ^oK	$Q_o \times 10^3$ ergs-cm^{-2} sec^{-1}	$V\cos\phi_c$ km/sec	ΔV_o km/sec	T 10^5 ^oK	$\Delta T/T$ %
$(\frac{T}{T_\perp}) = 1.0$	1	0	5.403	9.174	1.162	24.919	9.32	435	1.86	-2.59	400	+35	1.2	55
	2	45	5.207	8.504	1.174	25.337	9.36	306	1.86	-1.86	283	+23	1.2	55
	3	90	4.704	6.991	1.202	26.311	9.41	0	1.85	0	0	0	1.2	55
	4	135	4.156	5.640	1.226	27.194								
	5	180	3.916	5.128	1.228	27.505								
	6	225												
	7	270												
	8	315												
$(\frac{T}{T_\perp}) = 2.0$	1	0	5.276	9.37	1.269	27.26	9.106	443	2.065	-2.14	400	+43	1.35	53
	2	45	4.70	9.16	1.574	31.28	8.40	338	2.732	-0.91	283	+55	1.80	52
	3	90	4.57	7.24	1.314	28.47	9.170	7.6	2.070	0.335	0	+7.6	1.35	53
	4	135	4.65	5.37	1.057	26.00	10.30	-278	1.430	+3.169	-283	+5.0	0.90	59
	5	180	3.83	5.34	1.327	29.40								
	6	225	3.688	6.32	1.593	32.19								
	7	270	4.60	7.17	1.301	28.14								
	8	315	5.635	8.23	0.978	22.83								

Table 6 "Moment" Integrations. $\mathcal{Z}_o = 0.1$, $(T_{\shortparallel}/T_{\perp}) = 2.0$, $\Phi_o = 4.5$ volts

#	ϕ_c deg	M_o cm^{-3}	$M_1 \times 10^{-8}$ cm^{-2} sec^{-1}	$M_2 \times 10^{10}$ dynes cm^{-2}	$M_3 \times 10^3$ ergs-cm^{-2} sec^{-1}	n_o cm^{-3}	V_o km/sec	T_o 10^5 ^oK	$Q_o \times 10^3$ ergs $-cm^{-2}$ sec^{-1}	$V\cos\phi_c$ km/sec	ΔV_o km/sec	T 10^5 ^oK	$\Delta T/T$ %
1	0	7.023	10.37	1.315	28.01	12.40	352	1.61	-3.59	400	-48	1.35	19
2	45	6.050	9.836	1.591	31.66	10.54	285	2.23	-1.41	283	2	1.80	24
3	90	6.50	8.203	1.394	30.28	12.65	26.5	1.573	+0.83	0	26.5	1.35	16.5
4	135	6.600	6.031	1.131	26.92	14.61	-231	1.063	+3.28	-283	52	0.90	18
5	180	5.375	6.000	1.440	31.60								
6	225	4.493	6.833	1.652	33.07								
7	270	6.152	7.906	1.352	29.45								
8	315	8.006	9.407	1.014	23.64								

Table 7 "Moment" Integrations. $\mathcal{Z}_o = 1.0$ $(T_{\shortparallel}/T_{\perp}) = 2.0$, $\Phi_o = 4.5$ volts

#	ϕ_c deg	M_o cm^{-3}	$M_i \times 10^8$ cm^{-2} sec^{-1}	$M_2 \times 10^{10}$ dynes cm^{-2}	$M_3 \times 10^3$ erges-cm^{-2} sec^{-1}	n_o cm^{-3}	V_o km/sec	T_o $\times 10^5$ ^oK	$Q_o \times 10^3$ ergs-cm^{-2} sec^{-1}	$V\cos\phi_c$ km/sec	ΔV_o km/sec	T $\times 10^5$ ^oK	$\Delta T/T$ %
1	0	6.820	10.22	1.302	27.79	12.250	344	1.621	-3.73	400	-56	1.35	20
2	45	5.936	9.779	1.588	31.62	10.888	270	2.158	-1.69	283	-13	1.80	20
3	90	6.330	8.110	1.379	29.93	12.413	20.46	1.591	+0.66	0	+20.46	1.35	18
4	135	6.690	6.084	1.139	27.21	14.350	0	0	+3.71	-283	0	0.90	0
5	180	5.427	6.002	1.438	31.52								
6	225	4.952	6.843	1.655	33.31								
7	270	6.083	7.856	1.347	29.27								
8	315	7.660	9.217	1.009	23.50								

Table 8 "Moment" Integrations. $Z_o = \infty$, $\Phi_o = 4.5$ volts

	#	ϕ_c deg	M_o cm^{-3}	$M_1 \times 10^8$ cm^{-2} sec^{-1}	$M_2 \times 10^{10}$ dyne cm^{-2}	$M_3 \times 10^3$ erg-cm^{-2} sec^{-1}	n_o cm^{-3}	V_o km/sec	T_o 10^5 ^oK	$Q_o \times 10^3$ erg-cm^{-2} sec^{-1}	$V\cos\phi_c$ km/sec	ΔV_o km/sec	T 10^5 ^oK	$\Delta T/T$ %
$(\frac{T_\parallel}{T_\perp}) = 1.0$	1	0	3.615	7.592	1.106	22.785	5.54	713	2.720	2.951	400	+313	1.2	126
	2	45	3.340	6.895	1.103	22.544	5.48	511	2.786	2.02	283	+228	1.2	132
	3	90	2.710	5.381	1.065	21.704	5.42	0	2.848	0	0	0	1.2	137
	4	135	2.140	4.102	1.004	20.525								
	5	180	1.924	3.640	0.9706	19.834								
	6	225												
	7	270												
	8	315												
$(\frac{T_\parallel}{T_\perp}) = 2.0$	1	0	3.657	7.91	1.213	25.095	5.68	701	2.92	+2.416	400	301	1.35	116
	2	45	3.523	8.09	1.524	29.777	6.014	467	3.577	+1.277	283	184	1.80	99
	3	90	2.791	5.71	1.174	24.185	5.582	0	3.050	-0.169	0	0	1.35	126
	4	135	1.901	3.41	0.780	16.345	5.105	-547	2.362	-2.604	-283	-264	0.90	162
	5	180	2.023	3.93	1.079	22.679								
	6	225	2.491	5.28	1.445	28.50	$(\frac{T_\parallel}{T_\perp})_o = 1.51$							
	7	270	2.790	5.71	1.174	24.354								
	8	315	3.204	6.20	0.884	18.949								

Table 9 "Moment" Integrations. $v_{to} = 0$, $\Phi_o = 4.5$ volts

		ϕ_c	M_o	$M_1 \times 10^{-8}$	$M_2 \times 10^{10}$	$M_3 \times 10^3$	n_o	V_o	T_o	$Q_o \times 10^3$	$V\cos\phi_c$	ΔV_o	T	$\Delta T/T$
	#	deg	cm^{-3}	cm^{-2} sec^{-1}	dyne cm^{-2}	erg-cm^{-2} sec^{-1}	cm^{-3}	km/sec	10^5 ^oK	erg-cm^{-2} sec^{-1}	km/sec	km/sec	10^5 ^oK	%
$(\frac{T''}{T_\perp}) = 1.0$	1	0	7.475	10.30	1.198	25.425	12.81	368	1.408	-2.789	400	-32	1.2	17
	2	45	7.175	9.51	1.211	26.04	12.86	259	1.405	-2.02	283	-24	1.2	17
	3	90	6.498	7.73	1.248	27.264	13.0	0	1.391	0	0	0	1.2	17
	4	135	5.689	6.18	1.282	28.061								
	5	180	5.337	5.59	1.291	28.214								
	6	225												
	7	270												
	8	315												
$(\frac{T''}{T_\perp}) = 2.0$	1	0	7.26	10.72	1.350	28.89	12.63	371	1.61	-3.056	400	-29	1.35	19
	2	45	6.104	9.92	1.603	31.74	11.04	282	2.12	-1.394	283	-1	1.80	18
	3	90	6.662	8.48	1.442	31.38	12.86	40	1.59	+1.360	0	+40	1.35	18
	4	135	6.440	5.96	1.117	26.495	14.59	-245	1.06	+2.589	-283	+38	0.90	18
	5	180	5.372	6.03	1.455	31.946								
	6	225	4.931	6.81	1.634	33.134								
	7	270	6.195	7.97	1.371	30.074								
	8	315	8.147	9.53	1.026	23.906								

Table 10 "Moment" Integrations. $\mathcal{Z}_o$ = 0.0, Φ_o = 0.0 volts

	#	ϕ_c deg	M_o cm^{-3}	$M_1 \times 10^{-8}$ cm^{-2} sec^{-1}	$M_2 \times 10^{10}$ dyne cm^{-2}	$M_3 \times 10^{3}$ erg-cm^{-3} sec^{-1}	n_o cm^{-3}	V_o km/sec	T_o 10^5 ^oK	$Q_o \times 10^3$ erg-cm^{-2} sec^{-1}	$V\cos\phi_c$ km/sec	ΔV_o km/sec	T 10^5 ^oK	$\Delta T/T$ %
Φ_o=4.5volts V=0km/sec $(\frac{T_{\perp}}{T_{\parallel}})$ = 1.5	1	0	6.1275	7.80	0.8924	18.6186	10.0001	400	1.286	0	400	0	1.286	0
	2	45	5.7335	7.62	1.066	21.5052	9.9998	280	1.543	0	283	-3	1.543	0
	3	90	5.0002	5.57	0.887	18.977	10.0002	0	1.286	0	0	0	1.286	0
	4	135	4.1043	3.70	0.7076	15.686	10.0003	-283	1.028	0	-283	0	1.028	0
	5	180	3.873	3.80	0.882	18.6186								
	6	225	4.2663	4.816	1.063	21.5057								
	7	270	5.00004	5.573	0.8872	18.9767								
	8	315	5.896	6.526	0.7117	15.692								
Φ_o=4.5volts V=0km/sec $(\frac{T_{\perp}}{T_{\parallel}})$ = 1.0	1	0	6.4327				12.8654				0			
	2	45	"				"							
	3	90	"				"							
	4	135	"											
	5	180	"											
	6	225	"											
	7	270	"											
	8	315	"											

Table 11

Average Properties of the Low-Speed Solar Wind

Parameter	Average Value
V, km/sec	300 - 325
n, cm^{-3}	8.7
T_e, ^oK	1.5×10^5
$(T_{\parallel}/T_{\perp})_e$	1.1
T_p, ^oK	4×10^4
$(T_{\parallel}/T_{\perp})_p$	2
B, gamma*	5

* 1 gamma = 10^{-5} gauss.

Table 12

Average Particle and Energy Flux Densities in the Low Speed Solar Wind

Parameter	Average Value
nV	2.4×10^8 cm^{-2}-sec^{-1}
$\frac{1}{2}$ V^3	0.22 ergs/cm^2/sec.
$nV(\frac{5}{2}kT)$	8×10^{-3} ergs/cm^2/sec.
q_e	7×10^{-3} ergs/cm^2/sec.
q_p	10^{-5} ergs/cm^2/sec.

Table 13

Average Properties of Solar Wind High-Speed Streams*

Parameter	Average Value
Vmax, km/sec**	741 ± 49
nV, (10^8 cm^{-2}-sec^{-1})	3.3 ± 0.5
T_p, 10^5 °K	2.3 ± 0.3
T_e, 10^5 °K	0.9 ± 0.08
E_{TP}, (10^{-3} ergs/cm^2/sec)***	24 ± 5
q_e r, (10^{-3} ergs/cm^2/sec)	2.8 ± 0.9
E_A, (10^{-3} ergs/cm^2/sec)†	11.6 ± 4.7
E_{flux}, ergs/cm^2/sec††	2.4 ± 0.5

* See Text for definitions.

** V_{max} is maximum velocity in high-speed stream. High-speed streams were selected by the criterion that Vmax $\geq$ 650 km/sec.

*** $E_{TP} = nV\ (\frac{5}{2}kT_p)$ is the enthalpy flux.

† $E_A = nV\ (\frac{5}{2}m_p \langle \delta V^2 \rangle)$ is the Alfven energy flux where $\langle \delta V^2 \rangle$ is the mean square velocity perturbation.

†† $E_{flux} = nV\ [1/2m_p V^2 + \frac{GM_\odot m_p}{r_\odot}]$ is the kinetic plus gravitational energy flux.

Table 14

Averages of Selected Parameters for High-Speed Streams

Parameter	Average Value
n, cm^{-3}	3.9 ± 0.6
V, km/sec	702 ± 32
T_p, (10^5 °K)	2.3 ± 0.3
T_e, (10^5 °K)	1.0 ± 0.08
T_α, (10^5 °K)*	4.2 ± 3.0
n_α/n_p†	0.048 ± 0.005

* T_α is the temperature of alpha particles.
† n_α is the density of alpha particles.

Table 15

The Basic "One-Fluid" Model of the Coronal Expansion ($r_c=7.5r_\odot$)*

	$r=r_\odot$	r=1AU	$r\to\infty$
Density, cm^{-3}	7.4×10^7	8	
Expansion Speed, km sec^{-1}	1.2	260	315
Temperature, ^oK	1.6×10^6	1.6×10^5	$\propto r^{-2/5}$

* r_c is the sonic critical point

Table 16

	n_o	σ	$1.03r_\odot$		$10r_\odot$		$215r_\odot$	
			n	$\int r$	n	$\int r$	n	$\int r$
1	7.69×10^8	6.787	6×10^8	-8.787	13454	-2.79	15.9	-2.035
2	3.027×10^8	6.589	3.026×10^8	-8.589	8112	-2.66	10.0	-2.032
3	2.93×10^8	7.262	2.03×10^8	-9.262	4288	-2.76	4.85	-2.035

Table 17

Distance	Profile#	V (km/sec)	T_{eff} (10^6 °K)	q_{eff} (ergs/cm^2/sec)	δ_T	δ_q	γ	(λ_{conv}/r)
$1.03r_\odot$	1	.50	1.24	1.14×10^5	-.280	-2.61	1.03	7×10^{-5}
	2	.60	1.26	7×10^4	-.287	-2.61	1.03	1.42×10^{-4}
	3	.31	1.176	3.53×10^4	-.266	-2.62	1.03	1.28×10^{-4}
$10r_\odot$	1	199	1.13	218	.09	3.11	1.03	.21
	2	227	1.13	130	.012	3.12	1.04	.345
	3	206	1.12	71	.032	3.09	1.01	.628
$215r_\odot$	1	425	.137	14.5×10^{-3}	.95	3.08	1.47	.122
	2	425	.133	8.66×10^{-3}	.95	3.08	1.47	.187
	3	425	.145	4.74×10^{-3}	.944	3.08	1.46	.439
∞	1	439	0	0	1.0	3	1.5	0
	2	439	0	0	1.0	3	1.5	0
	3	440	0	0	1.0	3	1.5	0

Table 18

Model #	n_o	ρ_o	a_1	a_2	a_3	a_4	a_5
1	1.32×10^{8}	2.414×10^{-16}	4.68×10^{-4}	6.68	1.16	-8.15	8.72
2	1×10^{8}	1.83×10^{-16}	4.28×10^{-4}	7.53	1.02	-7.25	6.76
3	7.5×10^{7}	1.372×10^{-16}	2.82×10^{-4}	6.85	7.98	-24.61	19.41

Table 19

	$r/r_{\odot}$	θ	n	V	V_{θ}	V_{ϕ}	V_{Ap}	T_{eff}	q_{eff}	δx	δ_{θ}
Solution 1	1.03	23	1.395 x 10^8	6.372	3.263	0.70	2880	1.050 x 10^6	6.91 x 10^5	-12.71	1.160
	r_s= 4.58	66.8	2.9 x 10^4	192.0	21.1	4.57	1266	2.17 x 10^6	2.20 x 10^3	-3.20	0.552
	10.27	70.3	2840	383.0	18.7	5.30	790.0	2.8 x 10^6	231	-2.65	0.469
	r_A= 18.4	71.5	702	500.0	14.13	4.66	500.0	2.580 x 10^6	41.6	-2.4	0.440
	215	73	3.34	715.0	1.70	0.76	50.70	4.18 x 10^5	18.0 x 10^{-3}	-2.04	0.405
Solution 2	1.03	23	1.375 x 10^8	4.49	2.285	0.7	2880	1.047 x 10^6	3.13 x 10^5	-12.71	1.160
	r_s= 5.18	67.5	1.967 x 10^4	154	14.8	5.0	1210	1.458 x 10^6	584	-3.06	0.535
	10.27	70.3	2839	268	13.1	5.7	790	1.552 x 10^6	83	-2.65	0.469
	r_A= 23	71.8	392	380	8.4	5.8	380	1.24 x 10^6	6.76	-2.36	0.433
	215	73	3.34	500	1.2	.986	50.7	2.18 x 10^5	7 x 10^{-3}	-2.04	0.405

Table 20

Average Values and rms Variations of Solar Wind Electron Parameters

Parameters	Average Values	
n_e, cm^{-3}	10.0 ± 4.8	
V, km/sec	425 ± 73	
T_c, ^oK	$(1.25 \pm 0.29)10^5$	
$(T_{\parallel}/T_{\perp})_c$	1.08 ± 0.08	
q_e, cgs	$(7.8 \pm 5.4)10^{-3}$	
E_{BA}, Volts	62.5 ± 13	
	Model #1 *	Model #2 *
n_H, cm^{-3}	0.57 ± 0.23	0.34 ± 0.15
n_H/n	0.065 ± 0.027	0.038 ± 0.017
V_H, km/sec	689 ± 369	1215 ± 579
V_c, km/sec	-48.8 ± 33	-49.0 ± 30
T_H, ^oK	$(6.9 \pm 1.1)10^5$	$(8.7 \pm 1.4)10^5$
$(T_{\parallel}/T_{\perp})_H$	1.22 ± 0.18	1.29 ± 0.28
T_H/T_c	5.7 ± 1.3	7.2 ± 1.4

* C_H given by Eq. (4.5b) for Model #1, Eq. (4.5c) for Model #2.